

E-ISSN: 2687 - 6167
Number 49
June 2022

JSR A

JOURNAL OF SCIENTIFIC REPORTS A

JOURNAL OF SCIENTIFIC REPORTS A - JUNE 2022 - NUMBER 49



Kutahya Dumlupınar University Scientific Reports A
Evliya Celebi Campus Tavşanlı Road 10 KM. 43270 Kutahya
Phone : (0274) 443 19 42
E-mail : joursra@gmail.com
gsjsra.com

Dumlupınar University Press

gate of
science



Owner

On Behalf of Kütahya Dumlupınar University
Prof. Dr. Kazım UYSAL (Rector),
On Behalf of Institute of Graduate Studies
Assoc. Prof. Dr. Arif KOLAY (Director)

Editorial Board

Prof. Dr. Önder UYSAL
Prof. Dr. Cengiz YENİKAYA
Prof. Dr. Cengiz KARAGÜZEL
Prof. Dr. Gürsel YANIK
Prof. Dr. Cemal PARLAK
Prof. Dr. Fatih ŞEN
Prof. Dr. Oktay ŞAHBAZ
Assoc. Prof. Nevzat BEYAZIT
Assoc. Prof. Levent URTEKİN
Assist. Prof. Ümrhan ERÇETİN
Assist. Prof. Ceren KARAMAN
Assist. Prof. Onur KARAMAN

Kütahya Dumlupınar University/ Mining Engineering
Kütahya Dumlupınar University/ Chemistry
Kütahya Dumlupınar University / Mining Engineering
Kütahya Dumlupınar University / Geological Eng.
Ege University / Physics
Kütahya Dumlupınar University / Biochemistry
Kütahya Dumlupınar University/ Mining Engineering
Ondokuz Mayıs University / Environmental Eng.
Ahi Evran University / Mechanical Eng.
Kütahya Dumlupınar University / Mechanical Eng.
Akdeniz University / Electrical and Energy
Akdeniz University / Medical Services and Tech.

Journal of Scientific Reports-A started its publication life in 2000 as name of Journal of Science and Technology of Dumlupınar University and is a national peer-reviewed journal published regularly twice a year in June and December. The language of the journal is English. Articles submitted to the journal are evaluated by at least two referees who are experts in the subject and selected by the editorial board. All articles submitted to the journal are evaluated by the double-blind method. Articles submitted to our journal for review should not be previously published, accepted for publication and in the process of being evaluated for publication in another journal. All responsibility for the articles published in the journal belongs to the author(s).

The journal aims to share scientific studies carried out in the fields of science and engineering at national and international level with scientists and the public. Original research articles, review articles and short notes in science and engineering disciplines are accepted for the journal. Original research articles are expected to contain theoretical and experimental results and should not be published in other journals. In the review articles, it is expected that scientific, technological and current developments on a specific subject are reflected by using an extensive bibliography and made a satisfying evaluation of these. Short notes should be brief writings prepared to announce the first findings of an original study.

Editorial Policy

The journal is open access and the article evaluation period is between 1-2 months.

Correspondence Address: Kütahya Dumlupınar Üniversitesi Evliya Çelebi Yerleşkesi Fen Bilimleri Enstitüsü
43270 KÜTAHYA

Phone: 0 274 443 19 42

E-mail: joursra@gmail.com

Fax: 0 274 265 20 60

Webpage: gsjsra.com

Section Editors

Civil Engineering Prof. Dr. M. Çağatay KARABÖRK	Kütahya Dumlupınar University
Mechanical Engineering Prof. Dr. Ramazan KÖSE	Kütahya Dumlupınar University
Electrical-Electronics Engineering Assist. Prof. Kadir VARDAR	Kütahya Dumlupınar University
Computer Engineering Assoc. Prof. Doğan AYDIN	Kütahya Dumlupınar University
Industrial Engineering Assist. Prof. Üyesi Kerem CİDDİ	Kütahya Dumlupınar University
Mining Engineering Assist. Prof. Uğur DEMİR	Kütahya Dumlupınar University
Geology Engineering Assist. Prof. Muzaffer ÖZBURAN	Kütahya Dumlupınar University
Metallurgical and Materials Engineering Prof. Dr. İskender IŞIK	Kütahya Dumlupınar University
Food Engineering Prof. Dr. Muhammet DÖNMEZ	Kütahya Dumlupınar University
Environmental Engineering Doç. Dr. Nevzat BEYAZIT	Ondokuz Mayıs University
Mathematics Assist. Prof. Cansu KESKİN	Kütahya Dumlupınar University
Physics Assoc. Prof. Huriye Sanem AYDOĞU	Kütahya Dumlupınar University
Chemistry Assoc. Prof. Bülent ZEYBEK	Kütahya Dumlupınar University
Biology Assist. Prof. Nüket Akalın BİNGÖL	Kütahya Dumlupınar University
Biochemistry Assoc. Prof. Derya KOYUNCU ZEYBEK	Kütahya Dumlupınar University
Occupational Health and Safety Prof. Dr. Cem ŞENSÖĞÜT	Kütahya Dumlupınar University

Advisory Board

Prof. Dr. Sibel AKAR	Eskişehir Osmangazi University / Chemistry
Prof. Dr. Abdurrahman AKTÜMSEK	Selçuk University/ Biology
Prof. Dr. Mustafa ALTUNOK	Gazi University / Tree-Jobs Industrial Engineering
Prof. Dr. Uğur ARİFOĞLU	Sakarya University / Electrical and Electr. Engineering
Prof. Dr. Oktay ARSLAN	Balıkesir University / Chemistry
Prof. Dr. Şükrü ASLAN	Sivas Cumhuriyet University / Environmental Engineering
Prof. Dr. Ülfet ATAV	Selçuk University / Physics
Prof. Dr. Mustafa BAYRAKTAR	TOBB Ekonomi ve Teknoloji University / Mathematics
Prof. Dr. Niyazi BİLİM	Konya Technical University / Mining Engineering
Prof. Dr. İsmail BOZTOSUN	Akdeniz University / Physics
Prof. Dr. Erdal ÇELİK	Dokuz Eylül University / Metallurgical and Material Eng.
Prof. Dr. Hayri DAYIOĞLU	Kütahya Dumlupınar University / Biology
Prof. Dr. Muhammet DÖNMEZ	Kütahya Dumlupınar University / Food Engineering
Prof. Dr. Mehmet Ali EBEOĞLU	Kütahya Dumlupınar University / Elec.and Electr. Eng.
Prof. Dr. İsmail Göktay EDİZ	Kütahya Dumlupınar University / Mining Engineering
Prof. Dr. İsmail EKİNCİOĞLU	Kütahya Dumlupınar University / Mathematics
Prof. Dr. Kaan ERARSLAN	Kütahya Dumlupınar University / Mining Engineering
Prof. Dr. Zeynal Abiddin ERGÜLER	Kütahya Dumlupınar University / Geological Eng.
Prof. Dr. Seyhan FIRAT	Gazi University / Civil Engineering
Prof. Dr. Remzi GÖREN	Sakarya University / Metallurgical and Material Eng.
Prof. Dr. Rasim İPEK	Ege University / Mechanical Engineering
Prof. Dr. Refail KASIMBEYLİ	Eskişehir Technical University / Industrial Engineering
Prof. Dr. Hamdi Şükür KILIÇ	Selçuk University / Physics
Prof. Dr. Yaşar KİBİCİ	Bilecik Şeyh Edebali University / Geological Eng.
Prof. Dr. İsmail KOCAÇALIŞKAN	Yıldız Technical University / Molecular Bio. and Gen.
Prof. Dr. Mahmut KOÇAK	Eskişehir Osmangazi University / Math-Computer
Prof. Dr. Muhsin KONUK	Üsküdar University / Molecular Biology and Gen.
Prof. Dr. Mustafa KURU	Başkent University / Molecular Biology and Gen.
Prof. Dr. Ömer İrfan KÜFREVİOĞLU	Atatürk University / Biochemistry
Prof. Dr. Halim MUTLU	Ankara University / Geological Engineering
Prof. Dr. Ekrem SAVAŞ	İstanbul Ticaret University / Mathematics
Prof. Dr. Murat TANIŞLI	Eskişehir Technical University / Physics
Prof. Dr. Ali Rehber TÜRKER	Gazi University / Chemistry
Prof. Dr. Mustafa TÜRKMEN	Giresun University / Biology
Prof. Dr. Abdülmecit TÜRÜT	İstanbul Medeniyet University / Physics Engineering
Prof. Dr. Eşref ÜNLÜOĞLU	Eskişehir Osmangazi University / Civil Engineering
Prof. Dr. Nurettin YAYLI	Karadeniz Technical University / Pharmacy
Prof. Dr. Yusuf YAYLI	Ankara University / Mathematics
Prof. Dr. Elçin YUSUFOĞLU	Uşak University / Mathematics
Prof. Dr. Hüseyin Serdar YÜCESU	Gazi University / Automotive Engineering
Prof. Dr. Mehmet Tevfik ZEYREK	Middle East Technical University / Physics

JOURNAL OF SCIENTIFIC REPORTS-A
E-ISSN: 2687-6167

CONTENTS

RESEARCH ARTICLES

- Synthesis and Characterization of a Novel Benzimidazole-Oxime Ligand and Its Fe(II), Co(II), Ni(II), Cu(II) and Zn(II) Complexes* 1-11
Halil İLKİMEN*
- A Complete Solution to Exam Scheduling Problem: A Case Study* 12-34
Abdullah ELEN*
- Evaluation of the Transmission Line Tower Exposed to Artificial Ground Motions and Wind Loads* 35-48
Asuman Isil CARHOGLU*
- Code Generation Using Transformer Based Language Model* 49-61
Umut Can ALAÇAM¹, Çağla GÖKGÖZ², Cahit PERKGÖZ^{3,*}
- The Effects of Different Heat Treatment and Coating Techniques on X120crmo29-2 Martensitic Stainless Steel* 62-73
Esad KAYA^{1*}, Mustafa ULUTAN², Ahmet AKBULUT³
- Morphological, Hematological and Histopathological Effects of Propyl Paraben on Endocrine Glands of Male Rats at Prepubertal Period* 74-91
Eda Nur İNKAYA¹, Gözde KARABULUT^{2,*}, Nurhayat BARLAS³
- The Effect of Anisotropy on the Dynamic Properties of Schist Rocks* 92-104
Mehmet ÖZDEMİR^{1*}, Sunay BEYHAN², Kaan ERARSLAN³
- Stabilized Fem Solution of Magnetohydrodynamic Flow in Different Geometries* 105-117
Harun SELVİTOPI*

Facial Expression Recognition on Partial Face Images Using Deep Transfer Learning 118-129
İsmail ÖZTEL^{1*}, Gözde YOLCU ÖZTEL², Veysel Harun ŞAHİN³

Properties of Porous Ceramics Produced by Sintering Terra Rossa-Alkali Mixes 130-138
Canan MERCAN¹, Mehmet Uğur TOPRAK^{2,*}, Eda TAŞÇI³, Musa AKMAN⁴

Location Proofing Using Video Similarity 139-157
Cavide Balkı GEMİRTER^{1,*}, Tacha SERİF²

Confinement Effects on the Transport Properties of Room Temperature Ionic Liquid Based Electrolytes in Supercapacitors 158-170
Betül URALCAN*

The Effect of Minor Ti and Sr Addition on the Microstructural, Mechanical, and Corrosion Properties of A Biodegradable Mg-5Sn-3Al Alloy 171-183
Selma ÖZARSLAN*

Optimization of Atmospheric Plasma Spray Process Parameters for Deposition of Thermal Barrier Coatings 184-197
Savaş ÖZTÜRK*

REVIEW ARTICLES

Proton Transfer Salts and Their Complexes and Mixed-Ligand Complexes of Pyridine Dicarboxylic Acids and Piperazines: A Short Review 198-235
Nurgün BÜYÜKKIDAN*



RESEARCH ARTICLE

SYNTHESIS and CHARACTERIZATION of a NOVEL BENZIMIDAZOLE-OXIME
LIGAND and ITS Fe(II), Co(II), Ni(II), Cu(II) and Zn(II) COMPLEXES

Halil İLKİMEN*

* Kütahya Dumlupınar University, Faculty of Art and Sciences, Department of Chemistry, halil.ilkimen@dpu.edu.tr,
ORCID: 0000-0003-1747-159X

Receive Date: 30.09.2021

Accepted Date: 18.04.2022

ABSTRACT

(1E, 2Z)-2-(1H-benzoimidazol-1-yl)-2-(hydroxyimino)acetaldehyde oxime (H₂L) and its metal(II) complexes (**1-5**) (Fe, Co, Ni, Cu and Zn) were obtained using *anti*-monochloroglyoxime (glyox) and 1H-benzimidazole (HBI) in absolute ethanol for the first time. The H₂L was characterized by ¹H-NMR, elemental analysis, IR, and UV-Vis methods while IR, elemental analysis, UV-Vis, ICP-OES, TGA, molar conductivity and magnetic susceptibility techniques were applied to analyse of metal complexes (**1-5**).

Keywords: 1H-benzoimidazole, vic-dioxime, metal complex

1. INTRODUCTION

The coordination chemistry of vic-dioximes has been studied extensively. Many transition metal complexes of these ligands have been synthesized and continue to be synthesized. Potential applications of vic-dioximes and coordination compounds are useful in chemical industry, biological chemistry, pigment, medicinal chemistry, analytical and model compounds [1-5]. Vicinal dioximate ligands with a conjugated N=C-C=N system often form N,N-chelated metal complexes. The presence of slightly acidic hydroxy groups and slightly basic nitrogen atoms forms adjacent dioxime amphoteric ligands that form square-pyramidal, square-planar, corrine-type or octahedral complexes with metal ions such as cobalt, nickel, copper, zinc, palladium and cadmium as central atoms [6-17].

Benzimidazoles are involved in a great variety of biological processes [18]. They usually coordinate to the metal ions with their nitrogen atoms [19] and some of their complexes derivatives have been proven to possess antibacterial, fungicide and anti-hermitic activities [20-23]. A few reports on synthesis of metal complexes of dioxime and benzimidazole derivatives have been synthesized [24-29].

In this study, we prepared *anti*-monochloroglyoxime (glyox) and 1H-benzimidazole (HBI) according to literature [30-32] then we combined them to give a novel oxime ligand, named (1E, 2Z)-2-(1H-benzoimidazol-1-yl)-2-(hydroxyimino)acetaldehyde oxime (**1**). In addition, complex compounds of H₂L with metal(II) ions {Fe for **1**, Co for **2**, Ni for **3**, Cu(II) for **4** and Zn(II) for **5** salts were synthesized. The H₂L was characterized by ¹H-NMR, elemental analysis, IR, and UV-Vis methods

while IR, elemental analysis, UV-Vis, ICP-OES, TGA, molar conductivity and magnetic susceptibility techniques were applied to analyse of metal complexes (**1-5**).

2. EXPERIMENTAL

2.1. General Methods and Materials

All chemicals used were commercially purchased from Merck. Elementar Vario III EL for elemental analyses, Bruker DPX FT NMR for $^1\text{H-NMR}$, Bruker Optics Vertex 70 for IR, Perkin Elmer SII Exstar 6000 TG/DTA 6300 for thermal analyses, SHIMADZU UV-2550 for UV-Vis, Sherwood Scientific Magway MSB MK1 for magnetic moment measurements and WTW Cond 315i/SET for molar conductance instruments were used for the analysis of the structures.

2.2. Synthesis of Ligand H_2L .

We prepared *anti*-monochloroglyoxime (glyox) and 1*H*-benzimidazole (HBI) according to literature [30-32]. A solution of *anti*-monochloroglyoxime (1.22 g) in 25 mL pure ethanol was join to the solution of 1*H*-benzimidazole (1.18 g) in 25 mL pure ethanol. The *pH* of the mixture was adjusted from 3.5 to 7.0 with the addition of 0.1 M KOH solution. The yellow precipitated product was filtered and dried (m.p: 140 °C, 1.26 g, 65% yield). The structure of H_2L is given in Fig. 1.

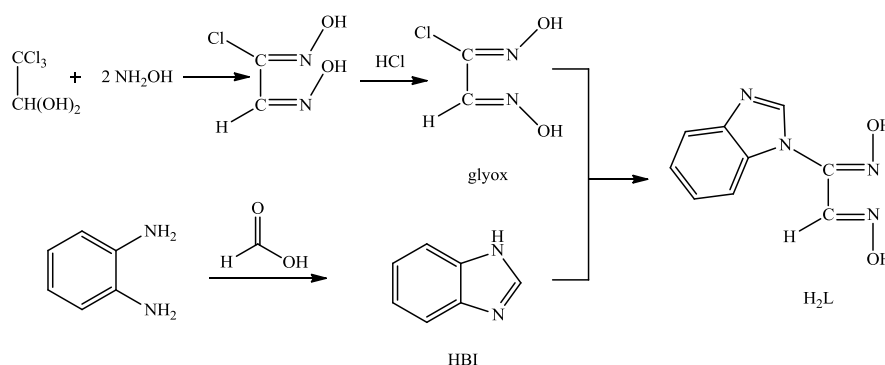


Figure 1. Synthesis of H_2L .

2.3. Synthesis of **1-5**.

A solution of 0.139 g $\text{FeSO}_4 \cdot 7\text{H}_2\text{O}$ for **1**; 0.1245 g $\text{Co}(\text{Ac})_2 \cdot 4\text{H}_2\text{O}$ for **2**; 0.124 g $\text{Ni}(\text{Ac})_2 \cdot 4\text{H}_2\text{O}$ for **3**; 0.099 g $\text{Cu}(\text{Ac})_2 \cdot \text{H}_2\text{O}$ for **4** and 0.111 g $\text{Zn}(\text{Ac})_2 \cdot 2\text{H}_2\text{O}$ for **5** in 10 mL water was added to the 0.194 g H_2L in 10 mL ethanol. The solids powder {violet for **1** (0.368 g, 69% yield), as brown for **2** (0.292 g, 70% yield), as red for **3** (0.963 g, 73% yield), as bottle green for **4** (0.372 g, 80% yield) and as yellow for **5** (0.604 g, 77% yield)} that precipitated in the reaction medium was filtered and dried. The structures of **1-5** are given in Figure 2.

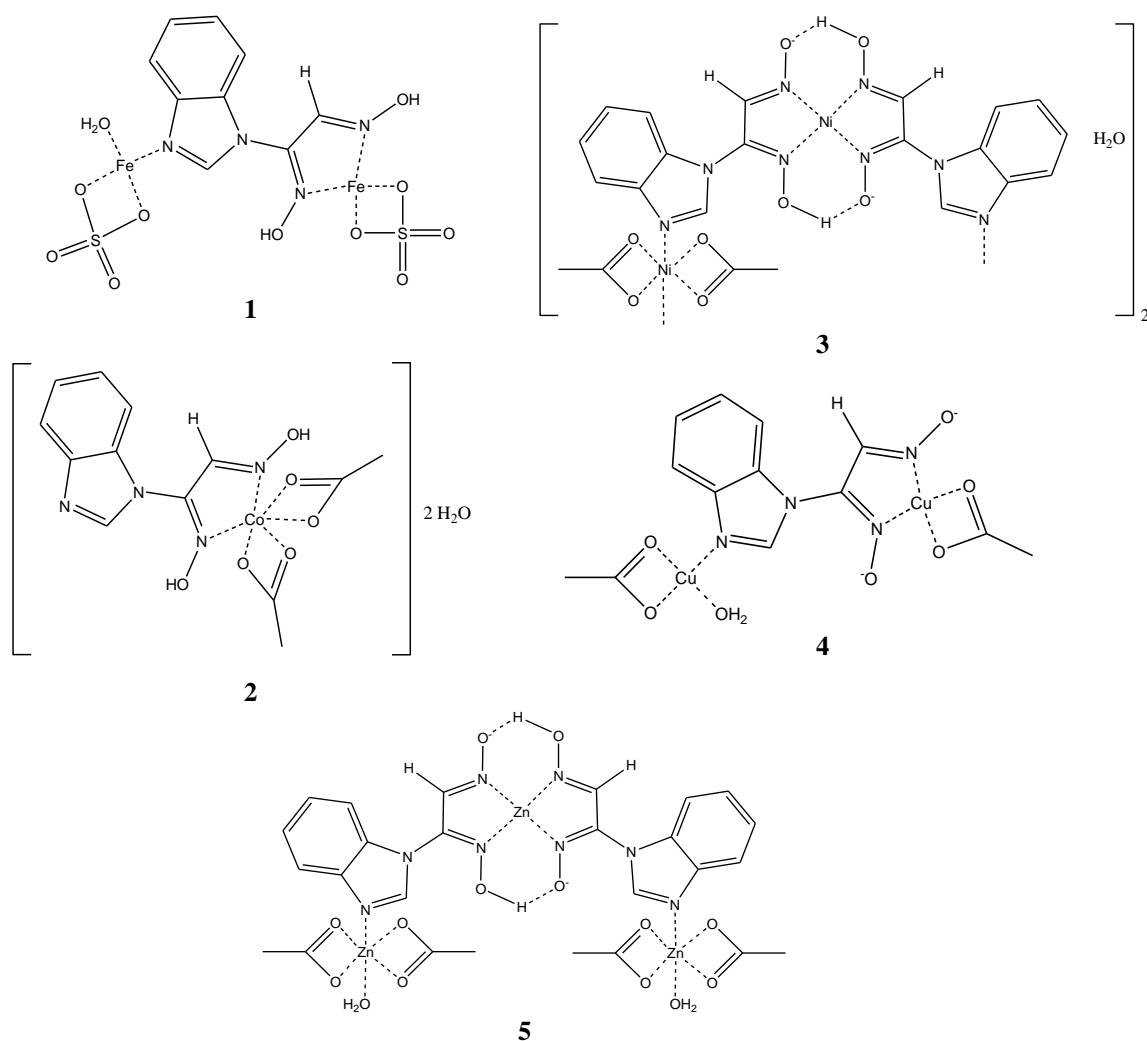


Figure 2. The compound 1-5.

Anal. Calcd. for **1** ($C_9H_8N_4O_2$) ($M = 204.19$ g/mol): C, 52.95%, H, 3.97%, N, 27.45%, Found: C, 52.94%, H, 3.95%, N, 27.44%. Anal. Calcd. for **2** ($C_9H_{10}N_4O_{11}S_2Fe_2$) ($M = 526.02$ g/mol): C, 20.50%, H, 1.90%, N, 10.65%, S, 12.20%, M, 21.00, Found: C, 20.55%, H, 1.92%, N, 10.65%, S, 12.19%, M, 21.23. Anal. Calcd. for **3** ($C_{13}H_{18}N_4O_8Co$) ($M = 417.24$ g/mol): C, 37.40%, H, 4.45%, N, 13.40%, M, 14.10, Found: C, 37.42%, H, 4.35%, N, 13.43%, M, 14.12. Anal. Calcd. for **4** ($C_{44}H_{22}N_{16}O_{18}Ni_4$) ($M = 1319.69$ g/mol): C, 40.01%, H, 3.39%, N, 16.97%, M, 17.70, Found: C, 40.04%, H, 3.36%, N, 16.98%, M, 17.79. Anal. Calcd. for **5** ($C_{13}H_{14}N_4O_7Cu_2$) ($M = 465.37$ g/mol): C33.57, %, H, 3.04%, N, 12.02%, M, 27.30, Found: C, 33.55%, H, 3.03%, N, 12.04%, M, 27.31. Anal. Calcd. for **6** ($C_{26}H_{30}N_8O_{14}Zn_3$) ($M = 784.73$ g/mol): C, 35.76%, H, 3.50%, N, 12.80%, M, 22.40, Found, C, 35.70%, H, 3.46%, N, 12.81%, M, 22.43.

3. RESULTS AND DISCUSSION

3.1. ¹H-NMR Result of H₂L.

The ¹H-NMR spectrum (Figure 3) and ¹H-NMR values (Table 1) of H₂L was obtained in d₆-DMSO at 25 °C.

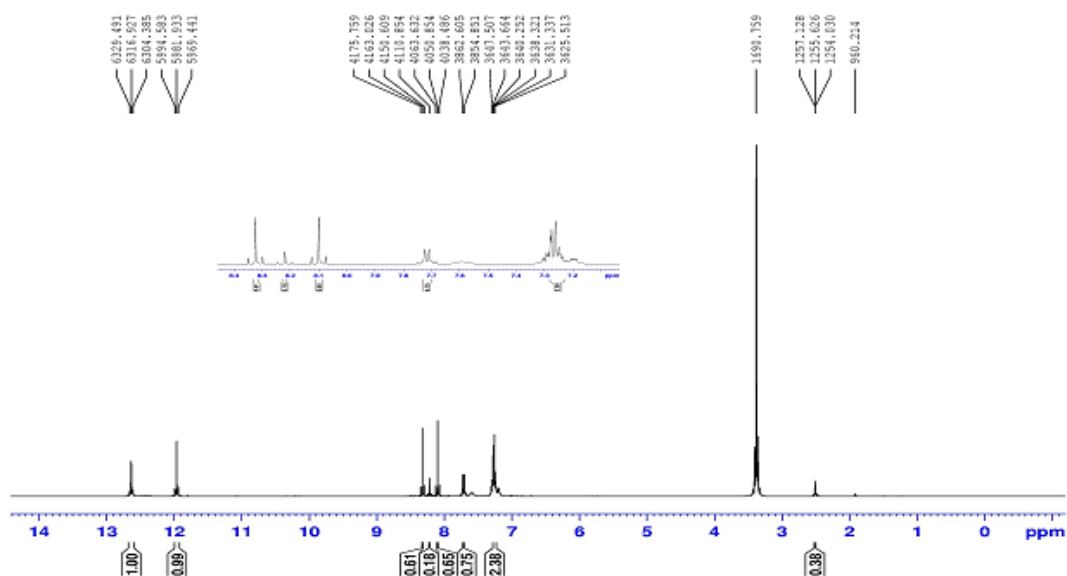


Figure 3. ¹H-NMR spectrum of compound H₂L.

Table 1. ¹H-NMR values for H₂L.

Proton	Chemical Shift (ppm)	Integration
H ¹	12.65	1.00
H ²	11.95	0.98
H ³	8.10	0.91
H ⁴	7.72	0.93
H ⁵ , H ⁶ and H ⁷	7.28	2.93

H ¹	12.65 (1H, s)
H ²	11.95 (1H, s)
H ⁴	8.33 (1H, s)
H ³	8.10 (1H, s)
H ⁸	7.72 (1H, d) [³ J _{H8-H7} = 7.75 Hz]
H ⁵ , H ⁶ and H ⁷	7.28 (3H, m) [³ J ≈ 7 Hz]

The ¹H-NMR spectrum of H₂L also contains two singlet peaks oxime part (H¹ and H²) at 12.65 ppm and 11.95 ppm, respectively, with the intensity of 1H atom for each. The CH proton of oxime part (H³) is easily distinguishable as singlet with the intensity of 1H atom at 8.10 ppm. The H⁴ proton of H₂L was observed at 7.72 ppm with the intensity of 1H atom. H⁵, H⁶ and H⁷ protons of H₂L are

observed at 7.28 ppm ($^3J \approx 7$ Hz) multiple with 3H intensity. H⁸ proton of H₂L is doublet as expected and arisen at 7.72 ppm ($^3J_{H8-H7} = 7.75$ Hz) with the intensity of 1H atom.

3.2. FT-IR Results

The IR data of all compounds are given in Table 2. There are broad vibration peaks between 3300 and 3320 cm⁻¹ attributed to the $\nu(\text{OH})$ vibrations of all compounds (except HBI). There is a medium vibration peak at 3114 cm⁻¹ attributed to the $\nu(\text{N-H})$ vibrations of HBI. This peak is not observed in compound H₂L due to replacing H atom of N-H in HBI with oxime group after reaction (Figure 1). $\nu(\text{C=N})$ of H₂L and $\nu(\text{C=N})_{\text{oxime}}$ and/or $\nu(\text{C=N})_{\text{HBI}}$ of **1-5** vibration are in the range of 1635-1610 cm⁻¹ with similar pattern. These frequencies are shifted to higher or lower energies when compared with free glyox (1605 cm⁻¹) and HBI (1615 cm⁻¹) indicating the coordination between metal ion and $\nu(\text{C=N})$ groups of H₂L (Figure 2). The peaks at the range of 3022-2823 cm⁻¹ (weak), 3100-3055 cm⁻¹ (weak), 1405-1587 cm⁻¹ (strong) are assigned $\nu(\text{C-H})$ methylene, $\nu(\text{C-H})$ aromatic (except glyox) and $\nu(\text{C=C})$ of all compounds, respectively. In the complexes (**1-5**), the peaks at the range of 475-469 and 579-531 cm⁻¹ can be assigned for the $\nu(\text{M-O})$ and $\nu(\text{M-N})$ modes also showing the coordination between metal ions and H₂L, respectively [33-35].

Table 2. IR data of all compounds (cm⁻¹).

	Glyox	HBI	H ₂ L	1	2	3	4	5
$\nu(\text{OH})$	3298(br)	-	3300(br)	3285(br)	3275(br)	3320(br)	3256(br)	3318(br)
$\nu(\text{NH})$	-	3114(m)	-	-	-	-	-	-
$\nu(\text{C-H})_{\text{Ar}}$	-	3061(w)	3055(w)	3050(w)	3065(w)	3100(w)	3059(w)	3059(w)
$\nu(\text{C-H})$	3022(w) 2883(w)	2939(w) 2857(w)	3000(w) 2823(w)	3005(w) 2912(w)	3007(w) 2920(w)	3023(w) 2997(w)	3000(w) 2997(w)	3000(w) 2992(w)
$\nu(\text{C=N})$	1605(s)	1615(s)	1630(s) 1609(s)	1635(s) 1610(s)	1636(s) 1610(s)	1636(s) 1609(s)	1631(s) 1609(s)	1636(s) 1610(s)
$\nu(\text{C=C})$	-	1587(s) 1499(s) 1478(s) 1456(s)	1542(s) 1500(s) 1480(s) 1457(s)	1542(s) 1499(s) 1456(s) 1412(s)	1545(s) 1499(s) 1455(s) 1420(s)	1548(s) 1501(s) 1454(s) 1412(s)	1559(s) 1499(s) 1457(s) 1405(s)	1548(s) 1506(s) 1481(s) 1456(s)
$\nu(\text{M-N})$	-	-	-	531(w)	548(w)	551(w)	543(w)	579(w)
$\nu(\text{M-O})$	-	-	-	472(w)	475(w)	474(w)	475(w)	469(w)

3.3. Thermal Analyses of Compounds 2-6.

TG-DTG and DTA curves of **1-5** are given in Figure 4-8, respectively, and their values are given in Table 3.

All complexes thermally decomposed in three steps. The endothermic first stage corresponds to the loss of two, two two one and two moles of water molecule for **1-5**. The endothermic second stage is consistent to the loss of C₉H₈NO₂, four, four, two and four moles acetate molecules and in the endothermic third stage S₂N₃O₈, one, four, one and two moles H₂L for **1-5**. The final product left undecomposed are FeO, CoO, NiO, CuO and ZnO, respectively.

Table 3. Thermal analyses results of compounds **1-5**.

Compound	Temperature (°C)	DTG _{max} (°C)	Leaving Group	Found (%)	Calculated (%)
1	35-157	63	2H ₂ O	3.20	3.42
	157-301	189, 238	C ₉ H ₈ NO ₂	30.70	30.83
	301-800	304, 314	S ₂ N ₃ O ₈	44.60	44.52
	-	-	FeO	21.50	21.23
2	35-195	55	2H ₂ O	7.90	8.55
	195- 401	291	4Ac	28.40	28.32
	401-900	439, 466	H ₂ L	49.40	49.00
	-	-	CoO	14.30	14.21
3	35-126	78	2H ₂ O	2.80	2.70
	126-300	289	4Ac	17.60	17.80
	300-650	376	4HL	61.70	61.70
	-	-	NiO	17.90	17.78
4	35-143	94	H ₂ O	3.80	3.88
	143-252	237	2Ac	18.50	18.48
	252-650	266, 271, 301	H ₂ L	50.50	50.33
	-	-	CuO	27.20	27.31
5	35-164	59	2H ₂ O	4.10	4.12
	164-255	221	4Ac	16.60	16.66
	255- 750	452, 538, 561	2H ₂ L	56.70	56.79
	-	-	ZnO	22.60	22.43

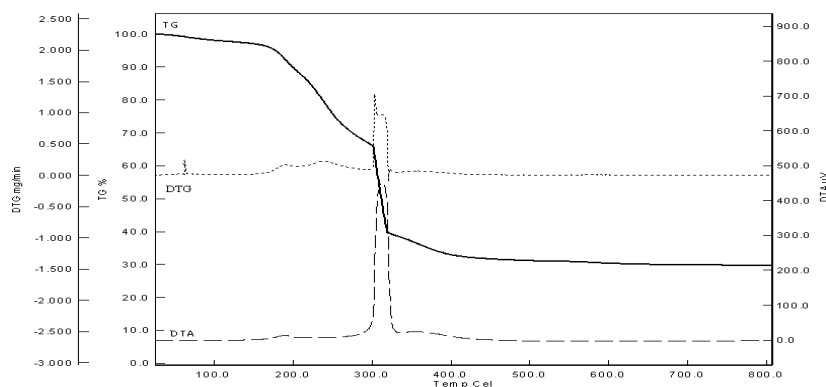


Figure 4. Thermal analysis results of **1**.

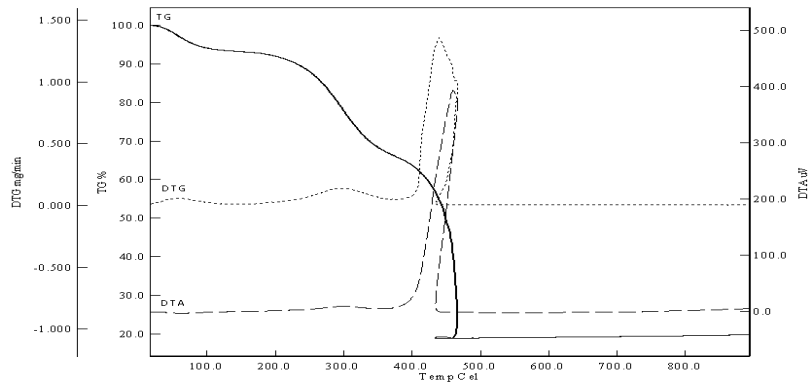


Figure 5. Thermal analysis results of 2.

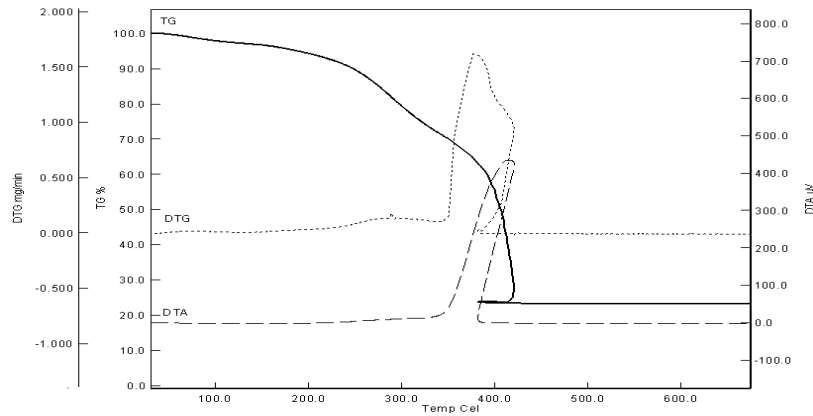


Figure 6. Thermal analysis results of 3.

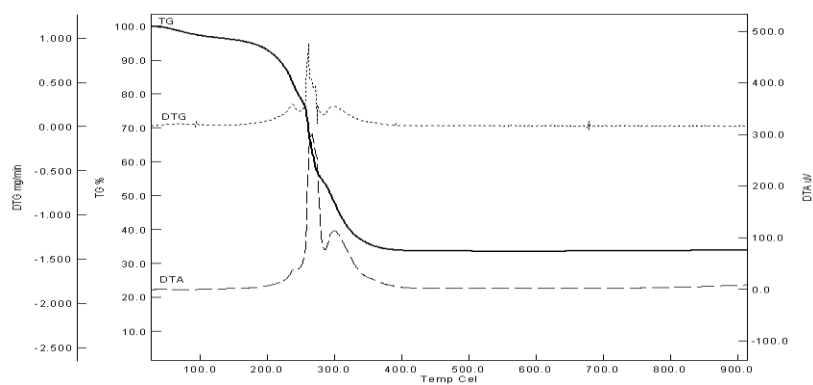


Figure 7. Thermal analysis results of 4.

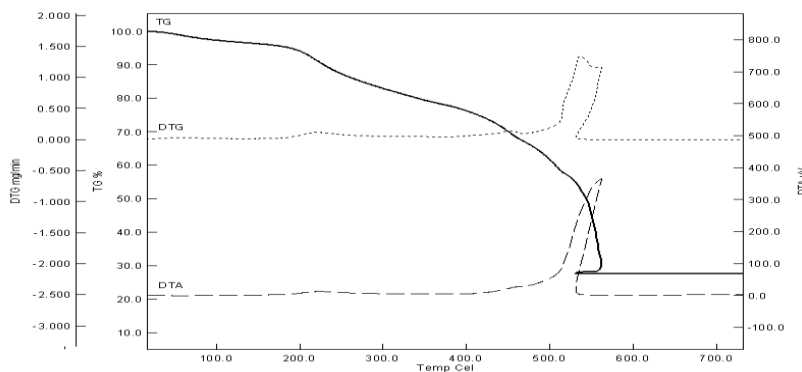


Figure 4. Thermal analysis results of **5**.

3.4. UV-vis Spectra, Molar Conductivities and Magnetic Susceptibilities

The UV-Vis spectra of glyox, HBI, H₂L and **1-5** were recorded in DMSO (1×10^{-3} M). The π - π^* transitions are seen in the spectra of free ligands glyox (239 and 289 nm) and HBI (288 nm), H₂L (236 and 289 nm), of **1** (236 and 286 nm), of **2** (288 and 294 nm), of **3** (288 and 294 nm), of **4** (294 and 360 nm) and of **5** (289 and 328 nm). The d-d transitions bands of **1-4** are observed at 794, 769, 802 and 821 nm, respectively. The d-d transition for **5** have not been observed due to containing Zn(II) ion (d^{10}).

The molar conductivity data in DMSO of **1-5** is the 0.9, 1.5, 2.0, 0.5 and 3.1 $\Omega^{-1}\text{cm}^2 \text{mol}^{-1}$, respectively, indicating that **1-5** are non-ionic [36]. These results agree that sulfate ion for **1** and acetate ions for **2-5** complexes are coordinated to the metal ions.

Magnetic moments **1-5** are 4.88, 3.75, 2.79, 1.70 and 0 BM per metal(II) ion, indicating the presence of four, three, two, one and zero unpaired electrons, respectively.

4. CONCLUSIONS

In this study, non-ionic metal(II) complexes (Fe, Co, Ni, Cu and Zn) (**1-5**) with a novel *vic*-dioxime compound, named (1*E*, 2*Z*)-2-(1*H*-benzoimidazol-1-yl)-2-(hydroxyimino)acetaldehyde oxime (H₂L) were prepared and characterized by analysis methods results. According to these results the structures of complexes are proposed tetrahedral (**1** and **4**), octahedral (**2**) and square plane/octahedral (**3** and **5**). Different application areas of the synthesized compounds should be examined.

ACKNOWLEDGEMENT

This work was supported by Dumlupınar University Research Foundation (Grant No: 2010-02) and was carried out at the Chemistry Department of same University. In addition, the author would like to thank Prof. Dr. Cengiz YENİKAYA.

REFERENCES

- [1] Coban, B., Eser, N., Babahan, I., (2017), DNA binding by copper (II) complexes of semithiocarbazone containing ligands, *Bulgarian Chemical Communications*, 49(4), 908-913.
- [2] Deveci, P., Taner B., (2013), Synthesis, spectroscopic, and cyclic voltammetric studies of ferrocene containing *vic*-dioxime ligand and its complexes with Ni(II), Cu(II), Co(II), Cd(II) and Zn(II), *Inorganica Chimica Acta*, 405, 326-330.
- [3] Motaleb, M. A., Selim, A. A. (2019), Dioximes: Synthesis and biomedical applications, *Bioorganic Chemistry*, 82, 145-155.
- [4] Tuyun, A. F., Bayrak, N., Yıldırım, H., Yıldız, M., Kara, E. M. Celik, B. O., (2021), Bis(Substituted Phenylamino)Glyoxime derivatives: Synthesis, characterization, and antimicrobial evaluation, *Journal of Molecular Structure*, 1242, 130812.
- [5] Findik, M., Ucar, A., Türkkkan E., Pehlivanoglu, S., Ozcan E., (2021), Synthesis of *anti*-4-phenoxyphenylaminoglyoxime and its some transition metal complexes: Spectral, DFT, electrochemical and anticancer activity studies, *Journal of Molecular Structure*, 1215, 128190.
- [6] Deveci, P., Taner, B., Kılıç, Z., Solak, A.O. and Özcan, E., (2012), Synthesis and structural and electrochemical characterization of novel macrocyclic *vic*-dioxime ligand and its mononuclear transition and nontransition metal complexes, *Turkish Journal Of Chemistry*, 36, 25-36.
- [7] Yenikaya, C., Kaya, M. and Demir, İ., (2008), Synthesis of a imine *vic*-dioxime ligand and its Ni(II), Co(II), Cu(II) complexes, *Asian Journal of Chemistry*, 20(7), 5651-5657.
- [8] Kaya, M., Demir, İ. and Yenikaya, C., (2008), Synthesis and characterization of complexes of *vic*-dioxime derivatives with transition metal. *Asian Journal of Chemistry*, 20(3), 2221-2228.
- [9] Kaya, M., Yenikaya, C., Demir, İ. and Kalfa, O.M., (2008), Synthesis and characteristics of N-(glyoxyldioxime)-N'-(2-hydroxybenzylidene)-1,4-diaminonaphthalene and its metal complexes, *Russian Journal of General Chemistry*, 78(5), 939-945.
- [10] Kaya, M., Yenikaya, C., Çolak, A.T. and Çolak, F., (2008), Synthesis, spectral, thermal and biological studies of Co(III) and binuclear Ni(II) complexes with a novel amine-imine-oxime ligand, *Russian Journal of General Chemistry*, 78(9), 1808-1815.
- [11] Canpolat, E., Yazıcı, A., Kaya, M. (2004), Synthesis and Characterization of Co(II), Ni(II), Cu(II), and Zn(II) Complexes with a new *vic*-dioxime (E,E)-N'-hydroxy-2-(hydroxyimino)-N-(4-[(2-phenyl-1,3-dioxolan-4yl)methyl]amino)butyl)ethanimidamide. *Russian Journal of Coordination Chemistry*, 30(2), 87-93.
- [12] Poyraz, M., Yenikaya, C. and Çolak, A.T., (2008), Synthesis and Structural Studies of Bidentate Schiff Bases and Their Complexes with Cu(II), Ni(II), Co(II), Cd(II) and Zn(II), *Asian Journal of Chemistry*, 20(5), 3515-3524.

- [13] Gök, Y. and Demirbas, A., (1989), The Synthesis and Complex Formation of Dibenzo [e,k]-2,3-Bis(Hydroxyimino)-1,4-Diaza-7,10-Dithia-2,3,8,9-Tetrahydrocyclododecine, *Synthesis and Reactivity in Inorganic and Metal-Organic Chemistry*, 19(5), 681-689.
- [14] Gül, A. and Bekaroglu, O., (1983), Syntheses of *NN'*-bis(4'-benzo[15-crown-5])diaminoglyoxime and its complexes with copper(II), nickel(II), cobalt(II), cobalt(III), palladium(II), platinum(II), and uranyl(VI), *Journal of the Chemical Society, Dalton Transactions*, 12, 2537-2541.
- [15] Kurtoğlu, M and Serin, S., (2002), Syntheses and characterization of 4-(11-chloro-3,6,9-trioxaundecyloxy) phenylamino-glyoxime and its complexes with copper(II), nickel(II), and cobalt(II), *Synthesis and Reactivity in Inorganic and Metal-Organic Chemistry*, 32(3), 629-637.
- [16] Durmus, M., Ahsen, V., Luneau, D. and Pécaut, J., (2004), Synthesis and structures of morpholine substituted new *vic*-dioxime ligand and its Ni(II) complexes, *Inorganica Chimica Acta*, 357(2), 588-594.
- [17] Atilla, D., Asma, S. and Gurek, A., (2009), Highly soluble Ni(II) *vic*-dioxime complexes containing branched thioether with alkyl chains of different lengths:synthesis and characterization, *Journal of Coordination Chemistry*, 62(18), 3050–3059.
- [18] Walia, R., Md, H., Naaz, S.F., Iqbal, K. and Lamba H.S., (2011), Benzimidazole derivatives – an overview, *International Journal Of Research In Pharmacy and Chemistry*, 1(3):565-573.
- [19] Téllez, F., López-Sandoval, H., Castillo-Blum, S.E. and Barba-Behrens, N., (2008), Coordination behavior of benzimidazole, 2-substituted benzimidazoles and benzothiazoles, towards transition metal ions, *Arkivoc*, (v), 245-275.
- [20] Pawar, N.S., Dalal, D.S., Shimpi, S.R. and Mahulikar, P.P., (2004), Studies of antimicrobial activity of N-alkyl and N-acyl 2-(4-thiazolyl)-1H-benzimidazoles, *European Journal Of Pharmaceutical Sciences*, 21, 115-118.
- [21] Özden, S., Atabey, D., Yildiz S. and Göker, H., (2005), Synthesis and potent antimicrobial activity of some novel methyl or ethyl 1*H*-benzimidazole-5-carboxylates derivatives carrying amide or amidine groups, *Bioorganic & Medicinal Chemistry*, 13(5), 1587-1597.
- [22] Ören, I., Temiz, Ö., Yalcin, I., Sener, E. and Altanlar, N., (1998), Synthesis and antimicrobial activity of some novel 2, 5-and/or 6-substituted benzoxazole and benzimidazole derivatives, *European Journal Of Pharmaceutical Sciences*, 7, 153-160.
- [23] He, Y., Ww, B., Yang, J., Robinson, D., Risen, L., Ranken, R., Blyn, L., Sheng, S. and Swayze, E.E., (2003), 2-Piperidin-4-yl-benzimidazoles with broad spectrum antibacterial activities, *Bioorganic & Medicinal Chemistry Letters*, 13(19): 3253-3256.
- [24] Varhelyi, Cs. Jr., Kovacs, A., Nemcsok, D., Nemeth, Z., Kuzmann, E., Vertes, A., Vekey, K., Varhelyi, Cs., Pokol, G., (2007), Spectroscopic and thermal studies of [Fe(dioximato)(amine)]mixed chelates, *Journal of Coordination Chemistry* 60(4), 379-392.

- [25] Gok, Y., Ertepinar, H., (1992), Synthesis and Characterization of Novel Polyamidoxime Transition Metal Complexes. *Synthesis and Reactivity in Inorganic and Metal-Organic Chemistry*, 22(10), 1495–1505.
- [26] Ertepinar, H., Gök, Y., Küçükislamoğlu, M. (1995), Synthesis and characterizations of new polyamidoximes and their crosslinking by metal ions. *European Polymer Journal*, 31(6), 603–608.
- [27] Kraska, J., Czajkowski, W.,(1982), Metal complex pigments, Poland, PL123437 B2
- [28] Zsako, J., Varhelyi, C., Demeter-Vodnar, J., Liptay, G., (1992), On the dioxime complexes of transition metals. XCV. New iodo-amino-bis-dimethylglyoximatocobalt(III)-nonelectrolytes, *Periodica Polytechnica, Chemical Engineering*, 36(4), 271-278.
- [29] Zsako, J., Varhelyi, C., Sarvari, T., (1989), On the dioximine complexes of transition metals. LXXIX. Some new chelates of iron with nioxime and trioxime, *Studia Universitatis Babeş-Bolyai, Chemia*, 34(2), 10-15.
- [30] Houben, J. and Kaufman, H., (1913), Über Chlor-glyoxime, Oxim-Derivate des Oxalylchlorids und Oxalsäure-halbchlorids und über Cyan-formyl-chloridoxim, *Berichte der deutschen chemischen Gesellschaft*, 46, 2821-2835.
- [31] March, J., (1977), *Advanced Organic Chemistry: Reaction, Mechanisms, Structure*, 609.
- [32] Phillips, M.A., (1931), CCCXVII.—The formation of 2-substituted benzimidazoles, *Journal of the Chemical Society*, 1143-1153.
- [33] Ueno, K. and Martell, A.E., (1956), Infrared studies on synthetic oxygen carriers, *The Journal of Physical Chemistry*, 60, 1270-1275.
- [34] Nakamoto, K. and Martell, A.E., (1960), Infrared Spectra of Metal Chelate Compounds. VI. A Normal Coordinate Treatment of Oxalato Metal Complexes, *The Journal of Chemical Physics*, 32, 588-588.
- [35] Coleman, W.M. and Taylor, L.T., (1971), Pentadentate ligands. I. Nickel(II) complexes of the linear Schiff base ligands derived from substituted salicylaldehydes and diethylenetriamine and 2,2'-bis(aminopropyl)amine, *Inorganic Chemistry*, 10, 2195-2199.
- [36] Geary, W.J., (1971), The Use of Conductivity Measurements in Organic Solvents for the Characterisation of Coordination Compounds. *Coordination Chemistry Reviews*, 7, 81-122.



RESEARCH ARTICLE

A COMPLETE SOLUTION to EXAM SCHEDULING PROBLEM: A CASE STUDY

Abdullah ELEN*

*Bandırma Onyeddi Eylül University, Faculty of Engineering and Nature Science, Devision of Software Engineering,
aelen@bandirma.edu.tr, ORCID: 0000-0003-1644-0476

Receive Date: 14.10.2021

Accepted Date: 30.03.2022

ABSTRACT

Exam scheduling is a complex task that higher education institutions (universities, colleges, etc.) must prepare each semester depending on their academic calendar. The preparation of exam schedules requires a multi-dimensional analysis and experience. It is also a quite time-consuming sequence of operations. Exam times should not overlap when preparing the schedules and needed constraints are expected to be complied with as much as possible. Therefore, it takes a long time to form a complete solution. In this study, a Genetic Algorithm based exam scheduling method was developed to create a complete solution for the Vocational School of T.O.B.B. Technical Sciences, Karabuk University. During the test phase, four different experiments were performed in different constraints and criteria. As a result of these experiments, all solutions gave appropriate results until 2000 iterations. There was no overlap in any of the exam schedules and significant success was achieved in the desired constraints.

Keywords: *Exam Scheduling, Genetic Algorithm, Metaheuristics, Karabuk University.*

1. INTRODUCTION

Universities are higher education institutions in a complex structure with many students, academic and administrative staffs. In these institutions, educational activities are carried out on course and exam schedules [1]. Therefore, it is necessary to prepare two or more (midterm, final exam etc.) exam schedules for all academic programs in each semester. When preparing exam schedules, distribution of exam halls (or classroom) according to departments, in which sessions will take part in lectures, the specific conditions of some courses, special requirements of examiners and course executives, capacity of exam halls, the number of students taking a course, possibility of some students being assigned to more than one exam session at the same time, exams can be held within a certain date range and limited time periods etc. many different situations have to be considered [2, 3]. Also, it may be necessary to revise the exam schedules depending on personal or institutional reasons. In summary, there are many parameters and constraints in exam schedules. Real-world optimization problems with many variables, such as exam/course/job scheduling, cannot be optimally solved at reasonable computational times [4]. Therefore, scheduling tasks are known as NP-hard [5] optimization problems. Also, it is difficult to talk about a general solution for this type of problem. The first studies on scheduling problems were done by Henry Laurence Gantt [6], an American mechanical engineer. These studies initially aimed at understanding the common problem structure by combining the

problems. These problems were tried to be produced with simple models. Towards the end of the 20th century, heuristic methods came to the fore according to the problem. Since 1990s, modern heuristic methods have been used for the solution of some problems [7, 8]. Heuristic algorithms do not guarantee that they will find the exact result, but they do guarantee that they will get a solution within a reasonable time [9]. In other words, the definitive solution is unknown, but the closest solution is a problem in which we want to determine what is good for determining quality of the solutions. For a problem to be solved by optimization algorithms, the constraints that the algorithm must comply with are defined. Then, an objective function is created by taking these constraints into consideration [10]. Two types of constraints are generally preferred for studies on exam scheduling problems in the literature. These are hard and soft constraints. Hard constraints are mandatory rules, while soft constraints are constraints are rules that are desired but not obligatory [11].

In recent years, meta-heuristic methods have been widely used in solving the exam scheduling problem. For instance, Santiago-Mozos et al. [12] proposed a two-step heuristic method for obtaining personalized schedules for some courses for a university in Spain. In this method, students can determine the groups they prefer on a given subject and their priority in the lessons. In the first stage of the method, the constraints of the problem are solved, and in the second stage, the solutions found are tried to be improved. Dammak et al. [13] developed a simple heuristic method to perform exam-classroom assignments to solve an exam scheduling problem. Their method tries to assign one exam in each classroom. If the method fails to provide this, it assigns a maximum of two exam halls. Pillay and Banzhaf [14] used the Informed Genetic Algorithm (IGA) as a two-step method for solving the exam scheduling problem. In the first stage, a GA is used to generate timetables that do not violate any hard constraints, and in the second stage, a GA is used to optimize the soft constraint costs of the schedules created in the first stage. Turabieh and Abdullah [15] proposed a hybrid approach that combines the principle of electromagnetic-like mechanism with the Great Deluge (GD) algorithm for the solution of the exam scheduling problem. The purpose of their proposed method is to move the sample points towards a high quality solution while avoiding local optimization using a calculated force value. This dynamically calculated value is evaluated as a distortion rate in determining the level within the GD algorithm. Shatnawi et al. [16] aimed to create the exam schedules of the Arab East College for High Education in Saudi Arabia with the least amount of overlap, considering some constraints. Their proposed method has two stages: the greedy algorithm and the genetic algorithm. They reported that by running these two algorithms in cooperation, they significantly reduced exam days and overlaps. Keskin et al. [17] proposed a two-step solution approach to Pamukkale University Faculty of Engineering's exam scheduling problem. They reported that the method they proposed produced faster results than commercial software IBM-CPLEX and Gurobi Optimization. Güler et al. [18] proposed mixed integer programming models for solving the exam scheduling and supervisor assignment problem. They stated that by integrating these models into a web-based decision support system, a complete timetable can be prepared in about two minutes. Aldeeb et al. [19] investigated the Intelligent Water Drops (IWD) algorithm for solving the university exam scheduling problem. They proposed a hybrid method based on local search algorithm to improve the disadvantages of the IWD. They reported that it achieved the best results on the three datasets compared to the best-known results in their experimental work. Hao et al. [20] A unified evolutionary multitasking graph-based hyper-heuristic (EMHH) framework is proposed in which the concept of evolutionary multitasking and graph heuristics are used as high-level search methodology and low-level heuristics, respectively. The EMHH was evaluated on the exam schedule and graphic coloring problems. Their experimental results indicate that the proposed unified framework improves efficiency, efficiency, and generality when compared to single-task hyper-heuristics.

In this study, the exam schedules were automatically generated by using the student course information of the 2018-2019 fall semester of Vocational School of T.O.B.B. Technical Sciences, Karabuk University. This paper is organized as follows; In the first section, creation of a relational database for solving the exam scheduling problem, determining the number of exam branches, creating the chromosome structure, and defining constraints and fitness function are mentioned. In the second section, four experimental studies were conducted according to different criteria and the results obtained were evaluated. In the last section, this paper is summarized.

2. MATERIALS AND METHODS

The categorical data in the database prepared in this study are as follows. There are 421 courses, 54 lecturers, 27 academic programs and 21 classrooms. In order to solve the problem, the model of the database was created with the E-R diagram shown in Fig. 1. This database was prepared based on the curricular relations of academic programs. Additional tables were also used to determine some specific limitations. For example, some lessons are taught in the laboratory only exams, common exams (for common courses taught in all departments) of the date/time intervals to be predetermined, according to the demands of lecturers are made according to the individual date/time criterion.

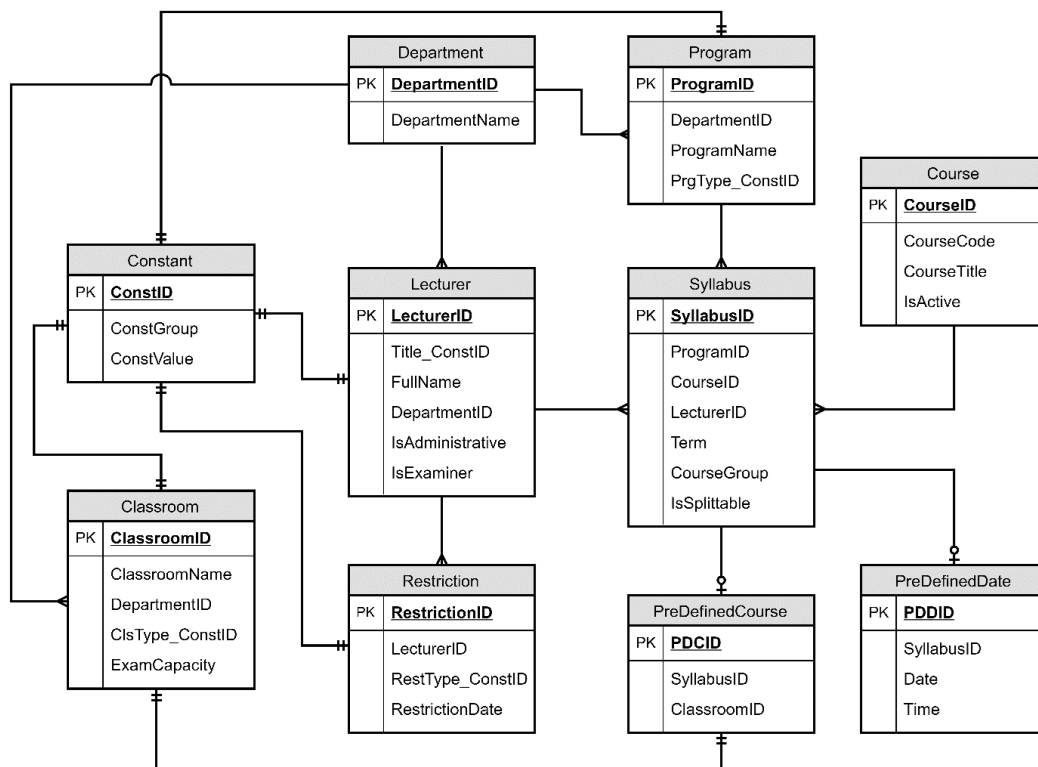


Fig. 1. E-R diagram of the database schema for exam scheduling problem.

2.1. Pre-processing

Before start of the scheduling, several pre-processes are required. These processes are as follows; loading the data into the system completely, combining the grouped courses, defining the pre-defined exams which have a fixed time or place in the table. Some of the exams of the courses are grouped for a variety of reasons. For this, the process of joining the grouped courses is done as shown in Algorithm 1. Where C represents the entire course list. For each course is checked whether it belongs to a group. If a course has a group, the number of students taking the course is determined and added to the main course. The function of $getIndex(g)$ is used to determine the index of the main course. In the last step, the group courses that are completed in the merge process are removed from the list.

The courses with group joining are passed through a final phase and the exam branches are determined. The $CreateExamSections$ function in Algorithm 2 is used for this process. The input parameters of this function are as follows; C is course list, $splitVal$ is number of students to be placed in a classroom and $tolerance$ is placement tolerance for a classroom.

Algorithm 1. Merge all grouped courses.

```
1:  function MergeGroupedCourses( $C$ : Course list)
2:    for  $i \leftarrow 1$  to  $C.count()$  do
3:      set  $g \leftarrow getGroupCourse(C[i])$ ;
4:      if  $g$  is not empty then
5:        set  $sci \leftarrow getStudentCount(C[i])$ ;
6:        set  $scg \leftarrow getStudentCount(C[getIndex(g)])$ ;
7:         $scg \leftarrow scg + sci$ ;
8:         $setStudentCount(C[getIndex(g)], scg)$ ;
9:         $C.remove(C[i])$ ;
10:     end if
11:   end for
12:   return  $C$ ;
13: end function
```

Algorithm 2. Create exam sections using merged course list.

```

1:  function CreateExamSections(C, splitVal, tolerance)
2:    set S[], index = 1;
3:    for i ← 1 to C.count() do
4:      set section ← truncate(getStudentCount(C[i]) / splitVal);
5:      for j ← 1 to section do
6:        S[index] ← C[i];
7:        setStudentCount(S[index], splitVal);
8:        index ← index + 1;
9:      end for
10:     set remain ← getStudentCount(C[i]) mod splitVal;
11:     if (remain > tolerance) then
12:       S[index] ← C[i];
13:       setStudentCount(S[index], splitVal);
14:       index ← index + 1;
15:     else
16:       set part ← truncate(remain / section);
17:       set partRemain ← remain mod section;
18:       for j ← 1 to S.count() do
19:         set sc ← getStudentCount(S[j]);
20:         setStudentCount(S[j], (sc + part));
21:         if (partRemain > 0 and j = 1) then
22:           setStudentCount(S[j], (sc + part + partRemain));
23:         end if
24:       end for
25:     end if
26:   end for
27:   return S;
28: end function

```

The purpose of this function is to determine the number of students to be placed in each class according to the given input parameters and the examination sessions depending on these procedures. According to Algorithm 1, each course is examined separately in terms of the number of students taking the course, the number of students to be placed in a class and their tolerance. The parameters required for this algorithm are set as shown in Fig. 2 through the values specified in the “Number of Students” section.

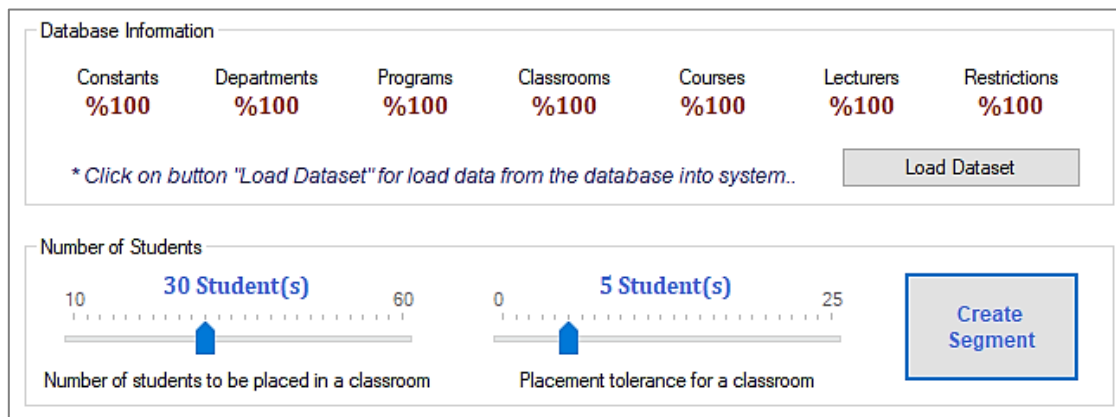


Fig. 2. Dataset loading and student segmentation process.

In Table 1, four different scenarios are given as an example for determining the number of exam branches (EB). The calculations are made by using the information of 421 courses registered in the database as mentioned before. Where means S_p , number of students to be placed in a classroom and S_T , placement tolerance for a classroom. In summary, the EB values we obtain directly affect the structure (chromosome length) and performance of the algorithm to be used in the solution of the problem. The chromosome length of the algorithm varies dynamically according to EB .

Table 1. Determination of the number of exam sections according to S_p and S_T parameters.

Scenarios	S_p	S_T	ES
Sce-1	30	5	350
Sce-2	30	10	338
Sce-3	35	5	333
Sce-4	35	10	305

The final processing steps before running the scheduling algorithm are the determination of the exam schedule as in the Graphical User Interface (GUI) shown in Figure 3. From this interface, the active semester, the type of the exam, the start and end date interval of the exams (D_R), the time intervals to be used during the day (T_R) and the duration of the exams (T_D) are determined. Then holidays and/or school's closed times (D_C) are added to the list. Finally, it is determined whether the faculty member will be assigned for exams outside of their own courses (fmo) and all parameters are prepared. The exact dates for the preparation of the exam schedules (D_E) are determined as shown in Eq. (1).

$$D_E = \forall x (x \in D_R \wedge x \notin D_C) \quad (1)$$

Where x refers to any date in the start and end of the exams. According to the date range given in Fig. (3), the number of elements of the D_E (number of days) is equal to 10 when the days corresponding to the weekend are removed (From 5 to 16, except November 10 and 11).

Fig. 3. Exam calendar and overall restrictions.

The flowchart of the proposed method and pre-process is as shown in Fig. (4). The first process collects the necessary information from the database. Then, group courses are combined into a single course. The user creates exam branches as shown previously in Fig. (2). The constraint rules are set in the last processing step before the algorithm is executed. Thus, all necessary parameters are provided for the genetic algorithm.

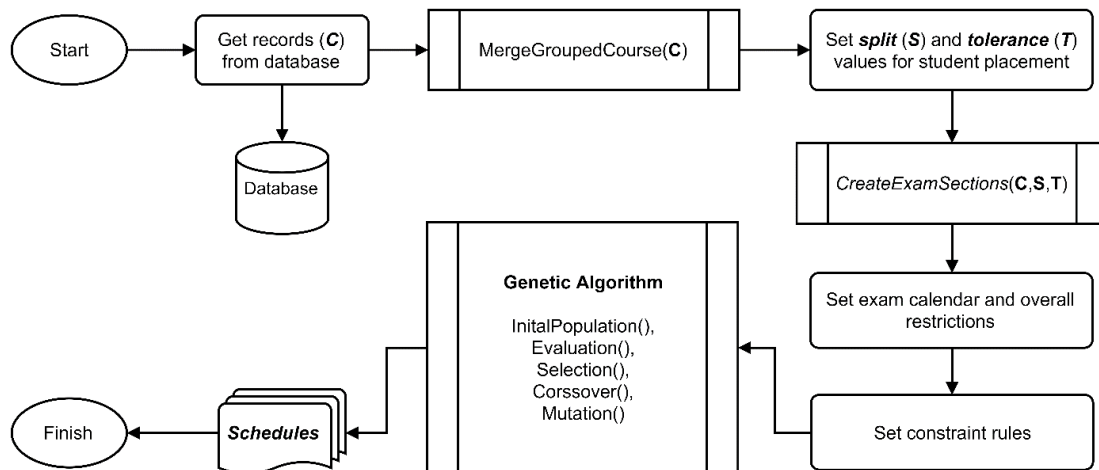


Fig. 4. Flowchart of the proposed method.

2.2. Structure of the Chromosome

The length of the chromosome in the GA to be used in solving the problem is determined by the interface as shown in Table 1 before. That is, the length of a chromosome is equal to EB . Fig. (5) shows a representative chromosome and the structure of a gene. Each gene has 14 different information. Some of these (from G_7 to G_{13}) are used for control purposes. G_0 and those for control purposes are not subject to any genetic processing.

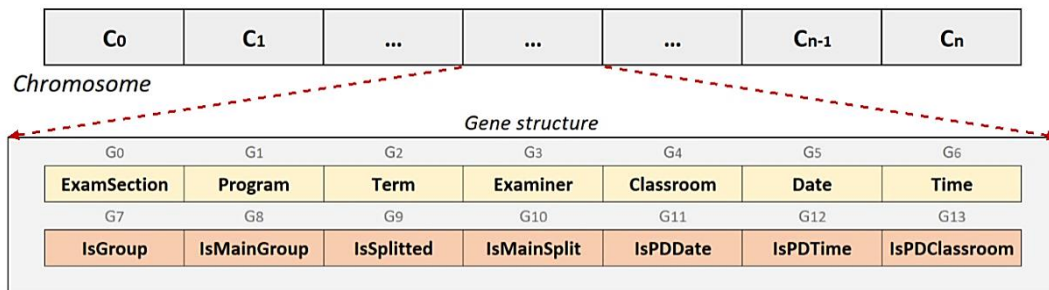


Fig. 5. Structure of the chromosome and gene.

While describing the location of the genes with the chromosome variable ($C_{i,j}$); where is $i \in \{0,1, \dots, n\}$ the gene index on the chromosome and $j \in \{0,1, \dots, 13\}$ refers to the field index in the gene. C_i identifies a gene on the chromosome. The explanations of the features of the structure of the gene are given in Table 2. Where G_0 represents an exam branch. G_1 to G_6 are information that appears directly on the schedule. G_6 and G_7 determine whether a course has been tested. G_9 and G_{10} stores the information that the exam branch does not belong to a divided course.

Table 2. Descriptions of the gene parameters.

Index	$C_{i,j}$	Parameter	Description
G_0	$C_{i,0}$	ExamSection	<i>The exam that was created during pre-processing.</i>
G_1	$C_{i,1}$	Program	<i>Academic program.</i>
G_2	$C_{i,2}$	Term	<i>The academic term of the program.</i>
G_3	$C_{i,3}$	Examiner	<i>The lecturer who was tasked for the examination.</i>
G_4	$C_{i,4}$	Classroom	<i>The place where the examination will be held.</i>
G_5	$C_{i,5}$	Date	<i>The date when the examination will be held.</i>
G_6	$C_{i,6}$	Time	<i>The time when the examination will be held.</i>
G_7	$C_{i,7}$	IsGroup	<i>Is there a group of the course that is connected to this</i>
G_8	$C_{i,8}$	IsMainGroup	<i>Is main group that the course is connected to this exam?</i>
G_9	$C_{i,9}$	IsSplitted	<i>Is that the course was splitted connected to this exam?</i>
G_{10}	$C_{i,10}$	IsMainSplit	<i>Is main split that the course is connected to this exam?</i>
G_{11}	$C_{i,11}$	IsPDDate	<i>Is there a predefined date for this exam?</i>
G_{12}	$C_{i,12}$	IsPDTime	<i>Is there a predefined time for this exam?</i>
G_{13}	$C_{i,13}$	IsPDClassroom	<i>Are there any predefined classrooms for this exam?</i>

Where G_0 holds some information about the course to which an exam is attached. These statements keep the “SyllabusID” field, which is the primary key in the table (T_{SYL}) named “Syllabus”, in an array. It is an array that holds the “CourseID” field if it is a divided course and/or a group course. This information is used to establish the relationship between the curriculum and the exam schedules to be created. The parameters used in the genetic algorithm are as follows; The selection method is “Elite” the crossover rate is 90%, the mutation rate is 3%, the population is 100.

2.3. Constraints

Some rules must be fulfilled for the generation of genes in the chromosome. These rules and restrictions are presented separately under the four headings below. Also, it was divided into three main categories as “*soft*”, “*middle*” and “*hard*” to define the constraints as more flexible. Objective functions calculate a fitness value based on constraint definitions. When calculating these fitness values, it can be maxima or minima depending on the type of problem.

2.3.1. Examiner and faculty member

The knowledge that every faculty member can be an examiner for the exam is stored in the table (T_{LEC}) named “*Lecturer*” in the database. Accordingly, the examiner list (L_E) to be used in the genes on the chromosome is as in Eq. (2).

$$L_E = \{i | i \in \{0, \dots, n\}, (T_{LEC}[i, 5] \text{ is True} \rightarrow T_{LEC}[i, 0])\} \quad (2)$$

Where n is the number of records in the table, $T_{LEC}[i, 5]$ the table area (*IsExaminer*) that keeps track of whether the examiner is assigned for the faculty member in the i -th, $T_{LEC}[i, 0]$ refers to the faculty member’s ID (*LecturerID as primary key*). If faculty members only want to be examiners in their own courses, the examiner list is determined as in Eq. (3).

$$L_{FMT} = \{ 'assist.prof', 'assoc.prof', 'prof' \}, \quad (3)$$

$$L_E = \{i | i \in \{0, \dots, n\}, ((T_{LEC}[i, 5] \text{ is True} \wedge T_{LEC}[i, 1] \notin L_{FMT}) \rightarrow T_{LEC}[i, 0])\}$$

Where L_{FMT} represents the degree list of faculty members, $T_{LEC}[i, 1]$ represents the degree of the faculty member in the i -th row/record line.

2.3.2. Pre-defined dates and classrooms

As mentioned earlier, some exams are stored in the database named *PreDefinedDate* (T_{PDD}) table as a predetermined date. Accordingly, the date ($C_{i,5}$) and time ($C_{i,6}$) information of each gene that satisfies the $C_i \in T_{PDD}$ condition on the chromosome is updated according to the table T_{PDD} . Then the control fields of *IsPDDate* ($C_{i,11}$) and *IsPDTime* ($C_{i,12}$) are set to logic “1”. If the place for the exam to be made, such as workshops, laboratories, etc. are made in the table (T_{PDC}) called *PreDefinedClassroom*; The Classroom ($C_{i,4}$) information of each gene that satisfies the $C_i \in T_{PDC}$ requirement on the chromosome is updated according to the table T_{PDC} . Then the control field of *IsPDCClassroom* ($C_{i,13}$) is set to logic “1”. Pre-defined areas of these genes are not mutated during genetic procedures. Otherwise, this process has no meaning.

2.3.3. Examiner date and time ranges

The “*Restriction*” table (T_{RST}) in the database contains the date and time interval information that faculty members do not want to be assigned to the exam. As seen in Table 3, these constraints can be defined in three different ways. There are “*If possible*” and “*Absolutely*” options for each constraint. Accordingly, if “*If possible*” option is selected for any of these three constraints, P_M is used as penalty point and P_H is used if possible “*Absolutely*” option is selected.

Table 3. Date and time range constraints for examiners.

ID	Examiner constraints	If possible	Absolutely
K_{BN}	<i>I do not want to be tasked before-noon</i>		
K_{AN}	<i>I do not want to be tasked afternoon</i>	P_M	P_H
K_{SD}	<i>I do not want to be tasked on the date specified</i>		

Accordingly, the penalties for each constraint are calculated as shown Eq. (4), (5) and (6).

$$K_{BN} = p \sum_{i=0}^n \sum_{j=0}^m \begin{cases} 1, & (T_{RST}[j,1] = C_{i,3}) \wedge (C_{i,6} < \text{time}(12:00)) \\ 0, & \text{otherwise} \end{cases}, \quad p \in \{P_M, P_H\} \quad (4)$$

$$K_{AN} = p \sum_{i=0}^n \sum_{j=0}^m \begin{cases} 1, & (T_{RST}[j,1] = C_{i,3}) \wedge (C_{i,6} > \text{time}(12:00)) \\ 0, & \text{otherwise} \end{cases}, \quad p \in \{P_M, P_H\} \quad (5)$$

$$K_{SD} = p \sum_{i=0}^n \sum_{j=0}^m \begin{cases} 1, & (T_{RST}[j,1] = C_{i,3}) \wedge (C_{i,5} \neq T_{RST}[j,3]) \\ 0, & \text{otherwise} \end{cases}, \quad p \in \{P_M, P_H\} \quad (6)$$

Where, P_M is the middle level penalty point, n the number of genes in the chromosome, m the number of records in the table, $T_{RST}[j, 1]$ the examiner ID found in the j -th record line in the table, $T_{RST}[j, 3]$ the date information in the same row of the table, $C_{i,3}$ examiner information in the i -th gene of the chromosome, $C_{i,5}$ and $C_{i,6}$ refer to the date and time information in the gene, respectively.

2.3.4. Other constraints

Under this heading, other constraints are mentioned. The GUI shown in Fig. (6) has three different constraints. ‘‘Low, Middle and High’’ options are given for each constraint feature to be used. The penalties of these options are equal to P_S, P_M, P_H respectively.

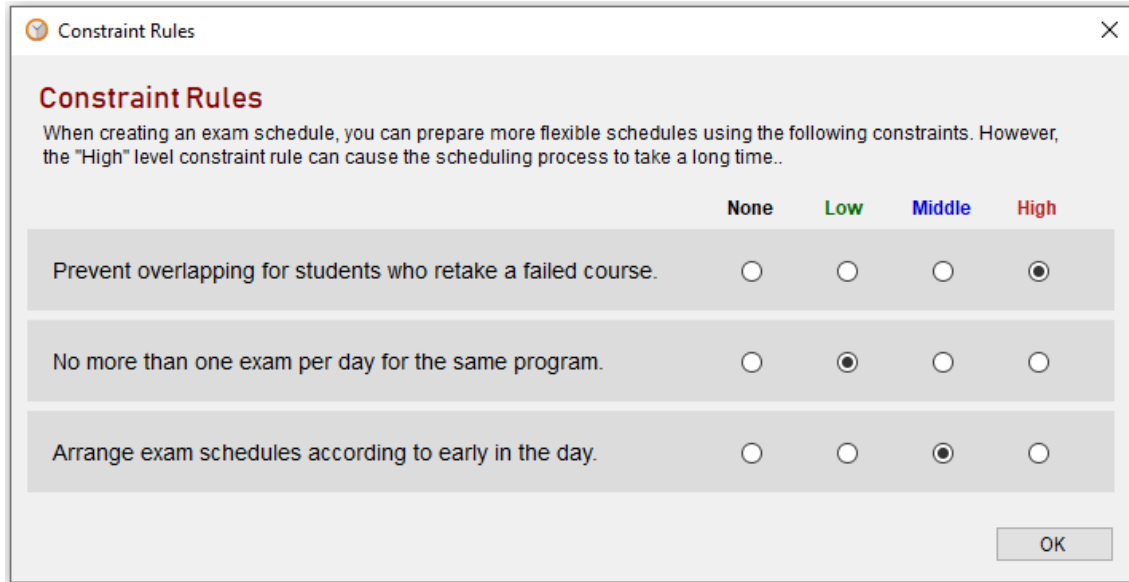


Fig. 6. Constraint rules for the exam scheduling.

The functions that calculate the constraint penalties are shown in Eq. (7) “Prevent overlapping for students who retake a failed course” (K_{SE}), shown in Eq. (8) “No more than one exam per day for the same program” (K_{PE}) and shown in Eq. (9) “Arrange exam schedules according to early in the day” (K_{DE}), respectively. The operating principle of these functions is like sorting algorithms. Two consecutive gene (eg: $C_{i,5} - C_{i+1,5}$) information on a chromosome are passed through comparative logical tests. If the necessary conditions are met, the penalty value is increased, otherwise it is ineffective.

$$K_{SE} = p \sum_{i=0}^{n-1} \sum_{j=i+1}^n \begin{cases} 1, & C_{i,1} = C_{j,1} \wedge C_{i,5} = C_{j,5} \wedge C_{i,6} = C_{j,6}, p \in \{P_S, P_M, P_H\} \\ 0, & otherwise \end{cases} \quad (7)$$

$$K_{PE} = p \sum_{i=0}^{n-1} \sum_{j=i+1}^n \begin{cases} 1, & C_{i,1} = C_{j,1} \wedge C_{i,2} = C_{j,2} \wedge C_{i,5} = C_{j,5}, p \in \{P_S, P_M, P_H\} \\ 0, & otherwise \end{cases} \quad (8)$$

$$K_{DE} = \frac{p}{\text{count}(T_R)} \sum_{i=0}^n \begin{cases} \frac{C_{i,6} - \text{median}(T_R)}{\max(T_R) - \text{median}(T_R)} & C_{i,6} \geq \text{median}(T_R), p \in \{P_S, P_M, P_H\} \\ 0 & otherwise \end{cases} \quad (9)$$

Where p is the optional penalty value, n is the number of genes in the chromosome, $C_{i,1}$, $C_{i,2}$, $C_{i,5}$ and $C_{i,6}$ the academic program in the i -th gene, academic period, the date, time and T_R express the time interval of the exam.

2.4. Fitness Function

For scheduling problems, the most important parameters of the fitness function are undoubtedly overlapping. Three different methods are used for examiners, students and classrooms to calculate penalties in these overlaps. In these calculations, each is considered as a separate layer, as shown in Fig. (7).

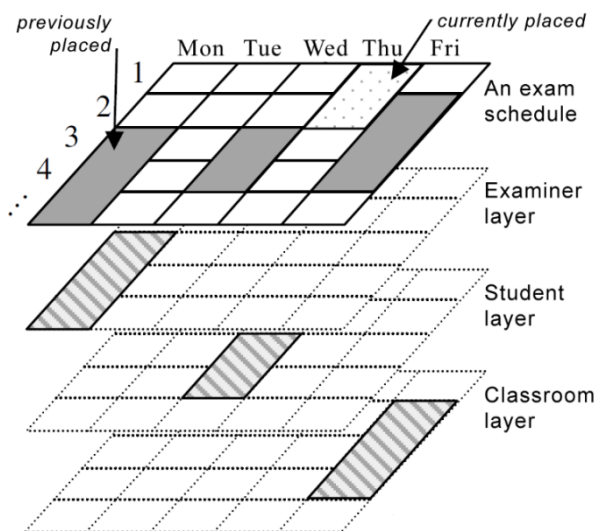


Fig. 7. Presentation of an exam schedule as a layer.

Accordingly, to avoid overlaps, the rules that must be followed in each layer are as follows.

- **Examiner layer:** A examiner cannot be found in different places (*classrooms*) in the same time frame.
- **Student layer:** A student cannot take more than one exam at the same time-period and only one exam can be done in the same period for the relevant semester of the academic program to which he/she is affiliated.
- **Classroom layer:** In a classroom, more than one exam cannot be done at the same time-period.

According to these general rules, functions that calculate overlap penalties are as follows; The examiner overlaps (O_E) shown in Eq. (10), the student overlaps (O_S) shown in Eq. (11), and classroom overlaps (O_C) shown in Eq. (12).

$$O_E = P_H \sum_{i=0}^{n-1} \sum_{j=i+1}^n \begin{cases} 1, & C_{i,3} = C_{j,3} \wedge C_{i,5} = C_{j,5} \wedge C_{i,6} = C_{j,6} \\ 0, & \text{otherwise} \end{cases} \quad (10)$$

$$O_S = P_H \sum_{i=0}^{n-1} \sum_{j=i+1}^n \begin{cases} 1, & C_{i,1} = C_{j,1} \wedge C_{i,2} = C_{j,2} \wedge C_{i,5} = C_{j,5} \wedge C_{i,6} = C_{j,6} \\ 0, & \text{otherwise} \end{cases} \quad (11)$$

$$O_C = P_H \sum_{i=0}^{n-1} \sum_{j=i+1}^n \begin{cases} 1, & C_{i,4} = C_{j,4} \wedge C_{i,5} = C_{j,5} \wedge C_{i,6} = C_{j,6} \\ 0, & \text{otherwise} \end{cases} \quad (12)$$

Where the values mean; n is the number of genes in the chromosome, P_H is the penalty value for hard constraints, $C_{i,1}$, $C_{i,2}$, $C_{i,3}$, $C_{i,4}$, $C_{i,5}$ and $C_{i,6}$ the academic programs academic period, examiner, classrooms, date and time expresses the information in the i -th gene respectively. A logical “AND” operator was used for each gene in the chromosome. Another issue that needs to be considered when preparing the exam schedules is that the number of exam tasks per examiner should be as balanced as possible. As shown in Eq. (13) as part of the fitness function, average distribution of tasks (μ_E), standard deviation (σ_E) and balance coefficient (B_E) for the examiners were calculated. Accordingly, if all examiners take equal number of exams, the standard deviation value will be equal to zero. As a result, the balance coefficient will be zero.

$$e_k = \sum_{i=0}^n \begin{cases} 1, & C_{i,3} = T_{LEC} [k, 0] \\ 0, & \text{otherwise} \end{cases}, \quad \mu_E = \frac{1}{m} \sum_{k=0}^m e_k, \quad \sigma_E = \sqrt{\frac{1}{m} \sum_{k=0}^m (e_k - \mu_E)^2},$$

$$B_E = \left(\sum_{k=0}^m \begin{cases} e_k, & e_k > \lceil \mu_E \rceil \\ 0, & \text{otherwise} \end{cases} \right) / \left(\sum_{k=0}^m \begin{cases} 1, & e_k > \lceil \mu_E \rceil \\ 0, & \text{otherwise} \end{cases} \right) \sigma_E P_S \quad (13)$$

The parameters of Eq. (13) have the following meanings; e_k is the number of examinatory duties of k -th faculty members, n is the number of genes in the chromosome, T_{LEC} is the “Lecturer” table in the database, $T_{LEC}[k, 0]$ is the faculty members ID found in the k -th line in the table, m is the number of examiners, P_S is soft restricted penalty score. Another balance element in the shedule is that the exams of academic programs are distributed as balanced as possible within the calendar. When this criterion is not taken into consideration, a program may have multiple exams on the same day. This negatively affects the performance of students. The function that calculates the program/exam balance according to the calendar interval is shown in Eq. (14).

$$t_k = \sum_{i=0}^n \begin{cases} 1, & C_{i,1} = T_{PRG} [k, 0] \\ 0, & \text{otherwise} \end{cases},$$

$$d_k = \sum_{i=0}^{n-1} \sum_{j=i+1}^n \begin{cases} 1, & C_{i,1} = C_{j,1} \wedge C_{i,1} = T_{PRG} [k, 0] \wedge C_{i,5} = C_{j,5} \\ 0, & \text{otherwise} \end{cases}, \quad (14)$$

$$B_P = P_S \sum_{k=0}^m \frac{d_k}{(t_k - 1)}, \quad t_k > 1$$

The parameters of Eq. (14) have the following meanings; t_k is the total number of exams for the k -th program, d_k is the number of exams performed more than once in the same day for the k -th program, n is the number of genes in the chromosome, $C_{i,1}$ and $C_{i,5}$ is the academic program and date information in the i -th gene, respectively. T_{PRG} is the program table in the database, $T_{PRG}[k, 0]$ is the

program ID on k -th row in the table. According to Eq. (14), the ratio of d_k and t_k for each program is summed by multiplying the P_S soft constraint as penalty. Thus, we calculate the program balance coefficient (B_P). The total penalties calculated for a chromosome are shown in Eq. (15).

$$\begin{aligned} f_{Overlap} &= O_E + O_C + O_P, \\ f_{Constraint} &= K_{BN} + K_{AN} + K_{SD} + K_{SE} + K_{PE} + K_{DE}, \\ f_{Balance} &= B_E + B_P, \\ F &= f_{Overlap} + f_{Constraint} + f_{Balance} \end{aligned} \quad (15)$$

Where $f_{Overlap}$ is the total overlap in the chromosome, $f_{Constraint}$ is the sum of the constraints, the $f_{Balance}$ is total balance coefficient, and F is the sum of all the calculated all penalties points. The fitness function of Eq. (16), which is used in the solution of the problem, aims to find the minimum penalty points.

$$fitness = \min \{i | i \in \{0, 1, \dots, n\}, F_i\} \quad (16)$$

Where n is the number of the population. Accordingly, the fitness function finds the chromosome with the lowest penalties of the population in each iteration. The smallest fitness score of all time is found in Eq. (17).

$$fitness_{BEST} = \begin{cases} fitness_i & fitness_i < fitness_{BEST}, i | i \in \{0, 1, \dots, n\} \\ fitness_{BEST} & otherwise \end{cases} \quad (17)$$

Where n is the number of iterations. Accordingly, if the fitness value in i -th iteration is smaller than the best, the current fitness is determined to be the best. This process is repeated continuously in each iteration until the algorithm terminated.

3. EXPERIMENTAL RESULTS

Tests of the proposed method were carried out in consideration of the following items. Accordingly, four different experimental sets were prepared, and evaluations were made for each. The prepared test parameters are shown in Table 4. The summary information for T.O.B.B. Vocational School of Technical Sciences, Karabuk University is as follows:

- The total number of courses is 421. Since 32 of these courses are related to profession practice, their exams are held in special places such as workshops and laboratories.
- There are 21 educational places: 10 classrooms, 1 amphitheater, 3 laboratories, 6 workshops and 1 seminar room. The usage rate of 10 exam halls, which are classrooms, in exam schedules is approximately 95%. Other places are used for practice exams or for private purposes only. In addition, capacities of these classrooms vary between 35-40 students.

- The number of academic programs is 27. However, as some programs are no longer available for students, the number of students can vary greatly depending on academic programs. For this reason, some courses are grouped together, and the exams are asked to be made jointly.
- The number of registered faculty member for the exam system is 54. However, only 37 of them are examiners. In addition, the 12 of them have the degree of faculty member (*Assist.prof.*, *Assoc.prof.*, *Prof.*).
- The mid-term exams for 2018-2019 fall semester were held between 05/11/2018 and 16/11/2018 (for 2 weeks). However, it was decided not to hold an exam on 11/11/2018 (Sunday). It was also reported that exam hours would be between 09:00 and 18:00.
- It was stated that six of the faculty members will not take part in exams. In addition, three people declared that they did not want to task in the afternoon if possible.

According to the exam distribution, the number of examiners and classrooms for the number of examiners was 37 and the number of classrooms was 10. The calculated numerical distributions according to the EB value for each experiment are as in Table 4.

Table 4. Tested parameters of the four different experiments.

Experiments	S_P	S_T	ES	D_E	$p(K_{SE})$	$p(K_{PE})$	$p(K_{DE})$	fmo
Exp-1	30	5	350	11	none	none	low	True
Exp-2	30	10	338	11	middle	low	none	False
Exp-3	35	5	333	11	middle	low	low	True
Exp-4	35	10	305	11	high	middle	low	False

For each experiment, graphs of fitness function, determined constraints and balance conditions were drawn. In balance status graphs, it is required that the exam task per examiner is as equal as possible and for the academic programs, the exams should approach to zero in order to make the optimal distribution according to the determined calendar days. It is expected that each criterion will be reduced to a minimum level in the graphs where the constraint rules are shown.

3.1. Experiment I

In this experiment, a total of 350 exam sessions with 30 students in each class were created for the exam branches (tolerance is 5). The placement of the exams based on the early hours was determined as a constraint. For Exp-1, the fitness, constraint and balance values in each iteration are shown in Fig. 8. According to obtained results; the number of exam tasks per examiner is between 9-11; 21 faculty members with 9 exams, 15 faculty members with 10 exams, one faculty members with 11 exams. The exams evenly were equally distributed according to dates. However, as there were common exams (pre-determined exam dates) on November 5-6, 2018, there was an accumulation in these two days. The exams were placed into the early hours by 80% according to K_{DE} criteria. The number of overlaps in this test table is zero. As a further constraint, all of the K_{SD} constraints were successfully applied for six faculty members. Only one of the K_{AN} constraints could not be fulfilled for three faculty members.

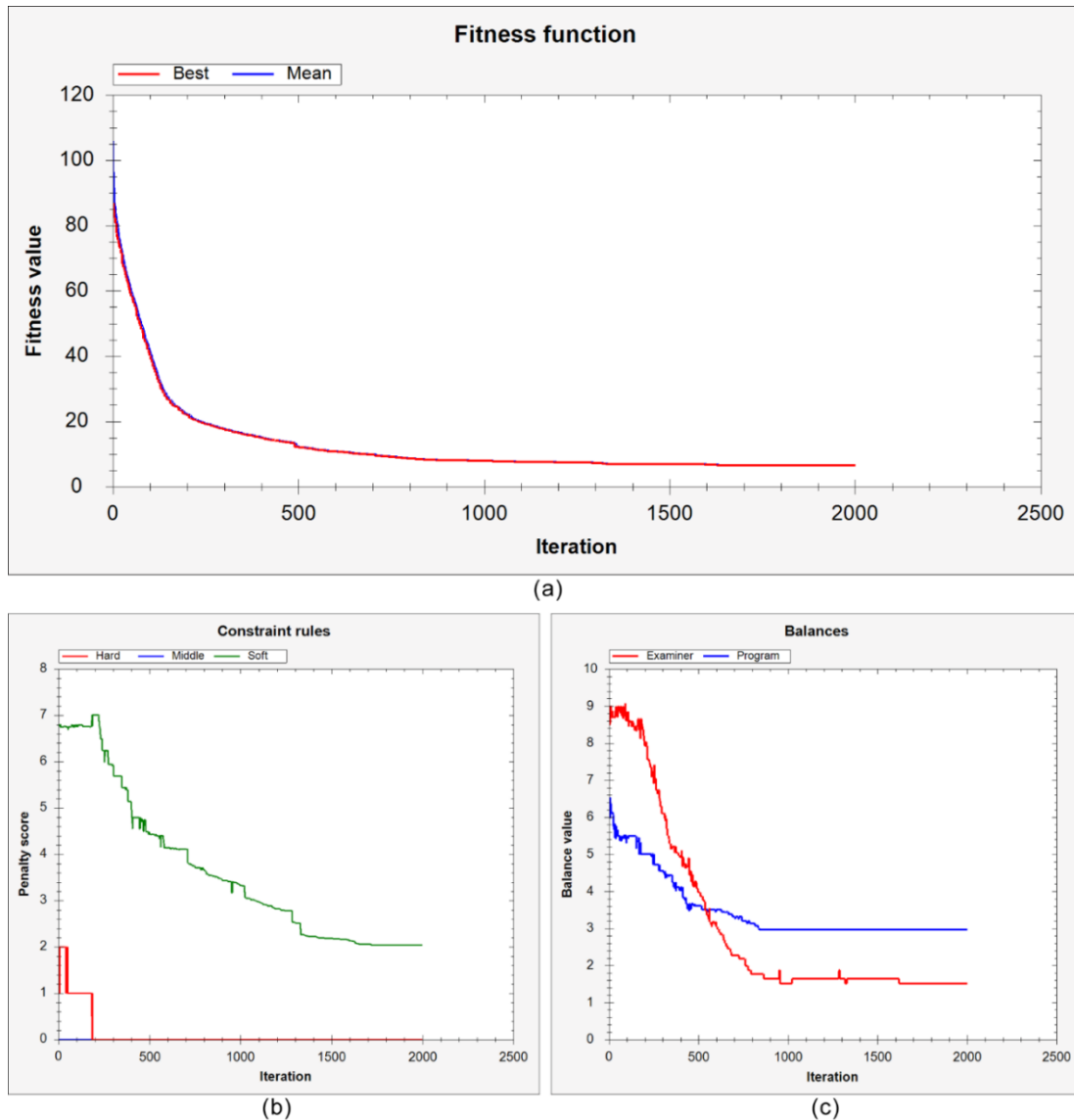


Fig. 8. Exp-1; (a) fitness function, (b) constraint rules, (c) balances.

3.2. Experiment II

In this experiment, a total of 338 exam sessions with 30 students in each class were created for the exam branches (tolerance is 10). In the exams, students who took courses from previous periods were asked not to overlap the exam times in different periods of the same program. In addition, an academic program was asked not to do more than one exam per day. Finally, faculty members were asked not to take exams task outside their own courses. For Exp-2, fitness, constraint, and balance values in each iteration are shown in Fig. (9).

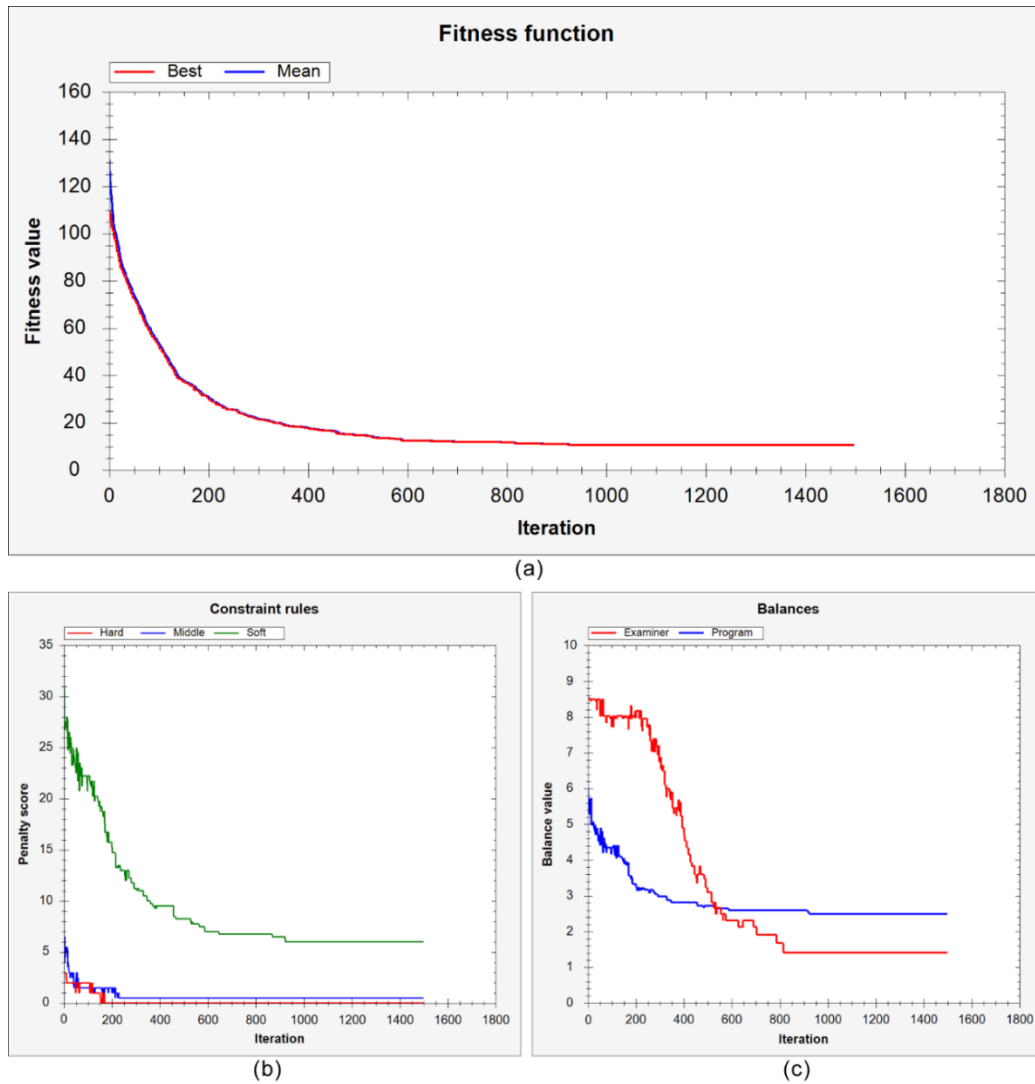


Fig. 9. Exp-2; (a) fitness function, (b) constraint rules, (c) balances.

According to obtained results; the number of exam tasks per examiner (except for 12 faculty members) is between 11-13; 23 faculty members with 11 exams, one faculty members with 12 and 13 exams. According to the K_{SE} criterion, exams are conducted at the same time-period for only 1 of the 338 exams for the students taking the courses from previous periods. According to the K_{PE} criterion, there are 24 exams in all academic programs on the same days. Finally, all of the K_{SD} (for six faculty members) and K_{AN} (for three faculty members) constraints were successfully applied.

3.3. Experiment III

In this experiment, a total of 333 exam sessions with 35 students in each class were created for the exam branches (tolerance is 5). The desired process in the experiment is that; K_{SE} , K_{PE} and K_{DE}

criteria are fulfilled at the specified levels. For Exp-3, fitness, constraint, and balance values in each iteration are shown in Fig. (10).

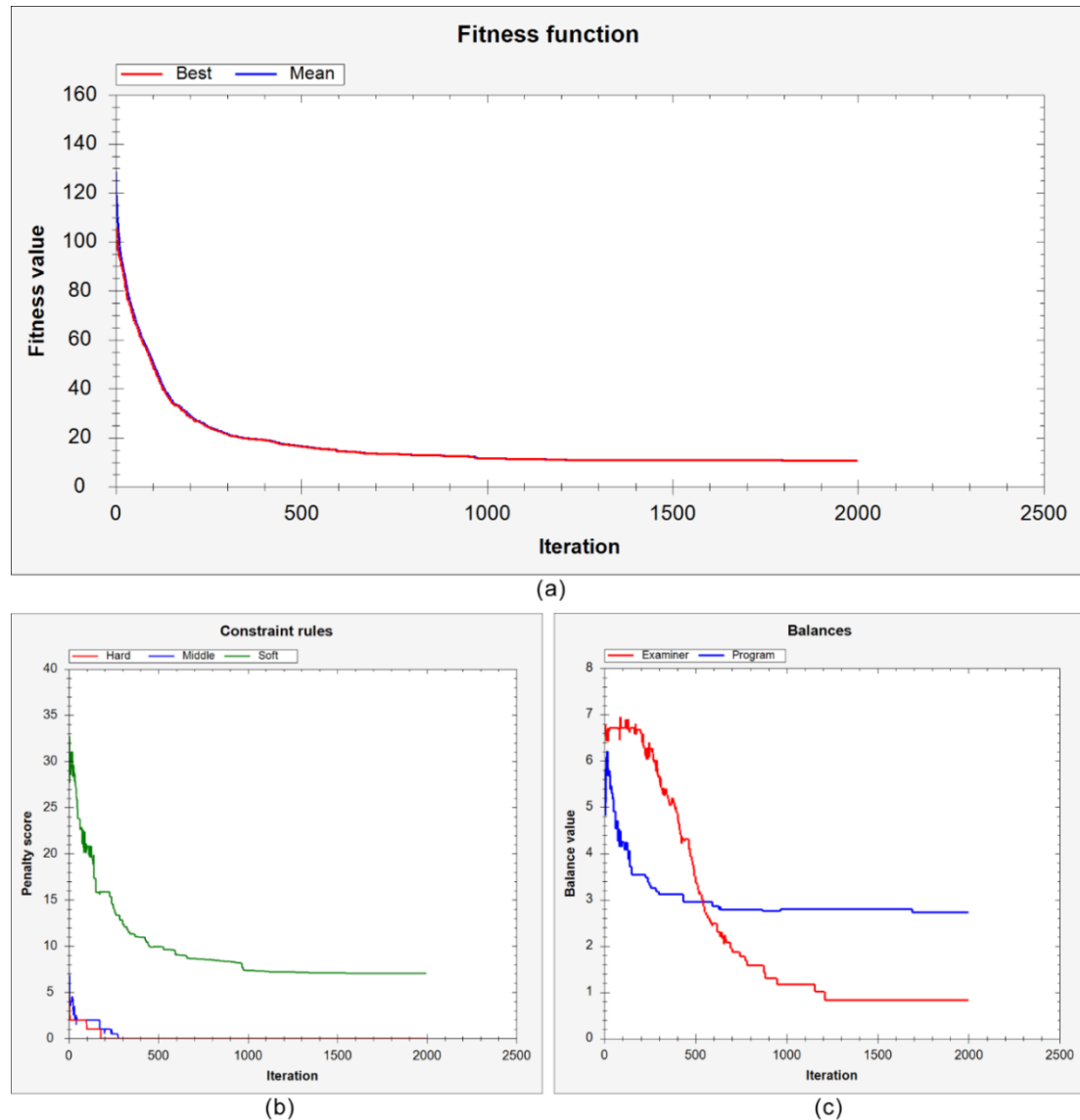


Fig. 10. Exp-3; (a) fitness function, (b) constraint rules, (c) balances.

According to obtained results; the number of exam tasks per examiner is between 8-10; 2 faculty members with 8-10 exams, 33 faculty members with 9 exams. Exams According to the K_{SE} criterion, all exams were placed appropriately for students who took courses from previous periods. According to the K_{PE} criterion, there are 22 exams conducted in the same days in all academic programs. In addition, all of the K_{SD} (for 6 faculty members) and K_{AN} (for 3 faculty members) constraints were

successfully applied. Finally, the exams were placed into early hours with 85% success according to K_{DE} criteria.

3.4. Experiment IV

In this experiment, a total of 306 exam sessions with 35 students in each class were created for the exam branches (tolerance is 10). The desired process in the experiment is that; K_{SE} , K_{PE} and K_{DE} criteria are fulfilled at the specified levels. In addition, faculty members were asked not to take exams task outside their own courses. For Exp-4, fitness, constraint, and balance values in each iteration are shown in Fig. (11).

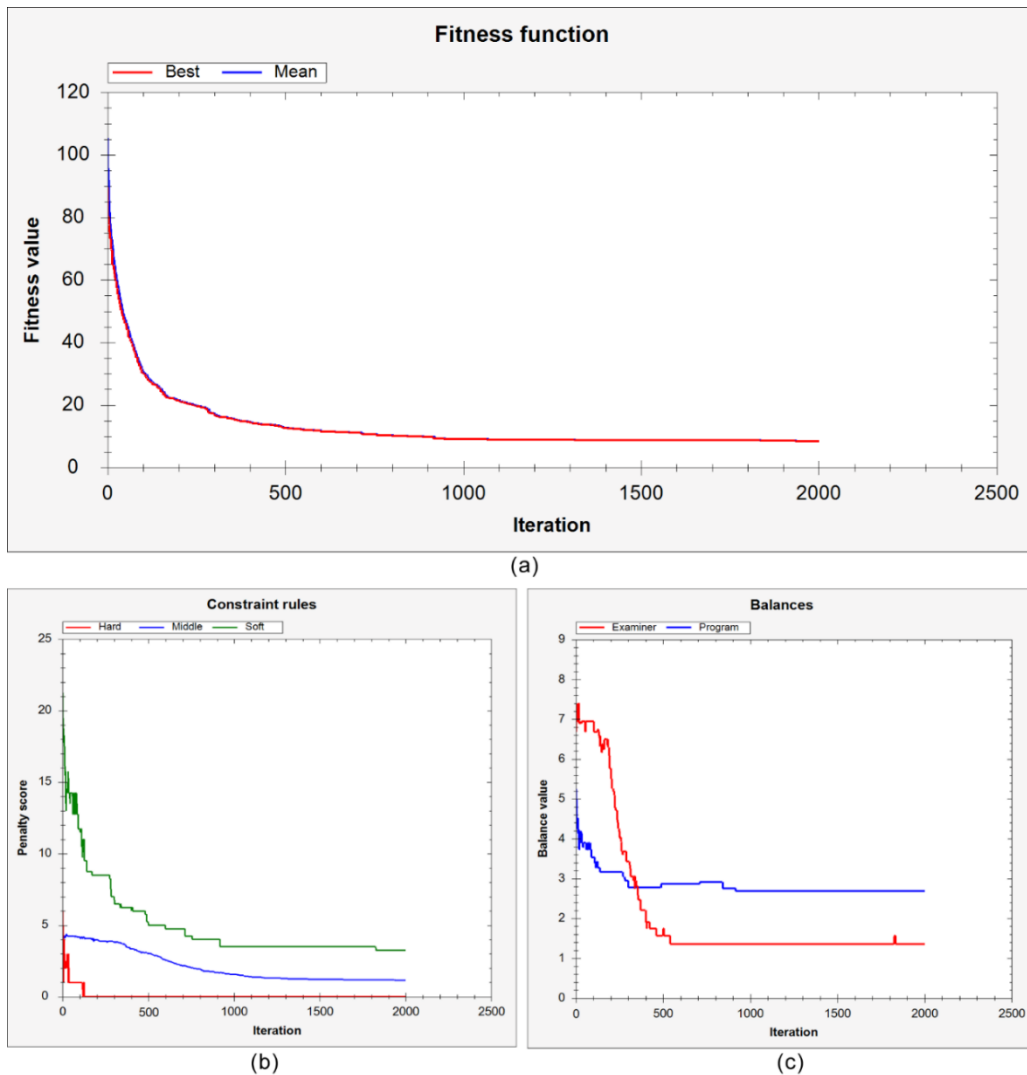


Fig. 11. Exp-4; (a) fitness function, (b) constraint rules, (c) balances.

According to obtained results; the number of exam tasks per examiner (except for 12 faculty members) is between 9-11; six faculty members with 9 exams, 18 faculty members with 10 exams, 1 faculty members with 11 exams. Exams According to the K_{SE} criterion, all exams were placed appropriately for students who took courses from previous periods. According to the K_{PE} criterion, there are 13 exams conducted in the same days in all academic programs. Finally, the exams were placed into early hours with 85% success according to K_{DE} criteria.

3.5. Numerical Evaluation of Experiments

The numerical results obtained from the four experimental studies done above were kept with tables. In the Experimental Results section (Experiments 1 to 4), some values from Prevent overlapping for students who retake a failed course (K_{SE}), Arrange exam schedules according to early in the day” (K_{DE}), No more than one exam per day for the same program (K_{PE}) and I do not want to be tasked before-noon (K_{BN}) were not determined as optional constraints, so no values were specified in the table below. The fitness values obtained from the experimental studies are shown in Table 5.

Table 5. Fitness values of experiments.

Experiments	O_E	O_S	O_C	K_{AN}	K_{BN}	K_{SD}	K_{SE}	K_{PE}	K_{DE}	B_E	B_P	F
Exp-1	0	0	0	0,25	—	0,00	—	—	1,79	1,51	2,96	6,51
Exp-2	0	0	0	0,00	—	0,00	1,00	6,75	—	1,14	2,89	11,78
Exp-3	0	0	0	0,00	—	0,00	0,00	5,5	1,53	0,82	2,72	10,57
Exp-4	0	0	0	0,00	—	0,00	0,00	3,25	1,17	1,35	2,68	8,45

Table 5 shows that there is no overlap even in different rules and situations. That is, the scheduling process was performed 100% accurately without any overlap. Table 6 shows the number of examiners and the number of exams per classroom. Table 7 shows distribution of the number of exams according to calendar dates. Table 8 shows distribution of the number of exams according to the hours intervals.

Table 6. The number of examiners and exams per classroom (exam hall).

	Exp-1		Exp-2		Exp-3		Exp-4	
	Examiner	Exam	Examiner	Exam	Examiner	Exam	Examiner	Exam
Min	9	22	11	26	8	24	9	20
Max	11	44	13	42	10	40	11	36
μ	9,46	33,6	11,12	32,4	9	31,8	9,8	29,2
σ	0,56	6,39	0,44	5,46	0,33	4,82	0,5	4,66

Table 7. Distribution of exam numbers according to calendar dates.

Experiments	05	06	07	08	09	10	11	12	13	14	15	16
Exp-1 (350)	42	37	29	29	30	34	—	33	29	29	29	29
Exp-2 (338)	28	31	29	28	29	27	—	29	32	35	32	38
Exp-3 (333)	26	42	28	31	30	29	—	30	28	30	28	31
Exp-4 (305)	32	28	26	28	27	26	—	29	28	27	27	27

Table 8. Distribution of the numbers of exams according to hours intervals.

Experiments	09:00-10:59	11:00-12:59	13:00-14:59	15:00-16:59	17:00-18:59	K_{DE}
Exp-1 (549)	117	109	78	25	21	80%
Exp-2 (528)	68	82	67	64	57	—
Exp-3 (490)	122	104	75	21	11	85%
Exp-4 (486)	101	105	66	14	19	85%

4. CONCLUSIONS

Today, while planning in any branch of business (education, production, transportation, service, finance, etc.), time scheduling problem is encountered. The developed application can be used not only in universities but also in any scheduling distribution. In this respect, the developed application has a dynamic structure, and it can easily be scheduled under different conditions. Academic units at universities prepare exam schedules to make exams at a specific time in the academic education period. The preparation process of the exam schedules is still carried out in many faculties, colleges, and vocational schools with the help of the spreadsheet program such as Microsoft Excel. This process is both difficult and time consuming. According to the findings obtained from the experimental studies conducted in this study, the preparation time of the exam schedules for Karabük University (T.O.B.B. Technical Sciences Vocational School) without any overlap is average 4 minutes and below 2000 iterations. The performance of the proposed method was tested with 421 courses, 54 lecturers, 27 academic programs and 21 classrooms, and the exam schedules were automatically prepared correctly. Also, the proposed method was tested in different situations. Other studies on this issue in the literature are generally based on departments. The proposed method can produce solutions to all kinds of rules and constraints at a faculty and vocational school level. The proposed method accurately creates exam schedules without overlapping, depending on the constraints determined. Thanks to flexible constraint and rule options, any university can perform exam planning. In addition, it is extremely important in terms of time cost compared to traditional methods.

ACKNOWLEDGEMENTS

The dataset in this study has been prepared on basis of the 2018-2019 fall term student information system of the Vocational School of T.O.B.B. Technical Sciences, Karabuk University.

REFERENCES

- [1] Elen, A., & Çayıroğlu, İ., (2010), Solving of Scheduling Problem with Heuristic Optimization Approach. *Teknoloji (Engineering Science and Technology, an International Journal)*, 13(3), 159-172.
- [2] Soghier, A., & Qu, R., (2013), Adaptive selection of heuristics for assigning time slots and rooms in exam timetables. *Applied Intelligence*, 39(2), 438–450. <https://doi.org/10.1007/s10489-013-0422-z>

- [3] Çayiroğlu, İ., & Elen, A., (2012), A Heuristic Optimization Approach for A Real-World University Timetabling Problem. *Advances in Computer Science and Engineering*, 9(2), 103-131.
- [4] Brunato, M., & Battiti, R., (2019), Combining intelligent heuristics with simulators in hotel revenue management. *Annals of Mathematics and Artificial Intelligence*. <https://doi.org/10.1007/s10472-019-09651-9>
- [5] Taheri, G., Khonsari, A., Entezari-Maleki, R., & Sousa, L., (2020), A hybrid algorithm for task scheduling on heterogeneous multiprocessor embedded systems. *Applied Soft Computing*, 106202. <https://doi.org/10.1016/j.asoc.2020.106202>
- [6] Gantt, H.L., (1910), “Work, Wages and Profit”. *Engineering Magazine*. New York.; republished as *Work, Wages and Profits*. Easton, Pennsylvania: Hive Publishing Company. 1974. ISBN 0-87960-048-9.
- [7] Coit, D. W., & Zio, E., (2018), The Evolution of System Reliability Optimization. *Reliability Engineering & System Safety*. <https://doi.org/10.1016/j.ress.2018.09.008>
- [8] Saldarriaga, J., Páez, D., Salcedo, C., Cuero, P., López, L. L., León, N., & Celeita, D., (2020), A Direct Approach for the Near-Optimal Design of Water Distribution Networks Based on Power Use. *Water*, 12(4), 1037. <https://doi.org/10.3390/w12041037>
- [9] Khosravanian, R., Mansouri, V., Wood, D. A., & Alipour, M. R., (2018), A comparative study of several metaheuristic algorithms for optimizing complex 3-D well-path designs. *Journal of Petroleum Exploration and Production Technology*. <https://doi.org/10.1007/s13202-018-0447-2>
- [10] Crown, W., Buyukkaramikli, N., Sir, M. Y., Thokala, P., Morton, A., Marshall, D. A., Tosh, J. C., Ijzerman, M. J., Padula, W. V., & Pasupathy, K. S., (2018), Application of Constrained Optimization Methods in Health Services Research: Report 2 of the ISPOR Optimization Methods Emerging Good Practices Task Force. *Value in Health*, 21(9), 1019–1028. <https://doi.org/10.1016/j.jval.2018.05.003>
- [11] Chávez-Bosquez O, Hernández-Torruco J, Hernández-Ocaña B, Canul-Reich J., (2020), Modeling and Solving a Latin American University Course Timetabling Problem Instance. *Mathematics* 8(10), 1833. <https://doi.org/10.3390/math8101833>
- [12] Santiago-Mozos, R., Salcedo-Sanz, S., DePrado-Cumplido, M., & Bousoño-Calzón, C., (2005), A two-phase heuristic evolutionary algorithm for personalizing course timetables: a case study in a Spanish university. *Computers & Operations Research*, 32(7), 1761–1776. <https://doi.org/10.1016/j.cor.2003.11.030>
- [13] Dammak, A., Elloumi, A., & Kamoun, H., (2006), Classroom assignment for exam timetabling. *Advances in Engineering Software*, 37(10), 659–666. <https://doi.org/10.1016/j.advengsoft.2006.02.001>

- [14] Pillay, N., & Banzhaf, W., (2010), An informed genetic algorithm for the examination timetabling problem. *Applied Soft Computing*, 10(2), 457–467. <https://doi.org/10.1016/j.asoc.2009.08.011>
- [15] Turabieh, H., & Abdullah, S., (2011), An integrated hybrid approach to the examination timetabling problem. *Omega*, 39(6), 598–607. <https://doi.org/10.1016/j.omega.2010.12.005>
- [16] Shatnawi, A., Fraiwan, M., & Al-Qahtani, H. S., (2017), Exam scheduling: A case study. 2017 Ninth International Conference on Advanced Computational Intelligence (ICACI). <https://doi.org/10.1109/icaci.2017.7974498>
- [17] Keskin, M. E., Döyen, A., Akyer, H., & Güler, M. G., (2018), Examination timetabling problem with scarce resources: a case study. *European J. of Industrial Engineering*, 12(6), 855. <https://doi.org/10.1504/ejie.2018.096394>
- [18] Güler, M. G., Geçici, E., Köroğlu, T., & Becit, E., (2021), A web-based decision support system for examination timetabling. *Expert Systems with Applications*, 183, 115363. <https://doi.org/10.1016/j.eswa.2021.115363>
- [19] Aldeeb, B. A., Azmi Al-Betar, M., Md Norwawi, N., Alissa, K. A., Alsmadi, M. K., Hazaymeh, A. A., & Alzaqebah, M., (2021), Hybrid Intelligent Water Drops Algorithm for Examination Timetabling Problem. *Journal of King Saud University - Computer and Information Sciences*. <https://doi.org/10.1016/j.jksuci.2021.06.016>
- [20] Hao, X., Qu, R., & Liu, J., (2020), A Unified Framework of Graph-based Evolutionary Multitasking Hyper-heuristic. *IEEE Transactions on Evolutionary Computation*, 25, 1. <https://doi.org/10.1109/TEVC.2020.2991717>



RESEARCH ARTICLE

**EVALUATION of the TRANSMISSION LINE TOWER EXPOSED to ARTIFICIAL
GROUND MOTIONS and WIND LOADS**

Asuman Isil CARHOGLU*

*Suleyman Demirel University, Civil Engineering Department, Isparta, isilcarhoglu@sdu.edu.tr, ORCID:0000-0003-2325-1788

Receive Date:06.10.2020

Accepted Date: 06.05.2022

ABSTRACT

Electricity transmission towers play an important role in the transmission of electricity. These buildings are very important to meet the many requirements related to electricity during natural disasters such as earthquakes and storms. Within the scope of this study, an electrical transmission line tower was analyzed and different wind velocities and different ground motion records were applied to the structure. In addition to it, the artificial earthquake acceleration records for different earthquake levels and soil classes were obtained for Istanbul by using Turkey Building Earthquake Regulation 2018. During the analysis, three wind speeds and the artificial earthquake acceleration records obtained by taking into account the different earthquake levels and ground classes were used. The wind pressure values acting on the structures are determined according to ASCE 7-10 standard. The ground motion data were carried out time history analysis. As a result of the analysis, displacement, stress and base shear force values were obtained and compared.

Keywords:*Steel towers, Wind analysis, Time history analysis.*

1. INTRODUCTION

Electricity Transmission towers are structures that provide electricity transmission. The requirement for transmission towers has increased with the rapid advance of technology. Transmission towers are generally tower type delicate structures having different geometrical features and are under the effect of forces such as earthquake and wind. In terms of structural engineering, it is of great importance to examine behavior under the earthquakes and wind effects of these towers. Since electricity transmission towers are structures providing electricity transmission, it is very important following the earthquake.



Figure 1. The steel tower damaged by the strong wind in China [1].

Strong winds often occur in many regions of the earth. They occur in tropical regions especially and create destructive effects on coastal parts [2]. Storms such as earthquakes can have destructive effects in a number of regions of the world. The five towers were damaged during strong winds in China in 2010 [1;3]. The tower structures damaged in China are shown in Figure 1. These steel tower structures are under the effect of wind and earthquake loads. Examining the effect on the structures of wind loads is of great significance in terms of structural engineering. As the height of the structure increases, the wind load occurring on the structure will be greater.

Many studies investigating the behavior of the towers under the earthquake effect were performed. There are studies which take the wind effect as well as the earthquake effect into consideration. Liang et al. [4] examined the behavior of the towers under seismic loads by modeling two electric towers with different heights by SAP 2000 program. Bai et al. [5] investigated the behavior of the building under the earthquake effect by modeling an electrical tower with SAP 2000 program. Hadimani P. [6] modeled electrical tower structures with ANSYS program and performed static and dynamic analysis. They studied the behavior of the structure under the wind and earthquake effect. Partal [7] investigated the steel telecommunication tower structure which was exposed to the effect of wind and seismic forces. They modeled the tower with SAP 2000 program and examined the structural behavior of the tower under the effect of the earthquake and wind loads. Tuncer [8] examined in the behavior of PTT. Kars television transmitting tower. They compared the values obtained from test results by using SAP 90 program. They observed that the values were close. They carried out the static and dynamic analyzes. Furthermore, the comparisons were also made by performing the wind calculations. Rajasekharan et al. [9] dealt with 4 legged towers whose heights are 30m, 40m and 50m. They considered two different wind velocities in the course of the analysis. Additionally, the analysis was performed by using the modal analysis and response spectrum method. They determined displacement values for towers with different heights. Sharma et al. [10] discussed telecommunication towers with different heights and different bracing shapes. They carried out wind analysis for different wind zones in accordance with the regulation. They also carried out seismic analysis using the response spectrum analysis method. Long et al. [11] examined the collapse of transmission steel towers by using MATLAB and ANSYS programs. As a result of the performed analysis, it was seen that the finite particle method and the finite element method were compatible. In addition to this, it has been determined that the transmission tower is safe under the effect of earthquakes and resistant to collapse. Bhowmik et al. [12] performed the modal analysis of the transmission tower by using analytical and experimental studies. The transmission tower was designed as a prototype. In addition, the tower was modeled using the finite element program with ANSYS program. The first six frequency values were

determined and compared experimentally and analytically. It was obtained the differences as a result of analytical and experimental studies. Asgarian et. al. [13] examined the progressive collapse of a tower structure. Load increase factor was determined by performing analysis. The ratios of capacity-demand was obtained by using different scenarios for element removal. This values was compared with overload factor obtained by performing pushdown analysis. Tas [14] carried out the time history analysis of the steel telecommunication towers having different bracing shapes by considering different ground motion data. In addition to this, the analysis of the response spectrum and wind analysis were made. As a result of the analysis, The steel tower structures were compared in terms of different heights, bracing shapes, wind speeds and earthquakes. Korkmaz et. al. [15] performed nonlinear pushover analysis to determine the curve of force displacement by dealing with a wind turbine tower. Time history analysis was made by using the six different earthquake records. It was evaluated results obtained from the time history and nonlinear pushover analysis. Yalciner et al. [16] analyzed RC structure by using the different corrosion effects. It was examined fragility curves of structures subjected to 20 different ground motion data. According to the analysis results, It was obtained that the corrosion of steel is of great importance. Kumbasaroglu [17] investigated three RC buildings considering 20 ground motion data for the purpose of determining the effects of anchor bars. It was observed that the possibility of exceeding the performance level is reduced with anchor bars.

In this study, the electrical transmission tower structure, which can be damaged under the effects of loads such as wind and earthquake, is examined. Firstly, the behavior of an electrical transmission tower under the wind influence is investigated according to ASCE 7-10 regulation for different wind speeds [18]. Secondly, Considering Turkey Building Earthquake Regulation 2018, artificial acceleration records were obtained for earthquake level II and soil class C, and analyzes were performed using the time history method. The displacement, stress and base shear force values were obtained and the results were compared [19,20].

2. MATERIALS and METHODS

The structure modeled by using the finite element method is divided into a finite number of elements connected to each other at certain points. The elements and joints are shown in Figure 2. The displacements in the elements form the displacements at the joints. The unknown values are values at the nodal points. A set of the equation for the whole system is formed when the equations of the elements forming the system are combined. In this method, elements are classified by their dimensions and load forms. Elements can be modeled as bar, shell, solid and spring. The finite element model is shown in Figure 2 [21].

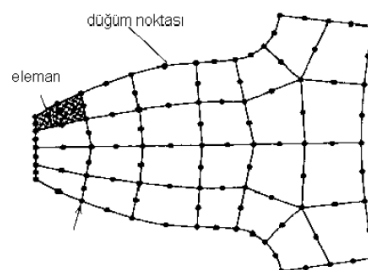


Figure 2. The finite element model [21].

In this study, the steel tower being 32m in height was designed. Tower design, modeling and analysis were performed with SAP 2000 finite element program [22]. The tower structure consists of 390 elements and 140 points as a frame. L profiles are used in the steel tower design. L 45 5, L 45 5 at beams and diagonals and L 80 8 on columns of the top parts are used, L 70. 7 on beams, L 80.8 and L 90.9 profiles on diagonals and columns are used on the bottom parts. The steel electrical tower with 32m height is shown in Figure 3.

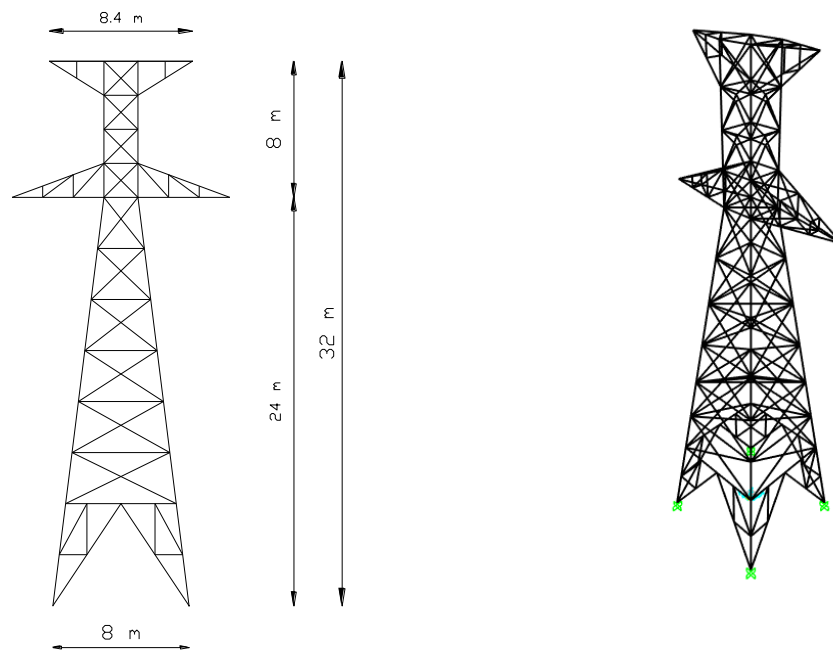


Figure 3. The view of the electrical tower structure.

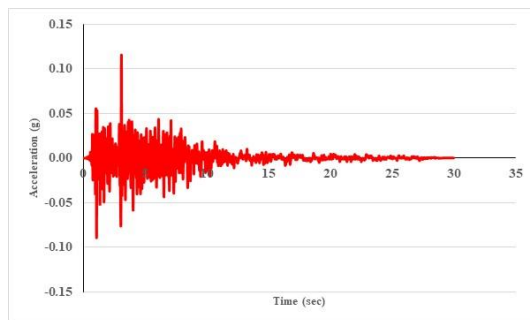
Tower structures are under the effect of many loads. These loads are snow, wind and earthquake loads. The earthquake is very important in our country since it is located in the seismic zone. So far, most of the earthquakes in our country have been destructive and caused great loss of life and property. Wind load is another important load as well as earthquakes all over the world. In this study, the behavior of the tower structure under the wind and earthquake loads effect is examined. The behavior that tower type delicate structures, being very high will show against wind and earthquake forces is quite important. Time history method is used for earthquake calculations. The calculation of the wind loads is determined in accordance with ASCE 7-10 [18].

In this study, firstly the behavior of the tower structure under the earthquake effect is examined. Time history analysis is used during the earthquake analysis. The artificial acceleration values were obtained by taking into account of the earthquake level 2 and soil class C. 11 earthquake records selected according to the Turkey Building Earthquake Regulations 2018 [19]. The values for spectrum curves were obtained according to Kocaeli province Gebze district [20]. Graphics including time-

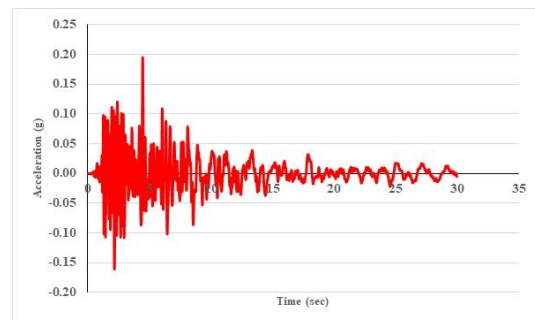
dependent acceleration values of artificial earthquakes are presented in Figure 4. The properties of the selected earthquakes are shown in Table 1 [23].

Table 1. The properties of the selected earthquakes [23].

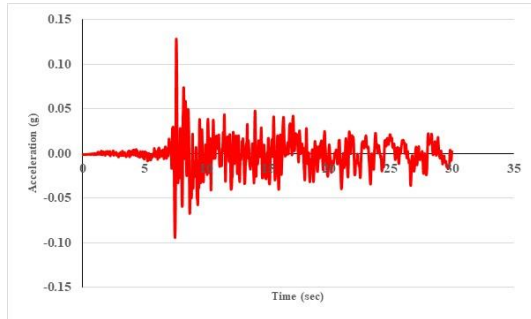
Earthquake Number	Earthquake Name	Station Name	V_s (m/s)	Focus Depth	Magnitude
1	Morgan Hill	Gilroy - Gavilan Coll	729.65	14.84	6.19
2	Morgan Hill	Gilroy Array #3	349.85	13.02	6.19
3	Imperial Valley-06	Calipatria Fire Station	205.78	24.6	6.53
4	Darfield, New Zealand	RKAC	295.74	16.47	7
5	Anza-02	Idyllwild - Kenworthy Fire Sta	382.44	20.34	4.92
6	Coyote Lake	Coyote Lake Dam - Southwest Abutment	561.43	6.13	5.74
7	Northridge -01	LA - UCLA Grounds	398.42	22.49	6.69
8	Imperial Valley-06	Bonds Corner	223.03	2.66	6.53
9	Coalinga-01	Slack Canyon	648.09	27.46	6.36
10	Chi-Chi Taiwan	TCU079	363.99	10.97	7.62
11	Duzce, Turkey	Duzce	281.86	6.58	7.14



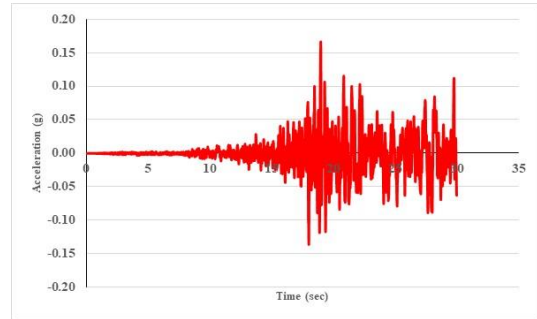
Earthquake Number 1



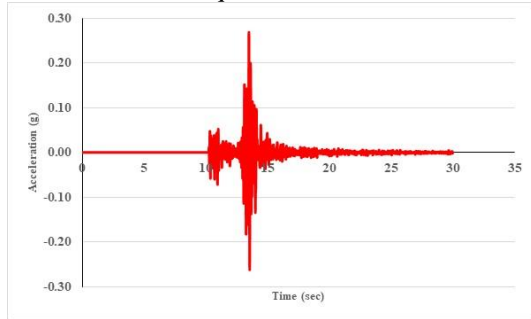
Earthquake Number 2



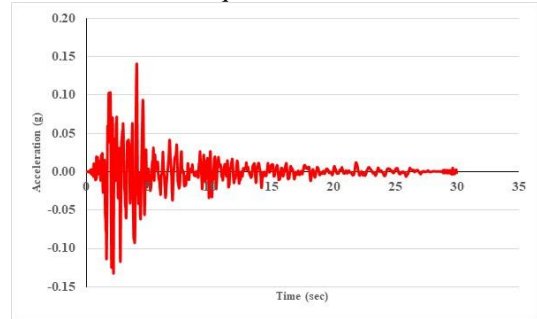
Earthquake Number 3



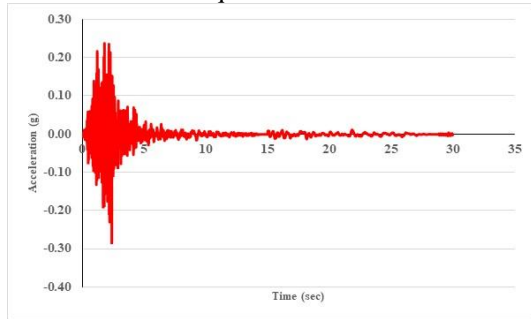
Earthquake Number 4



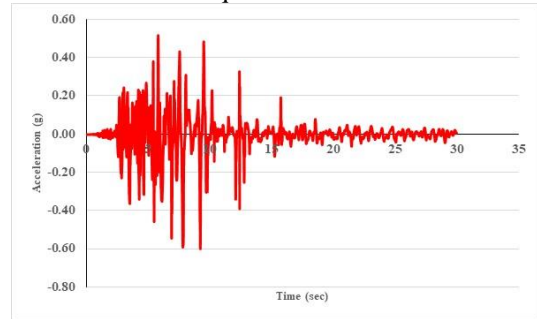
Earthquake Number 5



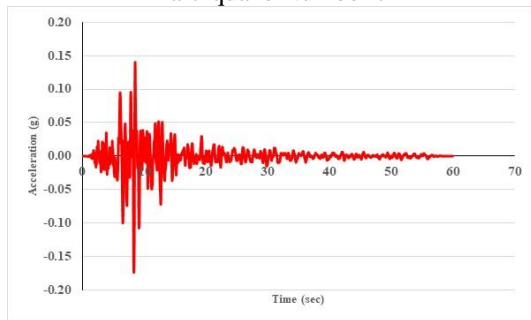
Earthquake Number 6



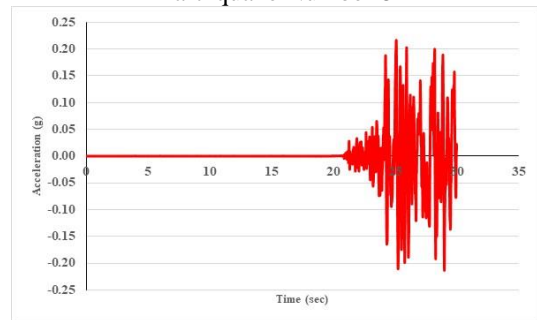
Earthquake Number 7



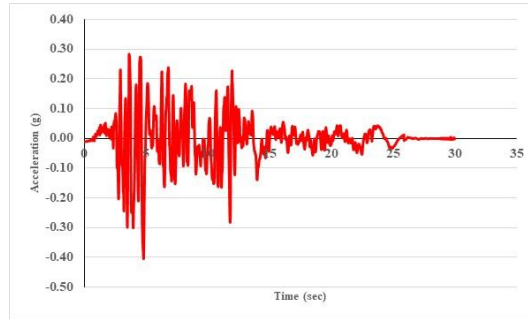
Earthquake Number 8



Earthquake Number 9



Earthquake Number 10



Earthquake Number 11

Figure 4. The artificial acceleration value for all the earthquake levels and soil classes.

Wind loads are also very important for tower type structures. In Table 2, the values obtained from the measurement of wind speed in three seconds and ten minute periods in ASCE 7-10 Regulation are presented by the risk categories [18;24]. In this study, 15 m/sec, 25 m/sec and 35 m/sec wind speeds were examined in accordance with the measurements carried out in 3-second periods.

Table 2. Wind velocities [18;24].

Risk Category	Wind Speed	
	T= 3 secPeriod	T= 10 minutePeriod
I	<35	<22
II	35-45	22-30
III	45-55	30-35
IV	55-65	35-40
V	>65	>40

Wind velocity pressure;

$$q_z, q_h = 0.613 \cdot K_z K_{zt} K_d \cdot I \cdot V^2 \quad (1)$$

V: Basic wind speed

K_d: Wind Direction Coefficient

K_z: Wind pressure exposure coefficient

K_{zt}: Topographic factor

I: Importance coefficient

Wind direction coefficient (K_d) is 0.85 for tower structures, topographic factor (K_{zt}) is 1. Exposure category is obtained according to surface roughness and is taken as B. K_z values are determined according to the standard depending on the height [18,24].

Design Wind Pressures;

$$P = q G C_p q_i (GC)_{pi} \quad (2)$$

q_i : internal pressure

$(GC)_{pi}$: Internal pressure coefficients

C_p : It is calculated by external pressure coefficient.

C_p is 0.8 perpendicular wall to the wind and -0.5 on the back wall.

The storm effect factor (G) should be determined for the design wind pressure calculation

$$G = 0.925 \left(\frac{1 + 1.7g_Q I_{\bar{z}} Q}{1 + 1.7g_v I_{\bar{z}}} \right) \quad (3)$$

$$I_z = c \left(\frac{10}{\bar{z}} \right)^{1/6} \quad (4)$$

$$L_{\bar{z}} = 1 \left(\frac{\bar{z}}{10} \right)^{\epsilon} \quad (5)$$

$$Q = \sqrt{\frac{1}{1 + 0.63 \left(\frac{B+h}{L_{\bar{z}}} \right)^{\epsilon}}} \quad (6)$$

Wind velocity pressure and design wind pressures are respectively determined by using Eq. (1) and Eq. (2). Q; Ground response factor is calculated by Eq. (6). The values of G were calculated as 0.82 by using Eq. (3), g_v ; Peak factor for wind response, g_Q ; Peak factor for ground response, B; Horizontal length of the building (in the direction perpendicular to the wind direction), h; Average building height [18,24]. The wind was applied perpendicular in the +X direction to the structure.

3. RESULTS AND DISCUSSION

In this study, the behavior of the steel electrical transmission tower height of which was 32m under the earthquake and wind effect was examined. 3 wind speeds and 11 artificial ground motion records were applied to the structure. In addition, the acceleration spectra were applied by considering all soil classes and earthquake levels. Period values and mode shapes occurring in the structure as a result of modal analyses are shown in Figure 5.

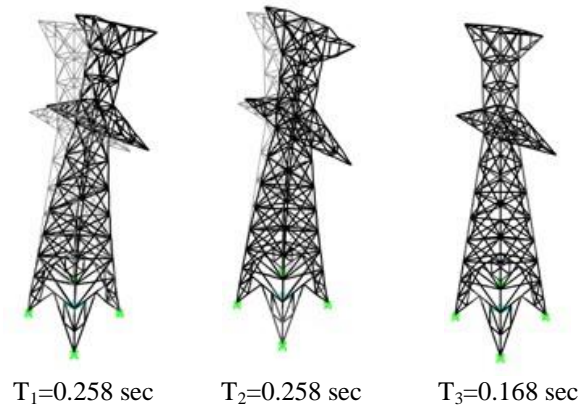
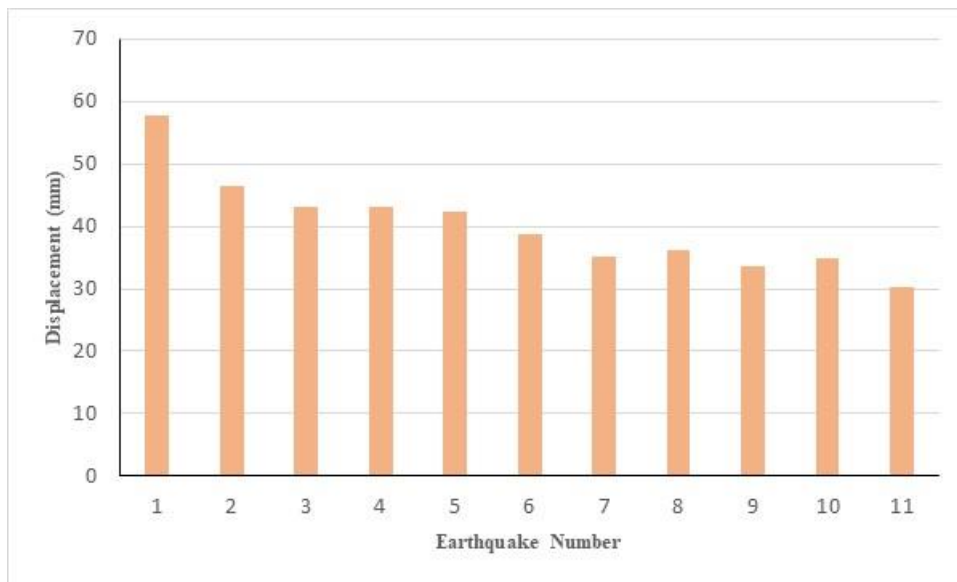
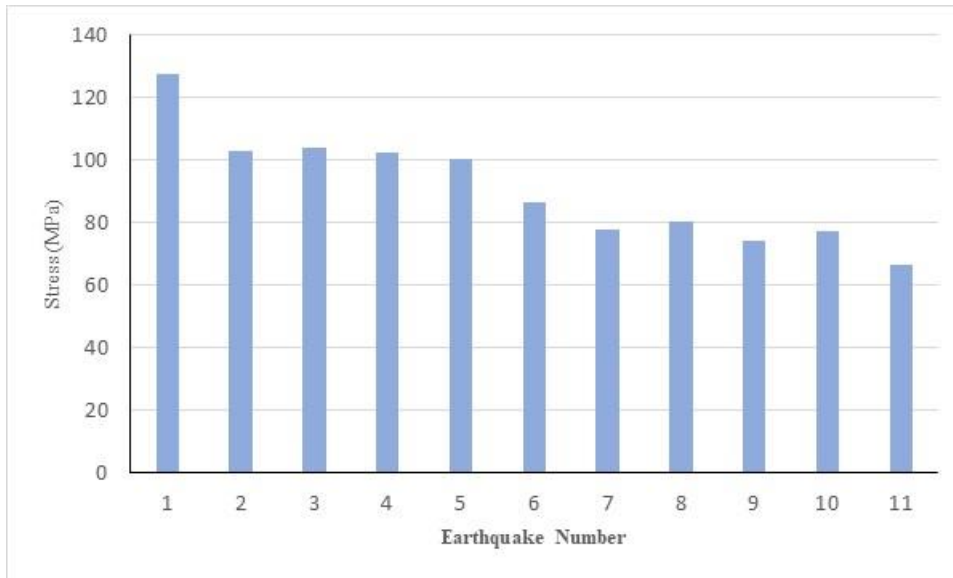


Figure 5. The values of the period and mode shapes of the electrical tower structure.

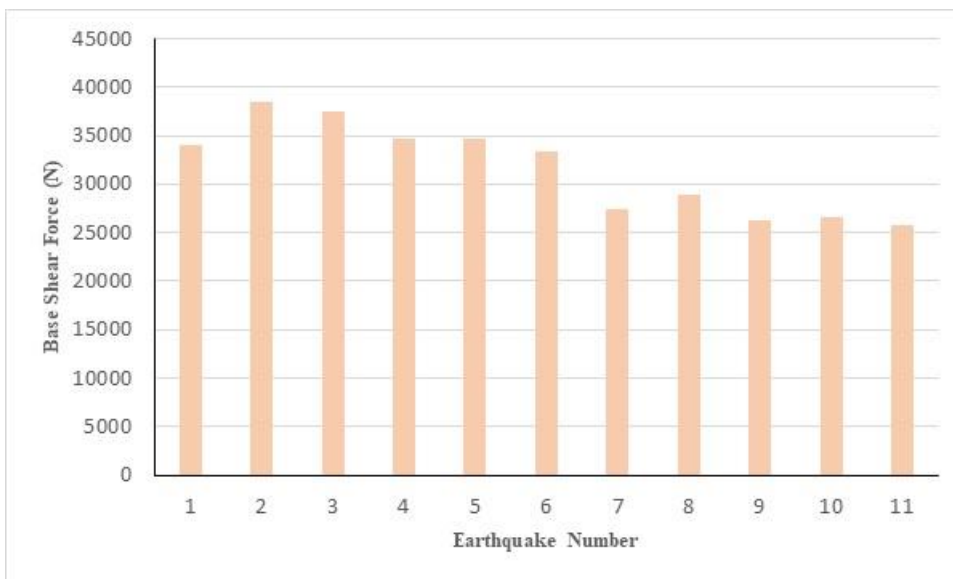
11 acceleration values dependent to time were selected in accordance with Turkish Earthquake Code 2018 and artificial acceleration records were obtained by considering Gebze district of Kocaeli province for the earthquake level 2 and the soil class C [19,20]. The values obtained from the results of the time history analysis performed with the artificial acceleration records obtained are shown in Figure 6.



a) The values of displacement



b) The values of stress



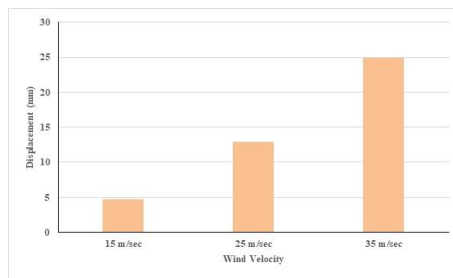
c) The values of base shear force

Figure 6. The values obtained as a result of the time history analysis.

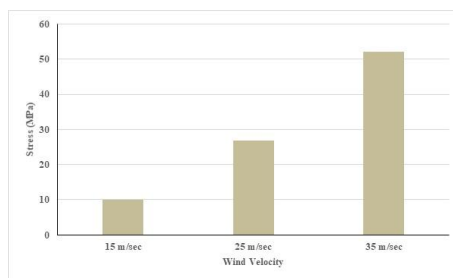
In the case of earthquake level 2 and soil class C, the biggest displacement value is found as 57.69 mm, base shear force value is found as 34076.45 N and stress value is found as 127.64 N/mm² for 1

numbered Morgan Hill Earthquake. The smallest values were obtained in the case of the 11 numbered Duzce, Turkey Earthquake and the value of displacement is 30.34 mm, the value of base shear force is 25751.06 N and the value of stress is 66.47 N/mm². The effective ground acceleration values of 1 and 11 numbered earthquakes obtained as the artificial are respectively 0.81g and 0.47g. When the ground velocity of 1 numbered earthquakes is 729.65 m/s, the ground velocity of 11 numbered earthquake is 281.86 m/s. When the values are viewed from the largest to the smallest; It is seen that the 2 numbered Morgan Hill earthquake which has an effective ground acceleration of 0.70 g is in the second place. It is seen that the displacement value obtained as a result of the application of the 2 numbered Morgan Hill earthquake to the structure is 46.44 mm, the base shear force value is 38395.69 N and the stress value is 103.08 N/mm². The biggest displacement values were obtained in the upper parts of the tower, and the values of the biggest stress were obtained in the wings of the tower.

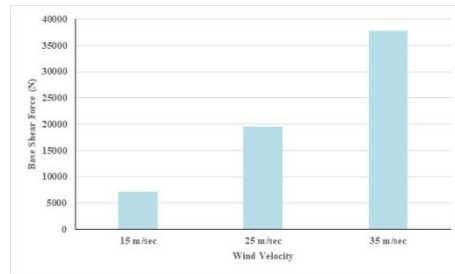
The values of the effective ground acceleration of 4 and 5 numbered artificially produced earthquakes are very close to each other. While the magnitude of the 4 numbered earthquake is 7, the magnitude of 5 numbered earthquake is 4.92. However, the ground velocity of 4 and 5 numbered earthquakes were 295.75 m/s, 382.44 m/s respectively. The displacement values obtained from 4 and 5 numbered earthquakes are 43.00 mm, 43.12 mm, base shear force values are 37411.65 N, 34703.36 N, stress values are 103.94 N/mm² and 102.42 N/mm², respectively. Although the magnitudes of the earthquakes are quite different, the values obtained due to other factors are quite close.



a) The values of displacement



b) The values of stress



c) The values of base shear force

Figure 7. The values obtained under the wind loading effect.

The values of the pressure of the wind velocities of which were 15m/sec, 25 m/sec ve 35 m/sec were applied to the building. The values of the displacements, stresses, base shear forces obtained depending on the height occurred in the building because of the effect of these winds are presented in Figure 7. When the wind velocity is 25 m/sec, while the displacement values of the first floor occur 0.4 mm, the displacement value of the top floor occurs 12.86mm. While the displacement value of the first and the top of the floor are respectively 0.80 mm and 24.95 mm at 35 m/sec wind speed, the displacement value is 4.7 mm in the case of 15 m/sec wind speed. As the wind speeds were 15 m/sec, 25 m/sec and 35 m/sec, the stress values occurred as respectively 9.9 MPa, 26.82 MPa and 52.04 Mpa. However, the values of base shear force were obtained as 7172 N, 19456.22 N and 37746.06 N.

4. CONCLUSION

In this study, the structural behavior of an electric transmission tower under the effect of the earthquake and wind loads was investigated. Wind analysis was carried out according to the ASCE 7-10 standard, it was used to the time history analysis method for earthquake analysis. Wind analysis were performed for wind speeds of 15 m/sec, 25 m/sec, and 35 m/sec. In earthquake analysis, 11 earthquakes with different characteristics produced artificially were used. It was observed that the behavior of the structure under the wind effect was important as well as the earthquake effect.

The artificial acceleration records were obtained by taking into account of the earthquake level 2 and soil class C for Gebze Kocaeli. Considering the values obtained, it is seen that 11 artificial acceleration records were created by taking 11 time-dependent acceleration values and the values of the displacement, base shear force and stress were found. While the biggest values were obtained at 1 numbered Morgan Hill earthquake, the smallest values were obtained in the 11 numbered Duzce Earthquake. The smallest values were found in 11 numbered Morgan Hill Earthquake. It is seen that the values obtained changed depending on the effective ground acceleration, earthquake velocity and focus depth values.

Considering the results of the wind load analysis; it is seen that as the wind speed increases, the values of displacement, shear force and stress occurring at the building increase. The wind load acting on the structure increases as the height of the structure increases, and it is seen that the values obtained increases depending on the height.

Slender tower-type structures are structures that can be highly affected by the effects of earthquakes and winds. In future studies, the collapse status of tower structures can be examined. While

performing the failure analysis, probability analysis can be done by considering the effect of wind and earthquake loads. In addition, different regulations and methods can be used while performing wind analysis.

ACKNOWLEDGEMENT

The author declares that there are no conflict of interests.

REFERENCES

- [1] Tian L, Yu Q, Ma R. and Wang C., (2014), The collapse analysis of a transmission tower under wind excitation. *The Open Civil Engineering Journal*, 8, 136-142.
- [2] Polat Ö.O, (2010), Comparison of wind loading on buildings by using ASCE 7-05, Eurocode 1-4 and TS 498, İstanbul Technical University, Master's Thesis, İstanbul.
- [3] Kamarudin S.A., Usman F. and Baharuddin I.N.Z., (2018), Review on analysis and design of lattice steel structure of overhead transmission tower. *International Journal of Advanced and Applied Sciences*, 5 (1) , 73-80.
- [4] Liang J. Z., Hao H., (2008), Performance of Power Transmission Tower in PMA under Simulated Earthquake Ground Motion. In *Proceedings of the 14th World Conference of Earthquake Engineering*, October 12-17, Beijing, China.
- [5] Bai, F. L., Hao, H. and Li, H. N., (2009), Response analysis of a transmission tower-line system to spatial ground motions. In *Australian Earthquake Engineering Society Conference*, Newcastle, Australia.
- [6] Hadimani P., Kulkarni S.,(2017), Static and Dynamic Analysis of Transmission Line Tower. *International Journal of Emerging Research in Management &Technology*, 6 (2), 147-154.
- [7] Partal Ş.D., (2012), Structural behaviour of steel lattice telecommunication towers under the seismic action with other actions, Gaziantep University, Master's Thesis, Gaziantep.
- [8] Tuncer M., (1993), Dynamic Analysis of tower structures a case study: PTT Kars Television Tower, Master's Thesis, Middle East Technical University.
- [9] Rajasekharan J., Vijaya, S., (2014), Analysis of Telecommunication Tower Subjected to Seismic & Wind Loading, *International Journal of Advancement in Engineering Technology, Management and Applied Science*, 1(02).
- [10] Sharma K.K., Duggal S.K., Singh D.K. and Sachan A.K., (2015), Comparative Analysis Of Steel Telecommunication Tower Subjected To Seismic & Wind Loading, *Civil Engineering and Urban Planning: An International Journal (CiVEJ)*, 2(3).

- [11] Long, X., Wang, W. and Fan, J. (2018), Collapse analysis of transmission tower subjected to earthquake ground motion, Modelling and Simulation in Engineering, ID 2687561.
- [12] Bhowmik, C., Chakraborti, P. (2020), Analytical and experimental modal analysis of electrical transmission tower to study the dynamic characteristics and behaviors. KSCE Journal of Civil Engineering, 24 (3), 931-942.
- [13] Asgarian, B., Eslamlou, S. D., Zaghi, A. E. and Mehr, M., (2016), Progressive collapse analysis of power transmission towers. Journal of Constructional Steel Research, 123, 31-40.
- [14] Tas H.H.(2019), Investigation of structural behavior of tower structures of steel telecommunication tower structures, Suleyman Demirel University, Master's Thesis, Isparta.
- [15] Korkmaz, K. A., Çarhoğlu, A. I. and Kural, M. E., (2008), Sürdürülebilir enerji kaynaklarından rüzgâr türbinlerinin davranışlarının deprem etkisi altında incelenmesi. İstanbul Ticaret Üniversitesi Fen Bilimleri Dergisi, 7(14), 1-13.
- [16] Yalciner, H., Sensoy, S., and Eren, O., (2012), Time-dependent seismic performance assessment of a single-degree-of-freedom frame subject to corrosion, Engineering Failure Analysis, 19, 109-122.
- [17] Kumbasaroglu, A., (2020), Effect of anchor bars on seismic behavior of infilled walled frames. KSCE Journal of Civil Engineering, 24(10), 2980-2992.
- [18] ASCE 7-10, (2010), Minimum design loads for buildings and other structures, American Society of Civil Engineers, Reston, Virginia.
- [19] TBDY, Türkiye Bina Deprem Yönetmeliği, Ankara, 2018.
- [20] Afet ve Acil Durum Başkanlığı, (AFAD), 2019, <https://www.afad.gov.tr>
- [21] Babur A., (2012), Finite element modeling and simulation of tower structures under earthquake loads, Ondokuz Mayıs University, Master's Thesis, Samsun.
- [22] Wilson E., Habibullah A., (1998), SAP 2000 Integrated Finite Element Analysis and Design of Structures Basic Analysis Reference Manual, Berkeley, Computers and Structures.
- [23] Pacific Earthquake Engineering Research (PEER) Center, <https://ngawest2.berkeley.edu/>
- [24] Özlek C., (2015), A comparison of wind loads acting on structures by means of using ASCE 7-10, Eurocode 1-4 and TS 498, Istanbul Technical University, Master's Thesis, Istanbul.



RESEARCH ARTICLE

CODE GENERATION USING TRANSFORMER BASED LANGUAGE MODEL

Umut Can ALAÇAM¹, Çağla GÖKGÖZ², Cahit PERKGÖZ^{3,*}

¹Eskisehir Technical University, Faculty of Engineering, Department of Computer Engineering,,
umutcanalacam@eskisehir.edu.tr, ORCID: 0000-0002-6376-0352

²Eskisehir Technical University, Faculty of Engineering, Department of Computer Engineering,, caglagokgoz@eskisehir.edu.tr,
ORCID: 0000-0003-1214-3546

^{3,*}Eskisehir Technical University, Faculty of Engineering, Department of Computer Engineering,,
cahitperkgoz@eskisehir.edu.tr, ORCID: 0000-0003-0424-7046

Receive Date:09.03.2022

Accepted Date: 12.05.2022

ABSTRACT

Machine Learning has attracted researchers in the last decades and has been applied to different problems in many fields. Deep Learning methods which is a subfield of Machine Learning have started to be utilized to solve complex and hard problems with the improvement of computer technologies. Natural language processing is one of the challenging tasks that still needs to be improved for different applications such as code generation. Recently, general-purpose transformer based autoregressive language models achieved promising results on natural language generation tasks. Code generation from natural utterance using deep learning methods could be a promising development in terms of decreasing mental effort and time spent. In this study, a layered approach to generate Cascading Styles Sheets rules is proposed. The abstract data is obtained using a large-scale language model from natural utterances. Then the information is encoded into Abstract Syntax Tree. Finally, Abstract Syntax Tree structure is decoded in order to generate the Cascading Styles Sheets rules. In order to measure the performance of the proposed method an experimental procedure is constructed. Using pre-trained transformers and generated training data for Cascading Styles Sheets rules, different tests are applied to different datasets and the accuracies are obtained. Promising results for Cascading Styles Sheets code generation tasks using structural and natural prompt design are achieved. 46.98% and 66.07% overall accuracies are obtained for structural and natural prompt designs, respectively.

Keywords: *Natural Language Processing, Transformers, Abstract Syntax Tree, Code Generation, Deep Learning*

1. INTRODUCTION

The styles of web pages are defined with Cascading Styles Sheets (CSS) rules which are groups of CSS properties. HTML elements can be customized with these CSS properties. Therefore, modifying the style of a web page needs to have a better understanding of the schema of CSS and familiarity with computer programming languages which requires a significant mental effort. Generating CSS rules with natural utterances might reduce this effort and increase the productivity of designers. However, converting natural utterances to logical forms such as CSS codes is a challenging task and requires semantic parsing practices with natural language processing.

Prior to the description of the transformer model architecture [1], it should be noted that RNN models are commonly utilized for code generation tasks where current state is determined by the past information [2-5]. The earlier models were based on the sequence-to-sequence methodology [5, 6]. However, such purely sequence oriented methods could cause loss of structural information [7]. Therefore, subsequent studies depend on a grammar tree structure that improves the generalization and reliability capabilities of code generation models [8-10]. In recent reports, it is presented that transformers can also compete with the state-of-the-art models for semantic parsing tasks, such as code generation [7, 11-13]. Hence, transformer-based code generation and completion models have been advanced by the industry and integrated into the commercial products including integrated development environments (IDEs) [10, 14].

Recently, general purpose autoregressive language models have provided favorable results on natural language generation tasks [15]. The recent auto regressive transformer model of OpenAI, Generative Pre-trained Transformer-3 (GPT-3), scaled up the transformer based autoregressive models to 175 billion parameters and presented impressive results on multiple tasks [15]. Despite the semantic parsing tasks does not naturally fit into the paradigm of these models, a recently reported work shows that auto-regressive language models achieve reasonable results with few examples [12]. Inspired from the low data demand and existing capabilities of GPT-3, we propose a three-layer approach for generating CSS rules with given natural utterances.

First, a verbal expression is converted into text if the input is given in speech format. Then, the information needed for generating a CSS rule is extracted from natural utterance, after which the extracted information encoded into an Abstract Syntax Tree (AST). Lastly, the AST structure is decoded, and the corresponding CSS Rule is obtained for the given natural utterance.

The flow of the context is as follows; a summary of Natural Language Processing (NLP) concepts that is relevant to this work is provided in the second section. Later, the details of three-level approach are described in order to utilize an autoregressive language model for code generation tasks. In results section, different prompts for GPT-3 are experimented and the results are compared.

2. METHODS

While developing a system that modifies web page styles dynamically, using a natural language interface, an input from the user should be construed clearly, and a compliant CSS rule should be generated. The operators should be able to decorate any web page by describing their request in natural language (e.g. "Enlarge the headings."). In the following subsections, the background needed to introduce this work is summarized.

2.1. Transformers in Natural Language Processing

Natural Language Processing is generating abstract data from a language either in speech or text. By it is nature NLP is a hard problem to solve since most of the tasks contain messy data. In 2017, the paper "Attention is all you need" introduced a novel model architecture called transformers for language models [1]. The transformers are quickly embraced by the industry and became state-of-the-art architecture for seq2seq language models [11].

In transformers, the input is not processed sequentially. However, sequence of the words or positions comprises valuable information of the semantic meanings of a text given in natural language [7].

Therefore, in order to capture the positional relations, a positional embedding mechanism applied to each token [1]. Additional to the positional relations, the self-attention-mechanism estimates the relations between each token of the input [16]. With self-attention mechanism the model is able to capture the dependencies between tokens more reliably [7].

Unlike RNN based models, transformers do not suffer from vanishing gradient problem as the input sequence gets longer. The transformers are also advantageous to RNN based models in training time since it allows to process input sequence in parallel. Therefore, training process is much faster than RNN based models [1].

2.2. GPT-3

GPT-3 is the third generation natural language deep neural network model from OpenAI's Generative Pretrained Transformer model family. Technically, GPT-3 is a seq2seq language model which generates a completion for a given token sequence by calculating the probabilities of the next tokens [17]. These tokens are the smallest units of a text data that the model can process. The tokens can represent sentences, words, or a small fraction of words. The architecture of GPT-3 consists of two main parts: encoder and decoder. The input words are encoded, and a vector representation is obtained which is used to predict the next words. Then the probabilities of possible words are decoded from the input and the generated vector by the encoder.

GPT-3 remained as the biggest natural language model with 175 billion parameters until another transformer language model with 1 trillion parameters is announced in 2021 [18]. GPT-3 is trained with a very large corpus that contains different languages, domains, or grammar structures [1]. As the work proposed, language models yield to learn multiple tasks for different domains since the model is capable of capturing the information about different task domains. Therefore, GPT-3 shows strong performance on various tasks without fine tuning. In some cases, GPT-3 performs close or outperforms to the domain specific state-of-the-art fine-tuned models [1].

GPT-3 is able to carry out various tasks by designing a prompt that provides a brief explanation of the task with few examples [1]. For any given prompt, GPT-3 generates a completion which maximizes the likelihood with the corpora that is given to the model while training [13]. Thus, the design of the prompt is crucial for the accuracy of the obtained results.

3. PROPOSED APPROACH

A three-level pipeline is designed, in a high-level view, as an Artificial Intelligent (AI) agent. The AI agent accepts user request in text or speech format and generates a CSS rule that satisfies the user request. Such an approach provides a good level of abstraction for the internal structure. Abstraction of internal details makes the agent more reliable and useful when it is used within a complex application.

In a more detailed view, each input is processed in a pipeline of three components. These components, also called as layers, takes the input from previous component, and generates the output for the next component. The layered structure of the CSS code generation and connections are shown in Figure 1.

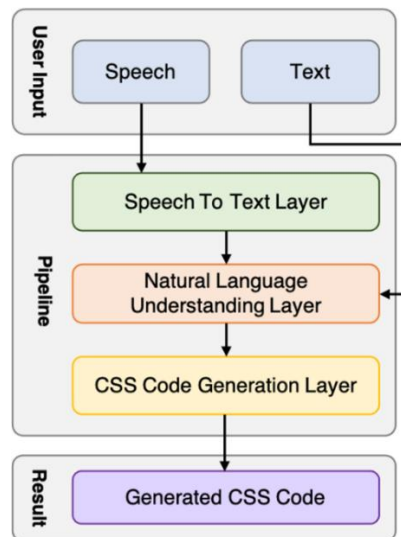


Figure 1. Layered Structure of CSS Code Generation.

3.1. Pipeline Layers

Each of the layers in the pipeline takes on different responsibilities in order to generate CSS code from user requests. When a request is received with a verbal expression: Speech to Text (STT) layer converts user speech to the text format. Then Natural Language Understanding (NLU) layer extracts the required information for generating a CSS rule by processing the user request. Finally, CSS Code Generation Layer parses the information extracted by NLU layer and generates a syntactically valid CSS rule that can be injected into the HTML code of the web site.

Pipeline layers, abstracts their internal implementation from other layers. Layered approach makes the development of software easier, more reliable and makes possible to replace or improve a layer independently. For example, in STT layer any third-party software that converts voice data to text data can be used or STT engine can be implemented without concerning about other components.

3.1.1. Speech to text layer

Speech to text layer is responsible for converting user speech into the text. This layer gets user input in audio signals and transcribes user speech. Thus, the NLU layer can process the user request and extract the properties of CSS rule which is going to be generated. If the input is already given in text format, this layer is skipped, and the user request directly passed to the NLU layer. This layer is ignored when measuring the accuracy of our NLU implementation since the speech to text transformation process is not relevant to the success of our NLU implementation.

3.1.2. Natural language understanding layer

Natural Language Understanding layer processes the user request in text format and extracts the required features of the CSS rule that is compliant with the user request. The NLU layer utilizes the GPT-3 for processing and extracting features from the text. These extracted features are the CSS selector, CSS property, and the value of the property. NLU layer encodes these features in a data structure called Abstract Syntax Tree (AST) for further processing by CSS Code Generation layer.

The abstract syntax tree structure represents the syntactical structure and content related features of a CSS rule such as CSS selectors, CSS property, the value for the extracted property, keywords like important etc.

CSS AST only includes the required syntactical properties of CSS in this study. In Figure 2, the structure of CSS AST is shown. According to the AST structure, a CSS document consists of many CSS rules, where each CSS rule consists of many selectors and declarations. The declarations consist of property, value and can also have an important keyword and so on.

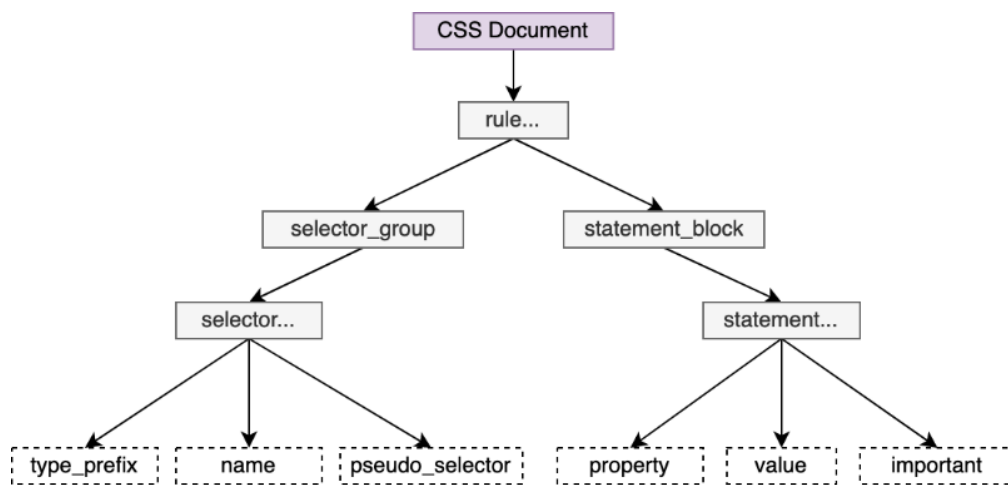


Figure 2. CSS AST Model.

In Figure 3, the CSS rule body {background: black}, which indicates the background color of the body element is black, is shown in AST format. The AST structure provides a general and compact representation of CSS documents. Currently, in this work only one CSS rule is generated per request. Therefore, the AST approach might be simplified to the simple entity mappings by extracting the selectors, properties and the values. However, the entity mapping approach would not represent the complete syntactical structure of CSS and cannot be generalized enough to decouple CSS code generation layer with NLU layer.

Using the generalization capability of the AST approach, the CSS code generation implementation does not need to be modified whenever NLU capabilities are decided to be extended. It is also not needed to be modified existing AST structure and AST decoding procedure of CSS code generation layer even though the AST can be generated in a better way and more accurate in the future, since the syntactical structure of CSS does not change.

The AST approach also ensures the consistency of generated CSS rules by eliminating the invalid CSS statements that could be generated. If GPT-3 generates an invalid output, it is not possible to build a valid AST. Therefore, the inconsistent outputs can be detected and eliminated without effecting the style of the website.

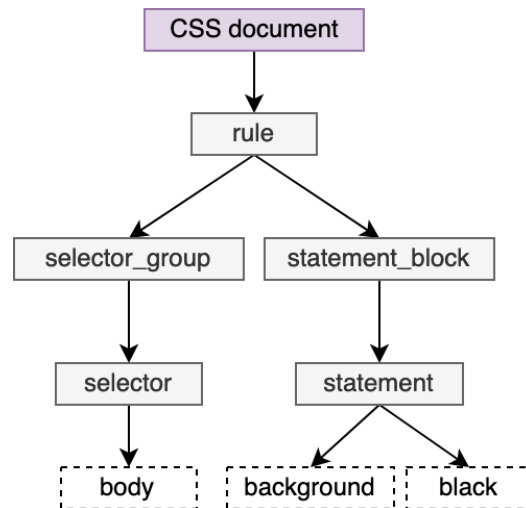


Figure 3. AST Example for the CSS Rule: `body {background: black}`.

3.1.3. CSS code generation layer

CSS Code Generation layer decodes the AST that is generated by the NLU layer and generates the CSS code. Since the AST contains syntactical hierarchy and content related features of the CSS code, it is easy to convert AST data into a syntactically valid CSS code. Since the AST schema is decoded with a deterministic procedure, it is possible to guarantee that the output of the CSS code layer is always syntactically valid. However, the content related features such as CSS selector, property and values might be inconsistent. For example: the property can be extracted as "color" and the value might be extracted as "12px" which are not compliant with each other. This issue can be achieved by checking if the AST attributes are valid. However, this is not concerned because the most browser engines ignore attribute errors covered in this way.

4. EXPERIMENTAL RESULTS

Meaningful representation of CSS code highly depends on the utilization of GPT-3 to construe the requests and generation of the AST as mentioned before. Since GPT-3 captures the context of the problem within the prompt, prompt design is crucial for the accuracy [11]. To achieve better accuracy and discovering the nature of auto-regressive language models, the three-level approach in this study is tested with different prompt designs.

4.1. Dataset

For discovering the capabilities of our NLU approach, a dataset which contains hand annotated user request examples with their expected CSS equivalents is created.

The natural utterances that NLU layer is going to handle, have differences in terms of how the features are explained and how much of the information is given. Therefore, it would be more beneficial to examine natural utterances in different categories. Hence, test data is grouped into three categories which are property update requests, relative update requests and decoration requests.

Property update requests contains clear and distinct information about the style rule. The utterance contains all features of AST: selector, property, and value. (e.g., “*Make heading one color blue*”).

Relative update requests clearly describe the target and the property of the rule. However, the value is not clear and described with a comparison to its older value. (e.g., “*Make headings bigger*”).

Decoration requests describes a new design feature that will modify the webpage. These examples do not clearly describe the property and value unlike the target which is clearly described. (e.g., “*Add text shadows to the hyperlinks*”).

4.2. Experimental Procedure

In order to measure the performance of the layered approach in this work, the tests are applied separately to all categories of the dataset to find out the capabilities of our NLU layer on different categories of requests which are property update requests, relative update requests and decoration requests. The accuracy is calculated by comparing the model output with the ground truth for each of the example in dataset. However, the nature of CSS allows different properties and values to behave effectively same. For example, the rules using background-color property and background property behaves identical when the value is a color. As a result, there exists more than one compliant CSS rule for a particular natural utterance. Therefore, counting only the exact matches lead incorrect measurements since the outputs that are compliant with the user request. In order to overcome this situation, the generated CSS rules that behaves compliant with the user requests are accepted as accurate outcomes. The equation for output accuracy is shown in Eqn. 1.

$$OutputAccuracy = \frac{TrueOutputs}{NumberOfGeneratedAST} \times 100 \quad (1)$$

where *OutputAccuracy* represents the ratio of the accurate outputs that is generated. The term *TrueOutputs* is the number of the outputs that is compliant with the user request and behaves effectively same with the ground truth. The term *NumberOfGeneratedAST* is the number of successfully generated ASTs. Note that generation of a valid AST only guarantees that the generated output can be converted into a syntactically valid CSS rule. The generated AST may include wrong entities and not compliant with the true CSS rule.

As mentioned before, in order to create an AST from a natural utterance, it is required to extract selector, property and value entities. Therefore, performance of detecting these entities is also essential for understanding the strengths and weaknesses of the method. Hence, accuracies of detecting each entity are also calculated.

$$SelectorAccuracy = \frac{TrueSelectors}{NumberOfGeneratedAST} \times 100 \quad (2)$$

$$PropertyAccuracy = \frac{TrueProperties}{NumberOfGeneratedAST} \times 100 \quad (3)$$

$$ValueAccuracy = \frac{TrueValues}{NumberOfGeneratedAST} \times 100 \quad (4)$$

The accuracies of extracted entities are calculated with the equations given in Eqns. 2, 3 and 4. The terms: *TrueSelector*, *TrueProperties* and *TrueValues* represent the number of the entities that semantically match the ground truth.

4.3. Prompt Design

In NLU layer, the behavior of the GPT-3 with different prompt designs is investigated to find out how to create a promising prompt design. We proposed two different prompt designs that have structural and contextual differences.

4.3.1. Structural representation

First approach to the prompt design requires syntactical rules that GPT-3 requires to follow. In order to retrieve the information that GPT-3 produced; a meaningful representation of AST is proposed. Using this meaningful representation, it is possible to build an AST thereby, a syntactically valid CSS rule can be generated.

The prompt contains a set of examples to encourage GPT-3 for generating outputs in form of our meaningful representation. Each line represents a single example, which consists of a natural utterance and its meaningful representation.

Make body background black => [selector:"body", property:"background", value:"black"];

An example from the prompt is shown above. The example is separated into natural utterance and meaningful representation sections with the characters: '=>'. The natural utterance section represents an example user request in natural language. The meaningful representation section represents the AST which is compliant with this natural utterance. The meaningful representation is given between the square brackets, and contains the entities required for a CSS rule: selector, property, and value. Finally, a semi-colon character ';' is used for limiting the output of the GPT-3.

4.3.2. Natural representation

The second approach for the prompt design aims to provide data in more convenient structure for GPT-3. Despite GPT-3 mostly focused on natural language, the corpora given to the model contains considerable amount of CSS code [15]. Therefore, the model is more familiar with the rules of CSS language than particular syntactic design in this work.

Similar to the previous prompt design, each line in the prompt contains an example of user request and the meaningful representation of this request. However, in this approach, the meaningful representation follows the original CSS syntax, which is in the same format of HTML style attributes.

Make body background black => body { background: black }

The example of this representation is shown above. As shown in the example, the meaningful representation section follows the original CSS syntax. Since the CSS rules are already structural, it is possible to create an AST for validating the output of GPT-3.

4.4. Test Results

For discovering the capabilities of both prompt designs: structural representation and natural representation are tested on the request categories: property updates, relative updates and decorations. The prompts consist of 4 property update, 4 relative update and 3 decoration request examples that are randomly picked from the data set.

4.4.1. Results with structural representation prompt design

As mentioned before, the first approach to the meaningful representation was a custom syntactical representation proposed within this research. The results obtained with this representation is given in Table 1.

Table 1. Results of Structural Representation Prompt Design.

Data Set	Selector Accuracy (%)	Property Accuracy (%)	Value Accuracy (%)	Output Accuracy (%)
<i>Property Updates</i>	83.54	82.90	82.59	68.28
<i>Relative Updates</i>	77.25	72.39	-	46.32
<i>Decorations</i>	63.04	54.86	55.29	26.35
<i>Overall</i>	74.61	70.05	68.94	46.98

The test results show that the accuracy in property update requests, clearly outperforms other categories. Additionally, the output accuracy show that the model produces promising results on property update requests with a unique syntactical data format that the model is not familiar with.

For relative update requests, the accuracy of the model significantly decreases. Despite the selector accuracy and property accuracy are promising, the output accuracy is not as good as property update requests output accuracy. However, the model still produces reasonable results with very little amount of data.

The model had difficulties on decoration requests, which is the most challenging kind of requests, and has the lowest accuracy as a result. Even though the model captures the selector correctly in general, since the property and value are not given clear in the natural utterance, model performance is not satisfying for property and value detection.

In general, it is seen that the model has a higher accuracy on selector detection on all kinds of requests, followed by property and value detections respectively.

4.4.2. Results with natural representation prompt design

As mentioned before, the second approach to the prompt design was the standard CSS syntax, which is expected to GPT-3 is already familiar with. The results obtained with this representation is given in Table 2.

Similar to the results of the structural representation prompt design, the accuracy on the property update requests is significantly higher than other categories. Additionally, it is seen that the model performs slightly better with the natural representation than the structural representation.

Using a natural representation also increases the accuracy on relative update requests. Even though the property detection accuracy is slightly decreased, the output accuracy on relative update requests is significantly higher when compared to the structural representation.

Table 2. Results of Natural Representation Prompt Design.

Data Set	Selector Accuracy (%)	Property Accuracy (%)	Value Accuracy (%)	Output Accuracy (%)
<i>Property Updates</i>	85.38	84.40	84.19	70.75
<i>Relative Updates</i>	85.00	68.75	-	60.42
<i>Decorations</i>	78.38	81.08	70.00	70.27
<i>Overall</i>	84.71	77.13	82.37	66.07

The results show the performance on the decoration requests dramatically increased with the natural representation prompt design. When compared to the previous output accuracy for decorations, which is 26.35%, using natural representation prompt design interestingly leads to a dramatic increase on output accuracy: 70.27%.

For all categories of requests in the dataset, the natural representation prompt design clearly outperforms the structural representation that is originally defined within this research.

Therefore, it is seen that prompt design is a major factor for the accuracy and using a meaningful representation that GPT-3 is already consumed before, significantly increases the performance of the model.

In the literature, there are different research works reporting generating codes using pretrained language methods [19-21]. In [19], current methods are analyzed and compared, however there is no clear accuracy information that is provided, and these methods do not mention about the CSS codes. However, in [20], a code generation from natural language queries using pretrained models to generate SQL queries is proposed. It is mentioned that with the developed decoding method, the accuracy is improved from 49% to 72%. In [21], GPT-3 is fine tuned to generate python codes with several models. These models improved the percentage of solved problems to a best value of 72.5%. Hence, these accuracy results, although not generated for CSS codes, are comparable to our results.

5. CONCLUSIONS and DISCUSSIONS

In this study, a layered code generation structure is proposed using Natural Language Processing based on transformers. The model provides promising results for the internal structure. The reliability and the accuracy of the results depend on the details of the representations and the prompt design. The natural prompt design results with an overall accuracy of 66.07% are better than the structural prompt design which has an overall accuracy of 46.98%.

The prompt design is crucial for the accuracy of auto-regressive language models such as GPT-3. Therefore, focusing on a better prompt design strategy is an opportunity for significant improvement of the accuracy. In the next paragraphs, some interesting future work ideas which are mostly about the prompt design, are summarized.

Dynamic example selection for prompts might be an opportunity for improving the accuracy. According to the structure and existing CSS classes of the target web page, a prompt could be generated by picking up the examples that is more appreciate with the content of the web page. Recent studies show such an approach can improve accuracy of the autoregressive language models for tasks of semantic parsing [12]. However, this approach strongly relies to the quality and the size of the example dataset. Therefore, extending the dataset could be a significant improvement.

Generating prompt with in-context examples could also improve the accuracy. For each user request, a prompt could be generated by picking the examples that semantically similar to the user request. Additionally, fine tuning could reduce the cost by each request with smaller prompt sizes and improve the accuracy of generated ASTs.

CSS document building with natural utterances might be a good practice for styling a webpage. The users could describe their style rules in a text document line by line. For each line, a CSS rule could be generated in AST structure. The generated ASTs could be combined into one general AST that can be decoded into a complete CSS document which comprises all generated rules.

ACKNOWLEDGEMENT

This work is supported by Eskisehir Technical University scientific research projects with the project number of 21GAP084. We acknowledge the support provided by Greg Brockman from OpenAI, for allowing academic access to the GPT-3 beta program.

REFERENCES

- [1] Vaswani, A., Shazeer, N., Parmar, N., Uszkoreit, J., Jones, L., Gomez, A. N., Kaiser, Ł., and Polosukhin, I., (2017), Attention is all you need. *Advances in Neural Information Processing Systems*, 30.
- [2] Yin, P., and Neubig, G., (2019), Reranking for neural semantic parsing. In *Proceedings of the 57th Annual Meeting of the Association for Computational Linguistics*.
- [3] Zhang, J., Wang, X., Zhang, H., Sun, H., Wang, K., and Liu, X., (2019), A novel neural source code representation based on abstract syntax tree. In *2019 IEEE/ACM 41st International Conference on Software Engineering (ICSE)*, 783-794, IEEE.
- [4] Uma, M., Sneha, V., Sneha, G., Bhuvana, J., and Bharathi, B., (2019), Formation of SQL from natural language query using NLP. In *2019 International Conference on Computational Intelligence in Data Science (ICCIDS)*, 1-5, IEEE.
- [5] Galassi, A., Lippi, M., and Torrioni, P., (2020), Attention in natural language processing. *IEEE Transactions on Neural Networks and Learning Systems*, 32, 4291-4308.
- [6] Sun, Z., Zhu, Q., Mou, L., Xiong, Y., Li, G., and Zhang, L., (2019), A grammar-based structural cnn decoder for code generation. In *Proceedings of the AAAI Conference on Artificial Intelligence*, 7055-7062.

- [7] Shiv, V., and Quirk, C., (2019), Novel positional encodings to enable tree-based transformers. *Advances in Neural Information Processing Systems*, 32.
- [8] Sun, Z., Zhu, Q., Xiong, Y., Sun, Y., Mou, L., and Zhang, L., (2020), Treegen: A tree-based transformer architecture for code generation. In *Proceedings of the AAAI Conference on Artificial Intelligence*, 8984-8991.
- [9] Quirk, C., Mooney, R., and Galley, M., (2015), Language to code: Learning semantic parsers for if-this-then-that recipes. In *Proceedings of the 53rd Annual Meeting of the Association for Computational Linguistics and the 7th International Joint Conference on Natural Language Processing (Volume 1: Long Papers)*, 878-888.
- [10] Kim, S., Zhao, J., Tian, Y., and Chandra, S., (2021), Code prediction by feeding trees to transformers. In *2021 IEEE/ACM 43rd International Conference on Software Engineering (ICSE)*, 150-162.
- [11] Ferraro, G., and Suominen, H., (2020), Transformer semantic parsing. In *Proceedings of the The 18th Annual Workshop of the Australasian Language Technology Association*, 121-126.
- [12] Shin, R., Lin, C. H., Thomson, S., Chen, C., Roy, S., Platanios, E. A., Pauls, A., Klein, D., Eisner, J., and Van Durme, B., (2021), Constrained language models yield few-shot semantic parsers. In *Proceedings of the 2021 Conference on Empirical Methods in Natural Language Processing*, 7699-7715.
- [13] Shah, M., Shenoy, R., and Shankarmani, R., (2021), Natural language to python source code using transformers. In *2021 International Conference on Intelligent Technologies (CONIT)*, 1-4, IEEE.
- [14] Svyatkovskiy, A., Deng, S. K., Fu, S., and Sundaresan, N., (2020), Intellicode compose: Code generation using transformer. In *Proceedings of the 28th ACM Joint Meeting on European Software Engineering Conference and Symposium on the Foundations of Software Engineering*, 1433-1443.
- [15] Brown, T., Mann, B., Ryder, N., Subbiah, M., Kaplan, J. D., Dhariwal, P., Neelakantan, A., Shyam, P., Sastry, G., and Askell, A., (2020), Language models are few-shot learners. *Advances in Neural Information Processing Systems*, 33, 1877-1901.
- [16] Liddy, E. D., (2001), Natural language processing. In *Encyclopedia of Library and Information Science*, (2nd Ed.) NY. Marcel Decker, Inc.
- [17] Egonmwan, E., and Chali, Y., (2019), Transformer and seq2seq model for paraphrase generation. In *Proceedings of the 3rd Workshop on Neural Generation and Translation*, 249-255.
- [18] Narayanan, D., Shoeybi, M., Casper, J., LeGresley, P., Patwary, M., Korthikanti, V., Vainbrand, D., Kashinkunti, P., Bernauer, J., Catanzaro, B., Phanishayee, A., and Zaharia, M., (2021), Efficient large-scale language model training on GPU clusters using megatron-LM. In

Proceedings of the International Conference for High Performance Computing, Networking, Storage and Analysis, p Article 58, Association for Computing Machinery, St. Louis, Missouri.

- [19] Xu, F. F., Alon, U., Neubig, G., and Hellendoorn, V. J., (2022), A systematic evaluation of large language models of code. arXiv preprint arXiv:2202.13169.
- [20] Poesia, G., Polozov, O., Le, V., Tiwari, A., Soares, G., Meek, C., and Gulwani, S., (2022), Synchronesh: Reliable code generation from pre-trained language models. arXiv preprint arXiv:2201.11227.
- [21] Chen, M., Tworek, J., Jun, H., Yuan, Q., Pinto, H. P. d. O., Kaplan, J., Edwards, H., Burda, Y., Joseph, N., and Brockman, G., (2021), Evaluating large language models trained on code. arXiv preprint arXiv:2107.03374.



RESEARCH ARTICLE

**THE EFFECTS of DIFFERENT HEAT TREATMENT and COATING TECHNIQUES on
X120CrMo29-2 MARTENSITIC STAINLESS STEEL**

Esad KAYA^{1*}, Mustafa ULUTAN², Ahmet AKBULUT³

¹Eskişehir Osmangazi University, Faculty of Engineering and Architecture, Division of Mechanical Engineering,
esatkaya@ogu.edu.tr, ORCID: 0000-0002-7332-6154

²Eskişehir Osmangazi University, Faculty of Engineering and Architecture, Division of Mechanical
Engineering, mulutan@ogu.edu.tr, ORCID: 0000-0003-1821-6486

³IGSAS, Kütahya Integrated Facilities, Research and Development Center Department, ahmet.akbulut@igsas.com.tr, ORCID:
0000-0001-7522-5341

Receive Date: 24.02.2022

Accepted Date: 13.05.2022

ABSTRACT

This research article investigated the effects of various heat treatment and coating processes on the tribological performance of X120CrMo29-2 martensitic stainless steel materials. The effects of deep cryogenic treatment, plasma nitriding, and high-velocity oxy-fuel (HVOF) thermal spraying methods on microstructural, mechanical, and tribological properties were investigated. The as-quenched condition was taken as the reference group. In the experimental studies, it was observed that the wear resistance of the deep cryogenic heat treated and coated samples were improved 1,2-6,7 times in comparison to the reference group. In terms of microstructure and mechanical properties, more homogeneous general structural hardness was obtained in the deep cryogenically treated samples, while high surface hardness values (980 HV₁₀₀_{gf,10 sec}) were found in coated samples. In terms of tribological properties, it was observed that the wear resistance of the coated samples was higher than the deep cryogenically treated samples. It is seen that nitride coatings have superior tribological properties to the HVOF sprayed sample. The lowest coefficient of friction (COF) and highest wear resistance was observed in plasma nitrided samples.

Keywords: *Wear, Friction, Tribology, Coatings, Nitriding*

1. INTRODUCTION

Martensitic stainless steels have superior mechanical properties to other stainless steel groups due to the high Cr and C ratio in their content. [1]. For this reason, martensitic stainless steels are used in different areas such as turbine blades, bearings, surgical apparatus, and machine parts that provide fluid transport in corrosive environments [2, 3]. Although martensitic stainless steels exhibit high mechanical and tribological properties, this is insufficient for some industrial application areas. Therefore, martensitic stainless steels properties still need to be improved for some applications. This situation is primarily encountered in pump impellers, balancing discs, rotors, and valves used to transport hot corrosive fluids where high thermal stability is required. [1]. Different surface engineering techniques can be applied to improve the surface properties of martensitic stainless steels

and create new areas of use [4-6]. One of these techniques is the deep cryogenic heat treatment process which is additive process to quenching. Deep cryogenic heat treatment is complementary to the traditional heat treatment procedure. [7]. In this process, the austenite, which remains retained in the microstructure after quenching, is transformed into martensite and forms secondary carbide with the free carbon element. [8]. These transformations increase the overall hardness and wear resistance of the material. In addition, different coating methods are used to improve the surface properties of martensitic stainless steels. One of these is the high-velocity oxy-fuel (HVOF) technique. In this process, the powder mixture brought to a spray gun chamber with carrier gas is burned with a liquid-gas fuel mixture and transferred to the surface to be coated in semi-melt form. With this process, coatings with a thickness of ~200 μm with low porosity on the surface can be obtained [9, 10]. The HVOF technique can be applied to any machine part subject to different types of wear under impact load [11]. The resulting coatings have relatively low porosity, high deposition volume, and hardness [12]. In line with these desired properties and due to the high melting temperature, carbides and oxides (WC, TiC, Al_2O_3 , etc.) are highly preferred in this method [13]. Another method used to improve the surface properties of stainless steel is the nitriding method. Today, nitriding can be applied with gas, salt bath, plasma ion nitriding types [14]. Ammonia and cyanide salts are used as N_2 donor media in gas and salt bath methods. Machine parts made of steel materials pose major disadvantages if the processing temperatures exceed 700°C for effective coating thickness and low processing time [1]. For this reason, the plasma nitriding process, which is carried out in the ionized gas phase and at low temperature, is highly preferred [15]. This process is a plasma assisted thermochemical process and uses the workpiece as a cathode. As a result of ionized gas bombardment, coating layers with high load carrying ability and hardness are obtained on the surface [16]. These structures formed on stainless steel surfaces are supersaturated $\gamma\text{-N}$ and S phases in terms of N_2 [1, 17]. In the studies, it is seen that the plasma-assisted ion nitriding process at low temperatures prevents the formation of hard and brittle $(\text{Metal})_2\text{N}$. It is known that nitrides formed from this chemical composition deteriorate the tribomechanical properties of the $\gamma\text{-N}$ and S phases [1, 16, 17]. Therefore, when low temperature plasma assisted nitriding, carburizing, nitrocarburizing processes are investigated, it is known that these processes improve the mechanical, microstructural and tribological properties of different types of stainless steels and non-ferrous materials [14, 18, 19].

When the studies in the literature are examined, it is pretty common to improve the surface properties of austenitic stainless steels due to high corrosion, low hardenability, and wear resistance [20-22]. It has been observed that studies on the improvement of the properties of martensitic stainless steels are few. In this study, the tribomechanical properties of X120CrMo29-2 quality martensitic stainless steel, which is frequently used to manufacture pump impeller material carrying corrosive fluid at high temperatures, were tried to be improved by different heat treatment and coating methods.

2. MATERIAL and METHOD

2.1. Material

Commercial type X120CrMo29-2 martensitic stainless steel material obtained from IGSAŞ (Istanbul Gübre Sanayi Anonim Şirketi) was used in the study. The material was formed into cubes with a side of 12.70 mm by the EDM method. Conventional metallographic sample preparation processes were applied to all cube samples' surfaces and polished so that their average surface roughness was below $0.5 \mu\text{m}$. Table 1 shows the chemical composition of the material and the control groups in the

experimental studies. Experimental studies were carried out in five different control groups. The first group samples were taken as a reference (Q) and, after austenitization at 840°C for 1 hour, quenched and tempered at 200°C for 3 hours. In the second group of samples (QC), deep cryogenic treatment was applied in addition to the traditional heat treatment procedure. The process was carried out in an MMD Cryo brand computer-controlled device. The specimen was kept at a deep cryogenic temperature of -196°C at a 2°C/min rate for 36 hours. After processing, the sample was tempered at 200°C for 1 hour. Plasma nitriding was applied to the third and fourth group samples (N1, N2). After polishing the sample surfaces, metallographic processes were subjected to plasma nitriding at 450°C and 520°C temperatures, during a 12-hour waiting period under 2 mbar pressure in 75% N₂ + 25% H₂ gas atmosphere. After the process, the samples were left to cool to room temperature in a vacuum media. WC-Co coatings were applied to another group of samples by the high-velocity oxy-fuel method (HVOF). The process was carried out on a Metco Diamond Jet 2700 device. Mixture powders consisting of 83% WC and 17% Co by mass. During the process, powders were heated to 165 °C and the workpiece temperature to 204 °C. The process was operated at a pressure of 0.6 MPa using air as the carrier gas. The powder feed rate was used as 30 gr/min.

2.2. Method

Of the samples whose production processes were completed, coated samples were cut with the wet abrasive cutting method, and their surfaces were polished. Metallographic polishing was applied to one surface of the heat-treated samples. After polishing, the surfaces were etched with 2% Nital solution. The microstructures of the etched samples were investigated by SEM-EDS analysis. JEOL JSM-5600LV scanning electron microscope was used for analysis. EDS analyzes were also performed at the time of SEM acquisition. X-ray diffraction technique was used to determine the phases formed in the samples. Panalytical Empyrean device was used in the experiments. The XRD examination was performed with the Cu-K_α radiation and a wavelength of 1.54060 Å. For coatings and samples, X-ray diffraction patterns were obtained by scanning at 2θ angles between 20°-100° with a step size of 0.02 at a speed of 0.5°/min. The obtained diffraction patterns were analyzed with the X'pert HighScore Plus package program. The hardness values of the samples were made using the microhardness measurement technique. Hardness measurements were made on a Future Tech FM-800 type device. The hardness of the samples, which were subjected to heat treatment and plasma nitriding, was determined at 25 gf load and 10 seconds dwelling time, and the hardness of the HVOF sample was determined at 100 gf load and 10 seconds dwelling time. The wear tests were performed on all specimens in spherical-disc type geometry in a CSM Tribometer device per ASTM G-99 standards. In the experiments, balls with Ø 3 mm diameter, 91.6 HRA hardness, 700 GPa elastic modulus, certified spherical, with 96% WC-4% Co content, were used as counter body material. The experiments were carried out with a load of 5 N, a diameter of 3 mm, a wear distance of 50 meters, and a sliding speed of 3 cm/s (189 rpm). The formed worn channels on the surfaces were measured with Mitutoyo SJ-400 surface roughness device and Gauss filtering technique in ISO R97 standard. Worn channels were observed by SEM-EDS techniques to examine the wear mechanisms in detail.

Table 1. Chemical composition of martensitic stainless steel material used in experimental studies and control groups.

The Chemical Content of X120CrMo29-2					
C	Si	Cr	Mn	Mo	Fe

1,10	2,00	28,00	1,00	2,25	Bal.
Control Groups					
Specimen	Description				
Q	1 hour austenitizing at 810°C +Quenching 3 hours at 300°C Tempering				
QC	Q+36 hours 196°C Deep Cryogenic Treatment + 1-hour Tempering at 200°C				
N1	Q+ 450°C Nitriding Process				
N2	Q+ 420°C Nitriding Process				
HVOF	Q+ HVOF WC-Co Coating				

3. RESULTS AND DISCUSSION

3.1. Microstructure Analysis

Figure 1 shows SEM-EDS analyzes of martensitic stainless steel samples with different heat treatments and coatings. When the samples are examined in general, there are no discontinuities and defects in the structures due to production, heat treatment, and coating processes. Figures 1.a-b show the neat quenching (Q) and deep cryogenically treated (QC) samples, respectively. One can be understand from the figure, the microstructure is composed of perlite and cementite phase due to the high temperature tempering process. In the deep cryogenic treated sample, it is seen that the structure is preserved in a similar situation. It has been observed that the general improvement mechanisms seen in the microstructure of tool steels by deep cryogenic treatment are not very effective in martensitic stainless steels [23].

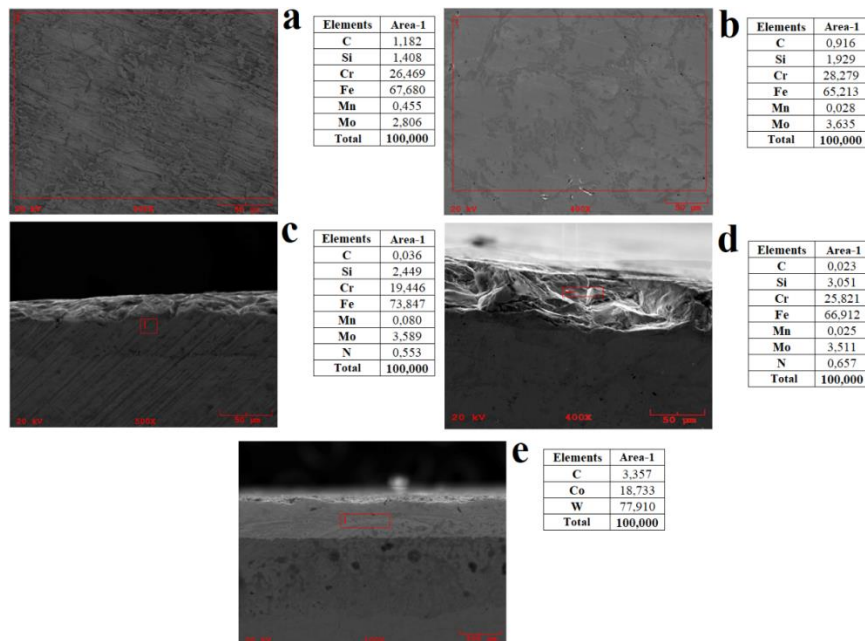


Figure 1. SEM-EDS analyzes of samples: a)Q, b)QC, c)N1, d)N2, e)HVOF.

Figure 1.c-d shows cross-sectional SEM-EDS analyzes of plasma nitrided samples. It is seen that there is a nitriding layer with a homogeneous thickness distribution of 50-70 μm . In addition, the nitriding layer formed does not contain any defects and voids. This situation is an indication that the nitriding layer production parameters were selected effectively. When the EDS analyzes are examined, it is seen that the obtained layer mainly contains Fe-Cr-N. The substrate's high Fe and Cr content indicates that the resulting nitriding layer is predominantly composed of Fe-Cr-N compounds. Figure 1.d shows the cross-sectional SEM-EDS analysis of the WC-Co coated sample with the HVOF technique. When the coating cross-section SEM photograph is examined, it is seen that the coating forms homogeneously on the surface without any porosity, cracks, or discontinuities along the surface. It is seen that the obtained coating layer thickness is approximately 200 μm . Figure 2 shows the X-ray diffraction patterns of the samples. When the diffraction pattern of the conventional heat-treated and deep cryogenic treated samples (Figure 2.a-b) is examined, it is seen that the structures are composed of carbide, martensite, and austenite phases. It is observed that the intensity of the carbide peaks increased and the intensity of the austenite peaks decreased in the deep cryogenically treated sample. It is thought that after the applied deep cryogenic heat treatment, the retained austenite in the microstructure turns into martensite and forms a carbide with the free element Cr. When the plasma nitrided samples are examined (Figure 2.c-d), it is seen that the structures are composed of nitrides containing Fe and Cr. In addition, it was determined that $(\text{Metal})_2\text{N}$ was not observed, which is extremely brittle and hard. This observation shows that the applied process is carried out under the most suitable conditions. Figure 2.d shows the diffraction pattern of the WC-Co coated sample with the HVOF technique. When the obtained diffraction pattern is examined, it is seen that the structure mainly consists of WC peaks and rarely Co peaks. 83% by mass of the powder mixture desired to be coated on the surface contains WC. For this reason, it is seen that the peak intensities obtained are compatible with the mass content thrown to the surface.

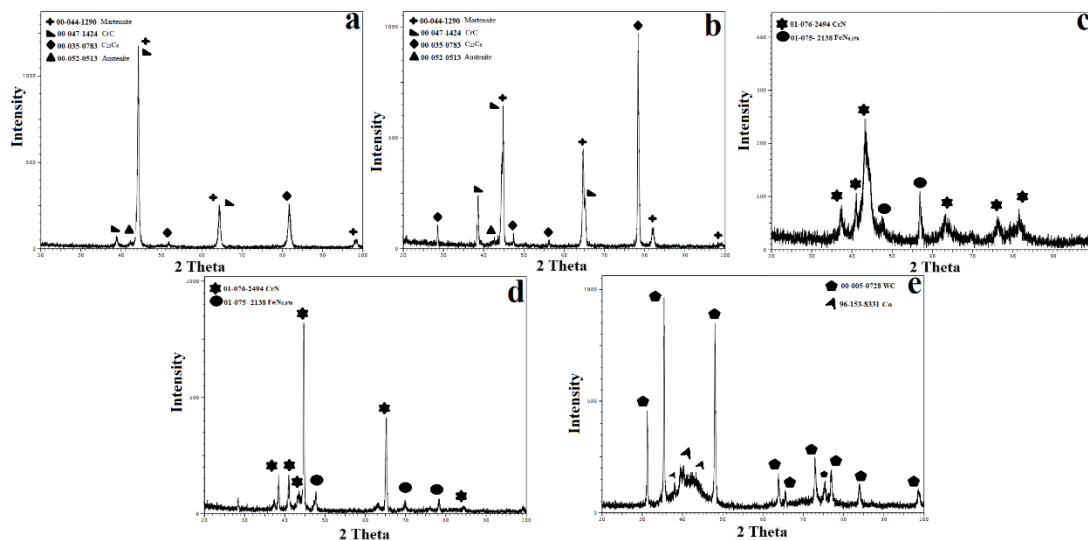


Figure 2. X-ray diffraction patterns of the samples: a)Q, b)QC, c)N1, d)N2, e)HVOF.

3.2. Mechanical and Tribological Analysis

Figure 3. It shows the hardness values of the samples. While the hardness values of the conventional heat-treated and deep cryogenic heat-treated samples are average (480 HV_{25gf,10s}), the hardness values of the plasma nitrided and HVOF-coated samples show the change of the coating surface towards the substrate material. Since WC is one of the hardest carbides known, the highest average hardness values are seen in the sample coated with WC-Co with the HVOF technique (980 HV_{100gf,10s}). When the hardness values obtained were compared with the SEM analysis of the coating (Figure 1-e), it was observed that high hardness behavior was exhibited throughout the coating section and decreased by 50% in the transition region. Another high hardness value is seen in plasma nitrided samples. The hardness measurements show that the hardness varies between 700 HV and 900 HV throughout the layer thickness. The average hardness values obtained from the nitriding process at 450°C and 520°C were measured as 715 HV_{25gf,10s} and 665 HV_{25gf,10s}, respectively. It is seen that the obtained hardness values are consistent with the cross-sectional SEM analyzes of the nitride layers. It is thought that the high hardness obtained by nitriding at low temperatures is due to the CrN layers formed with low thermal stress. Healing effects such as austenite-martensite transformation and secondary carbide formation provided by the deep cryogenic heat treatment in the microstructure are also seen in the hardness values. With the measurements made, it is seen that the average hardness value of the deep cryogenic treated sample increased by about 10% compared to the reference sample (494 HV_{25gf,10s}).

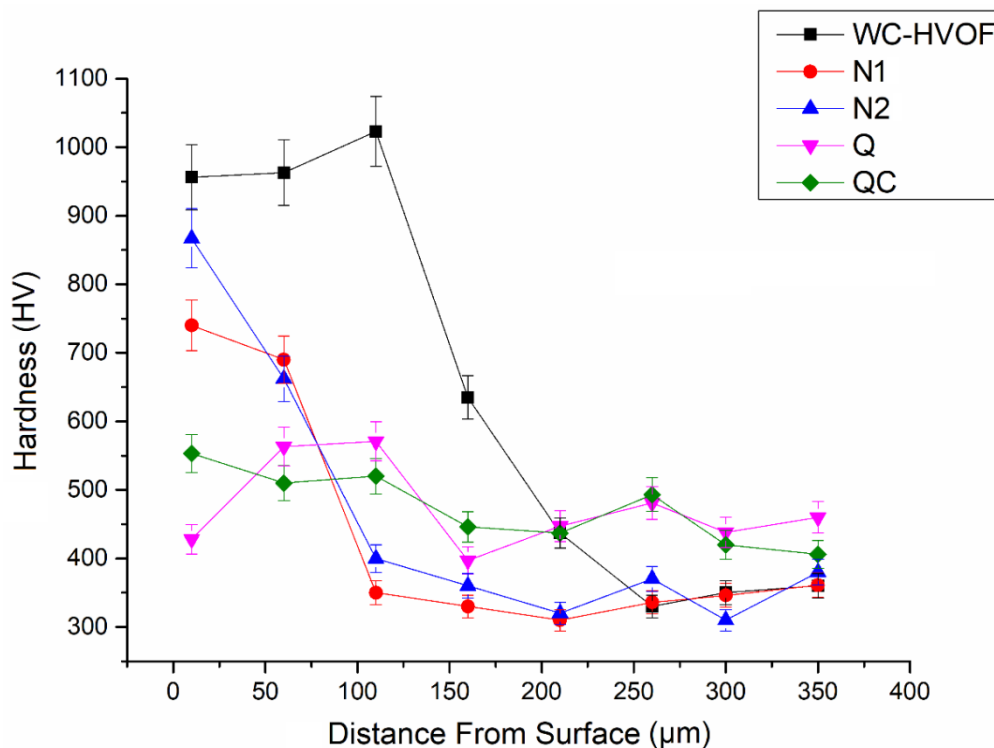


Figure 3. Hardness variation graphs of the samples.

Figure 4. shows the specific wear rate-friction coefficient variation graph of all samples. It is seen that there is a parallelism between the change in friction coefficient values and the change in wear rates. As expected, wear, and friction behavior improvements were observed in all applied heat treatments and coating techniques compared to the reference group. As can be seen from the figure, the highest wear rate of $8.77 \times 10^{-5} \text{mm}^3/\text{Nmm}$ was determined in the reference sample. The application of deep cryogenic treatment increased the wear resistance by about 10%. With the WC-Co coating applied with the HVOF technique, the wear resistance was improved by 20% compared to the reference sample. On the other hand, the plasma nitriding process improved the wear resistance of the samples between 5.0 and 6.7 times.

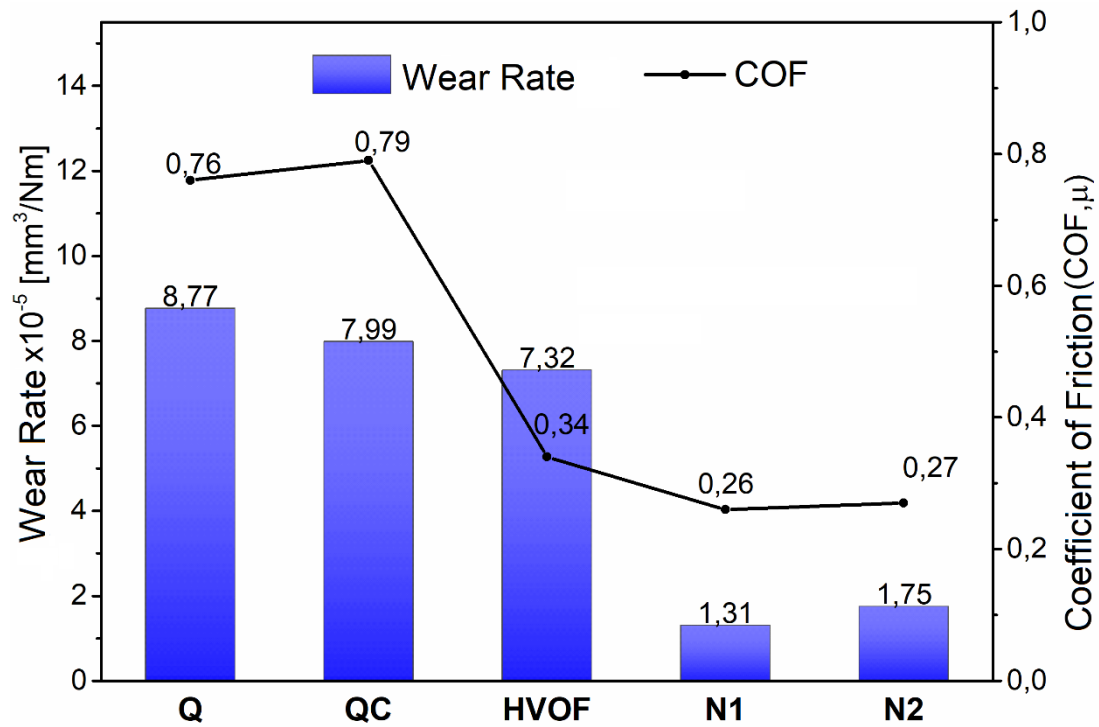


Figure 4. The wear rate of the samples and the average friction coefficient variation graph.

Figure 5. shows the instantaneous COF change graph of all samples during the wear test. As a result of the experiments, the lowest average friction coefficient is observed in plasma nitrided samples (~0.25). The highest average friction coefficient was observed in the heat-treated groups as expected (~0.75). The friction coefficient data obtained from the experiment are similar to the wear rates. When the friction behaviors are examined, it is seen that the friction behavior of the plasma nitrided samples is in a regular regime at low values. The main reason for the regular regime in nitrided layers is that the abrasive three bodies are not formed during wear, and the wear behavior is not exacerbated. The high surface roughness of the HVOF coating layer compared to plasma nitrided coatings causes hard WC hard particles to break off from the surface during the wear test. They are included in the contact

area of the broken particles again and react with O₂ and N₂ to form tribochemical residues. These formed structures trigger three-body abrasive wear, causing an increase in the wear rate relatively compared to nitride layers. Extreme fluctuations were observed in the reference and deep cryogenic treated samples, where the highest COF values were observed. The main reason for this situation is the direct interaction of the opposite body at the contact point, which shows that three-body abrasive wear is effective.

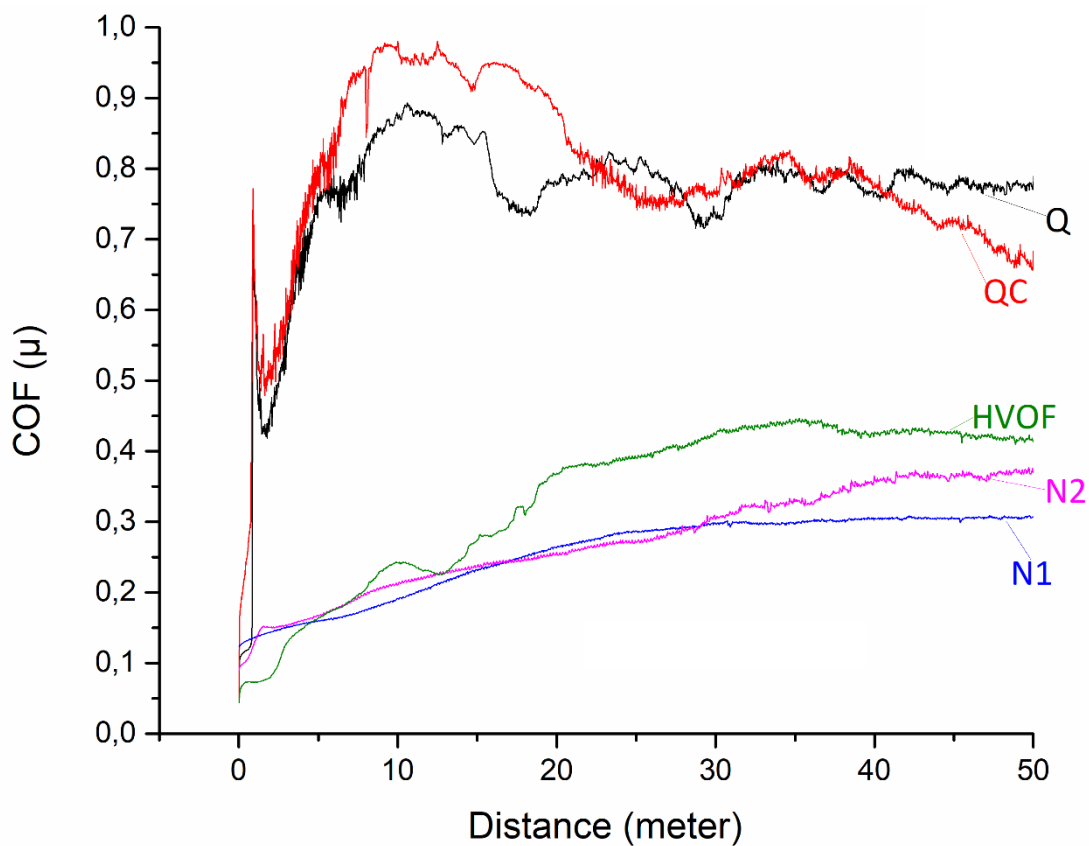


Figure 5. Instantaneous COF alteration graph of the samples during the wear test.

Figure 6 shows the SEM-EDS analyses of the samples after the wear test. When the surface analysis of the quenched and deep cryogenically treated samples, which have the lowest wear resistance, is examined, deep abrasive traces (Figure 6.b-5) and oxidation traces (Figure 6.a-1) are observed. It is thought that an active three-body abrasive wear mechanism forms these deep scars. When the EDS analysis of the surfaces was examined, it was determined that the highest amount of W, Co, and O. Therefore, it is seen that the dominant wear mechanisms are adhesive and abrasive. When the wear surface SEM-EDS analyses of nitride coatings are examined exhibiting low friction behavior (Figure 6.c-d), it is seen that the effects of abrasive and adhesive wear are pretty superficial and low as expected. It is seen that the worn nitriding layers have the lowest ratio of W, Co, and O. It has been

observed that these layers with high stability did not initiate three-body abrasive wear during wear and prevented the aggravation of wear. When the HVOF coating sample was examined, it was determined that the abrasive traces formed on the surfaces were shallow according to the quenching and deep cryogenic treatment conditions but deep compared to the nitriding layers. Despite their high hardness properties, the high average surface roughness of the HVOF layers reduces the load-bearing ability of these layers. The parts that break off from the surface with increasing wear distance (Figure 6.e-3) intensify the wear and decrease the wear resistance. For this reason, with increasing wear distance, they wear more than nitride layers with thinner thickness and become insufficient.

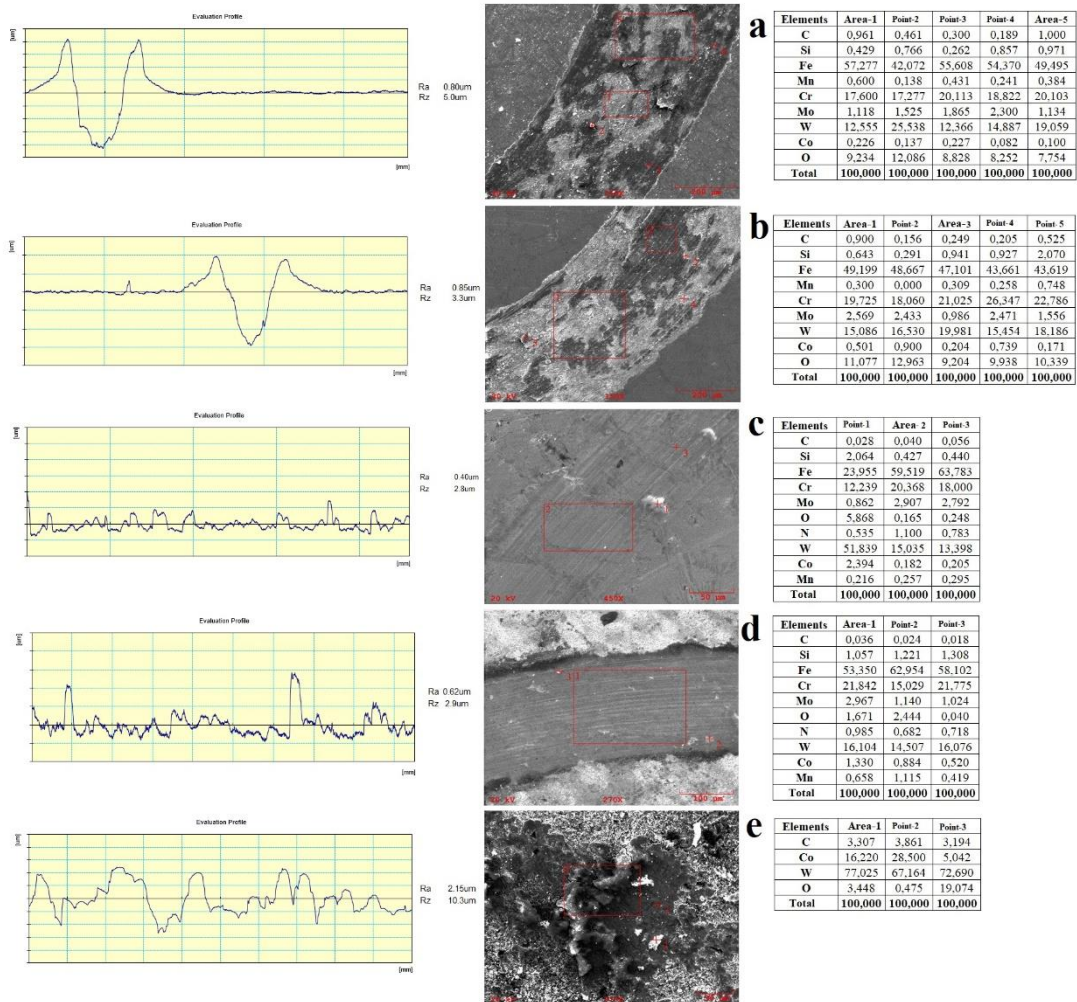


Figure 6. Wear SEM-EDS analysis of samples: a)Q, b)QC, c)N1, d)N2, e)HVOF.

6. CONCLUSION

This study applied different heat treatments and coating techniques on X120CrMo29-2 martensitic stainless steels. By examining the microstructure and mechanical properties of the samples, the most suitable surface modification process was tried to be determined. The findings obtained in the experimental studies are summarized as follows:

Heat treatments and coatings were successfully applied in all control groups. It has been determined that there are no cracks, gaps, or discontinuities in the heat treatment applications and on the coating surfaces.

In the X-ray diffraction analysis, decreases in the austenite phase peak intensities were detected in the deep cryogenically treated samples. It was determined that the nitride layers were mainly composed of Cr and Fe. It was determined that WC peaks were dominant in the HVOF layer.

Compared to the reference sample (480 HV_{25gf,10s}), a 10% increase in hardness was detected in deep cryogenically treated samples and 2 to 3 times in plasma nitride and HVOF coatings. The highest in-depth hardness increase was obtained with HVOF coatings (980 HV_{100gf,10s}).

The lowest average COF was observed in the plasma nitrided layers (~0.25), while the highest average COF was found in the reference group (~0.75).

In all applied heat treatments and coating techniques, the wear resistance has been increased compared to the reference sample. While the highest wear rate was observed in the reference sample with $8.77 \times 10^{-5} \text{mm}^3/\text{Nmm}$, the lowest was found in the plasma nitrided sample at 450°C with $1.31 \times 10^{-5} \text{mm}^3/\text{Nmm}$.

ACKNOWLEDGMENT

This study was carried out with the project permission of ATAP A.Ş. and the R&D division of the İGSAŞ company with code 69592. The authors are thankful for the great support of Er&Mir Makine Ltd., which provided the plasma nitriding process.

REFERENCES

- [1] Lee, I., (2019), Combination of plasma nitriding and nitrocarburizing treatments of AISI 630 martensitic precipitation hardening stainless steel. *Surface and Coatings Technology*, 376: p. 8-14.
- [2] Lyu, Z., Yutaka, S., Shun, T., Yue, Z., Jinlong, J., Aiping, W., (2021), Microstructural distribution and anisotropic tensile behavior in a 2Cr13 martensitic stainless steel thin wall fabricated by wire arc additive manufacturing. *Materials Today Communications*, 29.

- [3] Baghjari, S.H., Akbari, S., (2013), Effects of pulsed Nd:YAG laser welding parameters and subsequent post-weld heat treatment on microstructure and hardness of AISI 420 stainless steel. *Materials & Design*, 43: p. 1-9.
- [4] Alonso, F., Arizaga, A., Garcia, J., Oñate, I., (1994), Tribological effects of yttrium and nitrogen ion implantation on a precipitation hardening stainless steel. *Surface and Coatings Technology*, 66(1-3): p. 291-295.
- [5] Tesi, B., Bacci, T., Poli, G., (1985), analysis of surface structures and of size and shape variations in ionitrided precipitation hardening stainless steel samples. *Vacuum*, 35(8): p. 307-314.
- [6] Leyland, A., Lewis, D., Stevensom, P., Matthews, A., (1993), Low temperature plasma diffusion treatment of stainless steels for improved wear resistance. *Surface and Coatings Technology*, 62(1-3): p. 608-617.
- [7] Sert, A., (2020), AISI M2 Takım Çeliğinin Mikroyapısı ve Mekanik Davranışları Üzerine Derin Kriyojenik Isıl İşlemin ve Temperlemenin Etkisi. *Deu Muhendislik Fakultesi Fen ve Muhendislik Dergisi*, 22(66): p. 801-811.
- [8] Kara, F., Özbek, O., Özbek, N., Uygur, İ., (2021), Investigation of the Effect of Deep Cryogenic Process on Residual Stress and Residual Austenite. *Gazi Journal of Engineering Sciences*, 7(2): p. 143-151.
- [9] Mann, B., Arya, V., (2003), HVOF coating and surface treatment for enhancing droplet erosion resistance of steam turbine blades. *Wear*, 254(7-8): p. 652-667.
- [10] Mann, S., Arya, V., Joshi, P., (2005), Advanced High-Velocity Oxygen-Fuel Coating and Candidate Materials for Protecting LP Steam Turbine Blades Against Droplet Erosion. *Journal of Materials Engineering and Performance*, 14(4): p. 487-494.
- [11] Moskowitz, L., Trelewicz, K., (1997), HVOF coatings for heavy-wear, high-impact applications. *Journal of Thermal Spray Technology*, 6(3): p. 294-299.
- [12] Buytoz, S., Ulutan, M., Islak, S., Kurt B., Çelik, O.N., (2013), Microstructural and Wear Characteristics of High Velocity Oxygen Fuel (HVOF) Sprayed NiCrBSi-SiC Composite Coating on SAE 1030 Steel. *Arabian Journal for Science and Engineering*, 38(6): p. 1481-1491.
- [13] Ozkavak, H.V., Sahin, S., Sarac, M.F., Alkan, Z., (2020), Wear properties of WC-Co and WC-CoCr coatings applied by HVOF technique on different steel substrates. *Materials Testing*, 62(12): p. 1235-1242.
- [14] Cheng, Z., Li, C., Dong, H., Bell, T., (2005), Low temperature plasma nitrocarburising of AISI 316 austenitic stainless steel. *Surface and Coatings Technology*, 191(2-3): p. 195-200.

- [15] Reddy, C.A.K., Srinivasan, T., Venkatesh, B., (2021), Srinivasan, and B. Venkatesh, Effect of plasma nitriding on M50 NiL steel – A review. *Materials Today: Proceedings*.
- [16] Zhang, Z.L., Bell, T., (2013), Structure and Corrosion Resistance of Plasma Nitrided Stainless Steel. *Surface Engineering*, 1(2): p. 131-136.
- [17] Menthe, E., Rie, K.T., Schultze, S.C., Simson, S., (1995), structure and properties of plasma-nitrided stainless steel. *Surface and Coatings Technology*, 74-75: p. 412-416.
- [18] Bell, T., Sun, Y., Suhadi, A., (2000), Environmental and technical aspects of plasma nitrocarburising. *Vacuum*, 59(1): p. 14-23.
- [19] Lei, M.K., Ou, Y.X., Wang, K.S., Chen, L., (2011), Wear and corrosion properties of plasma-based low-energy nitrogen ion implanted titanium. *Surface and Coatings Technology*, 205(19): p. 4602-4607.
- [20] Haruman, E., Sun, Y., Adenan, M.S., (2020), A comparative study of the tribocorrosion behaviour of low temperature nitrided austenitic and duplex stainless steels in NaCl solution. *Tribology International*, 151.
- [21] Yangyang, L., Dong, L., Heng, M., Xiliang, L., Meihong, W., Jing, H., (2021), Enhanced plasma nitriding efficiency and properties by severe plastic deformation pretreatment for 316L austenitic stainless steel. *Journal of Materials Research and Technology*, 15: p. 1742-1746.
- [22] Naofumi, O., Koyo, M., Mitsuhiro, H., Kenji, K., (2021), Investigation of admixed gas effect on plasma nitriding of AISI316L austenitic stainless steel. *Vacuum*, 193.
- [23] Hariharan, K.B., Savaranan, S., Parkunam, N., (2020), Life time improvement of D7 tool steel by cryogenic treatment. *Materials Today: Proceedings*, 21, p. 619-621.



RESEARCH ARTICLE

**MORPHOLOGICAL, HEMATOLOGICAL and HISTOPATHOLOGICAL EFFECTS OF
PROPYL PARABEN on ENDOCRINE GLANDS of MALE RATS at PREPUBERTAL
PERIOD**

Eda Nur İNKAYA¹, Gözde KARABULUT^{2*}, Nurhayat BARLAS³

¹Hacettepe University, Science Faculty, Department of Biology, edanurinkaya@gmail.com, ORCID: 0000-0001-7032-1537

²Dumlupınar University, Science Faculty, Department of Biology, gozde.karabulut@dpu.edu.tr, ORCID: 0000-0002-4513-1907

³Hacettepe University, Science Faculty, Department of Biology, barlas@hacettepe.edu.tr, ORCID: 0000-0001-8657-2058

Receive Date: 09.03.2022

Accepted Date: 29.06.2022

ABSTRACT

Propyl paraben (propyl 4-Hydroxybenzoate) is frequently used in various products due to its physical and chemical properties and cheapness, and its use is increasing day by day due to the development of the industrial industry. This study is conducted on the side effects of propyl paraben on male rats' endocrine glands. Accordingly, each oil control, positive control (3 mg/kg/day flutamide=FLU), negative control (0.4 mg/kg/day testosterone propionate = TP) and 10, 250 and 750 mg/kg/day testosterone propionate + propyl paraben 6 groups were formed, one of which had six rats.

While a decrease was observed in thymus and spleen weights in the 10, 250 and 750 mg/kg/day testosterone propionate + propyl paraben dose groups compared to the fat control group, an increase was observed in the weight of the thyroid tissue in the 250 mg/kg/day testosterone propionate + propyl paraben dose group compared to the positive control and 10 mg/kg/day testosterone propionate + propyl paraben dose groups. It has also been shown with various damages in endocrine organs in histopathological examinations. Therefore, we can say that propyl paraben has a negative effect on the endocrine organs examined.

Keywords: *Propyl paraben, Endocrine glands, Toxicity, Prepubertal male rats*

1. INTRODUCTION

To utilize antimicrobial efficiency of parabens, they are used alone or mixed as a preservative in pharmaceutical products, foods and cosmetic products such as shampoos, lotions, deodorants etc. [1-3]. They are effective in between pH 4.5-7.5 and have several preservative criteria which is ideal such as not causing to fade in colors, being odor free and tasteless and continuing their efficiency by remaining stable in wide temperature interval [4]. Parabens can be taken by gastrointestinal tract, breathed their dust particles or absorbed through the skin. When parabens are taken orally, they are metabolized in the liver and intestines to the main metabolite parahydroxybenzoic acid (PHBA). They are eliminated from body by being conjugated in three

ways which are p-carboxyphenyl sulphate, p-hydroxybenzoyl glucuronide, p-carboxyphenyl glucuronide and they leave body through urine and feces [5].

By the 2000s, packaged and processed food production began to increase and parabens began to be added to the foods produced in this way. Researchers had not yet expressed their concerns about parabens until this period [6,7,8].

Propyl paraben (PP) is frequently used in cosmetic products due to its antimicrobial effect [9,10,11]. In addition, it is considered suitable for use because it is odorless and does not add any color or taste to the product it is added to. When all these features are added to the fact that it is cheap, institutions such as the USA FDA have authorized many institutions for its use. [9,11].

For a chemical to be used in any product, it is an extremely serious task to first determine whether it has toxic effects for both the environment and humans. Each country has different regulations and rules for the use of any chemical [12]. Here, in order to determine the properties of a chemical, researchers have determined evaluation criteria with their studies [13] and it has been seen that propyl paraben is an endocrine disruptor.

There are more than one way to be exposed to a paraben, mainly by ingestion and inhalation, and depending on these exposure pathways, the duration of metabolism and excretion also changes [14,15]. It is then metabolized and conjugated by the enzyme esterase. Parabens can accumulate in the body, and much of this build-up occurs with daily use of them as a cosmetic [16]. Oral parabens, on the other hand, are metabolized by the esterase enzyme and removed from the body through urine and feces [17].

Parabens have estrogenic action, since they can bind to estrogen receptors. This process could affect the hormonal balance of the body. They have the ability to block 17-hydroxysteroid dehydrogenase, an estrogen-inactivating enzyme [18]. Parabens are lipophilic pollutants that have been shown to build up in fatty tissue [19]. Shin et al. [20] established a pharmacokinetic model for PP, which may also be used to examine the pharmacokinetics and toxicokinetics of other parabens. In summary, orally administered PP was swiftly absorbed (less than 2 hours) and totally removed [20]. The European Union (EU) and the Association of Southeast Asian Nations (ASEAN) banned five parabens in 2014 and 2015. (isopropylparaben, isobutylparaben, phenylparaben, benzylparaben, and pentylparaben). Studies on propyl paraben, methyl paraben, ethyl paraben and butyl parabens, which are frequently used parabens, have been shown to have toxic effects on mitochondrial activity and DNA [7]. However, no clear relationship has been shown between paraben exposure and cancer risk. Parabens have been proven in animal models to operate as weak xenoestrogens, with activity rising with the length of the alkyl group. In a study with mice, it was observed that the administration of paraben caused some epigenetic differences [21].

It has also been supported by studies that more than one ailment in humans, such as infertility and cancer, is associated with parabens [22]. It has been observed that propyl paraben application causes a decrease in follicle growth [23]. In terms of endocrine disruption, parabens were found to have the ability to bind to estrogen receptors, indicating estrogenic activity [24, 25]. Despite what is known about parabens' toxicological effects on the reproductive system, there is still a lack of research about their harmful effects on endocrine organs and the mechanisms that underpin them.

Therefore, in this work, because of the limited research on PP, it was selected and examined the toxicological effects on endocrine glands of prepubertal male rats. It is aimed that the results obtained will contribute to the limited literature available and be a start to the parts that need to be clarified on this subject.

2. MATERIALS and METHODS

2.1. Chemicals

Hangzhou Dayang Chem. Co., Ltd. supplied testosterone propionate (TP, 97%). Sigma-Aldrich provided flutamide (FLU, 98%) and propyl paraben (PP, 98%). Because androgen ligands are hydrophobic, all test compounds were dissolved in oil.

2.2. Animals and Laboratory Conditions

36 prepubertal male Wistar albino rats, 6 weeks old, weighing 170-210 g, were obtained from the Experimental Animals Production Center of Hacettepe University. Afterwards, the experiment was started with the permission of the ethics committee (2015/86-13) obtained from the Hacettepe University Ethics Committee. All rats were kept in polypropylene cages at 22°C and 50% relative humidity in a room with a cycle of 12 hours of light and 12 hours of dark throughout the experiment. Pellets were given as feed and drinking water in glass bottles.

2.3. Grouping Experimental Animals and Doses

Subcutaneous injections of testosterone propionate (TP) were used. Flutamid (FLU) and PP were given for 10 days through oral gavage with oil. For oral administration, the total dosage amount was 5 ml/kg/bw/day. The Hershberger Bioassay OCSPP Guideline 890.1400 was used to calculate the daily dosages of TP (0.4 mg/kg/day) and FLU (3 mg/kg/day). This test is A Short-term Screening Assay for (Anti) Androgenic Properties it also shows toxicity in endocrinal glands such as liver, kidney and adrenal glands. It has been preferred because it is an optional short-term test that has been used frequently recently [26, 27].

At the age of six weeks, rats were castrated and allowed eight days to recover. After the recovery period, the animals were randomly assigned to one of six groups (n = 6) based on their body weights: an oil control group (5 mg/kg/day oil), a negative control group (0.4 mg/kg/day TP), a positive control group (3 mg/bw/day FLU plus 0.4 mg/kg/day TP), and three propyl paraben dose groups (10, 250, and 750 mg/kg/day plus 0.4 mg/kg/day TP). Food and water consumption, as well as body weights, were noted daily, and the daily dosage was adjusted for body weight. Using sterilized needles, dosages were delivered to the dorsal-scapular region for subcutaneous injection. Subcutaneous and oral deliveries were modified with total dose volumes of 0.5 ml/kg and 5 ml/kg, respectively [28]. The rats were killed within 24 hours of the last injection following 10 days of therapy. The pancreas, adrenal gland, thymus, thyroid, and spleen were all removed and weighed.

2.4. Histopathologic Analysis

After the tissue samples were taken, they were weighed and kept in Bouin's solution for 8 hours. Following this technique, tissue were sliced and stained with Hematoxylin and eosin. An Olympus BX51 light microscope was used to view stained preparations. It was photographed with the Bs200prop software connected to this microscope and all the changes observed for each section were recorded.

Thyroid slices stained with H&E were assessed for epithelial height and follicular diameter. The outer follicle layers of the thyroid gland were defined as the marginal region and the middle region as the central region. Using a 40X objective lens, morphometric measurements were taken in the core and marginal areas of the thyroid glands [29,30]. The distance of luminal-basal cell membranes was measured for the height of the follicular epithelium. The size of the epithelium in the thyroid follicles was measured at 12.5 and 7 o'clock and recorded. An average of 20 follicles were counted from each rat thyroid preparation [31,32,33]. The data in the marginal and central regions were evaluated separately and presented as bar graphs.

2.5. Hematological Analysis

White blood cells (WBC), lymphocytes % (lym), monocytes % (mon), red blood cells (RBC), MCV (mean corpuscular volume), hematocrit level (Hct), mean erythrocyte hemoglobin concentration (MCHC), Hemoglobin (Hb) level, platelet count (Plt), mean erythrocyte hemoglobin (MCH) were calculated using a hematology analyzer MELET SCHLOESING MS9-5 (France).

2.6. Statistical Analysis

The data was statistically evaluated using the SPSS IBM-23 statistical software (USA). The variances were homogenous, according to Levene statistics. The analysis of variance (ANOVA) method was utilized. To establish the difference between groups, the Tukey post-hoc test was utilized. The mean and standard deviation of all data were reported (SD). Statistical significance was determined at $p \leq 0.05$ (n=6).

3. RESULTS

3.1. Body and Organ Weight Results

Organ weight results were given in Figure 1. There was a statistically significant decrease in thymus weights in the negative control and positive control groups and in all TP + PP application groups compared to the oil control group. In addition, a significant decrease in thymus weights was observed in the 10 and 250 mg/kg/day of TP + PP dose groups compared to the negative control group. The spleen weights of the 750 mg/kg/day TP + PP dose group decreased significantly when compared to the oil control, positive control, negative control, and 10 mg/kg/day TP + PP dose groups. In addition, a statistically significant decrease was observed in spleen weight in the 250 mg/kg/day of TP + PP dose group compared to the oil control and negative control groups. The positive control group had a significant decrease in thyroid weight when compared to the negative control and 250 mg/kg/day TP + PP dose groups. When compared to the negative control and the 250 mg/kg/day TP + PP dose group, the 10 mg/kg/day TP + PP dose group showed a significant decrease in thyroid weight. When TP + PP doses of 10, 250, and 750 mg/kg/day were compared to the negative control dose group, there was a significant decrease in adrenal weight. When compared to the oil control and positive control dose groups, the 10 mg/kg/day of TP + PP dose group showed a substantial decrease in adrenal weight. There was no statistically significant difference in pancreatic weights between the treatment and control groups. The data were not graphed since there was no statistically significant difference in pancreatic weights.

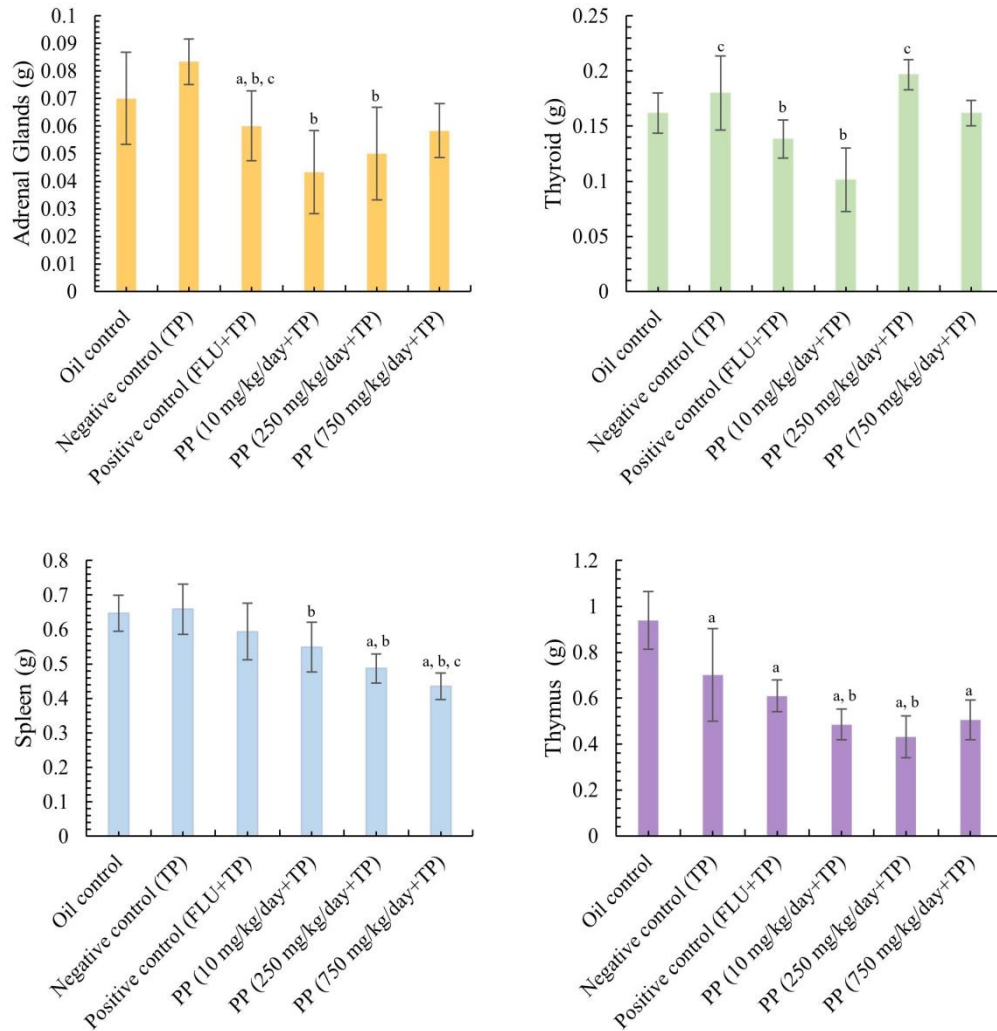


Figure 1. Absolute organ weights of controls and TP+PP dose groups. Values are given as mean \pm SD. ^a Significant difference from oil control, ^b Significant difference from negative control (TP) and ^c Significant difference from positive control (FLU+TP), $p < 0.05$ (Significance level $p \leq 0.05$).

3.2. Hematologic Analysis

Hematologic analysis results of rats belonging to application groups are shown in Table 1. In the 250 mg/kg/day of TP + PP group, a significant decrease was observed in lym %, mon % and plt values in general compared to the oil control and negative control groups. In addition, a significant decrease was observed in RBC and Hct values in comparison with the negative control group. WBC values were increased compared to the oil control and negative control groups.

Table 1. Results of hematologic analysis of male rats in the control and exposure to propyl paraben at dose of 10, 250, and 750 mg/kg/day.

Values are given mean \pm SD for six animals in each group. "n" number of rats. ^aSignificant difference from oil control,

Parameters	Oil Control	Negative Control (TP) 0.4 mg/kg/day	Positive Control (Flutamid+TP) 3 mg/kg/day	TP+PP 10 mg/kg/day	TP+PP 250mg/kg/day	TP+PP 750mg/kg/day
n	6	6	6	6	6	6
WBC	3.72 \pm 0.81	3.20 \pm 0.81	4.34 \pm 0.49	4.00 \pm 0.76	5.85 \pm 1.30 ^{a,b}	3.28 \pm 1.38
Lym %	80.58 \pm 7.28	85.08 \pm 5.38	68.20 \pm 4.91 ^{a,b}	3.10 \pm 0.75 ^{a,b}	3.98 \pm 0.69 ^{a,b}	7.12 \pm 7.43 ^{a,b}
Mon %	5.88 \pm 0.36	6.57 \pm 0.67	4.58 \pm 0.57 ^{a,b}	0.18 \pm 0.04 ^{a,b}	0.22 \pm 0.04 ^{a,b}	0.27 \pm 0.15 ^{a,b}
RBC	6.49 \pm 0.39 ^b	10.66 \pm 0.43 ^a	9.11 \pm 2.15 ^a	7.06 \pm 0.31 ^b	7.38 \pm 0.51 ^b	7.01 \pm 0.45 ^b
MCV	43.32 \pm 5.58	34.75 \pm 3.19	39.22 \pm 6.51	56.62 \pm 2.43	54.20 \pm 1.11	135.55 \pm 199.61
Hct	38.12 \pm 2.63 ^b	49.60 \pm 3.71 ^a	25.95 \pm 3.94 ^{a,b}	40.50 \pm 3.53 ^b	39.4 \pm 3.33 ^b	37.22 \pm 3.07 ^b
MCHC	18.43 \pm 0.94 ^b	39.90 \pm 2.88 ^a	31.20 \pm 1.36 ^{a,b}	35.58 \pm 0.35 ^{a,b}	37.00 \pm 1.57 ^a	35.08 \pm 4.19 ^{a,b}
Hb	13.47 \pm 0.83	14.62 \pm 1.08	10.22 \pm 2.31 ^{a,b}	14.62 \pm 1.29	14.25 \pm 0.40	13.97 \pm 1.17
Plt	4900.33\pm954.6 ^b	9335.67\pm257.40 ^a	4248.17\pm200.53 ^b	963.17\pm234.33 ^{a,b}	1129.17\pm72.70 ^{a,b}	885.83\pm124.94 ^{a,b}
MCH	35.70 \pm 1.57 ^b	17.95 \pm 0.83 ^a	11.82 \pm 1.15 ^a	20.28 \pm 0.79 ^{a,b}	19.78 \pm 1.12 ^a	19.83 \pm 0.69 ^{a,b}

^bSignificant difference from negative control (TP) (Significance level $p \leq 0.05$).

A significant decrease was observed in the lym %, mon % and plt values in the 10 mg/kg/day of testosterone propionate + propyl paraben group compared to the oil control and negative control groups. In addition, a significant decrease was observed in RBC and Hct values compared to the negative control group. There was an increase in MCHC values compared to the oil control group and a decrease compared to the negative control group. A significant decrease was observed in the lym %, mon % hct and hb values in the positive control group compared to the oil control and negative control groups. Plt values were found to be significantly lower in the positive control group than in the negative control group. In comparison to the oil control group, there was an increase in MCHC levels. When compared to the oil control group, the RBC, Hct, MCHC, and Plt values in the negative control group increased significantly. MCH levels were found to be significantly lower in the oil control group.

3.3. Histopathologic Analysis

The histopathological examination results of the tissues are shown in Figure 2 and 3. Degeneration was demonstrated in the adrenal tissue in the negative control group. Congestion and edema were found in 250 and 750 mg/kg/day TP+PP dose groups. Cell melting was observed in the positive control group and 750 mg/kg/day TP+PP dose group. In thyroid tissue, colloidal degeneration was shown in negative and positive control group, also all TP+PP group. Follicular degeneration was shown in 250 mg/kg/day TP+PP group. In thymus tissue, congestion, edema and cell degeneration were demonstrated in the negative control group.

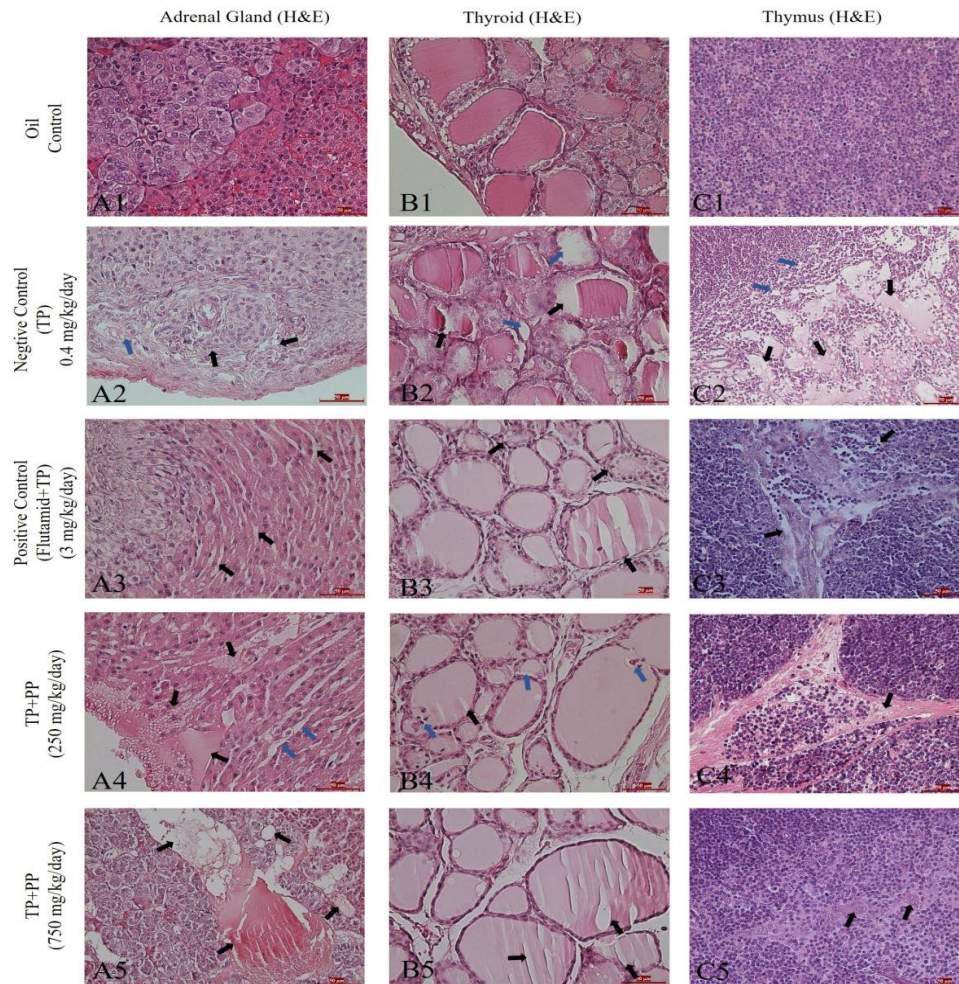


Figure 2. Histological images of the controls and TP+PP dose groups of the adrenal, thyroid and thymus glands with H&E stain. Histological images of the adrenal gland in oil control group (A1), degeneration (black arrow) and edema (blue arrow) in negative control group (A2), cell melting (black arrow) in positive control group (A3), congestion, edema (black arrow) and cell melting (blue arrow) in 250 mg/kg/day TP+PP group (A4), congestion and edema (black arrow) in 750 mg/kg/day TP+PP group (A5). Histological images of the thyroid in oil control group (B1), colloid degeneration (black arrow) in negative control group (B2), colloid degeneration in positive control group (B3), follicle degeneration (black arrow) and colloid degeneration (blue arrow) in 250 mg/kg/day TP+PP group (B4), colloid degeneration (black arrow) in 750 mg/kg/day TP+PP group (B5). Histological images of the thymus in oil control group (C1), congestion and edema (black arrow), cell degeneration (blue arrow) in negative control group (C2), degeneration (black arrow) in positive control group (C3), degeneration (black arrow) in 250 mg/kg/day TP+PP group (C4), megakaryocyte (black arrow) in 750 mg/kg/day TP+PP group (C5). 50µm bar, 400X magnification, H&E: Hematoxylin and eosin.

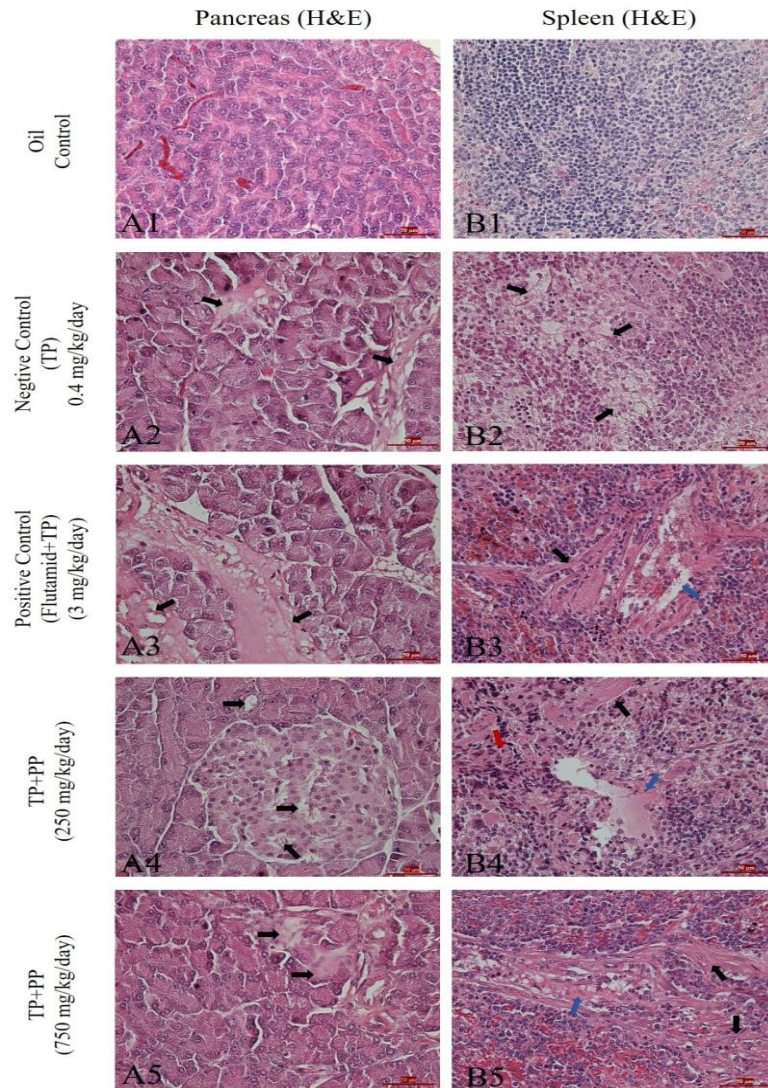


Figure 3. Histological images of the controls and TP+PP dose groups of the pancreas and spleen with H&E stain. Histological images of the pancreas in oil control group (A1), congestion and edema (black arrow) in negative control group (A2), congestion and edema (black arrow) in positive control group (A3), cellular degeneration (black arrow) in 250 mg/kg/day TP+PP group (A4), cellular degeneration (black arrow) in 750 mg/kg/day TP+PP group (A5). Histological images of the spleen in oil control group (B1), edema (black arrow) in negative control group (B2), connective tissue formation (black arrow), edema (blue arrow) in positive control group (B3), connective tissue formation (black arrow), edema (blue arrow), cell degeneration (red arrow) in 250 mg/kg/day TP+PP group (B4), connective tissue formation (black arrow), edema (blue arrow) in 750 mg/kg/day TP+PP group (B5). 50µm bar, 400X magnification, H&E: Hematoxylin and eosin.

Degeneration was observed in the positive control and 250 mg/kg/day TP+PP group. Megakaryocytes were also observed in the 750 mg/kg/day TP+PP group. Congestion and edema in pancreatic tissue were seen in negative and positive control groups. In addition, cell degeneration was found in 250 and 750 mg/kg/day TP+PP dose groups. In the spleen tissue, edema was shown in the negative and positive control groups. Cell degeneration was shown in the 250 mg/kg/day TP+PP dose groups. Connective tissue formation was also observed in the positive control and 250-750 mg/kg/day TP+PP dose groups.

Figure 4 shows the findings of the thyroid gland morphological measurements. In comparison to the oil control group, follicular epithelial heights increased in both the marginal and central areas. In the negative and positive control groups, as well as the 250 mg/kg/day TP+PP dosage group, these increases were statistically significant. In comparison to the oil control group, there was no statistically significant difference in follicular diameter in both the marginal and central areas.

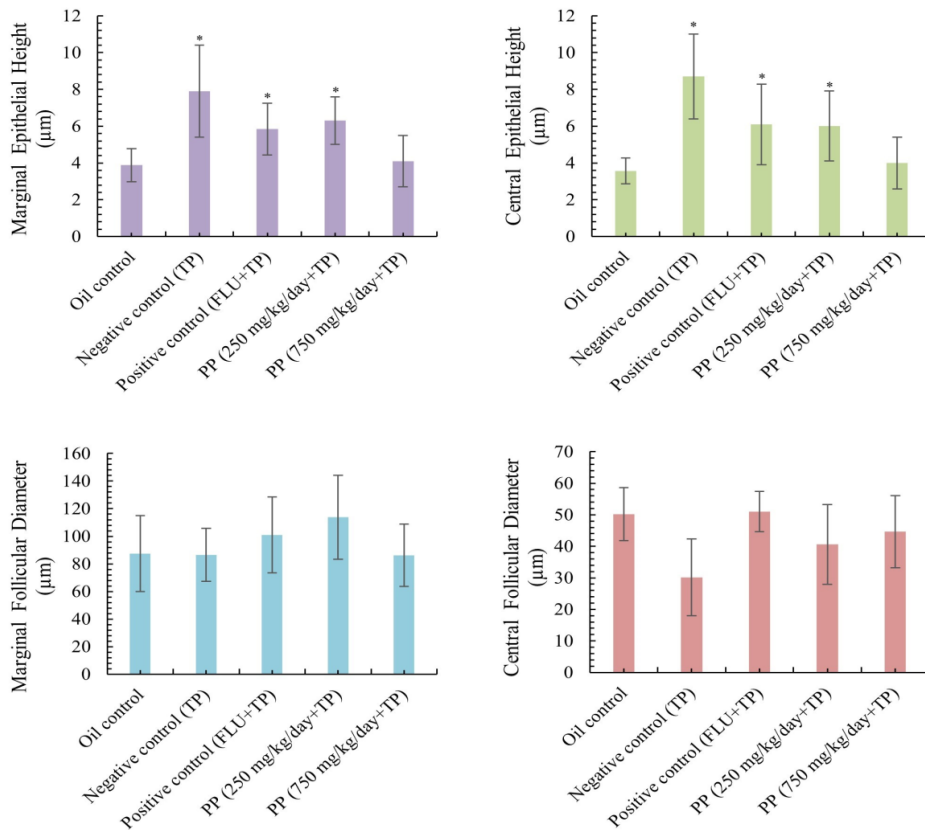


Figure 4. Thyroid gland morphometric measurement results. Values are given as mean ± SD. *statistically different from oil control group. (Significance level $p \leq 0.05$).

4. DISCUSSION

The use of parabens as preservatives can generally be made individually or in combination, and it is mostly found in cosmetic products in this way [34]. According to the US Food and Drug Administration's Voluntary Cosmetic Registry Program (VCRP) it has been shown that the most common paraben found in cosmetic products is methyl paraben [35].

It is known that propyl paraben dissolves in water and has a high concentration power [11]. It biodegrades rapidly under aerobic conditions and has a low to moderate bioaccumulation potential [36]. It has an estrogenic activity but is known to be lower compared to other chemicals [37]. They were considered harmless due to their low activity [38], but their occurrence in body fluids and cancerous tissues suggests that these chemicals may be more harmful than they appear [40,41]. PP was found in human urine at 75.3 g/L and below 0.27 g/L in cord blood plasma samples [42]. PP has been proven in animal studies to increase cell proliferation in the rat forestomach [43,44]. In another study with hamsters, it was shown that propyl paraben causes toxic effects on the urinary bladder [44]. It may also affect the viability of human sperm [45]. Furthermore, other studies have found that PP treatment reduced testosterone secretion in rats and mice [46]. As a result, inadvertent and ongoing exposure to this preservative has negative consequences for human and environmental health.

The harmful impact of parabens grows as the chain length in their chemical structure increases. When exposed on a regular basis, BP has the most damaging impact of any paraben. Despite studies demonstrating this reproductive toxicity with parabens, insufficient evidence has been found to determine whether it is related to estrogenic events. Recent research, notably PP [35], have generally shown that parabens have lower chronic toxicity than previous studies based on acceptable laboratory methods.

Recently it was found that parabens disrupt hormones function through to interfere with normal hormone functions on various levels, an effect that is linked to increased risk of the different diseases linked with the different hormones, such as obesity, cancer, allergic diseases [47,48]. As proof of this, it has been said that paraben has the ability to accumulate in body fluids such as blood. Nowak and his colleagues in 2018 say further studies are necessary to find out how parabens affect human health in their review [49].

In our investigation, the 10 mg/kg/day TP+PP dosing group had a substantial decrease in thyroid weight when compared to the negative control. Furthermore, the weights of the adrenal gland decreased in the 10, 250, and 750 mg/kg/day TP+PP dosing groups. Vo et al. (2010) discovered that female rats treated with several parabens (including butyl-, ethyl-, methyl-, propyl-, isopropyl-, and isobutyl-paraben) had substantial alterations in body and organ weights (adrenal glands, liver, ovaries, thyroid glands, and kidneys) [50]. According to studies, parabens can interact with thyroid hormone and sex hormone, altering the endocrine system by interfering with the previously stated hormones [51].

There is currently a scarcity of scientific evidence linking paraben exposure to particular harmful consequences on the thyroid hormone system. In pre-pubertal female rats, oral treatment of 250 mg PP mg/kg/day resulted in a 50% drop in blood T4 levels [50]. Despite this, no histological changes on the thyroid glands of the treated mice were observed, according to the authors. A study

was conducted by Meeker et al. on whether there is a relation between the presence of propyl paraben and methyl paraben in the urine and the level of thyroid hormone, and no correlation was found [52]. In addition, low maternal free T4 levels have been linked to propyl paraben, while high maternal T4 levels have been linked to methyl paraben [53].

Two studies have been conducted on parabens and their results have been different. Accordingly, no correlation was found between cortisol level and paraben concentration when looking at the blood of mothers and newborns [54], but a decrease in cortisol levels was seen in the fluids taken from the children of mothers associated with butyl paraben. Congestion, edema, degeneration, and cell melting were detected in the adrenal gland in the negative-positive controls and the 250-750 mg/kg/day TP+PP dosage groups. The effect of parabens on the decrease in adrenal gland hormones may be attributed to this harm, according to recent studies.

Degeneration of the thymus gland was seen in the 250 mg/kg/day TP+PP dosage group in our investigation. In addition, anomaly was observed in the pancreatic tissue. In a study with Vero cells, an increase in oxidative stress was observed when these cells were exposed to propyl paraben, and accordingly DNA damage was detected [55]. It was also found that the amount of toxicity was greater in combination exposure. This damage could have been caused by propyl paraben-induced oxidative stress.

There was an increase in DNA damage and oxidative stress after exposure to propyl paraben [56]. According to another study, it has been shown to be toxic in human lymphocyte cells and it was thought that its continuous use may increase this toxicity [57]. Identical results were reported in our study, which were similar to the detrimental effect of propyl paraben on blood cells seen in earlier studies. The number of lymphocytes and monocytes in the 10 and 250 mg/kg/day TP+PP dosage groups decreased dramatically.

In both animals and humans, parabens can affect the endocrine system and cause oxidative stress [58]. Poor pregnancy and fetal deterioration and long-term deterioration in health have been attributed to parabens [59]. As a result of the fact that the number of platelets produced in the bone marrow is not at a sufficient level, the number of platelets in the body decreases. When the spongy structure of the bone marrow is damaged, it cannot produce enough blood cells. Butyl paraben has been shown to have toxic effects on osteogenic and chondrogenic development, and it has been proven to do so by activating the peroxisome proliferator or glucocorticoid receptor [60]. Similar to the effect of butyl paraben, a remarkable decrease was observed in the amount of platelets at 10 and 250 mg/kg/day of TP+PP dose groups in our study. Parabens can cause oxidative damage by causing the formation of glutathione (GSH) [61]. If an individual's MCH value is lower than the specified reference range, it can be said that the person has a problem with the production of red blood cells or the amount of iron in the body. In spleen, in 250 and 750 mg/kg/day of testosterone propionate+propylparaben dose groups, there were congestion and connective tissue formation. The damage to the spleen as a result of the oxidative stress caused by propyl paraben, similar to other parabens, may have resulted in a decrease in the amount of MCH. Meanwhile, data from other pregnant cohorts show that urine paraben can influence circulating inflammation markers such as IL-6, IL-10, CRP, and TNF- α [62].

In this study, PP causes morphometric changes in the thyroid glands. The positive and negative control groups, as well as the 250 mg/kg/day TP+PP dosage group, all showed a substantial

increase in marginal and central thyroid epithelial height in comparison with the oil control. Studies have shown that endocrine disruptors and environmental contaminants increase the height of the thyroid gland follicular epithelium [63]. It is stated that the height of the follicular epithelium is associated with active follicles in the thyroid gland. These studies and our study suggest that substances classified as endocrine disruptors cause follicle hyper stimulation [64,65].

5. CONCLUSION

The studies discussed above have raised concerns about the reproductive system and hormonal changes in the general population of parabens, leading to a concentration of research in this area. Restrictions have been put on the use of parabens, trying to reduce the use of the most. In addition to these, studies should be carried out for new substances that can be used as an alternative to parabens. Paraben exposure has not been totally eliminated. On this issue, more research is required.

ACKNOWLEDGEMENTS

Nurhayat BARLAS designed the study, analyzed the data, and reviewed the text. The text was written by Gözde KARABULUT, who also evaluated the data and updated it. Eda Nur İNKAYA gathered the information, analyzed it, and reviewed the paper. This work was reviewed and approved by all authors.

We would like to express our gratitude to the writers for their dedication to this effort. The Hacettepe University Scientific Research Projects Coordination Unit provided financial assistance for this project (Project no: FHD-2017-13477). Eda Nur İNKAYA is supported by Council of Higher Education (YÖK), Turkey within the scope of YÖK 100/2000 PhD Scholarship.

REFERENCES

- [1] Soni, M.G., Carabin, I.G., Burdock, G.A., (2005), Safety assessment of esters of p-hydroxybenzoic acid (parabens), *Food and Chemical Toxicology*, 43,985-1015.
- [2] Watanabe, Y., Kojima, H., Takeuchi, S., Uramaru, N., Ohta, S., Kitamura, S., (2013), Comparative study on transcriptional activity of 17 parabens mediated by estrogen receptor α and β and androgen receptor, *Food and Chemical Toxicology*, 57:227-34.
- [3] Garner, N., Siol, A., Eilks, I., (2014), Parabens as preservatives in personal care products, *Chemistry in Action*, Vol. 103.
- [4] Melo, L.P., Queiroz, M.E.C.J., (2010), Simultaneous analysis of parabens in cosmetic products by stir bar sorptive extraction and liquid chromatography, *Separation Science*, Vol.33, 1849-1855.
- [5] Boberg, J., Taxvig, C., Christiasen, S., Hass, U., (2010), Possible endocrine disrupting effects of parabens and their metabolites, *Reproductive Toxicology*, Vol. 30(2):301-1255.

- [6] Kirchof, M.G., de Gannes, G.C., (2013), The health controversies of parabens, *Skin Therapy Letters*, 18(2):5–7.
- [7] Darbre, P.D., Harvey, P.W., (2008), Paraben esters: review of recent studies of endocrine toxicity, absorption, esterase and human exposure, and discussion of potential human health risks, *Journal of Applied Toxicology*, 28(5):561–78.
- [8] Golden, R., Gandy, J., Vollmer, G.A., (2005) Review of the endocrine activity of parabens and implications for potential risks to human health, *Critical Reviews in Toxicology*, 35(5):435–58.
- [9] Matwiejczuk, N., Galicka, A., Brzóška, M.M., (2020), Review of the safety of application of cosmetic products containing parabens, *Journal of Applied Toxicology*, 40(1):176–210.
- [10] Guo, Y., Kannan, K. A., (2013), Survey of phthalates and parabens in personal care products from the United States and its implications for human exposure. *Environmental science & technology*, 47(24):14442–9.
- [11] Soni, M., Burdock, G., Taylor, S.L., Greenberg, N., (2001), Safety assessment of propyl paraben: a review of the published literature, *Food and Chemical Toxicology*, 39(6):513–32.
- [12] Kassotis, C.D., Vandenberg, L.N., Demeneix, B., Porta, M., Slama, R., Trasande, L., (2020), Endocrine disrupting chemicals: economic, regulatory, and policy implications, *The Lancet Diabetes & endocrinology*, 8(8):719–30.
- [13] La Merrill, M.A., Vandenberg, L.N., Smith, M.T., Goodson, W., Browne, P., Patisaul, H.B., (2020), Consensus on the key characteristics of endocrine-disrupting chemicals as a basis for hazard identification, *Nature Reviews Endocrinology*, 16(1):45–57
- [14] Andersen, F.A., (2008), Final amended report on the safety assessment of methylparaben, ethylparaben, propylparaben, isopropylparaben, butylparaben, isobutylparaben, and benzylparaben as used in cosmetic products, *International Journal of Toxicology*, 27: 1-82.
- [15] Vela-Soria, F., Rodriguez, I., Ballesteros, O., Zafra-Gomez, A., Ballesteros, L., Cela, R., Navalon, A., (2014), Simplified matrix solid phase dispersion procedure for the determination of parabens and benzophenone-ultraviolet filters in human placental tissue samples, *Journal of Chromatography A*, 1371: 39-47.
- [16] Mathiesen, L., Zuri, G., Andersen, M., Knudsen, Le., (2013), A proposed study on the transplacental transport of parabens in the human placental perfusion model, *Alternatives to Laboratory Animals*, 41: 473-482.
- [17] Boberg, J., Taxvig, C., Christiansen, S., Hass, U., (2010) Possible endocrine disrupting effects of parabens and their metabolites, *Reproductive Toxicology*, 30: 301-312.

- [18] Engeli, R., Rohrer, S., Vuorinen, A., Herdinger, S., Kaserer, T., Leugger, S., (2017) Interference of paraben compounds with estrogen metabolism by inhibition of 17 β -Hydroxysteroid dehydrogenases, *International Journal of Molecular Sciences*, 18(9).
- [19] Darbre, P.D., Aljarrah, A., Miller, W.R., Coldham, N.G., Sauer, M.J., Pope, G.S., (2004), Concentrations of parabens in human breast tumors, *Journal of Applied Toxicology*, 24(1):5-13.
- [20] Shin, M.Y., Shin, C., Choi, J.W., Lee, J., Lee, S., Kim, S., (2019), Pharmacokinetic profile of propyl paraben in humans after oral administration, *Environment International*, 130:104917.
- [21] Hu, P., Kennedy, R.C., Chen, X., Zhang, J., Shen, C.L., Chen, J., Zhao, L., (2016), Differential effects on adiposity and serum marker of bone formation by post-weaning exposure to methylparaben and butylparaben, *Environmental Science and Pollution Research*, 23, 21957–21968.
- [22] Fransway, A.F., Fransway, P.J., Belsito, D.V., Yiannias, J.A., (2019), Paraben Toxicology, *Dermatitis*, 30, 32–45.
- [23] Gal, A., Gedye, K., Craig, Z.R., Ziv-Gal, A., (2019), Propylparaben inhibits mouse cultured antral follicle growth, alters steroidogenesis, and upregulates levels of cell-cycle and apoptosis regulators, *Reproductive Toxicology*, 89, 100–106.
- [24] Okubo, T., Yokoyama, Y., Kano, K., Kano, I., (2001), ER-dependent estrogenic activity of parabens assessed by proliferation of human breast cancer MCF-7 cells and expression of ER alpha and PR, *Food and Chemical Toxicology*, 39, 1225–1232.
- [25] Gonzalez, T.L., Moos, R.K., Gersch, C.L., Johnson, M.D., Richardson, R.J., Koch, H.M., Rae, J.M., (2018), Metabolites of nbutylparaben and iso-butylparaben exhibit estrogenic properties in MCF-7 and T47D human breast cancer cell lines, *Toxicological Sciences*, 164, 50–59.
- [26] OECD, (2018), "Hershberger Bioassay in Rats (H assay) (OECD TG 441) (including OECD GD 115 on the Weanling Hershberger Bioassay)", in Revised Guidance Document 150 on Standardized Test Guidelines for Evaluating Chemicals for Endocrine Disruption, OECD Publishing, Paris.
- [27] Özdemir, E., Barlas, N and Çetinkaya, M.A., (2018), Assessing the antiandrogenic properties of propyl paraben using the Hershberger bioassay, *Toxicology Research*, 7, 235 – 243.
- [28] U.S.E.P.A. (2009), Endocrine Disruptor Screening Program Test Guidelines OPPTS 890.1400: Hershberger Bioassay, EPA 740-C-09-008.
- [29] Abdel-Dayem, M. M., & Elgendy, M. S, (2009), Effects of chronic estradiol treatment on the thyroid gland structure and function of ovariectomized rats, *BMC Research Notes*, 2(1), 1-7.


- [30] Matsuu-Matsuyama, M., Shichijo, K., Matsuda, K., Fujimoto, N., Kondo, H., Miura, S., Kurashige, T., Nagayama T., Nakashima, M., (2021), Age-dependent effects on radiation-induced carcinogenesis in the rat thyroid, *Scientific Reports*, 11(1), 1-12.
- [31] Tani, Y., Maronpot, R. R., Foley, J. F., Haseman, J. K., Walker, N. J., & Nyska, A., (2004), Follicular Epithelial Cell Hypertrophy Induced by Chronic Oral Administration of 2, 3, 7, 8-Tetrachlorodibenzo-p-Dioxin in Female Harlan Sprague—Dawley Rats, *Toxicologic Pathology*, 32(1), 41-49.
- [32] Vasiliu, I., Ciobanu-Apostol, D. G., Armasu, I., Bredetean, O., Serban, I. L., & Preda, C., (2020), Protective role of selenium on thyroid morphology in iodine-induced autoimmune thyroiditis in Wistar rats, *Experimental and Therapeutic Medicine*, 20(4), 3425-3437.
- [33] Iglesias-Osma, M. C., Blanco, E. J., Carretero-Hernandez, M., Catalano-Iniesta, L., Sanchez-Robledo, V., Garcia-Barrado, M. J., Carretero, J., (2019), The influence of the lack of insulin receptor substrate 2 (IRS2) on the thyroid gland, *Scientific reports*, 9(1), 1-10.
- [34] SCCP, (2005), Extended Opinion on the Safety Evaluation of Parabens. SCCP/0873/05, European Union: Science Committee on Consumer Products.
- [35] Cherian, P., Zhu, J., Bergfeld, W. F., Belsito, D. V., Hill, R. A., Klaassen, C. D., Heldreth, B., (2020). Amended safety assessment of parabens as used in cosmetics, *International Journal of Toxicology*, 39(1_suppl), 5S-97S.
- [36] Siddique, S., Kubwabo, C., Harris, S.A., (2016), A review of the role of emerging environmental contaminants in the development of breast cancer in women, *Emerging Contaminants*, 2, 204–219.
- [37] Routledge, E.J., Parker, J., Odum, J., Ashby, J., Sumpter, J.P., (1998), Some alkyl hydroxy benzoate preservatives (parabens) are estrogenic, *Toxicology and Applied Pharmacology*, 153, 12–19.
- [38] Wu, C., Huo, W., Li, Y., Zhang, B., Wan, Y., Zheng, T., Zhou, A., Chen, Z., Qian, M., Zhu, Y., (2017), Maternal urinary paraben levels and offspring size at birth from a Chinese birth cohort, *Chemosphere*, 172, 29–36.
- [39] Wróbel, A.M., Gregoraszczyk, E.Ł., (2015), Action of methyl-, propyl- and butylparaben on GPR30 gene and protein expression, cAMP levels and activation of ERK1/2 and PI3K/Akt signaling pathways in MCF-7 breast cancer cells and MCF-10A non-transformed breast epithelial cells, *Toxicology Letters*, 238, 110–116.
- [40] Hu, P., Chen, X., Whitener, R.J., Boder, E.T., Jones, J.O., Porollo, A., Chen, J., Zhao, L., (2013), Effects of parabens on adipocyte differentiation, *Toxicological Sciences*, 131, 56–70.
- [41] Lee, J.H., Lee, M., Ahn, C., Kang, H.Y., Tran, D.N., Jeung, E.B., (2017), Parabens accelerate ovarian dysfunction in a 4-vinylcyclohexene diepoxide-induced ovarian failure model, *International Journal of Environmental Research and Public Health*, 14, 161.

- [42] Pycke, B.F.G., Geer, L.A., Dalloul, M., Abulafia, O., Halden, R.U., (2015), Maternal and fetal exposure to parabens in a multiethnic urban U.S. population, *Environment International*, 84, 193–200.
- [43] Shibata, M.A., Yamada, M., Hirose, M., Asakawa, E., Tatematsu, M., Ito, N., (1990), Early proliferative responses of forestomach and glandular stomach of rats treated with five different phenolic antioxidants, *Carcinogenesis*, 11, 425–429.
- [44] Hirose, M., Inoue, T., Asamoto, M., Tagawa, Y., Ito, N., (1986), Comparison of the effects of 13 phenolic compounds in induction of proliferative lesions of the forestomach and increase in the labelling indices of the glandular stomach and urinary bladder epithelium of Syrian golden hamsters, *Carcinogenesis*, 7, 1285–1289.
- [45] Samarasinghe, S.V.A.C., Krishnan, K., Naidu, R., Megharaj, M., Miller, K., Fraser, B., Aitken, R.J., (2018), Parabens generate reactive oxygen species in human spermatozoa, *Andrology*, 6(4):532-541.
- [46] Oishi, S., (2002), Effects of propyl paraben on the male reproductive system, *Food and Chemical Toxicology*, 40, 1807–1813.
- [47] Shimizu, Y., Kambayashi, Y., Tsujiguchi, H., Hara, A., Hori, D., Thi Thu Nguyen, T., Yoshikawa, T., (2018), Relationship between the Use of Parabens and Allergic Diseases in Japanese Adults—A Cross- Sectional Study, *Multidisciplinary Scientific Journal*, 1(1), 148-158.
- [48] Kim, J., Chevrier, J., (2020), Exposure to parabens and prevalence of obesity and metabolic syndrome: an analysis of the Canadian Health Measures Survey, *Science of The Total Environment*, 713, 135116.
- [49] Nowak, K., Ratajczak–Wrona, W., Górska, M., Jabłońska, E., (2018), Parabens and their effects on the endocrine system, *Molecular and Cellular Endocrinology*, 474, 238-251.
- [50] Vo, T.T.B., Yoo, Y.M., Choi, K.C., Jeung, E.B., (2010), Potential estrogenic effect(s) of parabens at the prepubertal stage of a postnatal female rat model, *Reproductive Toxicology*, 29,306–316.
- [51] Liu, H., Li, J., Xia, W., Zhang, B., Peng, Y., Li, Y., Liu, W., (2019), Blood pressure changes during pregnancy in relation to urinary paraben, triclosan and benzophenone concentrations: A repeated measures study, *Environment International*, 122, 185-192.
- [52] Meeker, J.D., Yang, T., Ye, X., Calafat, A.M., Hauser, R., (2011), Urinary Concentrations of Parabens and Serum Hormone Levels, Semen Quality Parameters, and Sperm DNA Damage, *Environmental Health Perspectives*, 119:252–257.
- [53] Aker, A. M., Johns, L., McElrath, T. F., Cantonwine, D. E., Mukherjee, B., Meeker, J. D., (2018), Associations between maternal phenol and paraben urinary biomarkers and maternal

- hormones during pregnancy: a repeated measures study, *Environment International*, 113, 341-349.
- [54] Kang, S., Kim, S., Park, J., Kim, H. J., Lee, J., Choi, G., Choi, K., (2013), Urinary paraben concentrations among pregnant women and their matching newborn infants of Korea, and the association with oxidative stress biomarkers, *Science of the Total Environment*, 461, 214-221.
- [55] Martín, J. M. P., Peropadre, A., Herrero, Ó., Freire, P. F., Labrador, V., Hazen, M. J., (2010), Oxidative DNA damage contributes to the toxic activity of propylparaben in mammalian cells, *Mutation Research/Genetic Toxicology and Environmental Mutagenesis*, 702(1), 86-91.
- [56] Martín, J. M. P., Freire, P. F., Daimiel, L., Martínez-Botas, J., Sánchez, C. M., Lasunción, M. A., Hazen, M. J., (2014), The antioxidant butylated hydroxyanisole potentiates the toxic effects of propylparaben in cultured mammalian cells, *Food and Chemical Toxicology*, 72, 195-203.
- [57] Güzel Bayülken, D., Ayaz Tüylü, B., Sinan, H., Sivas, H., (2019), Investigation of genotoxic effects of paraben in cultured human lymphocytes, *Drug and Chemical Toxicology*, 42(4), 349-356.
- [58] Watkins, D. J., Ferguson, K. K., Del Toro, L. V. A., Alshawabkeh, A. N., Cordero, J. F., Meeker, J. D., (2015), Associations between urinary phenol and paraben concentrations and markers of oxidative stress and inflammation among pregnant women in Puerto Rico, *International Journal of Hygiene and Environmental Health*, 218(2), 212-219.
- [59] Al-Gubory, K.H., (2014), Environmental pollutants and lifestyle factors induce oxidative stress and poor prenatal development, *Reproductive Bio Medicine Online*, 29: 17–31.
- [60] Hu, P., Overby, H., Heal, E., Wang, S., Chen, J., Shen, C.L., Zhao, L., (2017), Methylparaben and butylparaben alter multipotent mesenchymal stem cell fates towards adipocyte lineage, *Toxicology and Applied Pharmacology*, 15;329:48-57.
- [61] Nishizawa, C., Takeshita, K., Ueda, J. I., Nakanishi, I., Suzuki, K. T., Ozawa, T., (2006), Reaction of para-hydroxybenzoic acid esters with singlet oxygen in the presence of glutathione produces glutathione conjugates of hydroquinone, potent inducers of oxidative stress, *Free Radical Research*, 40(3), 233-240.
- [62] Zota, A.R., Geller, R.J., Romano, L.E., Coleman-Phox, K., Adler, N.E., Parry, E., Epel, E.S., (2018), Association between persistent endocrine-disrupting chemicals (PBDEs, OH-PBDEs, PCBs, and PFASs) and biomarkers of inflammation and cellular aging during pregnancy and postpartum, *Environment International*, 115, 9-20.
- [63] Boas, M., Feldt-Rasmussen, U., Skakkebaek, N. E., Main, K. M., (2006), Environmental chemicals and thyroid function, *European Journal of Endocrinology*, 154(5), 599-611.

- [64] de Lima Junior, N. C., Camilo, J. F., do Carmo, P. R., de Andrade, M. N., Braz, B. F., Santelli, R. E., Dias, G. R. M., (2021), Subacute exposure to lead promotes disruption in the thyroid gland function in male and female rats, *Environmental Pollution*, 274, 115889.
- [65] Rodrigues-Pereira, P., Macedo, S., Gaspar, T. B., Canberk, S., Selmi-Ruby, S., Máximo, V., Miranda-Alves, L., (2020), Relevant dose of the environmental contaminant, tributyltin, promotes histomorphological changes in the thyroid gland of male rats, *Molecular and Cellular Endocrinology*, 502, 110677.

APPENDIX A



T.C.
HACETTEPE ÜNİVERSİTESİ
Hayvan Deneyleri Yerel Etik Kurulu

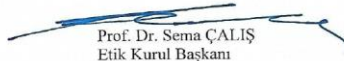
Sayı : 52338575-152

HAYVAN DENEYLERİ YEREL ETİK KURUL KARARI

TOPLANTI TARİHİ	: 05.11.2015 (PERŞEMBE)
TOPLANTI SAYISI	: 2015/08
DOSYA KAYIT NUMARASI	: 2015/86
KARAR NUMARASI	: 2015/86 – 13
ARAŞTIRMA YÜRÜTÜCÜSÜ	Prof.Dr. Nurhayat BARLAS
HAYVAN DENEYLERİNDE	
SORUMLU ARAŞTIRMACI	Ecem ÖZDEMİR
YARDIMCI ARAŞTIRMACILAR	: Arş.Gör. Güzde KARABULUT
ONAYLANAN HAYVAN TÜRÜ ve	: 42 adet wistar albino sıçan
SAYISI	

Üniversitemiz Fen Fakültesi Biyoloji Bölümü öğretim üyelerinden Prof.Dr. Nurhayat BARLAS'ın araştırma yürütücüsü olduğu 2015/86 kayıt numaralı "*Propil Parabenin Olgunlaşmamış Erkek Sıçanlarda Antiandrojenik Etkilerinin Araştırılması*" isimli çalışma Hayvan Deneyleri Yerel Etik Kurulu Yönergesi'ne göre uygun bulunarak oy birliği ile onaylanmasına karar verilmiştir.

Sorumlu araştırmacı deneylere başlangıç tarihini Etik Kurula bildirmekle yükümlüdür


Prof. Dr. Sema ÇALIŞ
Etik Kurul Başkanı

Hacettepe Üniversitesi Hayvan Deneyleri Yerel Etik Kurulu 06100 Sıhhiye-Ankara Ayrıntılı Bilgi için:
Telefon: 0 (312) 305 1090-1082 • Faks: 0 (312) 310 0580
www.etikkurul.hacettepe.edu.tr/index_hdk.php



RESEARCH ARTICLE

THE EFFECT of ANISOTROPY on the DYNAMIC PROPERTIES of SCHIST ROCKS

Mehmet ÖZDEMİR^{1*}, Sunay BEYHAN², Kaan ERARSLAN³

¹Kütahya Dumlupınar University, Engineering Faculty, Mining Engineering, mehmet.ozdemir@dpu.edu.tr,
ORCID: 0000-0002-8164-8874

² Kütahya Dumlupınar University, Engineering Faculty, Mining Engineering, sunay.beyhan@dpu.edu.tr,
ORCID: 0000-0002-6893-9298

³ Kütahya Dumlupınar University, Engineering Faculty, Mining Engineering, kaan.erarslan@dpu.edu.tr,
ORCID: 0000-0002-1875-4009

Receive Date: 13.04.2022

Accepted Date: 03.06.2022

ABSTRACT

Dynamic elastic properties of rocks such as modulus of elasticity and Poisson's ratio are important in some design stages of underground and surface engineering structures. Also, anisotropy is that rocks show different strength and deformation properties with the different orientation angles that they gain as a result of the effect of the direction, fabric, microstructure and discontinuities. Different lithological rock units with anisotropy characteristics are encountered in studies carried out in underground and surface engineering structures, and in cases with such characteristics, there are problems in terms of stability.

In this study, the effect of the anisotropic property of rock masses on elastic parameters such as dynamic young modulus and dynamic Poisson's ratio were investigated. For this purpose; samples with different orientations were obtained from schists, which are metamorphic rocks, at 0°, 15°, 30°, 45°, 60°, 75° and 90°. Experimental studies were carried out to determine the mechanical and physical properties of these samples. Dynamic young modulus and dynamic Poisson's ratio were determined by P and S velocity of wave propagation experiments. With the results obtained, while the young modulus and Poisson's ratio of samples belonging to the green schist rock unit with different orientations show a relatively stable structure, these values for the mica schist unit are quite variable and wavy. Therefore, the anisotropy feature of the rock must be taken into consideration in terms of the stability of the structure in engineering studies to be carried out in the mica schist unit.

Keywords: *Anisotropy, P and S wave, Rock dynamic properties*

1. INTRODUCTION

Anisotropy in rocks is the fact that rocks show different strength and deformation properties in different orientations and bedding. Different researchers have studied the strength and deformation changes of anisotropic rocks. [1–5]. It was determined that these values increased in the direction perpendicular to the bedding and decreased in the direction parallel to the bedding. However, these values may vary depending on the rock type.

P and S wave values are used to detect structures such as voids, discontinuities and cracks in the rock and concrete samples, and to find the dynamic modulus of elasticity and dynamic Poisson's ratios. [6]. The ultrasonic sound velocity experiment is not generally applied to anisotropic rocks. It is more suitable for rocks of low anisotropy levels [7].

Wang and Li [8] obtained P wave velocity increase at 0° and close values for S wave velocity in shale samples taken at 0° , 15° , 30° , 45° , 60° , 75° and 90° . This situation is explained by the fracture morphology obtained by computer tomography. It is thought that the excess in the number of voids and cracks increase these values.

Ribacchi et al. [9] applied P wave propagation velocity test at 0° , 45° and 90° in dried and saturated media to examine the schistosity structure of gneiss rock. It was stated that an increase was observed in the values in the saturated medium compared to the dry ones. It was mentioned that the values were close to each other in the saturated environment and there were differences in the dried media. It was stated that the values for both media are maximum at 90° and these observations were caused by the differences in bedding, void and crack structures in the rocks.

Khandelwal and Sing [10] reported that uniaxial compressive strength, tensile strength, density, Young's modulus and Poisson's ratio values were highly correlated with P wave velocity values in their experiments on coal, shale and sandstone samples, which are layered and anisotropic rocks.

Kim et al. [11], investigated the P wave velocity changes of gneiss, schist and shale samples at 0° , 15° , 30° , 45° , 60° , 75° and 90° . Maximum wave velocities were obtained at 90° and minimum wave velocities at 0° . It was stated that the stratified structure was effective in these values.

Ali et al. [12] studied the anisotropic behaviour of the banded amphibolite rock. Uniaxial and triaxial compressive strength and P-S wave propagation velocity tests were performed on the cores prepared at 0° , 30° , 60° and 90° . P and S wave velocity values in the direction parallel to the foliation plane (0°) were higher than that perpendicular (90°). The reason for this was stated as the excess of quartz and hornblende in these planes.

Huang et al. [13] tried to determine the fracture behaviour of coals with acoustic emission tests in the direction perpendicular and parallel to the bedding. By applying lateral pressures between 0-40 MPa, dynamic deformations were tried to be obtained by trying to create underground strength conditions with P and S ultrasonic wave velocity experiments. Acoustic emission rates perpendicular and parallel to the stratification gave different values. It was stated that maximum acoustic emission values were obtained especially in saturated coal samples. It was emphasized that water affected the fracture maximally. In addition, it was remarked that the dynamic deformation parameters (dynamic modulus of elasticity and dynamic Poisson's ratio) decreased with different lateral pressures. It was mentioned that lateral pressure had an opposite effect on dynamic deformations.

In this study, ultrasonic sound velocity tests were carried out on cores taken from green schist and mica schist rocks with anisotropic structures at 0° , 15° , 30° , 45° , 60° , 75° and 90° . The variation of P and S wave velocities, dynamic modulus of elasticity and dynamic Poisson's ratios were investigated. This study focused on the dynamic properties of anisotropic schist rocks due to their stratified structure, which can cause different values in different bedding orientations.

2. MATERIAL

The block and core samples used in this study were obtained from the copper field of the Hanönü district of Kastamonu, Turkey. The ore production in the field, which belongs to the private sector, is carried out by the open pit method (Fig. 1).

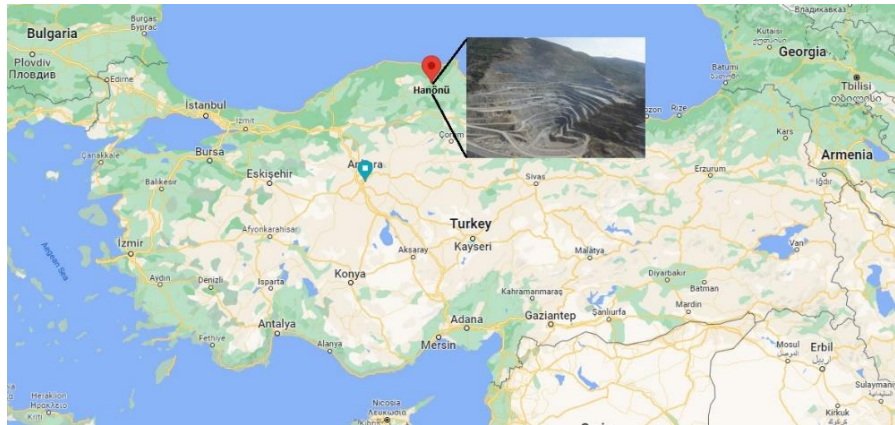


Figure 1. Research site location.

In the study, both drilling samples made by the enterprise and samples obtained from the blocks were used. Experimental studies were carried out at 0°, 15°, 30°, 45°, 60°, 75° and 90° on HQ diameter (63.5 mm) anisotropic samples (Fig.2 b,c). In Figure 2 (a), the degree (ϕ) system determined according to the loading axis is indicated.

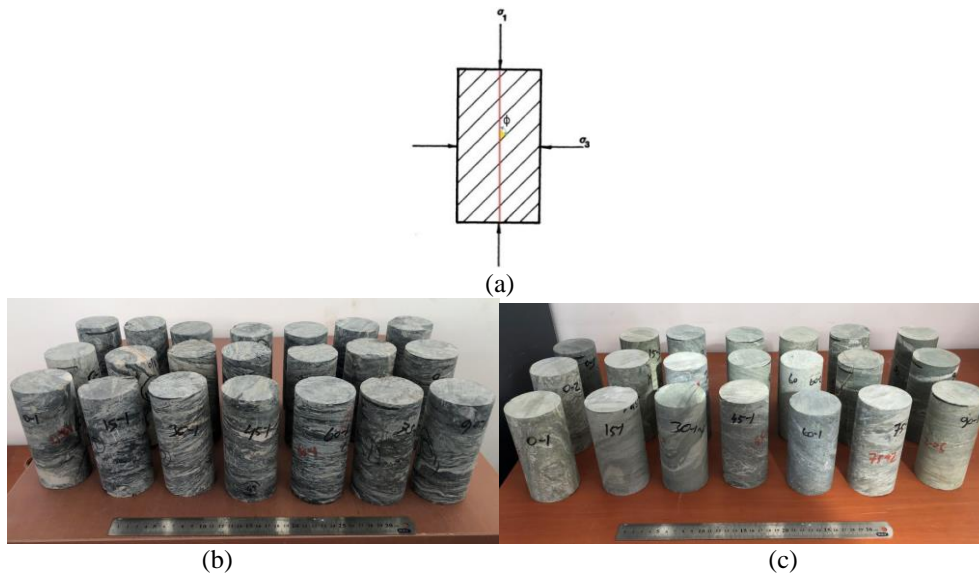


Figure 2. a. Core anisotropy (ϕ : degree), b. mica schist, c. green schist.

The samples were separated at the specified degrees and the experiments were carried out in dried and saturated environments. To determine the physical properties of the samples, density, water absorption rate by weight and volume, porosity and void ratio experiments were carried out. Ultrasonic sound velocity tests were applied to the samples at 0°, 15°, 30°, 45°, 60°, 75° and 90° in dried and saturated conditions. To determine the mineralogical and petrographic properties of the rocks, X-Ray diffractometry (XRD) and X-Ray fluorescence (XRF) tests were performed at the Advanced Technologies Center of Kütahya Dumlupınar University.

2.1. Kastamonu-Hanönü Geology

Stratigraphical section of the Akgöl Formation, Çağlayan Formation, Kapanboğazı Formation, Yemişliçay Formation, Gürsöku Formation and Akveren Formation observed in and around the mine site is given in Figure 3 [14]. The study area is in Akgöl formation and it contains medium-thick bedded, coarse pebble-block conglomerate, marble lenses, green-coloured, medium-thick bedded schist, black coloured, thin-medium-thick bedded schist and massive sulphide mineralization structures. The mine site is surrounded by Volcanogenic Massive Sulphite (VMS) type mineralizations associated with the Triassic-Jurassic Akgöl Formation along Taşköprü-Hanönü of Kastamonu province and mineral deposits associated with the Çangaldağ complex rocks [14,15].

Upper systems tract		Systems tract		FORMATION	THICKNESS(m)	LITHOLOGY	REMARKS		
PALEOGENE	NEOGENE	SERIES	LAYER						
CENOZOIC		Paleocene	Eocene	Akveren fm (Tpea)	~ 25-50	Schist, argillaceous limestone, limestone alternation			
					~ 40-50	River sediments (sand, conglomerate, alluvion) Loose-structured, unbalanced terrestrial conglomerate and sand			
MESOZOIC		CRETACEOUS		Gürsöku fm (Kg)	~ 625	Sandstone, shale alternation			
						Conglomerate			
		UP		Konisiyayen Santonian	Yemişliçay fm (Ky)	~ 200-1480	Agglomerate, tuff, limestone, marl		
								Thin-medium seamed, micritic limestone	
		DOWN		Konisiyayen Santonian	Kapanboğazı fm (Kk)	~ 160			
				Çağlayan fm (Kc)	~ 2000	Sandstone, shale alternation			
						Middle-thick seamed conglomerate consisting of coarse pebble-block			
JURASSIC		DOWN		Akgöl fm (TJda)	~ 1500-2000	Marble lenses Green, middle-thick seamed schist			
TRIASSIC						Metavolcanic Massive sulfide mineralization Black, thin-medium-thick seamed schist			

Figure 3. Stratigraphical section of the work area [14].

3. EXPERIMENTAL STUDIES

3.1. Physical Properties

Green schist and mica schist cores at 0°, 15°, 30°, 45°, 60°, 75° and 90° were dried in an oven at 105°C for 24 hours and then cooled in a desiccator for 30 minutes according to the method suggested by ISRM [7]. They were kept in distilled water until they became saturated. The physical properties obtained for both rocks are presented in Table 1.

Table 1. Physical properties of green schist and mica schist.

Samples	Dry Density (gr/cm ³)	Saturated Density (gr/cm ³)	Water Absorption by Weight (%)	Water Absorption by Volume (%)	Porosity(%)	Void Ratio
Green Schist	2,79	2,80	0,18	0,54	0,537	0,0054
Mica Schist	2,70	2,74	1,20	3,22	3,223	0,0336

According to Table 1, since mica schist has water absorption values of 1,20% and 3,22% by weight and volume, respectively, and green schist has water absorption values of 0,18% and 0,54% by weight and volume, it is understood that mica schist has more voided or porous structure.

3.2. Mineralogical and Chemical Analysis

XRD and XRF analyzes were performed to determine its mineralogy and chemical properties. For green schist; muscovite, albite, orthoclase, kaolinite and quartz minerals peaked. Albite and orthoclase were found in higher numbers for green schist than for other minerals. In the XRD of mica schist, muscovite, clinocllore (chlorite type), albite, kaolinite and quartz minerals peaked (Figures 4 and 5). Major oxide results of green schist and mica schist units are given in Table 2. According to these results; especially SiO₂ was more than 40% in both units.

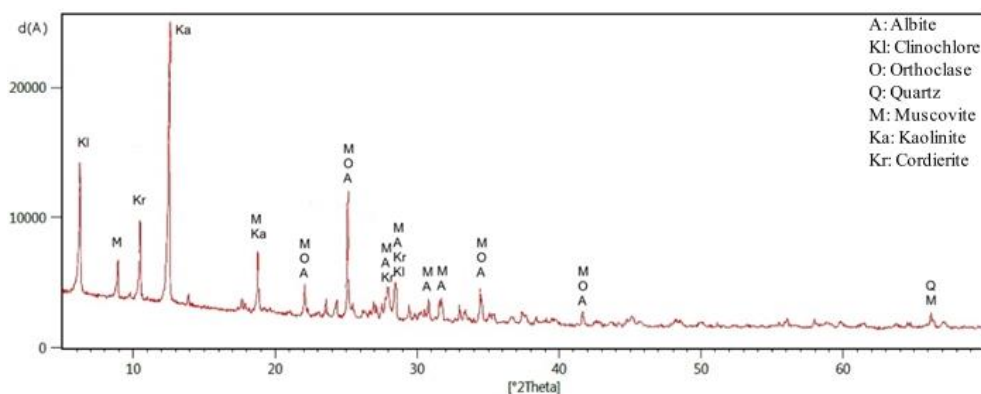


Figure 4. Green schist XRD analysis results.

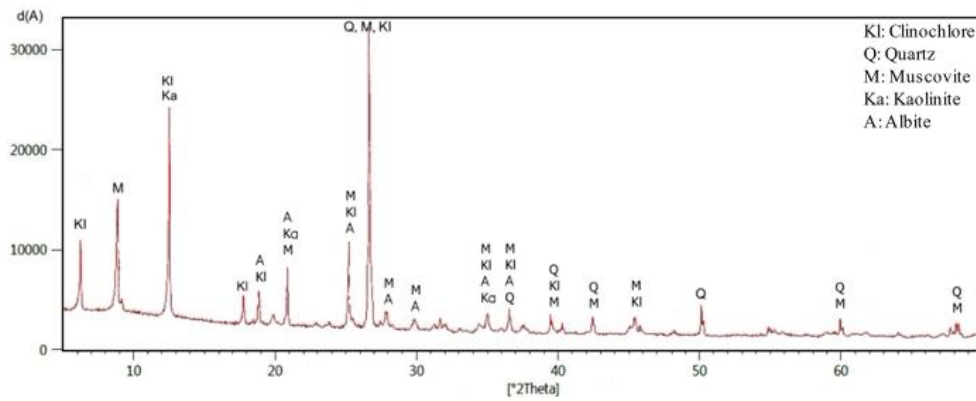


Figure 5. Mica schist XRD analysis results.

Table 2. Green and mica schist XRF results.

Sample	SiO ₂	Al ₂ O ₃	Fe ₂ O ₃	K ₂ O	MgO	CaO	Na ₂ O	TiO ₂	P ₂ O ₅	MnO	LOI
Mica Schist	50,11	23,07	9,87	4,45	2,58	1,68	0,92	0,85	0,78	0,95	4,82
Green Schist	40,33	14,26	15,94	0,96	10,71	9,73	1,78	1,67	0,14	0,27	4,19

3.3. Uniaxial Compressive Strength Tests

Green schist and mica schist cores at 0°, 15°, 30°, 45°, 60°, 75° and 90° were obtained according to the method suggested by ISRM [7] with a ratio of 2-2,5 L/D (L: Length, D: Diameter). Experiments were carried out in dry and saturated conditions. 10 core samples were used for each orientation angle in experiments.

According to uniaxial compression test results (Figure 6); In terms of strength values in dry and saturated conditions, in general, minimum results were obtained between 30° and 60°, maximum 0° and 90° for mica schist, minimum between 15°-30° and maximum between 60°-75° for green schist. It has been observed that the mica schist unit is highly affected by water.

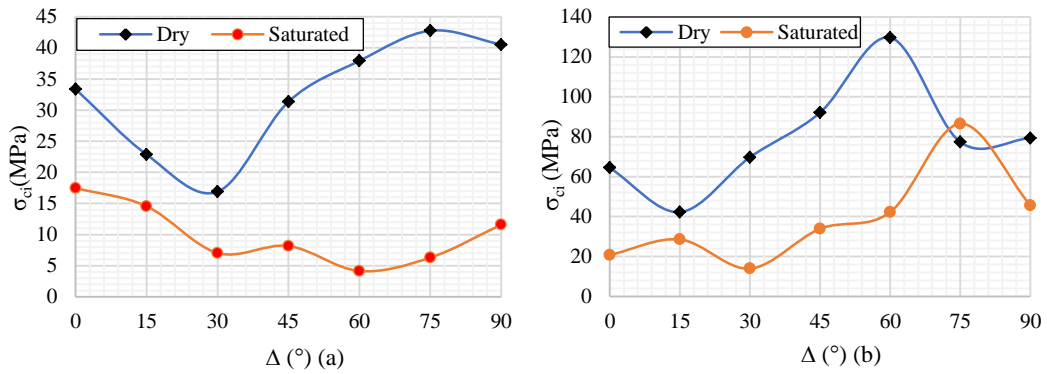


Figure 6. Dry and saturated uniaxial compressive strength values of mica schist (a) and green schist (b) (Δ (°)=Anisotropic angles) [16,17].

3.4. Ultrasonic Sound Velocity Experiments (P and S Waves)

Green schist and mica schist cores at 0°, 15°, 30°, 45°, 60°, 75° and 90° were obtained according to the method proposed by ISRM [7] with a ratio of 2-2,5 L/D (L: Length, D: Diameter). Experiments were carried out in dry and saturated conditions. 10 core samples were used for each orientation angle in experiments.

Within the scope of the study, the Proceq brand Pundit Lab+ device was used. Separate transducers were used for P and S waves. Apparatus with a frequency of 54 kHz for the P wave and 40 kHz for the S wave were used (Figure 7, 8).



Figure 7. P wave experiment set-up.

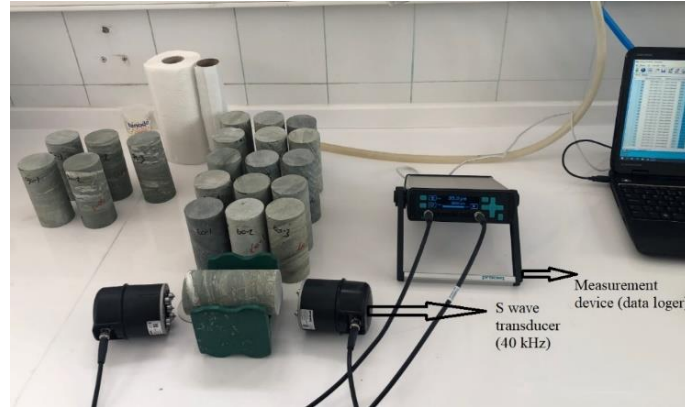


Figure 8. S wave experiment set-up.

Parameters in Table 3 are used to make measurements in P and S waves devices.

Table 3. P ve S wave parameters.

Parameters	P wave	S wave
Probe frequency	54 kHz	40 kHz
Pulse amplitude	auto (500 V)	500 V
Rx probe gain	auto (10x)	500 x
Calibration time	25,4 μ s	6,6 μ s

In order to find the dynamic modulus of elasticity and dynamic Poisson's ratios, the Equation proposed by ISRM [7] (Eq.1 and 2) were used;

$$\text{Dynamic Young modulus (Pa): } E_u = \rho V_s^2 \frac{(3V_p^2 - 4V_s^2)}{(V_p^2 - V_s^2)} \quad (1)$$

$$\text{Dynamic Poisson's ratio: } V_{dyn} = \frac{(V_p^2 - 2V_s^2)}{2(V_p^2 - V_s^2)} \quad (2)$$

where;

V_p : P wave velocity (m/s),

V_s : S wave velocity (m/s),

ρ : Rock density (kg/m^3).

The results obtained for green schist and mica schist are presented in Figures 9, 10, 11,12 and Table 4.

Table 4. P ve S wave speed results in dried and saturated conditioned for green schist and mica schist.

Rock Type	Degrees ($^{\circ}$)	Dried Conditioned P Wave Speed (m/sn)	Saturated Conditioned P Wave Speed (m/sn)	Dried Conditioned S Wave Speed (m/sn)	Saturated Conditioned S Wave Speed (m/sn)
	0	5788,67	5784,33	3820,00	3221,22
	15	6219,11	6137,67	4028,33	3370,78

Green Schist	30	4609,56	4335,44	3086,89	2330,11
	45	4856,56	4843,44	3369,22	2855,33
	60	4988,33	4875,56	2825,78	2520,78
	75	5106,33	4825,00	3424,00	3427,44
	90	5234,33	4972,67	3457,89	3440,22
Mica Schist	0	4338,11	4027,00	2662,11	2646,00
	15	3174,22	2850,00	2265,56	1770,00
	30	2654,78	1962,00	2217,11	1541,00
	45	1820,22	2304,00	1723,22	1500,00
	60	2764,22	2600,00	2528,00	2292,00
	75	3089,78	2710,00	2451,33	2020,00
90	2714,00	2558,00	2315,44	1559,00	

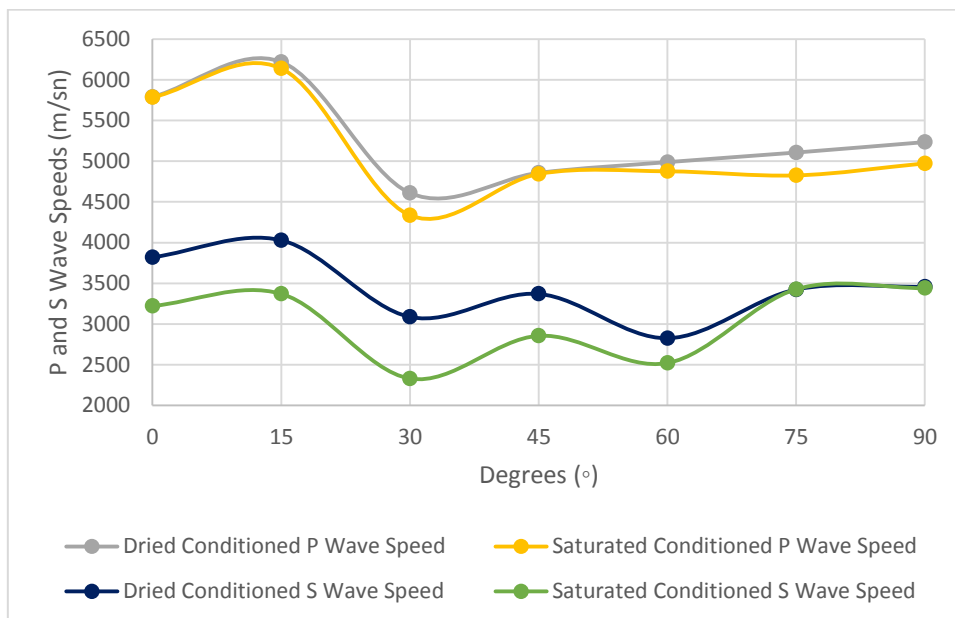


Figure 9. Green schist P and S waves values in dried and saturated conditions.

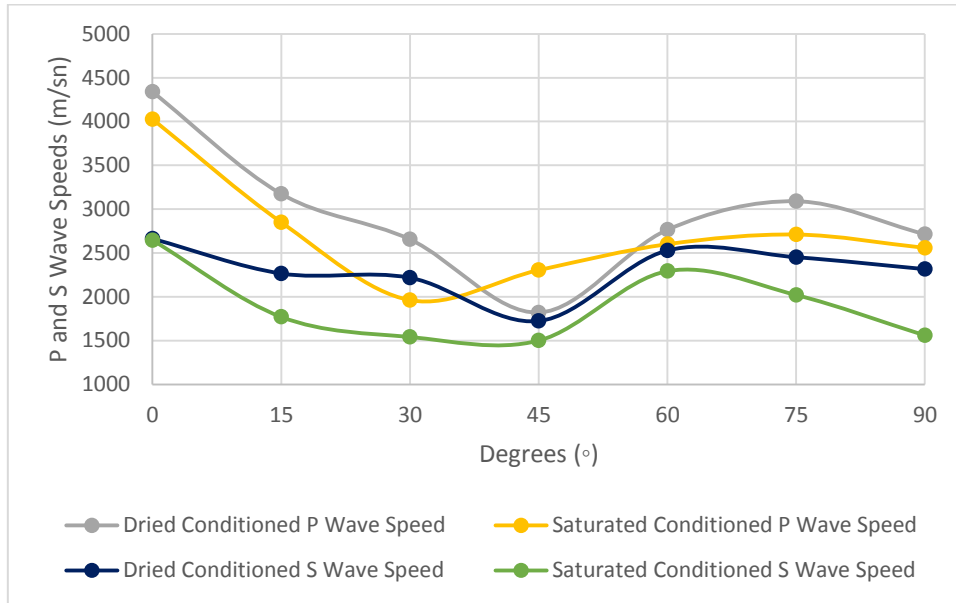


Figure 10. Mica schist P and S waves values in dried and saturated conditions.

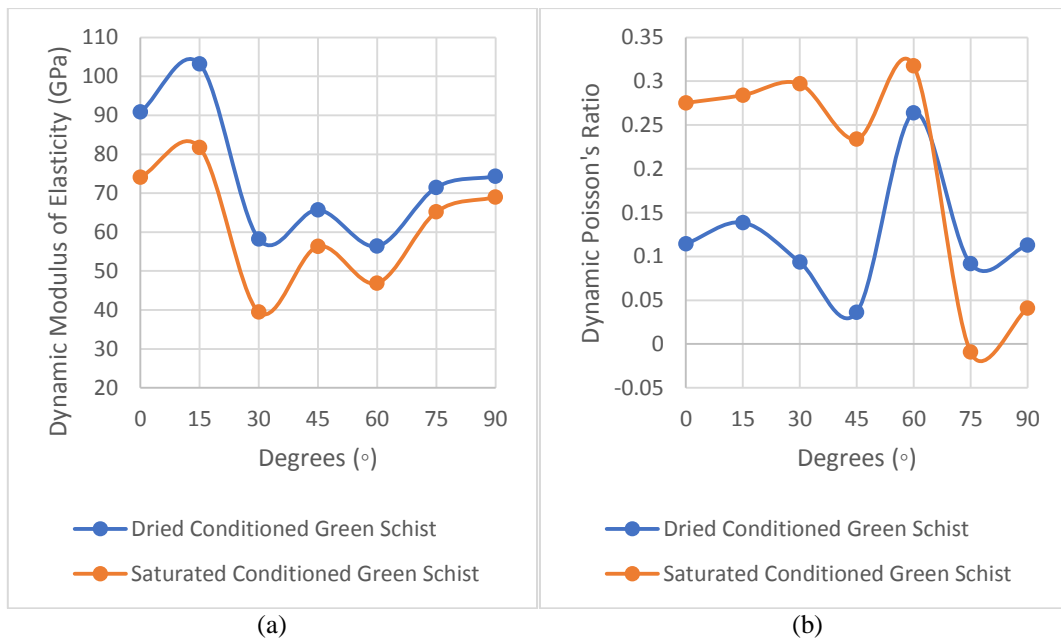


Figure 11. Green schist in dried and saturated conditions, dynamic modulus of elasticity (a) and dynamic Poisson's ratio (b) values.

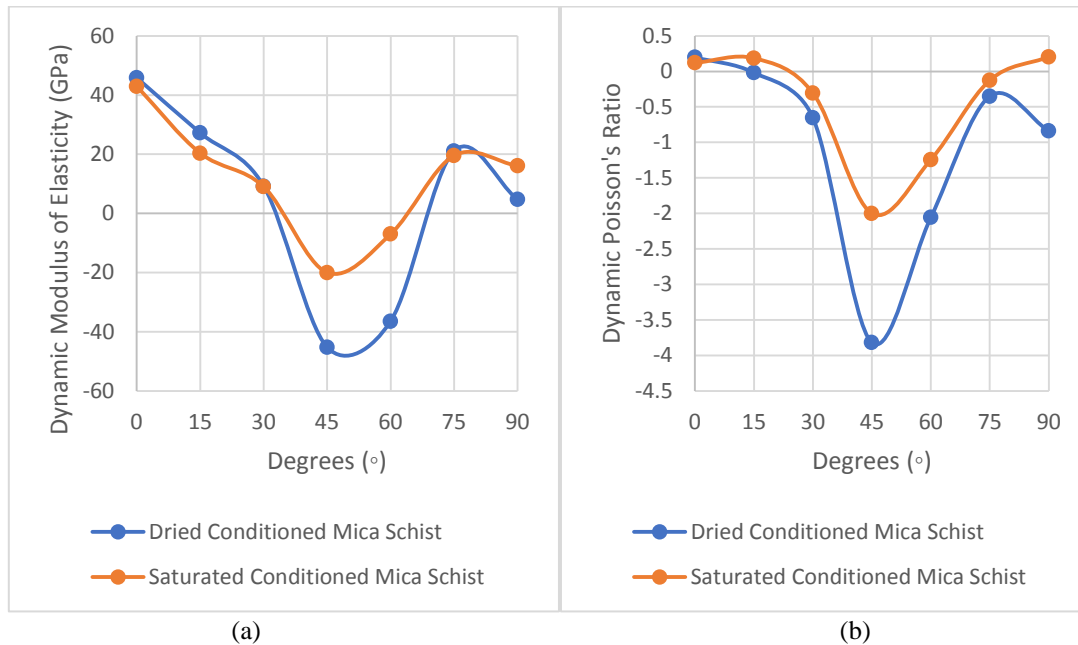


Figure 12. Mica schist in dried and saturated conditions, dynamic modulus of elasticity (a) and dynamic Poisson's ratio (b) values.

Based on the results of green schist and mica schist samples, P, S wave velocities and dynamic elasticity modulus values in dried and saturated conditions were generally minimum between 30°-60° and maximum results were obtained at 0°. Wave velocities in the saturated medium were lower than in the dried medium. Results close to the distribution of uniaxial compressive strength values based on degrees were obtained. For dynamic Poisson's ratios, values for green schist dried and saturated conditions were obtained at minimum 45° and 75° respectively, and maximum at 60° for both conditions. For mica schist, maximum at 0°, minimum between 45° and 60° results were obtained in both conditions.

4. CONCLUSIONS

Within the scope of this study, physical, mechanical tests, mineralogical and chemical analyzes and ultrasonic sound velocity tests were applied to the samples taken at 0°, 15°, 30°, 45°, 60°, 75° and 90° in dried and saturated conditions.

A certain distribution was observed in terms of wave velocities. The minimum values for both rocks were observed between 30° and 60° in dried and saturated conditions, and the maximum values were observed at 0°. The same distribution trend was found within the dynamic elasticity modulus. It is thought that this is due to the fact that bedding, voids and crack structures are encountered less frequently at 0° while providing wave propagation during the experiment, and that it cuts more into these structures between 30° and 60°. To reveal these structures more clearly, it is recommended to perform acoustic emission and computer tomography tests. In terms of wave propagation velocities, the values in the saturated medium were lower. Water had a negative effect on the results.

Uniaxial compressive strength values gave relatively close values to wave propagation velocities (P and S) and dynamic modulus of elasticity. In terms of dynamic Poisson's ratio values, the maximum values at 60° and 0° for green and mica schist respectively dried and saturated conditions. Minimum values were obtained between 45° and 75° for both rock types.

Mica schist rock gave negative results in dynamic modulus of elasticity and dynamic Poisson's ratio. This is due to the excess of the void and crack in the rock. Therefore, water affects this rock negatively. Also, there are negative results in dried conditioned for mica schist. It is thought that it would be beneficial to take precautions in terms of safety in engineering studies to be carried out in the mica schist rock.

The importance of investigating the distribution of strength and dynamic properties (Poisson's ratio and dynamic elasticity module) in rocks showing anisotropic structure is emphasized through this study. As a result, it is recommended to consider anisotropy in engineering projects to be carried out.

ACKNOWLEDGEMENT

Authors would like to thank to Kütahya Dumlupınar University for financial support to purchase the experiment device. Also, the authors are grateful to Res.Assist. Ahmet ÖZGÜR for support in experiments.

REFERENCES

- [1] Ramamurthy, T., Rao, G.V. and Singh, J., (1993), Engineering behaviour of phyllites Eng. Geol., 33, 209–225.
- [2] Saroglou, H. and Tsiambaos, G., (2007), Classification of anisotropic rocks 11th Congress of the International Society for Rock Mechanics (Lisbon, Portugal: ISRM), 191–196.
- [3] Saroglou, H. and Tsiambaos, G., (2008), A modified Hoek–Brown failure criterion for anisotropic intact rock, Int. J. Rock Mech. Min. Sci., 45, 223–234.
- [4] Zhang, X-P., Wong, L.N., Wang, S-J. and Han, G-Y., (2011), Engineering properties of quartz mica schist Eng. Geol., 121, 135–149.
- [5] Gao, Q., Tao, J., Hu, J. and Yu, X., (2015), Laboratory study on the mechanical behaviours of an anisotropic shale rock, J. Rock Mech. Geotech. Eng., 7, 213–219.
- [6] Corbett, D., (2016), Advances in ultrasonic testing - Research into the application of dry point contact transducers, 19th World Conference on Non-Destructive Testing 2016 Advances (Munich, Germany.), 1–7.
- [7] ISRM., (2007), The complete ISRM suggested methods for rock characterization, testing and monitoring., 1974-2006, ed R Ulusay and J A Hudson (Ankara: Kozan Ofset).
- [8] Wang, Y. and Li, C.H., (2017), Investigation of the P and S wave velocity anisotropy of a

- Longmaxi formation shale by real-time ultrasonic and mechanical experiments under uniaxial deformation ,J. Pet. Sci. Eng., 158, 253–267.
- [9] Ribacchi, R., Rotonda, T., Totaro, L. and Zaninetti, A., (1999), Evaluation of intrinsic and crack-induced elastic anisotropy in a gneissic rock, 9th ISRM Congress (Paris, France.), 661–666.
- [10] Khandelwal, M. and Singh, T. N., (2009), Correlating static properties of coal measures rocks with P-wave velocity, Int. J. Coal Geol., 79, 55–60.
- [11] Kim, H., Cho, J-W., Song, I. and Min, K-B., (2012), Anisotropy of elastic moduli, P-wave velocities, and thermal conductivities of Asan Gneiss, Boryeong Shale and Yeoncheon Schist in Korea, Eng. Geol., 147–148, 68–77.
- [12] Ali, E., Guang, W., Zhiming, Z. and Weixue, J., (2014), Assessments of strength anisotropy and deformation behaviour of banded amphibolite rocks, Geotech. Geol. Eng., 32, 429–438.
- [13] Huang, L., Liu, X., Yan, S., Xiong, J., He, H. and Xiao, P., (2020), Experimental study on the acoustic propagation and anisotropy of coal rocks, Petroleum.
- [14] Yıldız, H., Günay, K., Şahin, Ş., Niğdeli, S.F. and İçli, M.Y., (2014), Hanönü (Kastamonu) Copper Site (Ar: 201300022) mining geology report based on discovering request (Ankara).
- [15] Günay, K., Dönmez, C., Oyan, V., Yıldırım, N., Çiftçi, E., Yıldız, H. and Özkümüş, S., (2018), Geology and geochemistry of sediment-hosted Hanönü massive sulfide deposit (Kastamonu–Turkey), Ore Geol. Rev., 101, 652–674.
- [16] Özdemir, M., Beyhan, S. and Erarslan, K., (2020), Effect of anisotropic structure on strength in metamorphic rocks, ISRM International Symposium-EUROCK 2020, 1–10.
- [17] Özdemir, M., (2021), Slope stability analyzes in metamorphic rock masses with anisotropic behaviour, PhD Thesis, Kütahya Dumlupınar University, Institute of Graduate Programs, Kütahya, 154.



RESEARCH ARTICLE

STABILIZED FEM SOLUTION of MAGNETOHYDRODYNAMIC FLOW in DIFFERENT GEOMETRIES

Harun SELVİTOPI*

*Erzurum Technical University, Faculty of Science, Department of Mathematics, harun.selvitopi@erzurum.edu.tr,
ORCID:0000-0001-5958-7625

Receive Date:14.04.2022

Accepted Date: 16.06.2022

ABSTRACT

In this study, the stable numerical solution of the magnetohydrodynamic (MHD) flow in different geometries is presented using the stabilized finite element method (FEM). Numerical solution of coupled convection-diffusion type MHD equations have been acquired for the different Hartmann numbers (M_i) and different angles of the MHD flows. The resultant matrix-vector system has been solved as a whole with the reciprocal MHD flow and boundary conditions. We have observed from the solution of reciprocal MHD flow when the Hartmann number increases the velocity and the induced magnetic field of the flows decrease. We have been acquired the stable numerical solution for the $M_i = 10^2$ Hartmann number. The obtained stable numerical results are displayed by graphics.

Keywords: *Magnetohydrodynamic, Stabilized-FEM, Different Geometries*

1. INTRODUCTION

Magnetohydrodynamic flow is popular among researchers, due to the fluid is under the influence of the magnetic field, such that engineers, medical scientists, etc. Therefore there is a wide range of theoretical, experimental like in [1–3] and numerical studies about MHD flow. Because of the coupled nature of the problem the theoretical results can obtain special cases of the problem. Therefore the numerical methods have been used to obtain the numerical solution of MHD equations. The finite element solution of fully developed MHD flow in channels has been obtained by Singh and Lal in [4] for the steady-state form of the problem in the different geometries. The boundary element method (BEM) solution of MHD flow problems for the high values of Hartmann number has been obtained in [5]. In [6], numerical solution of the MHD flow problems is obtained using the dual reciprocity boundary element method (drbem) with the external electrically conducting medium. Aydın and Selvitopi [7] have been solved the MHD flow problems in an unbounded conducting medium using stabilized FEM in the pipe and BEM for the exterior region considering rectangular and circular pipe with the different angle of the induced magnetic field and high values of Reynolds number, magnetic pressure and magnetic Reynolds numbers. The BEM solution of magnetohydrodynamic channel flows has been obtained in [8] for the high Hartmann numbers. The numerical methods, FEM, finite difference method (FDM), BEM and meshless methods, etc., have been applied to obtain the

numerical solution of MHD flow problems in different geometries i.e. rectangular and circular duct case until this time.

In general, it has been considered in the studies that there is only one MHD flow in the pipe up to now. In this study, we have considered two MHD flow in the T-junction. Therefore, this study has two important novelty according to literature, the first one is the geometry of the pipe and the other is it has two MHD flow equations in junction. Tezer-Sezgin and Aydın [9] have obtained the numerical solution of the MHD flow in one, two and three parallel ducts which are separated by conducting walls and there is only one MHD flow in the all ducts using stabilized-FEM for the high Hartmann numbers. There are many studies in the literature about fluid flow in T-junction. The flow is organized in T-junction as division or the combination of a fluid flow. Vimmr and Jon'a'sov'a [10] have considered the coronary and femoral bypasses model and they solved the non-newtonian blood flow using finite volume method with the fourth order Runge-Kutta algorithm. In [11] the numerical modeling and Piv measurement comparison were presented for the division and the combined fluid flow in T-junction with two inlets and only one outlet. Moshkin and Yambangwai [12] have solved the pressure-driven startup laminar flows in T-junction using the finite volume method. Beneš, et al. [13] have been obtained the numerical simulation of the laminar and turbulent flows of Newtonian and non-Newtonian fluids in T-junction with one inlet and two outlets that the mathematical model of the flows is Reynolds averaged Navier-Stokes equations using finite volume method with the artificial compressibility method. Matos and Oliveria [14] have presented the numerical solution of the steady and unsteady non-Newtonian inelastic flows using the finite volume method in a planar T-junction for the high values of Reynolds numbers. The volume of the fluid solution of the ferrofluid microdroplets in T-junction with an asymmetric magnetic field has been given in [15]. In [16] the numerical solution of the Newtonian, incompressible and thermostatic flow in T-junction has been investigated using the volume of fluid method. The application of the FEM for the linear and non-linear physical problems is presented in [17,19].

In the present study, we have obtained the stable numerical solution of the MHD flow in a T-junction using streamline upwind Petrov–Galerkin (SUPG) type stabilized FEM for the different values of Hartmann number.

The paper is introduced as follows. In Section 2 physical problem and the mathematical model of the problem are given. The stabilized finite element formulation of the considered problem is presented in Section 3. The obtained numerical results using stabilized FEM are given and discussed in Section 4. The conclusion is given in the last section.

2. MATERIAL AND METHOD

2.1. Physical Problem And Mathematical Model

The steady, reciprocal MHD flow has been considered in a T-junction. In the T-junction, there are two different flows under the influence of the magnetic field with different angle. The length of the channel has been assumed enough long and the problem dimension is reduced to two-dimension.

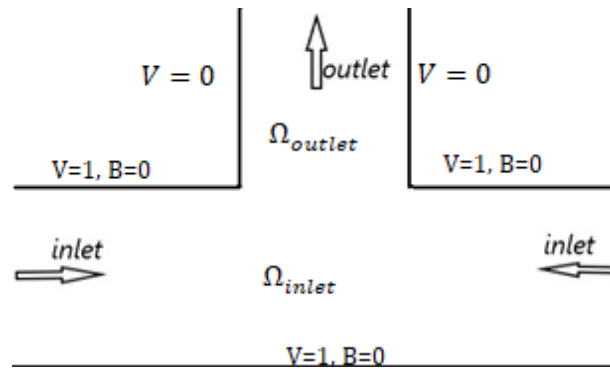


Figure 1. Problem domain.

The mathematical model of the considered problem is obtained by Navier-Stokes and Maxwell equations:

$$\begin{aligned} \nabla^2 V_i + \overline{M_{x_i}} \frac{\partial B_i}{\partial x} + \overline{M_{y_i}} \frac{\partial B_i}{\partial y} &= \Delta P_i \\ \nabla^2 B_i + \overline{M_{x_i}} \frac{\partial V_i}{\partial x} + \overline{M_{y_i}} \frac{\partial V_i}{\partial y} &= 0 \end{aligned} \quad i=1,2 \quad (1)$$

where $\overline{M_{x_i}} = M_i \sin \theta_i$, $\overline{M_{y_i}} = M_i \cos \theta_i$, $\Delta P_1 = -1$ and $\Delta P_2 = 1$. M_i is the nondimensional parameter (Hartmann Numbers), describing $M_i = B_0 L_0 \sqrt{\sigma} / \sqrt{\mu}$. Here θ_i is the angle between applied magnetic field and y -axis and L_0 , σ , μ are the characteristic length, electrical conductivity and viscosity of the fluid respectively. In the solution domain we have been considered the boundary condition as:

$$\begin{aligned} V=0, B=1 \text{ in } \Omega_{inlet} \\ \frac{\partial V}{\partial n} = 0 \text{ in } \Omega_{outlet} \end{aligned} \quad (2)$$

2.2. Stabilized Fem Formulation

Applying the standard finite element method to the coupled equations in (1), we get weak formulation using linear function space $L = (H_0^1(\Omega))^2$ as: Find $\{V_i, B_i\} \in \{L \times L\}$ such that

$$B(V_i; B_i, w_1; w_2) = (-\Delta P_i, w_1), \quad \forall \{w_1; w_2\} \in \{L \times L\} \quad (3)$$

where

$$\begin{aligned} B(V_i; B_i, w_1; w_2) = & (\nabla V_i, \nabla w_1) - \left(\overline{M_x} \frac{\partial B_i}{\partial x}, w_1 \right) - \left(\overline{M_y} \frac{\partial B_i}{\partial y}, w_1 \right) + (\nabla B_i, \nabla w_2) - \left(\overline{M_x} \frac{\partial V_i}{\partial x}, w_2 \right) - \\ & \left(\overline{M_y} \frac{\partial V_i}{\partial y}, w_2 \right) \end{aligned}$$

Then, the variational formulation is written by the choice of finite dimensional subspaces $L_h \subset L$, defined by triangulation of the domain. Specifying a finite element discretisation, the weak formulation becomes: Find $\{V_{i_h}; B_{i_h}\} \in \{L_h \times L_h\}$ such that

$$B(V_{i_h}; B_{i_h}, w_{1_h}; w_{2_h}) = (-\Delta P_{i_h}, w_{1_h}), \quad \forall \{w_{1_h}; w_{2_h}\} \in \{L_h \times L_h\}. \quad (4)$$

We have been decoupled the equations in (1), using the transformations $U_i = V_i + B_i$ and $Z_i = V_i - B_i$ to be able to apply the SUPG type stabilized FEM technique. Using the transformations $U_i = V_i + B_i$ and $Z_i = V_i - B_i$, we obtain the decoupled convection-diffusion type equations as:

$$\begin{aligned} \nabla^2 U_i + \overline{M}_x \frac{\partial U_i}{\partial x} + \overline{M}_y \frac{\partial U_i}{\partial y} &= \Delta P_i \\ \nabla^2 Z_i - \overline{M}_x \frac{\partial Z_i}{\partial x} - \overline{M}_y \frac{\partial Z_i}{\partial y} &= \Delta P_i \end{aligned} \quad i=1,2 \quad (5)$$

We have been considered the SUPG type stabilization technique to obtain the smooth behaviour of the induced magnetic field and the velocity for the large values of Ha which contained in the convection-dominated convection-diffusion type equations in (4). That is; find $\{U_{i_h}, Z_{i_h}\} \in \{L_h \times L_h\}$ such that

$$\begin{aligned} &(\nabla U_{i_h}, \nabla v_{1_h}) - \left(\overline{M}_x \frac{\partial U_{i_h}}{\partial x}, v_{1_h}\right) - \left(\overline{M}_y \frac{\partial U_{i_h}}{\partial y}, v_{1_h}\right) + \\ &(\nabla Z_{i_h}, \nabla v_{2_h}) + \left(\overline{M}_x \frac{\partial Z_{i_h}}{\partial x}, v_{2_h}\right) + \left(\overline{M}_y \frac{\partial Z_{i_h}}{\partial y}, v_{2_h}\right) \\ &+ \tau_K \left\{ \left(-\overline{M}_x \frac{\partial U_{i_h}}{\partial x} - \overline{M}_y \frac{\partial U_{i_h}}{\partial y} + \Delta P_{i_h}, -\overline{M}_x \frac{\partial v_{1_h}}{\partial x} - \overline{M}_y \frac{\partial v_{1_h}}{\partial y} \right) \right. \\ &+ \left. \left(\overline{M}_x \frac{\partial Z_{i_h}}{\partial x} + \overline{M}_y \frac{\partial Z_{i_h}}{\partial y} + \Delta P_{i_h}, \overline{M}_x \frac{\partial v_{2_h}}{\partial x} + \overline{M}_y \frac{\partial v_{2_h}}{\partial y} \right) \right\} \\ &= (-\Delta P_{i_h}, v_{1_h}) + (-\Delta P_{i_h}, v_{2_h}) \end{aligned} \quad (6)$$

$\forall \{v_{1_h}, v_{2_h}\} \in \{L_h \times L_h\}$, $v_{1_h} = w_{1_h} + w_{2_h}$, $v_{2_h} = w_{1_h} - w_{2_h}$ with the stabilization parameter [20]

$$\tau_K = \begin{cases} \frac{h_K}{2Ha} & \text{if } Pe_K \geq 1 \\ \frac{h_K^2}{12} & \text{if } Pe_K < 1 \end{cases} \quad (7)$$

Here, h_K is the diameter of the element K and $Pe_K = h_K \frac{Ha}{\epsilon}$ is the Peclet number.

Eventually, using the inverse transformations $V_i = (U_i + Z_i)/2$ and $Z_i = (U_i - Z_i)/2$ one can get the final system of the stabilized FEM discrete formulation for the induced magnetic field and the velocity:

$$\begin{aligned}
 & (\nabla V_{i_h}, \nabla w_{1_h}) - \left(\overline{M_x} \frac{\partial B_{i_h}}{\partial x}, w_{1_h} \right) - \left(\overline{M_y} \frac{\partial B_{i_h}}{\partial y}, w_{1_h} \right) + (\nabla B_{i_h}, \nabla w_{2_h}) - \left(\overline{M_x} \frac{\partial V_{i_h}}{\partial x}, w_{2_h} \right) \\
 & - \left(\overline{M_y} \frac{\partial V_{i_h}}{\partial y}, w_{2_h} \right) + \tau_K \left(\overline{M_x} \frac{\partial V_{i_h}}{\partial x} + \overline{M_y} \frac{\partial V_{i_h}}{\partial y}, \overline{M_x} \frac{\partial w_{1_h}}{\partial x} + \overline{M_y} \frac{\partial w_{1_h}}{\partial y} \right) \\
 & + \tau_K \left(\overline{M_x} \frac{\partial B_{i_h}}{\partial x} + \overline{M_y} \frac{\partial B_{i_h}}{\partial y}, \overline{M_x} \frac{\partial w_{2_h}}{\partial x} + \overline{M_y} \frac{\partial w_{2_h}}{\partial y} \right) \\
 & = (-\Delta P_{i_h}, w_{1_h}) + \tau_K \left(\Delta P_{i_h}, \overline{M_x} \frac{\partial w_{2_h}}{\partial x} + \overline{M_y} \frac{\partial w_{2_h}}{\partial y} \right)
 \end{aligned} \tag{8}$$

$\forall \{w_1, w_2\} \in \{L_h \times L_h\}$. Then, the solution of the system (8) has been given the induced currents and the velocity of the fluid.

3. NUMERICAL RESULTS

In this section, we have given the stabilized FEM solution of MHD equations (1) in a T-Junction for the different Hartmann numbers and different angles. We have been considered the $Ha = 1, 10$ and 100 . The angles between MHD flow and y -axis $\theta_{1,2} = \pi/4$ and $\pi/2$.

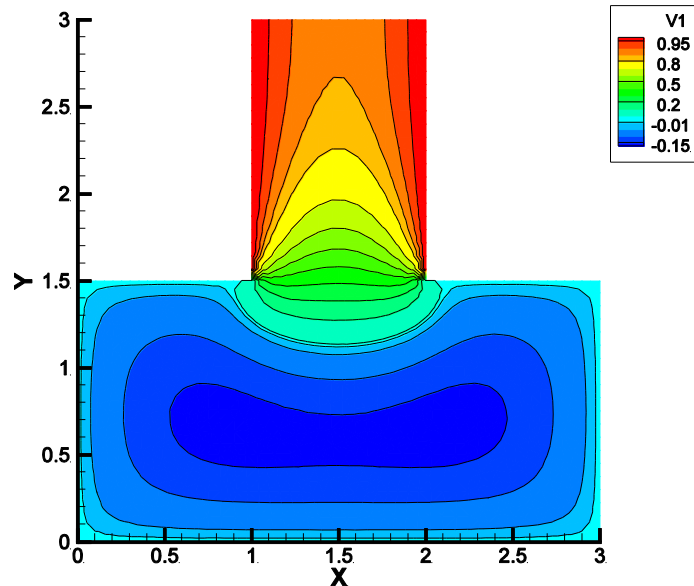


Figure 1. Velocity for $M_1 = 1$ and $\theta_1 = \pi/2$.

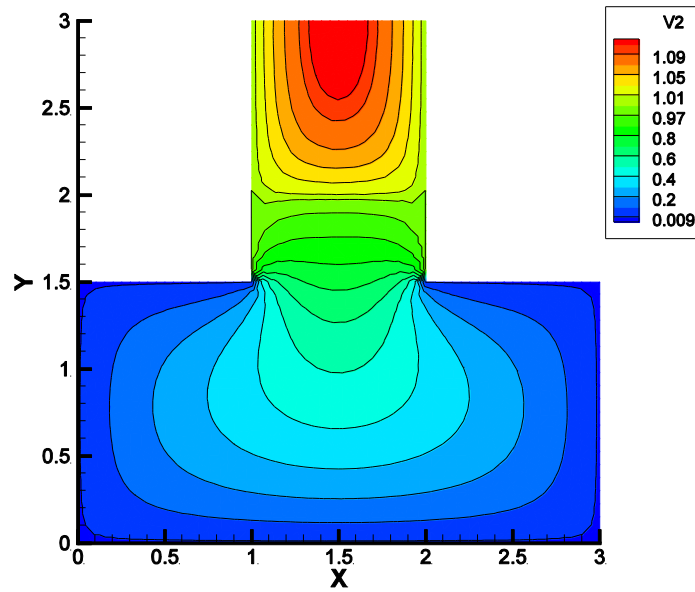


Figure. 2. Velocity for $M_2 = 1$ and $\theta_2 = \pi/2$.

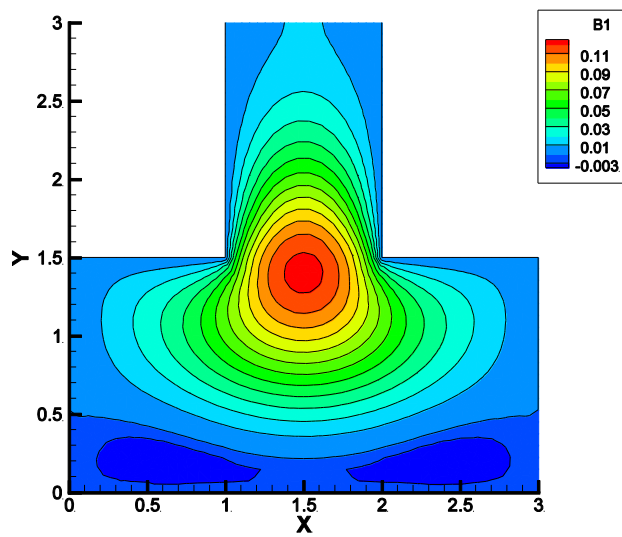


Figure. 3. Magnetic induction for $M_1 = 1$ and $\theta_1 = \pi/2$.

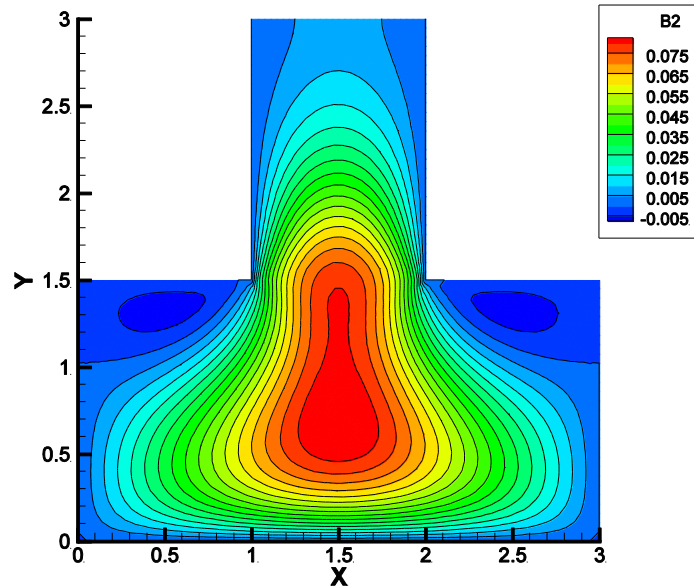


Figure. 4. Magnetic induction for $M_2 = 1$ and $\theta_2 = \pi/2$.

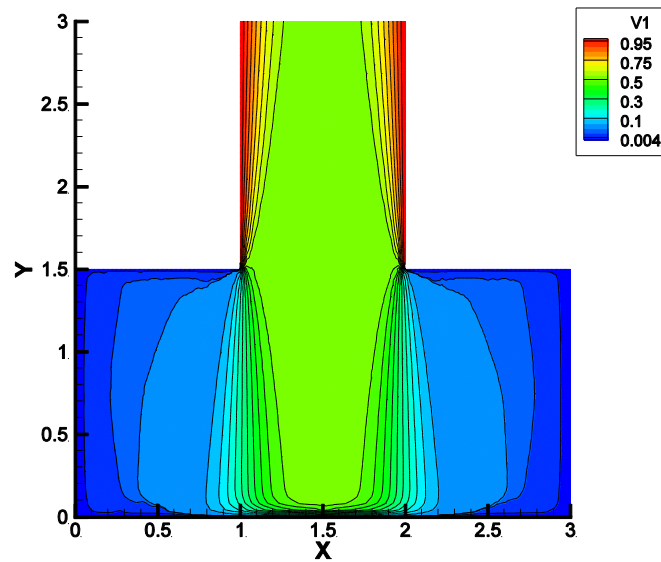


Figure. 5. Velocity for $M_1 = 100$ and $\theta_1 = \pi/2$.

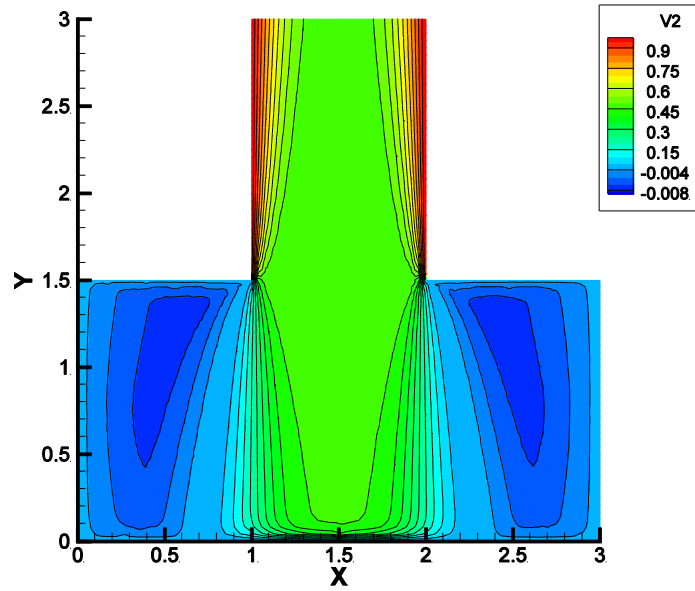


Figure. 6. Velocity for $M_2 = 100$ and $\theta_2 = \pi/2$.

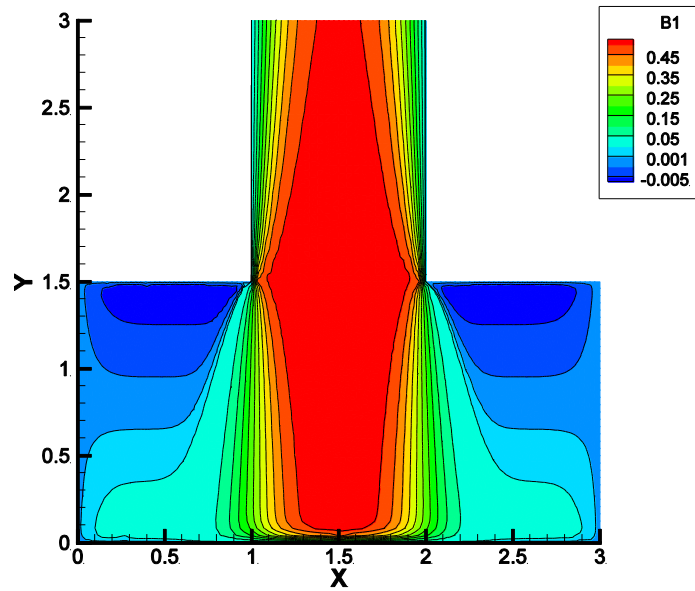


Figure. 7. Magnetic induction for $M_1 = 100$ and $\theta_1 = \pi/2$.

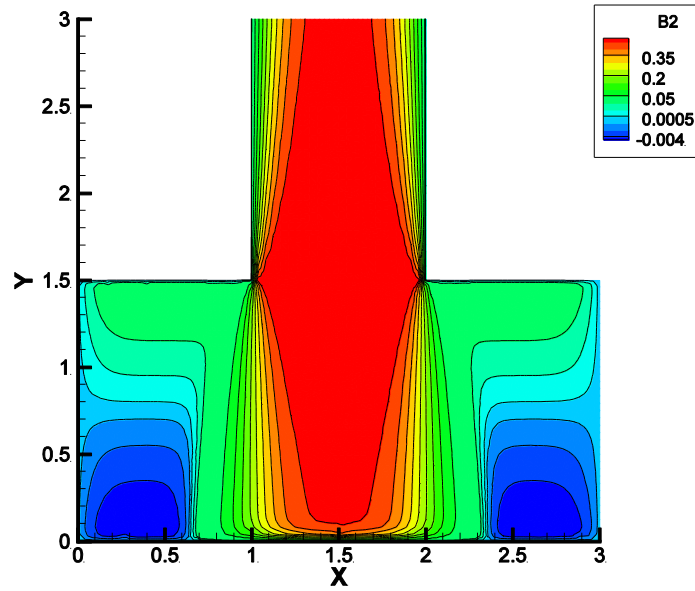


Figure. 8. Magnetic induction for $M_2 = 100$ and $\theta_2 = \pi/2$.

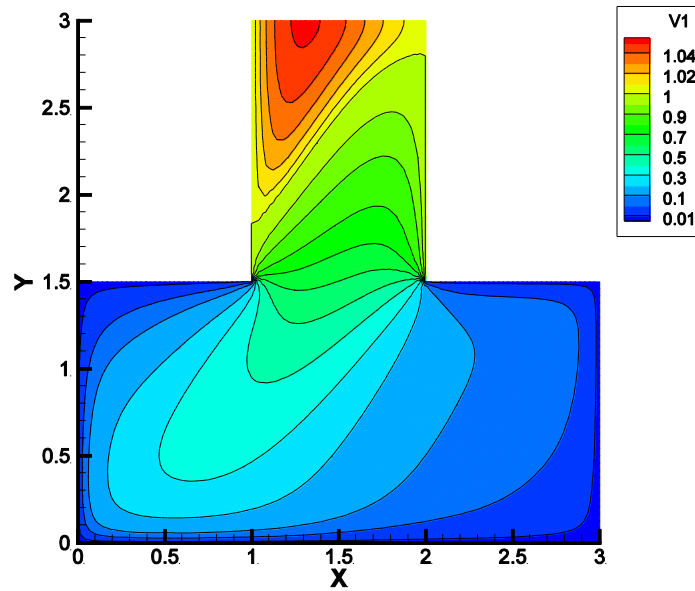


Figure. 9. Velocity for $M_1 = 10$ and $\theta_1 = \pi/4$.

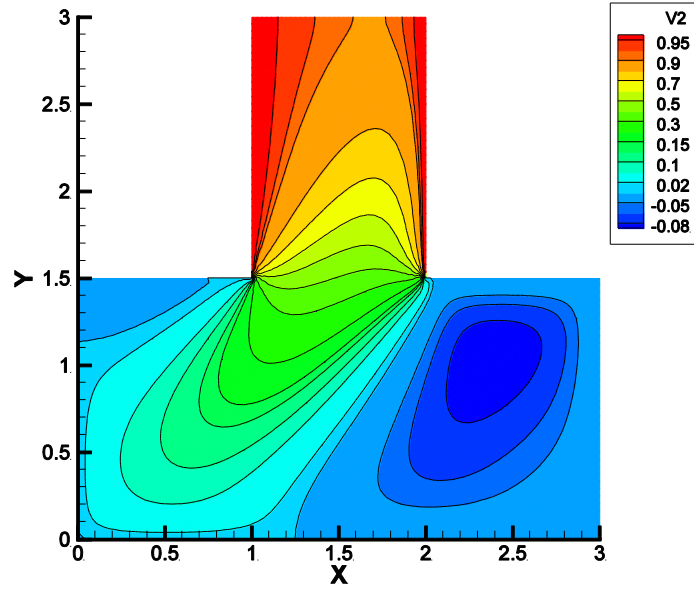


Figure. 10. Velocity for $M_2 = 10$ and $\theta_2 = \pi/4$.

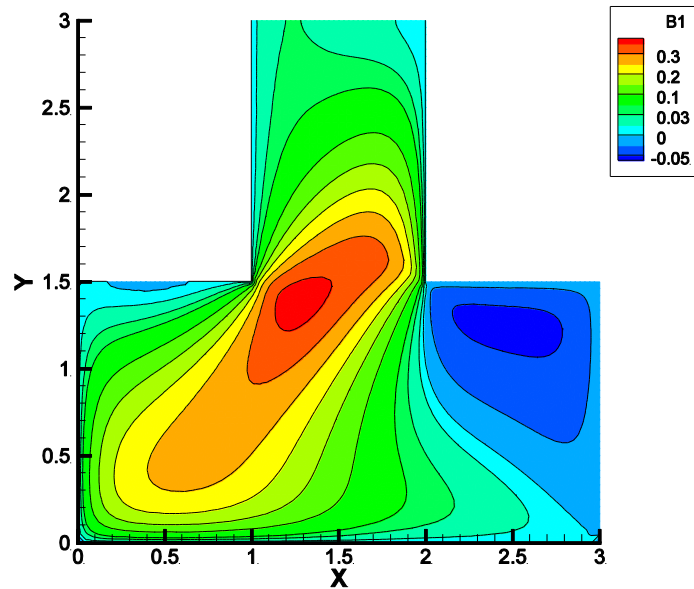


Figure. 11. Magnetic induction for $M_1 = 10$ and $\theta_1 = \pi/4$.

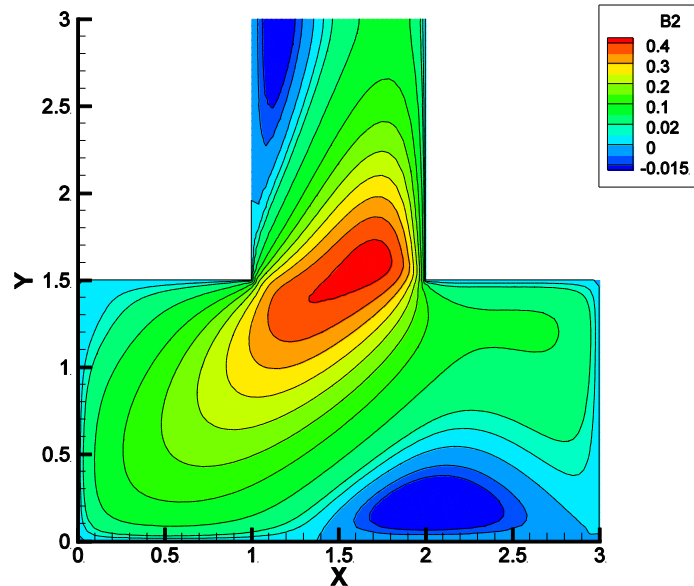


Figure. 12. Magnetic induction for $M_2 = 10$ and $\theta_2 = \pi/4$.

4. DISCUSSION AND CONCLUSION

The stabilized FEM solution of the MHD equations has been acquired for different Hartman numbers and different angles between induced magnetic fields and the y -axis in a T-Junction. In **Fig. 1,2,5,6,9** and **10**, one can observe the velocity contour of the fluid and in **Fig. 3,4,7,8,11** and **12** one can observe the contour of the magnetic induction.

We have been considered the angles $\theta_1 = \theta_2 = \pi/2$ with $M_1 = M_2 = 1$ and 100 for **Fig. 1.** to **Fig. 8.** and we have also been considered the angles $\theta_1 = \theta_2 = \pi/4$ with $M_1 = M_2 = 10$ for **Fig. 9.** to **Fig. 12.** We can see from the figures that the layers occur with changing of the angles. We can observe from **Fig. 3,4,7,8** the boundary layer in the inlet walls occurs for the magnetic induction when the Hartmann numbers increases. We can also observe from **Fig. 1,2,5,6** the flow approaches the walls for the large number of the Hartmann numbers.

One can also say that, the velocity of the first flow is dominant in the inlet and the velocity of the second flow is dominant in the outlet of the channels. The induced magnetic field is dominant in the all domain for the $\theta_1 = \theta_2 = \pi/2$.

As a result, in this work we have focused on the investigation of the MHD flow in different geometries numerically using SUPG type stabilized FEM. We have determined the dominant velocity and induced magnetic field of the flows according to the different values of Hartmann numbers and different angles.

ACKNOWLEDGMENT

The author thanks the reviewers for their valuable contributions and suggestions to improve the paper. In the revised version, all the reviewers' comments were taken into consideration, resulting in a substantial improvement with respect to the original submission.

REFERENCES

- [1] Jang, J., Lee, S.S., (2000), Theoretical and experimental study of MHD (magnetohydrodynamic) micropump, *Sens. Actua. A: Phys.*, 80(1), 84-89.
- [2] Kandev, N., Kagan, V., Daoud A., (2010), Electromagnetic DC pump of liquid aluminium: computer simulation and experimental study, *FDMP-Fluid Dynamics & Materials Processing*, 6(3), 291-318.
- [3] Bluck, M., Wolfendale, M., (2015), An analytical solution to electromagnetically coupled duct flow in MHD, *Journal of Fluid Mechanics*, 771, 595-623.
- [4] Singh, B., Lal, J., (1982), Finite element method in MHD channel flow problems, *International Journal for Numerical Methods in Engineering* 18, 1104-1111.
- [5] Tezer-Sezgin, M., Aydın, S.H., (2006), Solution of magnetohydrodynamic flow problems using the boundary element method, *Engineering Analysis with Boundary Elements Method*, 30, 411-418.
- [6] Aydın, S.H., Tezer-Sezgin, M., (2014), A DRBEM Solution for MHD Pipe Flow in a Conducting Medium, *Journal Computational and Applied Mathematics*, 259, 720-729.
- [7] Aydın, S.H., Selvitopi, H., 2018. Stabilized FEM–BEM coupled solution of MHD pipe flow in an unbounded conducting medium, *Engineering Analysis with Boundary Elements Method*, 87, 122-132.
- [8] Sedathatjoo, Z., Dehghan, M., Hoseinzadeh, H., (2018), A stable boundary elements method for magnetohydrodynamic channel flows at high Hartmann numbers, *Numerical Methods for Partial Differential Equations*, 34, 75-601.
- [9] Tezer-Sezgin, M., Aydın, S.H., (2020), FEM solution of MHD flow in an array of electromagnetically coupled rectangular ducts, *Progress in Computational Fluid Dynamics, an International Journal*, 20(1), 40-50.
- [10] Vimmr, J., Jonasova, A., (2010), Non-Newtonian Effects of Blood Flow in Complete Coronary and Femoral Bypasses, *Mathematics and Computers in Simulation*, 80, 1324-1336.

- [11] Stigler, J., Klas, R., Kotek, M., Kopecky, V., (2012), The Fluid Flow in the T-Junction, The Comparison of the Numerical Modeling and Piv Measurement. *Procedia Engineering*, 29, 19–27.
- [12] Moshkin, N.P., Yambangwai, D., (2012), Numerical Simulation of Pressure-Driven Startup Laminar Flows Through a Planar T-Junction Channel, *Communications in Nonlinear Science and Numerical Simulations*, 17, 1241-1250.
- [13] Benes, L., Louda, P., Karel, K., Keslerova, R., Stigler, J., (2013), Numerical Simulations of Flow Through Channels with T-Junction, *Applied Mathematics Computation*, 219, 7225-7235.
- [14] Matos, H.M., Oliveria, P.J., (2013), Steady and Unsteady Non-Newtonian Inelastic Flows in a Planar T-Junction, *International Journal of Heat and Fluid Flow*, 39, 102-126.
- [15] Aboutalebi, M., Bijarchi, M.A., Shafii, M.B., Hannani, S.K., (2018), Numerical Investigation on Splitting of Ferrofluid Microdroplets in T-Junctions Using an Asymmetric Magnetic Field with Proposed Correlation, *Journal of Magnetism and Magnetic Materials*, 447, 139-149.
- [16] Li, X., He, L., He, Y., Gu, H., Liu, M., (2019), Numerical Study of Droplet Formation in the Ordinary and Modified T-Junction, *Physics of Fluid*, 31, 082101.
- [17] Selvitopi, H., Yazıcı, M., (2019), Numerical results for the Klein-Gordon equation in de Sitter spacetime, *Mathematical Methods in the Applied Sciences*, 42(16), 5446-5454.
- [18] Selvitopi, H., (2022), Finite difference/Finite element simulation of the two-dimensional linear and nonlinear Higgs boson equation in the de Sitter space-time, *Engineering with Computers*, 38, 891-900.
- [19] Selvitopi, H., Zaky, M., Hendy, AS., (2021), Crank-Nicolson/finite element approximation for the Schrödinger equation in the de Sitter spacetime, *Physica Scripta*, 96, 124010.
- [20] Brooks, A.N., Hughes, T.J.R., (1982), Streamline upwind/Petrov-Galerkin formulations for convection dominated flows with particular emphasis on the incompressible Navier-Stokes equations, *Computer Methods in Applied Mechanics and Engineering*, Vol. 32, 199–259.



RESEARCH ARTICLE

FACIAL EXPRESSION RECOGNITION on PARTIAL FACE IMAGES USING DEEP TRANSFER LEARNING

İsmail ÖZTEL^{1*}, Gözde YOLCU ÖZTEL², Veysel Harun ŞAHİN³

^{1*}Sakarya University, Faculty of Computer and Information Sciences, Department of Computer Engineering, ioztel@sakarya.edu.tr, ORCID: 0000-0001-5157-7035

²Sakarya University, Faculty of Computer and Information Sciences, Department of Software Engineering, gyolcu@sakarya.edu.tr, ORCID: 0000-0002-7841-2131

³Sakarya University, Faculty of Computer and Information Sciences, Department of Software Engineering, vsahin@sakarya.edu.tr, ORCID: 0000-0002-3381-1702

Receive Date: 17.04.2022

Accepted Date: 11.06.2022

ABSTRACT

Facial expression recognition has a crucial role in communication. Computerized facial expression recognition systems have been developed for many purposes. People's faces can have occlusions because of scarves, facial masks, etc. in cases such as cold weather conditions or Covid-19 pandemic conditions. In this case, facial expression recognition can be challenging for automated systems. This study classifies facial images containing only the eyebrow and eye regions over six expressions with a deep learning-based approach. For this purpose, Radboud Face Database images have been used after cropping the area that includes eye and eyebrow regions. Some popular pre-trained networks have been trained and tested using the transfer learning approach. The Vgg19 pre-trained network achieved 91.33% accuracy over the six universal facial expressions. The experiments show that automated facial expression recognition can be applied with high performance by looking at the region containing eyes and eyebrows.

Keywords: *Convolutional Neural Networks, Deep Learning, Facial Expression Recognition, Transfer Learning*

1. INTRODUCTION

Facial expressions are produced by different contraction and relaxation of facial muscles. Human facial expressions are important for social communications. According to [1], in face-to-face communication, 7% of the message is transmitted by words, 38% by tone of voice, and 55% by body language. Facial expressions are also a type of body language.

Owing to technological developments, cameras became a part of our daily lives. Thus, facial expressions have been started to use in many fields. Facial expressions are essential for decision-making systems like criminal detection, patient follow-up, and driver attention monitoring. Although facial expressions are detected by the human brain effortlessly, it is pretty hard to detect for a machine. Particularly, a person's image with the same facial expression can show differences in the analysis due to brightness, background, etc. [2]. Also, there may be occlusions on human faces

because of some type of cloth like scarves, face masks, etc. Therefore, with the advances in computer vision, detecting facial expressions in a computerized manner has become a popular topic.

Detecting facial expressions using automated systems is one of the important topics of computer vision. Some areas that use automated facial expression recognition (FER) are avatar animation [3], medical applications [4], robotics [5], traffic [6][7], smart environments [8], human-computer interaction [9][10]. There are six universal facial expressions: anger, disgust, fear, happiness, sadness, and surprise. These expressions were identified by Ekman and Friesen [11]. The FER studies in the literature are generally based on these six expressions.

Recently, because of Covid-19 pandemic, people have used face masks. According to WHO reports, using a medical face mask can decrease the spread of disease. Currently, using medical face mask is mandatory in many countries. Face masks create facial occlusion on the human face. Thus, recognition of these people's facial expressions with mask becomes very hard.

The main motivation of the study is detecting the facial expressions for occlusion situations such as wearing a scarf or face mask. In this paper, a deep transfer learning-based FER system that works on partial face images is presented. The system detects facial expressions using just the top part of the face. In the context of the study, firstly, the face images have been prepared to include just the upper part of the face using the pre-processing methods. Then the system has been trained with different pretrained convolutional neural networks (CNN). During this stage, each network used the top part of the face as input and produced prediction label of the facial expression. The main contributions of this paper can be summarized as follows.

(1) The proposed approach uses just the top part of the face for FER. Therefore, it is robust to bottom face occlusions and motion.

(2) Using a large input image size in the input layer in the deep learning systems requires large memory and increases training and testing time. As the proposed approach uses the top part of the face image it requires a small input image size. Therefore, these disadvantages have been prevented.

In the literature, automated FER studies are examined in three main methods [12], [13]. These are geometric-based, appearance-based, and action unit (AU)-based approaches.

In the geometric-based analysis, face shape is examined. For example, in [14] the facial expressions were classified using the distances and angles between facial components using facial landmarks.

Appearance-based approaches examine features of the facial texture. For example, Saurav et al. [15] introduced several techniques that make use of dynamic local ternary patterns. In their work they applied kernel extreme learning machine classifier. Iqbal et al. [16] proposed neighborhood-aware edge directional pattern which is a local descriptor. Dagher et al. [17] presented a three-stage support vector machine (SVM) for FER. Ali et al. [18] proposed a new method that uses Rectangular HOG feature extractor with Label-Consistent KSVD classifier.

In AU-based approach, the facial muscles movements are identified using a system. This system is called the Facial Action Coding System (FACS) [19]. Morales-Vargas et al. [20] introduced a model

that recognizes facial expressions in terms of facial movements with the help of appearance features. They get help from the fuzzy models.

Also, Deep Learning approaches have shown outstanding performance in automated facial expression studies recently. For example, Jin et al. [21] introduced a small and effective deep network for FER named MiniExpNet. Their method is based on local facial regions. Fan et al. [22] introduced a new CNN namely hierarchical scale convolutional neural network (HSNet). Their approach enhances the information extracted from the network, kernel, and knowledge scale. Saurav et al. [23] presented CNNV3 approach. They used the approach in an intelligent embedded system that is developed to help visually impaired people. The system is a vision-based and deep-learning inspired system that performs haptic rendering of facial emotions. Happy et al. [24] introduced multi-face multi-part model. Their model makes use the information from part-based data augmentation. The facial parts which they used for training were obtained from different face samples of the same expression class. Jin et al. [25] proposed a discriminative deep association learning framework. In [26], Happy et al. proposed a weakly supervised learning approach. In their approach, they first train CNN with label smoothing. They do this in a supervised manner. Then, they adjust the weights simultaneously with labelled and unlabeled data. Luh et al. [27] utilized YOLOv3 to solve FER problem.

2. METHODOLOGY

The proposed system uses facial images as input, and it produces facial expression labels using just the eyes and eyebrows region of the face. For this purpose, first, just the eyes and eyebrows part of the facial images are cropped using the pre-processing methods. Then, using the deep transfer learning method, the facial expressions are classified. Different pre-trained networks have been used for this purpose and results have been compared. The system's pipeline is shown in Figure 1.

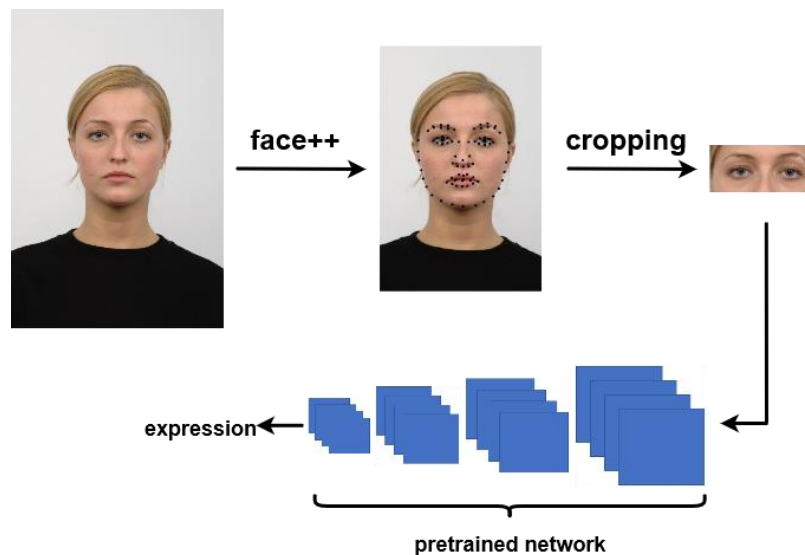


Figure 1. Proposed pipeline.

2.1 CNN

The feature extraction phase required in classical machine learning methods is a challenging process. Because experts must determine the features that affect the solution of a problem. This a very time-consuming process. On the contrary, deep learning processes raw data without feature extraction phase. Therefore, deep learning has eliminated the problems in feature extraction.

CNN consists of a combination of layers. These layers are input, convolution, pooling, activation, dropout, fully connected, and classification layer. In the convolution layer, the filters move over the image and perform the convolution operation. Feature maps are created by mapping the features revealed by each filter. The mathematical model of the convolution is shown in Eq. 1 [28].

$$S(i, j) = (I * K)(i, j) = \sum_m \sum_n I(i + m, j + n)K(m, n) \quad (1)$$

In the equation, S, I, and K represent the output, the input image, and the kernel respectively. Asterisk (*) is the convolution operation.

In the pooling layer, the input size is reduced in width and height. There is no change in depth. Pooling is not a mandatory layer. It may or may not be used according to the design.

In [18], it has been shown that CNNs using a nonlinear activation function like Relu are trained more quickly. Therefore, in this paper, Relu is used as the activation function. The mathematical model of Relu is shown in Eq. 2 [28].

$$f(x) = \max(0, x) \quad (2)$$

In the dropout layer, some nodes of the network are removed to prevent the network from being dependent on a particular neuron. The fully connected layer is dependent on all fields of the previous layer. Softmax converts the predictions to positive values. Also, the softmax applies normalization to get a probability distribution of classes. The mathematical model of softmax is shown in Eq. 3 [28].

$$\text{softmax}(x)_i = \frac{\exp(x_i)}{\sum_{j=1}^n \exp(x_j)} \quad (3)$$

In the equation, x_i represents the input of softmax, and it is obtained from the fully connected layer.

The last layer is the classification layer. The number of the output of the classification layer is equal to the number of classes.

In the literature, the performance of classification problems is usually measured by accuracy. Since facial expressions are classified in this study, the performance has been measured with accuracy and comparisons have been made on this metric. The accuracy formula is given in Eq. 4.

$$\text{Accuracy} = \frac{(TP + TN)}{(TP + TN + FN + FP)} \quad (4)$$

In the equation, TP represents true positives, TN represents true negatives, FN represents false negatives, and FP represents false positives.

2.2. Pre-trained Networks

From the network design and training viewpoint, two different approaches can be used in deep learning. The first one is to design and train a novel network from scratch. The second one is to get help from existing networks that are already trained. These networks are called pre-trained networks. The second approach is called transfer learning. Providing more accurate results with fewer data is one of the advantages of transfer learning. In addition, training a network using random weights is slower than transfer learning. Transfer learning allows the quick transfer of features. Therefore, new deep learning tasks can be achieved using fewer images in training phase.

In this study, nine different pre-trained networks have been used for FER on partial face images tasks. All of them were trained on the ImageNet database [29]. These networks were trained using over a million images. The networks can classify images into 1000 categories like the variety of animals, mouse, pencil, etc. Thus, the networks have robust feature representations for different images. An explanation of these networks is given below.

Nasnetmobile [30] has been introduced by Google. Its size is 20 MB, it has 5.3×10^6 parameters. It uses 224×224 sized input images. Shufflenet [31] is a CNN structure which is built especially for mobile devices with limited computing power. This network uses two new approaches to reduce computational costs. These approaches are pointwise group convolution and channel shuffle. Its size is 5.4 MB. It has 1.4×10^6 parameters and uses 224×224 sized input images. Googlenet [32] is a 22 layers deep learning network that is developed by Google researchers. Its size is 5.4 MB. It has 7.0×10^6 parameters. Its default input size is 224×224 . Mobilenetv2 [33] is a CNN structure that was developed especially for mobile devices. Its architecture includes the initial fully convolution layer with 32 filters, followed by 19 residual bottleneck layers. Its size is 13 MB. It has 3.5×10^6 parameters. Resnet50 [34] is a convolutional neural network that has 50 layers. It uses residual blocks to improve the accuracy. There is “skip connections” concept at the core of the residual blocks. This is the strength of resnet50. Its size is 96 MB, and it has 25.6×10^6 parameters. Its input size is 224×224 . The main approach for densenet201 [35] is the connections between the network layers. Its size is 77MB, it has 201 layers and 20×10^6 parameters. Alexnet [36] is a classic CNN architecture. In alexnet, grouped convolutions are designed for fitting the model across two GPUs. Its size is 227 MB, and it has 61×10^6 parameters. Vgg [37] has different versions. In this study both 16 depth and 19 depth version have been used. Vgg16 has 138×10^6 parameters and vgg19 has 144×10^6 parameters. These models use 224×224 sized input images.

In this study, first, the last two layers of the pre-trained networks (fully connected layers and classification layers) have been modified for six classes. Then, they have been re-trained using the eye and eyebrow parts of the facial images.

3. EXPERIMENTAL RESULTS

In this study, the learning rate has been determined as 0.0001 for densenet201, googlenet, mobilenetv2, nasnetmobile, resnet50, shufflenet, vgg16 and vgg19. Alexnet doesn't work with 0.0001. Thus 0.001 is used as the learning rate for alexnet. Also, the optimizer is sgd, learn rate drop factor

is 0.2, learn rate drop period is 5, the momentum is 0.9, the mini batch size is 8, validation frequency is 3 for all pre-trained networks. Each network has been trained using 50 epochs.

3.1. Dataset and Preprocessing

The Radboud Faces Database (RaFD) [38] was used in both training and testing phase in this study. The dataset contains whole face images of 67 people, including children and adults. The dataset includes three different gaze directions of people. These are looking left, looking frontal, looking right. In this study, the frontal faces are used for this task. There are eight expressions in RaFD. The facial expression recognition studies often investigate six main expressions. These are anger, disgust, fear, happiness, sadness and surprise. These expressions were defined in the early works of Ekman and Friesen [11]. The images used in this study have six universal facial expressions with different gaze directions (Figure 2). 1206 images were used in this study. 844 images were used for training and the rest of the images were used for testing.

As mentioned earlier, this study uses the upper part of the face for facial expression recognition. Therefore, the upper part of the face must be cropped from the raw image. For this purpose, firstly, the face keypoints were localized on the face images using Face++ toolkit [39]. This step is shown in Figure 1. In this phase, 83 facial keypoints were localized for each face image. Then the region between left and right contours of the face which have the same x-axis as the midpoint of the nose were cropped horizontally. Vertically, the bottom point is considered the nose midpoint. The vertical top point was determined using the equation of $horizontal\ area/vertical\ area = 0.2$. In cropped region 0.2 is determined experimentally. Since the wrinkles on the forehead are also a critical determinant in some facial expressions, these regions are especially included in the cropped image.

3.2. Comparative Results

In the proposed study, nine pre-trained networks have been restructured for image classification task and their performance have been compared in terms of accuracy. The comparison table is given in Table 2. As can be seen in the table, the best result obtained using vgg19 as 91.33%. Vgg16 is second behind it as 88.33%. It can be seen that vgg19 and vgg16 have the greater parameters compared to other networks. This success rate can be explained by the number of parameters. Although shufflenet's number of the parameter is less than nasnetmobile, its performance is better than nasnetmobile.

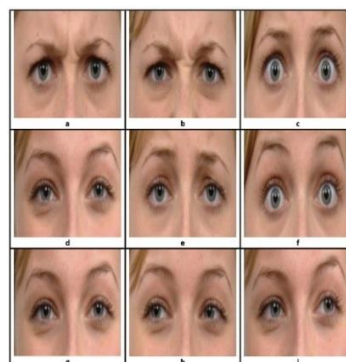


Figure 2. Sample images from the dataset for six expressions and three gaze directions ((a) anger, (b) disgust, (c) fear, (d) happy, (e) sad, (f) surprise, (g) looking frontal, (h) looking right, (i) looking left)

Table 2. Recognition accuracies using different pre-trained networks.

Pretrained network	Accuracy (%)
nasnetmobile	67.67
shufflenet	81.67
googlenet	82.00
mobilenetv2	82.00
resnet50	84.00
densenet201	85.67
alexnet	87.33
vgg16	88.33
vgg19	91.33

The confusion matrix of the vgg19 network that shows the best accuracy is given in Figure 3. As can be seen in the figure, sad expression is predicted as 100% success rate by the system. The system sometimes confuses surprise and fear expressions. When the sample images given in Figure 2 are examined, it can be seen that the eyes are more open than normal in both expressions. This may cause confusion.

The proposed approach has been compared to the other studies that use the same RaFD database. The comparison results are shown in Table 3. In the literature, the studies mostly used the whole face. Although the proposed study produced lower results than studies using whole faces, its performance is quite close to them using a small part of the face. In [40], five facial expressions were classified using partial faces. Our study produced a result close to that, despite the classification of six expressions in our study.

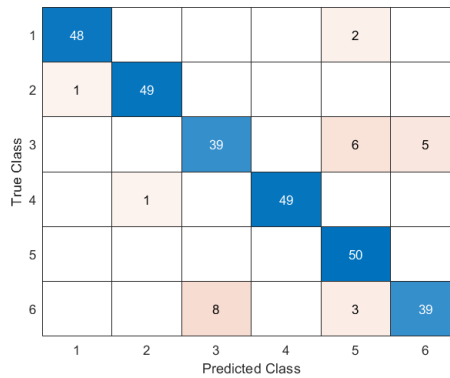


Figure 3. Confusion matrix of vgg19 (1: angry, 2: disgust, 3: fear, 4: happy, 5: sad, 6: surprise).

Table 3. Comparison with the studies used RaFD.

Study	#Expression	Whole/partial face	Accuracy
Oztel at al. [40]	5	whole	94.07
Nayak at al. [41]	6	whole	95.60
Ali at al. [18]	6	whole	98.80
Oztel at al. [40]	5	partial	92.59

Proposed approach with vgg19 6 partial 91.33

4. CONCLUSION

WHO recommends wearing a face mask to reduce the spread of Covid-19. In this case, an important part of the face for facial expression recognition is closed. Also, lower part of the face can be occluded some reasons such as wearing a scarf. In these case, facial expressions must be detected using only the eyes and eyebrows area. This is a challenging problem for machine learning. With this motivation, our study proposes a deep transfer learning-based approach for partial face. The system just uses upper part of the face for predicting facial expression. For this purpose, database images have been cropped to include just upper part of the face. Then the proposed system has been trained using nine different pre-trained networks and the results were compared. The vgg19 network produced the best result as 91.33%. The best score obtained for sad expression as 100%. Happy and disgust expression detected as 98%. The system sometimes confused surprise and fear expressions. This situation has been interpreted with images in the study. The study was also compared with other studies that use the same database in the literature and produced comparable results.

The proposed system can be useful for using facial expressions in situations where facial movement is active such as speaking, and in cases of occlusions due to scarf, mask, etc. It is planned to expand the same work for real time in the near future.

ACKNOWLEDGEMENT

This work was supported by the Sakarya University Scientific Research Projects Unit (Project Number: 2020-9-33-43).

REFERENCES

- [1] Mehrabian, A., (1968), Some referents and measures of nonverbal behavior, Behavior Research Methods & Instrumentation, 1, 203–207.
- [2] Lopes, A.T., de Aguiar E., De Souza A.F., and Oliveira-Santos T., (2016), Facial Expression Recognition with Convolutional Neural Networks: Coping with Few Data and the Training Sample Order, Pattern Recognition, 67, 610-628.
- [3] Zalewski, L. and Gong, S., (2005), 2D Statistical Models of Facial Expressions for Realistic 3D Avatar Animation, IEEE Computer Society Conference on Computer Vision and Pattern Recognition (CVPR'05), 2, 217–222.
- [4] Yolcu, G., Oztel, I., Kazan, S., Oz, C., Palaniappan, K., Lever, T.E. and Bunyak, F., (2017), Deep learning-based facial expression recognition for monitoring neurological disorders, IEEE International Conference on Bioinformatics and Biomedicine (BIBM), 1652–1657.

- [5] Bartlett, M.S., Littlewort, G., Fasel, I., Chenu, J., Kanda, T., Ishiguro, H., Movellan, J.R., (2003), Towards social robots: Automatic evaluation of human-robot interaction by face detection and expression classification, *Advances in Neural Information Processing Systems*, 16.
- [6] Zhang, Y. and Hua, C., (2015), Driver fatigue recognition based on facial expression analysis using local binary patterns, *Optik - International Journal for Light and Electron Optics*, 126(23), 4501–4505.
- [7] Shaykha, I., Menkara, A., Nahas, M. and Ghantous, M., (2015), FEER: Non-intrusive facial expression and emotional recognition for driver’s vigilance monitoring, *57th International Symposium ELMAR (ELMAR)*, 233–237.
- [8] Kim, J.-B., Hwang, Y., Bang, W.-C., Lee, H., Kim, J.D.K. and Kim, C.-Y., (2013), Real-time realistic 3D facial expression cloning for smart TV, *IEEE International Conference on Consumer Electronics (ICCE)*, 240–241.
- [9] Niforatos, E. and Karapanos, E., (2015), EmoSnaps: a mobile application for emotion recall from facial expressions, *Personal and Ubiquitous Computing*, 19(2), 425–444.
- [10] Terzis, V., Moridis, C.N. and Economides, A.A., (2013), Measuring instant emotions based on facial expressions during computer-based assessment, *Personal and Ubiquitous Computing*, 17(1), 43–52.
- [11] Ekman P. and Friesen W.V., (1971), Constants across cultures in the face and emotion., *Journal of Personality and Social Psychology*, 17(2), 124–129.
- [12] Hsu, C.-T., Hsu S.-C. and Huang, C.-L., Facial expression recognition using Hough forest, (2013), *2013 Asia-Pacific Signal and Information Processing Association Annual Summit and Conference*, 1–9.
- [13] Zhong, L., Liu, Q., Yang, P., Liu, B., Huang, J. and Metaxas, D.N., (2012), Learning active facial patches for expression analysis, *2012 IEEE Conference on Computer Vision and Pattern Recognition*, 2562–2569.
- [14] Khan, F., (2020), Facial Expression Recognition using Facial Landmark Detection and Feature Extraction via Neural Networks, *arXiv:1812.04510*.

- [15] Saurav, S., Saini, R. and Singh, S., (2021), Facial Expression Recognition Using Dynamic Local Ternary Patterns with Kernel Extreme Learning Machine Classifier, *IEEE Access*, 9, 120844–120868.
- [16] Iqbal, M.T.B., Abdullah-Al-Wadud, M., Ryu, B., Makhmudkhujaev, F. and Chae, O., (2020), Facial Expression Recognition with Neighborhood-Aware Edge Directional Pattern (NEDP), *IEEE Transactions on Affective Computing*, 11(1), 125–137.
- [17] Dagher, I., Dahdah, E. and Al Shakik, M., (2019), Facial expression recognition using three-stage support vector machines, *Visual Computing for Industry, Biomedicine, and Art*, 2(1).
- [18] Nair, V., Hinton, GE., (2010) Rectified Linear Units Improve Restricted Boltzmann Machines, *Proceedings of the 27th international conference on international conference on machine learning*, Omnipress, USA, 807–814
- [19] Ekman, P. and Friesen, W.V., (1978), Facial action coding system: a technique for the measurement of facial movement.
- [20] Morales-Vargas, E., Reyes-García, C. A. and Peregrina-Barreto, H., (2019), On the use of action units and fuzzy explanatory models for facial expression recognition, *PLoS One*, 14(10).
- [21] Jin, X., and Jin, Z., (2021), MiniExpNet: A small and effective facial expression recognition network based on facial local regions, *Neurocomputing*, 462, 353–364.
- [22] Fan, X., Jiang, M., Shahid, A.R. and Yan, H., (2022), Hierarchical scale convolutional neural network for facial expression recognition, *Cognitive Neurodynamics*.
- [23] Saurav, S., Saini, A.K., Saini, R. and Singh, S., (2022), Deep learning inspired intelligent embedded system for haptic rendering of facial emotions to the blind, *Neural Computing and Applications*, 34, 4595-4623.
- [24] Happy, S.L., Dantcheva, A. and Bremond, F., (2021), Expression recognition with deep features extracted from holistic and part-based models, *Image and Vision Computing*, 105, 104038.
- [25] Jin, X., Sun, W. and Jin, Z., (2020), A discriminative deep association learning for facial expression recognition, *International Journal of Machine Learning and Cybernetics*, 11(4), 779–793.

- [26] Happy, S. L., Dantcheva, A. and Bremond, F., (2019), A Weakly Supervised learning technique for classifying facial expressions, *Pattern Recognition Letters*, 128, 162–168.
- [27] Luh, G.-C., Wu, H.-B., Yong, Y.-T., Lai, Y.-J. and Chen, Y.-H., (2019), Facial Expression Based Emotion Recognition Employing YOLOv3 Deep Neural Networks, *2019 International Conference on Machine Learning and Cybernetics (ICMLC)*, 1-7.
- [28] Goodfellow, I., Bengio, Y. and Courville, A., 2016, *Deep learning*, MIT Press.
- [29] Krizhevsky, A., Sutskever, I. and Hinton, G.E., (2007), ImageNet Classification with Deep Convolutional Neural Networks, *Handbook of Approximation Algorithms and Metaheuristics*, 1–1432.
- [30] Zoph, B., Vasudevan, V., Shlens, J. and Le, Q.V., (2018), Learning Transferable Architectures for Scalable Image Recognition, *2018 IEEE/CVF Conference on Computer Vision and Pattern Recognition*, 8697–8710.
- [31] Zhang, X., Zhou, X., Lin, M. and Sun, J., (2018), ShuffleNet: An Extremely Efficient Convolutional Neural Network for Mobile Devices, *2018 IEEE/CVF Conference on Computer Vision and Pattern Recognition*, 6848–6856.
- [32] Szegedy, C., Liu, W., Jia, Y., Sermanet, P., Reed, S., Anguelov, D., Erhan, D., Vanhoucke, V. and Rabinovich, A., (2015), Going deeper with convolutions, *2015 IEEE Conference on Computer Vision and Pattern Recognition (CVPR)*, 1–9.
- [33] Sandler, M., Howard, A., Zhu, M., Zhmoginov, A. and Chen, L.-C., (2018), MobileNetV2: Inverted Residuals and Linear Bottlenecks, *2018 IEEE/CVF Conference on Computer Vision and Pattern Recognition*, 4510–4520.
- [34] He, K., Zhang, X., Ren, S. and Sun, J., (2016), Deep Residual Learning for Image Recognition, *2016 IEEE Conference on Computer Vision and Pattern Recognition (CVPR)*, 770–778.
- [35] Huang, G., Liu, Z., van der Maaten, L. and Weinberger, K.Q., (2017), Densely Connected Convolutional Networks, *Proceedings of the IEEE Conference on Computer Vision and Pattern Recognition (CVPR)*.

- [36] Krizhevsky, A., Sutskever, I. and Hinton, G.E., (2012), ImageNet Classification with Deep Convolutional Neural Networks, *Advances in Neural Information Processing Systems*, 25.
- [37] Simonyan K. and Zisserman A., (2015), Very Deep Convolutional Networks for Large-Scale Image Recognition, *International Conference on Learning Representations*.
- [38] Langner, O., Dotsch, R., Bijlstra, G., Wigboldus, D. H. J., Hawk, S. T. and van Knippenberg, A., (2010), Presentation and validation of the Radboud Faces Database, *Cognition & Emotion*, 24(8), 1377–1388.
- [39] Face++ Cognitive Services, (2022), Face++ Web Page, <https://www.faceplusplus.com>, Access Date: May 23, 2022.
- [40] Oznel, I., Yolcu, G., Oz, C., Kazan, S. and Bunyak, F., (2018), iFER: facial expression recognition using automatically selected geometric eye and eyebrow features, *Jornal of Electronic Imaging*, 27(2), 1.
- [41] Nayak, S., Happy, S.L., Routray, A. and Sarma, M., (2019), A Versatile Online System for Person-specific Facial Expression Recognition, *TENCON 2019 - 2019 IEEE Region 10 Conference (TENCON)*, 2513–2518.



RESEARCH ARTICLE

**PROPERTIES of POROUS CERAMICS PRODUCED by SINTERING TERRA ROSSA-
ALKALI MIXES**

Canan MERCAN¹, Mehmet Uğur TOPRAK^{2,*}, Eda TAŞÇI³, Musa AKMAN⁴

¹ Dumlupınar University, Engineering Faculty, Civil Engineering Department, cnanmercan@gmail.com,
ORCID: 0000-0002-8366-3576

^{2*} Dumlupınar University, Engineering Faculty, Civil Engineering Department, mugur.toprak@dpu.edu.tr,
ORCID: 0000-0001-5483-2871

³ Kütahya Dumlupınar University, Engineering Faculty, Materials Engineering Department, eda.tasci@dpu.edu.tr,
ORCID: 0000-0003-3346-8833

⁴ Kütahya Dumlupınar University, Engineering Faculty, Materials Engineering Department, musa.akman@ogr.dpu.edu.tr,
ORCID: 0000-0002-8677-9435

Receive Date: 25.04.2022

Accepted Date: 12.05.2022

ABSTRACT

Porous ceramics were produced by sintering terra rossa (TR) with alkalis for void formation at 1000 °C. Little cylinders (25x25 mm) were prepared with TR to investigate the influence of alkali type (NaOH, Na₂CO₃ and KOH) and amount (8, 10 and 12% by weight of TR) on the physical, mechanical and microstructure of porous ceramics (PC). The highest compressive strength (32 MPa) was obtained in series with no alkalis. The addition of alkalis decreased the unit weight and compressive strength of PC due to decreased sintering temperature, increased foaming and excessive formation of glassy phase causing the brittle structure. The unit weight of the PC produced with NaOH and Na₂CO₃ was considerably low (0.62-0.70 g/cm³) compared with PC comprising KOH (1.05-2.16 g/cm³). Corresponding compressive strengths were 3.17-4.46 MPa and 7.68-25.87 MPa revealing that it can be used as a decorative alternative to clay brick and autoclaved aerated concrete blocks.

Keywords: *Compressive strength, Porous ceramics, Sintering, Terra rossa*

1. INTRODUCTION

Terra rossa (TR) is reddish, clayey to silty clayey soil widespread in the Mediterranean region occurs as a discontinuous layer ranging from a few centimetres to several meters formed on calcareous main material (limestone or dolomite bedrock) [1-3]. Most important characteristics of TR are their free Fe₂O₃ (hematite) content of up to 8% and is usually between 4-6%, which gives bright red colors to TR. Soil formed on the greyish-blue crystalline limestones of TR has been found to have very little residual material. The most important chemical process here is decalcification and the water-soluble CaCO₃ is removed by washing [5, 6].

Bricks, floor and roofing tiles, etc. are produced by a sintering process. Properties of these depend on the clayey material's chemical and mineralogical composition [7, 8]. Na₂O can significantly reduce the

viscosity of the silicate melt by depolymerizing the silicate networks [9]. Ge et al. [10] observed that increasing the Na₂O contents reduced the viscosity of ceramic foams sintered. This caused expansion of the pores and reduced the bulk density of the product. SiO₂ itself is chemically inert.

Thermal expansion of SiO₂ is too little and resistance to thermal shock too much. Due to the high melting point (1723°C), network modifiers such as alkali/alkaline earth oxides were added to the SiO₂ glass to break the bridging oxygen bonds in the Si-O-Si bonds and reduce the melting temperature of the glass [11-15]. Feldspar, talc and dolomites comprises important amount of Na₂O, K₂O, MgO and CaO that increases the flux amount and induce the formation of an amorphous phase which acts as binder [16-18]. Production of Red-fired ceramics (tiles, bricks etc.) continues in Anatolia today, with about 500 factories producing brick and roofing tiles using clay raw materials from alluvial deposits, which are important soils for agriculture. Therefore, researching new clay sources for red ceramics is inevitable [19]. Low thermal insulation properties and high weight of conventional bricks limits their usage at new buildings. Various pore-forming agents were used to develop thermal properties of sintered clay bricks [20]. Bricks as light as lightweight aggregates (LWA) could be produced by using expansion agents (NaHCO₃ and CaCO₃) [21].

A significant part of the area of Kütahya-Turkey was occupied by mountain terrains/high lands, which are built up of meta-carbonate rocks (marbles). The most characteristic types of red soil over carbonate rocks are Terra Rossa. The TR can be suitable as raw material in the brick and roofing tile industry. The present study presenting the results of a master thesis [22] motivated by a lack of data on the sintering properties of TR-alkali mixes. Accordingly, this paper aims to determine the contribution of these alkali oxides to the physical and mechanical properties of porous ceramics (PC) produced by TR.

2. MATERIAL and METHODS

Terra rossa samples given in Fig. 1 were collected from the village of Çöğürler in Kütahya/Turkey. TR was ground by a ringed mill for 3 min to increase the surface area up to 4847 cm²/g. Porous ceramics were produced by i) mixing TR with technical grade alkali oxides (NaOH, Na₂CO₃ and KOH >99% purity obtained from Detsan Chemicals Company in Eskişehir/TURKEY) at ratios of 8, 10 and 12% by weight of TR ii) keeping the mixtures in plastic bags for a day, iii) pressing with 2% water by weight of mix and 3 kN molding force to form 25x25 mm cylinders iv) drying 1 day at 20±2 °C in laboratory and 1 day at 105±2 °C in oven v) sintering at 1000 °C in a tunnel kiln for 9 hours 45 minutes.



Figure 1. Terra rossa on limestone layer in Çögürler (Kütahya/Turkey) [22].

A total of 10 series with control (C) with no alkali addition were produced. Series with 8, 10 and 12% NaOH were labelled as N8, N10 and N12 respectively. Similarly, series with Na₂CO₃ or KOH were named as NC8, NC10, NC12 and K8, K10 and K12 respectively. Unit weight (UW) (TS EN 1097-6) [23], uniaxial compressive strength (UCS) of porous ceramics (PC) at 0.6 MPa/s loading rate was tested. Before the compressive strength test upper and lower surfaces of porous ceramics were smoothed with sandpaper. All the reported results are the means of three samples. Colorimetric analysis and optical microscopy analyses (broken surfaces taken from the centre of the samples) were conducted. To conduct a petrographic inspection, section samples were prepared from each terra rossa based porous ceramics respectively. Visual inspection was carried out under planar polarized light by using a petrographic microscope (Nikon Eclipse E200 Pol).

3. EXPERIMENTAL RESULTS

3.1. Characterization of the Terra Rossa

The TR was mainly composed of SiO₂, and Al₂O₃ (Table 1). The LOI of TR about 15.26 (wt%) was relatively high. By contrast, the number of alkaline oxides was very low. Fe₂O₃ (*hematite*) minerals content which gives red colors to TR as stated in literature [24] was 6.52%.

Table 1. Oxide content of terra rossa [22].

Oxide content	SiO ₂	Al ₂ O ₃	Fe ₂ O ₃	CaO	K ₂ O	Na ₂ O	CaO	MgO	TiO ₂	MnO	Cl	SO ₃	*LOI
% mass	56.07	15.98	6.52	1.91	1.93	0.14	1.91	1.27	0.57	0.11	0.06	0.05	15.25

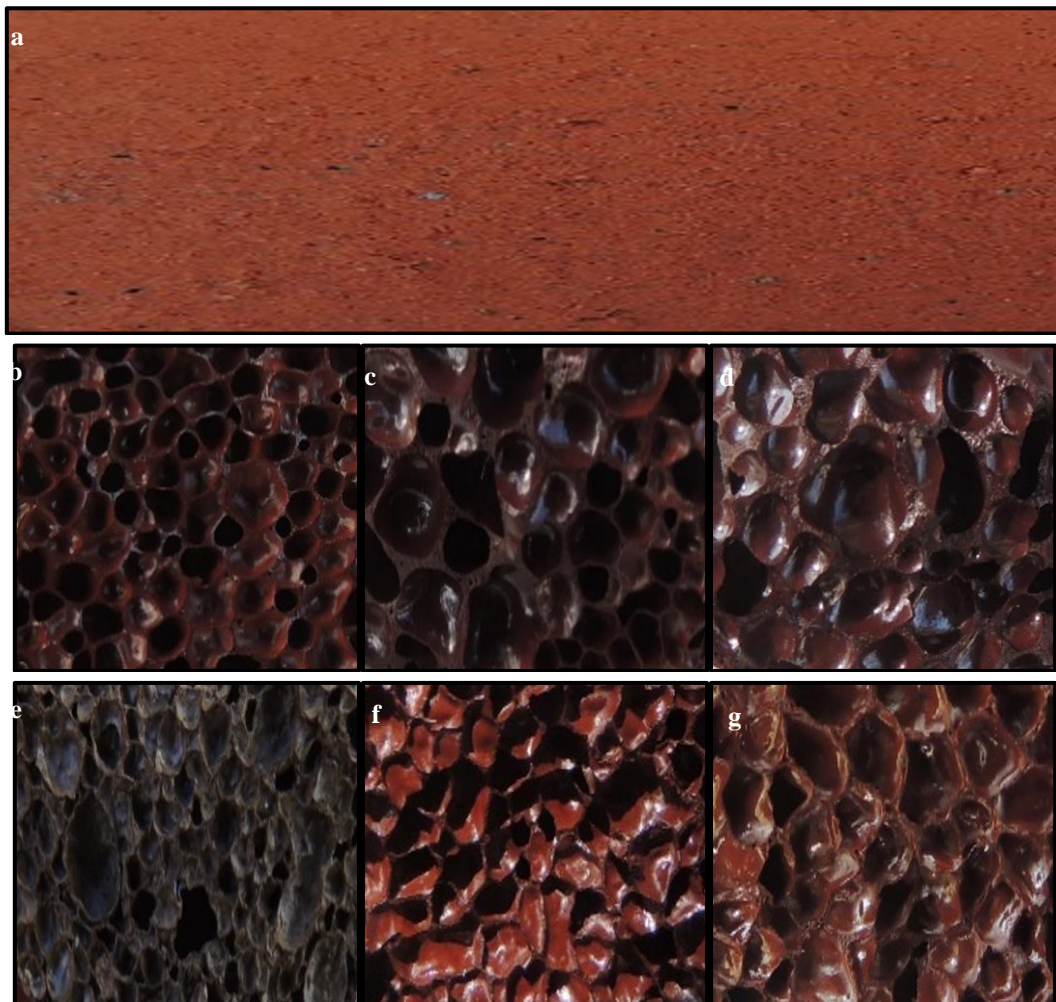
*LOI: Loss on ignition

3.2. Evaluation of Physical and Mechanical Properties

The pore structure of porous ceramics products with different alkali types and amounts were shown in Fig. 2. The iron element in oxidation state II was oxidised to state III after sintering could be responsible from darker colors of porous ceramics [25, 26]. Alkali type and amount significantly affected the colors of the porous ceramics as illustrated in Table 2. Numerical values of color analysis

were given in Table 2. Different colors were observed due to the type and amount of alkalis. The increase in NaOH content significantly reduced a^* and b^* values of the N series.

Alkalis lower the melting temperature in N and NC series. The unit weight and the compressive strength decreased with the increase in the alkali ratio. The pore sizes in N and NC series continued to increase gradually with increasing alkali content. Enhancement of foaming due to higher alkali amounts was probably responsible for these decreasements. However, in contrast, with the increase in KOH amount the pore sizes of K series were reduced while the UW and UCS of K series increased considerably. Maximum UCS was achieved for the K12 series. Homogeneous distribution of pores observed in K series. Contrary to other alkali series, increase in KOH amount considerably increased the compressive strength of porous ceramics.



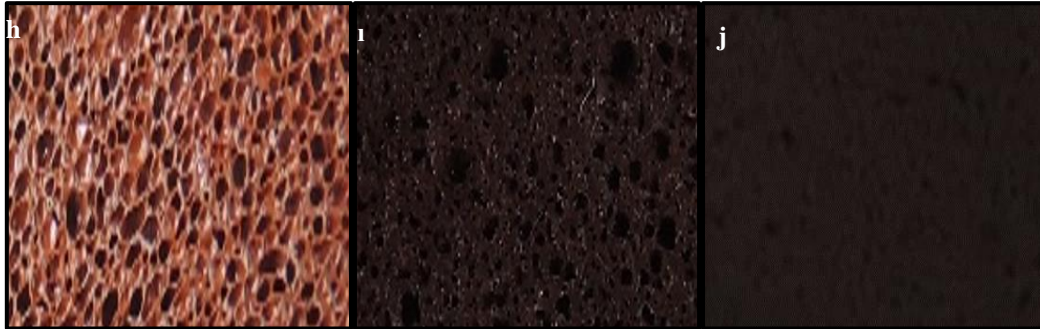


Figure 2. The cross-section of (a) C, (b) N8, (c) N10, (d) N12, (e) NC8, (f) NC10, (g) NC12, (h)K8, (i) K10 and (j) K12 [22].

According to TS EN 771-1 [27], hollow bricks are required to have a compressive strength of at least 2 MPa and the unit weight of them ranges between 600-700 kg/m³. According to TS EN 771-4 [28], autoclaved aerated concrete blocks must have a compressive of 2.2 MPa and their unit weight values are 350 to 500 kg/m³ [28]. Control series had a unit weight of 2.3 g/cm³ and compressive strength of 32 MPa. The unit weight of the PC produced with NaOH and Na₂CO₃ was considerably low (0.62-0.70 g/cm³) compared with PC comprising KOH (1.05-2.16 g/cm³). Corresponding compressive strengths were 3.17-4.46 MPa and 7.68-25.87 MPa revealing that it can be used as a decorative alternative to clay brick and autoclaved aerated concrete blocks.

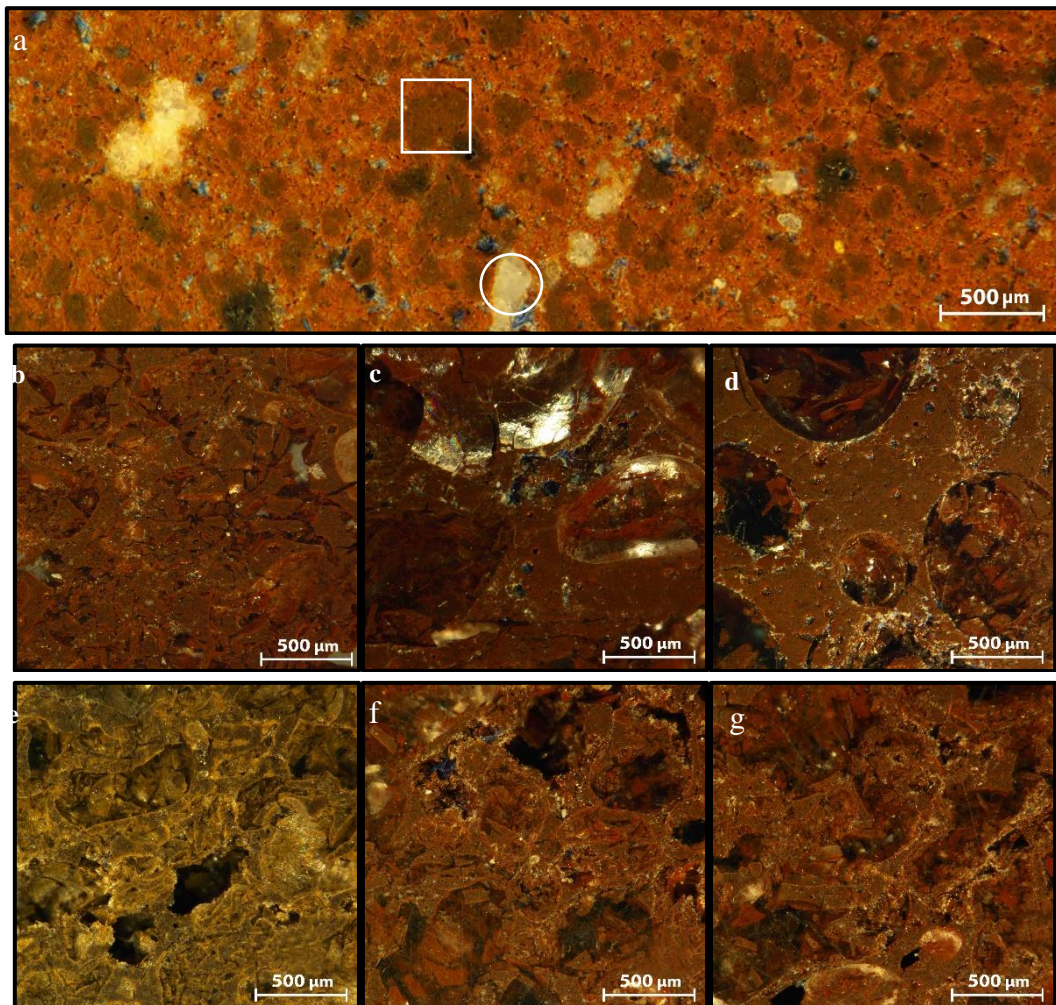
Table 2. Color Codes, physical and mechanical properties of porous ceramics [22].

		Sample codes									
		C	N8	N10	N12	NC8	NC10	NC12	K8	K10	K12
Color codes	L*	35.54	32.97	37.26	37.89	40.29	38.05	37.88	39.09	34.25	35.08
	a*	19.15	9.12	5.73	5.17	2.76	7.93	8.25	11.43	12.24	12.80
	b*	17.97	5.05	3.10	2.55	10.16	5.28	4.23	8.76	10.45	11.35
Properties	WA	6.25	0.98	1.09	2.41	0.91	1.38	1.95	0	0	0
	UW (g/cm ³)	2.30	0.67	0.64	0.62	0.70	0.68	0.65	1.05	1.73	2.16
	CS (MPa)	32.13	3.82	3.55	3.17	4.46	4.31	3.94	7.68	14.16	25.87

Note: The “L” axis gives the lightness: a white object has a L value of 100 and the L value of a black object is 0. The shades of grey, are on the L axis. The “a” axis is the green-red axis and the “b” axis goes from blue (-b) to yellow (+b).

3.3. Evaluation of Optical Microscopy Images

Fig. 3 (a) presents the C series. The microstructure suggests quartz (white circle) and hematite particles (white square) in size up to 2 cm embedded in the liquid phase. Since the grain size of the liquid phase was considerably fine the mineral type could not be determined by optical microscopy.



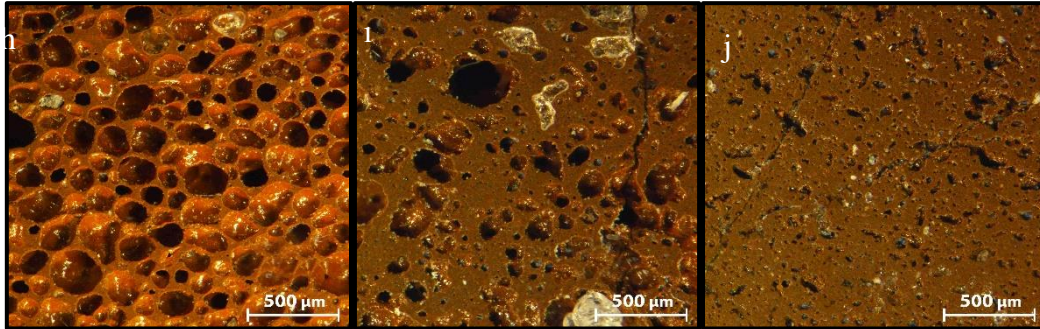


Figure 3. Optical microscopy images of (a) C, (b) N8, (c) N10, (d) N12, (e) NC8, (f) NC10, (g) NC12, (h)K8, (i) K10 and (j) K12 [22].

Some cracks were observed in all samples because of the shrinkage of the binding matrix. This was more pronounced for series produced with 12% alkalis. For K series closed pores were more spherical. N and NC series have more unconsolidated grains compared to the K series. It was concluded that the increasing KOH enhanced the vitreous structure. The compressive strength of porous ceramics enhanced up to 26 MPa for K12.

4. CONCLUSIONS

There are difficulties in finding suitable clay fields used as brick raw material and in obtaining clay from these fields. New brick factories are not licensed. A compact material having a unit weight of 2.3 g/cm^3 and compressive strength of 32 MPa obtained by sintering terra rossa. According to us high content of Fe_2O_3 acted as a flux increasing the compactness of the material and enhancing the mechanical strength. The addition of alkalis decreased the unit weight and compressive strength of PC. Porous ceramics with a unit weight of $1.05\text{-}2.16 \text{ g/cm}^3$ and compressive strengths of 7.68-25.87 MPa were produced using KOH as an expansion agent. Porous ceramics can be used as a decorative alternative to clay brick and autoclaved aerated concrete blocks. Potassium feldspates can be used as cheaper alkali source. The incorporation of expansion agents in TR can be a viable procedure, which turns TR into decorative porous ceramics.

ACKNOWLEDGMENT

The authors, gratefully, acknowledge Tulu Ceramics for sintering in an industrial furnace and the Center for Advanced Technologies (Kütahya Dumlupınar University) for their help in some measurements and analysis. This research did not receive any specific grant from funding agencies in the public, commercial, or not-for-profit sectors.

REFERENCES

- [1] Torrent, J., (2005), Mediterranean soils. In: Hillel, D. (Ed.), Encyclopaedia of soils in the environment, Elsevier Academic Press, Oxford, 2, 418-427.

- [2] Merino, E., Banerjee, A. and Dworkin, S., (2006), Dust, terra Rossa, replacement, and karst: serendipitous geodynamics in the critical zone, *Geochimica et Cosmochimica Acta*, 70-18.
- [3] Vingiani, S., Di Iorio, E., Colombo, C. and Terribile, F., (2018), Integrated study of red Mediterranean soils from southern Italy, *Catena*.
- [4] Durn, G., Ottner, F., Slovenac, D., (1999), Mineralogical and geochemical indicators of the polygenetic nature of terra rossa in Istria, Croatia, *Geoderma*, 91, 125-150.
- [5] Mater, B., (2012), Morphological properties and formations of some fossil terra Rossa in eastern Anatolia, *Geography Journal*, 3, 1988-1992.
- [6] Stipičević, S., Sekovanić, L., Drevenkar, V., (2014), Ability of natural, acid-activated and surfactant-modified terra Rossa, *Applied Clay Science*, 88-89, 56-62.
- [7] Capitâneo, J.L., Da Silva, F.T., Vieira, C.M.F. and Monteiro, S.N., (2005), Reformulation of the kaolinitic body for extruded floor tiles with phonolite addition, *Silicates Industriels*. 70, 161-165.
- [8] Elimbi, A., M. Dika, J., Chantale, N., (2014), Djangang effects of alkaline additives on the thermal behaviour and properties of Cameroonian poorly fluxing clay ceramics, *Journal of Minerals and Materials Characterization and Engineering*, 2, 484-501.
- [9] Kang, J., Wang, J., Zhou, X., Yuan, J., Hou, Y., Qian, S., Li, S., Yue, Y., (2018), Effects of alkali metal oxides on crystallization behaviour and acid corrosion resistance of cordierite based glass-ceramics, *J. Non-Cryst. Solids* 481, 184-190.
- [10] Ge, X., Zhou, M., Wang, H., Chen, L., Li, X., & Chen, X., (2019), Effects of flux components on the properties and pore structure of ceramic foams produced from coal bottom ash, *Ceramics International*, 45-9, 12528-12534.
- [11] Mohd H., Khamirul A., Sidek Hj. Ab Aziz, Zaidan A.W., Siti Syuhaida A. R., (2017), Effect of sintering on crystallization and structural properties of soda-lime-silica glass, *Science of Sintering*, 49, 409-417.
- [12] Wang, M. J. Cheng, M. Li, F. He and W. Deng, (2012), Viscosity and thermal expansion of soda-lime-silica glass doped with Gd₂O₃ and Y₂O₃, *Solid State Sci.*, 14.
- [13] Bagley, B. G., Vogel, E. M., French, W. G., Pasteur, G. A., Gan J. N. and Tauc, J. (1976), The optical properties of a soda-lime-silica glass in the region from 0.006 to 22 eV, *Non-Cryst. Solids*, 22.
- [14] Wang, M., Cheng J., Li, M., (2010), Effect of rare earth on viscosity and thermal expansion of soda-lime-silicate glass, *J. Rare Earth*, 28.
- [15] Mastelaro, V.R., Zanotto, E. D., (1996), Residual stresses in a soda-lime-silica glass-ceramic, *J. of Non-Cryst. Solids*, 194, 297-304.

- [16] Kingery, W.D., Bowen, H.K. and Uhlmann, D.R. (1995) Introduction to ceramics. John Wiley and Sons, New York.
- [17] Xuexiang, G., Zhou M., Wang H., Chen L., Li X., Chena, X., (2019), Effects of flux components on the properties and pore structure of ceramic foams produced from coal bottom ash. *Ceramics International*, 45,12528-12534.
- [18] Singh, N., M. M, S. Arya, (2018), Influence of coal bottom ash as fine aggregates replacement on various properties of concretes: a review, *Resour. Conserv. Recycle.*, 138, 257-271.
- [19] Çolak, M., Özkan, I., (2011), Sintering properties of the Bornova shale (Turkey) and its application in the production of red fired ceramics. *Industrial Ceramics*, 31-3.
- [20] Bories, C., Borredon, M.-E., Vedrenne, E., & Vilarem, G., (2014), Development of eco-friendly porous fired clay bricks using pore-forming agents: A review, *Journal of Environmental Management*, 143, 186-196.
- [21] Daniel Martínez, J, Betancourt-Parra, S., Carvajal-Marín, I., Betancur-Vélez, M., (2018), Ceramic light-weight aggregates production from petrochemical wastes and carbonates (NaHCO₃ and CaCO₃) as expansion agents, *Construction and Building Materials*. 180, 124-133.
- [22] Mercan, C., (2020), Alkaliler, uçucu kül ve sinterlemenin hafif agrega üretimine etkisi, Yüksek Lisans Tezi, Kütahya Dumlupınar Üniversitesi, Fen Bilimleri Enstitüsü, Kütahya.
- [23] EN 1097-6, (2015), Tests for mechanical and physical properties of aggregates - Part 6: Determination of particle density and water absorption, Comite European de Normalisation.
- [24] Vigneron, T.Q.G., Vieira, C.M.F., Delaqua, G.C.G., Vernilli Júnior, F., Cristante Neto, Â., (2019), Incorporation of mould flux waste in red ceramic, *Journal of Materials Research and Technology*, 8, 5707-5715.
- [25] De' Gennaro, R., Cappelletti, P., Cerri, G., de' Gennaro, M., Dondi, M., Guarini, G., Naimo, D., (2003), Influence of zeolites on the sintering and technological properties of porcelain stoneware tiles. *Journal of the European Ceramic Society*, 23 (13), 2237-2245.
- [26] Duvarcı, Ö.Ç., Akdeniz, Y., Özmihçı, F., Ülkü, S., Balköse, D., Çiftçioğlu, M., (2007), Thermal behaviour of a zeolitic tuff, *Ceramics International*, 33-5 795-801.
- [27] TS EN 771-1, (2005), Specification for masonry units-Part 1: Clay masonry units, Comite European de Normalisation.
- [28] TS EN 771-4, (2015), Specification for masonry units - Part 4: Autoclaved aerated concrete masonry units, Comite European de Normalisation.



RESEARCH ARTICLE

LOCATION PROOFING USING VIDEO SIMILARITY

Cavide Balkı GEMİRTER^{1,*}, Tacha SERİF²

^{1*}Yeditepe University, Division of Computer Engineering, cavidebalki.gemirter@std.yeditepe.edu.tr, ORCID: 0000-0003-3534-3129

²Yeditepe University, Division of Computer Engineering, tserif@cse.yeditepe.edu.tr, ORCID: 0000-0003-1819-4926

Receive Date:08.05.2022

Accepted Date: 16.06.2022

ABSTRACT

With the increasing availability of mobile devices and technological improvements, location-based services have become a vital part of our everyday lives. However, a layer of checks and verifications might be required to identify the user's declared location authenticity, since it is possible to bypass GPS or any other indoor location detection solutions. Existing location proofing solutions mainly propose techniques requiring some sort of an infrastructure, such as access points and/or beacons, or a co-located prover, witnesses and verifier formation to prove the presence of the user. This paper proposes a location proofing solution using the video similarity technique, which is based on the comparison of visual similarities in video pairs to determine the surrounding environment without any infrastructural overhead. The indoor location test results of our prototype indicate that it can achieve a verification accuracy of 97.05% on average in 9.67 seconds.

Keywords: *Location Proofing, Indoor Location Proofing, Video Similarity, Location-Based Services*

1. INTRODUCTION

In recent years, the growing smartphone market and innovation in mobile technologies have increased the importance of Location-Based Services (LBS) used by applications in many different fields such as finance, public services, and entertainment. For finance applications such as mobile payment systems or ATM withdrawals, verifying the user's physical location during the transaction request is of utmost importance - e.g. confirming that the customer is in front of the ATM machine. On the other hand, in assistive applications such as Foursquare, Google Maps, and Instagram, preventing fake check-ins is essential to eliminate fraudulent content introduction or inclusion.

Location proofs are plain items that enable the development of mobile applications requiring proof of the user location. A location proof is a piece of data that warrants a prover to a geographical place [1,2]. Bearing in mind that most people nowadays carry their cell phones with them all day long. To determine the behaviors and habits of these individuals, using their geolocation over Global Navigation Satellite Systems (GNSS) is a popular way of keeping track of mobile devices [3, 4]. The captured geolocation data needs an external validation mechanism because creating mock locations in these systems is a trivial task [5].

Conventionally, in location proofing solutions [6-12], the prover generally requests a Location Proof (LP) of her/his current position, where an LP is a certified meta-data containing the geographical location [6]. On the other hand, the LP verification mechanism that facilitates this service can either be centralized or decentralized. Centralized architectures [6,9,13] estimate the mobile user's location proximity by relying on wireless components such as a Wi-Fi Access Point (AP) or Bluetooth signal emitter devices [14,15]. However, on the contrary, the decentralized architectures [7,8,10-12,16-19] do not utilize central points, and every mobile device in the network acts as a witness to confirm the locations of other mobile entities. Though, in decentralized architecture, Prover-to-Prover (P-P) and Prover-to-Witness (P-W) collusions are the non-trivial, hard-to-solve security issues, in addition to the privacy concerns, which are created as a result of stored user location data. In a P-P collusion, a prover requests proof for a location where the attacker is not actually present. In a P-W collusion, the dishonest witness generates proof for a location where the witness, the prover, or both are not present.

Maia and Pardal [22] designed a location proof system, called CROSS, relying on Wi-Fi access points. The prototype is a location proofing system implemented as part of a reward-based tourism application scenario, keeping track of users traversing the provided route. The authors propose three different location proof strategies, namely scavenging, Time-based One-Time Password and kiosk. The scavenging strategy is operated in urban areas, employing scan results of Basic Service Set Identifiers (BSSID) as evidence for the Location Proof (LP). BSSID is the MAC address of the Access Points (AP). Time-based One-Time Password (TOTP) strategy is built on customized Wi-Fi APs, ensuring more security by dynamically changing broadcast SSID. The kiosk strategy validates the presence of the user physically. Because the system relies on Wi-Fi for location proximity, the capabilities of the Wi-Fi devices limit the accuracy. Another constraint is that the visitors should be present for at least five minutes in the proper location to guarantee the correctness of the verification results.

From a different perspective, Santos et al. [23] implemented a vehicle tracking system called Secure Transport Location Proofs (STOP), which is aimed to identify vehicles averting from their predefined track. In this solution, every truck driver is expected to utilize his/her mobile phone to log its movement coordinates using GPS data. Then, these collected logs can be used by inspectors to audit the truck's movements so far. The inspectors can use their own mobile devices to contact the driver's data via short-range Bluetooth and download all the logs. The evaluation results of the prototype show that the GPS quality is reduced in urban and densely populated areas due to the limitation of GPS, which requires line-of-sight for best performance. Hence, the worst physical locations from this point of view are the tunnels, which are blocks of concrete where phones totally disconnect from GPS satellites. The average error distance from the exact rotation is calculated between 5 and 9 meters, and the worst case has an error of up to 18.97 meters.

From a different perspective, Hasan and Burns [13] investigate the secure location provenance problem and propose a witness-based solution that generates collusion-resistant location proofs. In this proposed prototype, the user, who needs location verification, sends a request to a publicly accessible location authority, attaching the unique global identifier of the desired place. The location authority responds with a signed LP after making a simple presence check for the requester in the given place. Next, the prover searches for a closer witness through Bluetooth to endorse his LP by performing distance bounding. To guard against location history frauds, the authors also present two schemes set on hash chains and Bloom filters. Evaluation results indicate that 46 proof/second can be achieved with the Bloom filter scheme and 60 proofs/second with the hash chains. Although the

proposed solution eliminates dependency on trusted third parties, standing a centralized architecture is the drawback of the system.

Following suit, Zhu and Cao [8] proposed a neighbor-based solution that allows cooperation between co-located Bluetooth devices to generate LPs for each other. In the prototype, named Privacy-Preserving Location proof Updating System (APPLAUS), the prover broadcasts the request to the neighbor devices over Bluetooth and if there is no response, the prover generates a dummy LP for submitting the updated location to a centralized verification server. If a witness agrees to the proof request of the prover, he generates a response to send back to the prover. In order to increase privacy and protect the content from untrusted nodes, devices periodically change their pseudonyms. The evaluations of the system show that the client code uses less than 2.5% of the available memory, with a CPU utilization between 3% and 5% when communicating with other devices and less than 2.5% power consumption. The authors evaluate the solution's performance for different update and contact intervals ratios. It has been revealed that if the location proof update interval is more than 1.5 of the contact interval, the performance reaches a satisfactory level - above 93%. The weakness of the solution is that it only protects against simple collusion attacks, which do not gather bogus LPs from honest witnesses. The short communication range of Bluetooth constrains the system's efficiency, and periodically generated dummy proofs to preserve privacy cause a communication overhead.

Nosouhi et al. [16] propose a decentralized, blockchain-based, secure, and privacy-aware LP generation and verification approach. The main actors are the prover, the witnesses, the bridge, and the verifier. When a witness endorses the location of the prover, he adds the selected target bridge ID to the LP and sets a timer before sending the message back to the prover after signing the LP request. The timer prevents the Prover-Prover collusions, which have a remote dishonest prover. The witness that receives the response in the given time creates the transaction and forwards it to a nearby bridge. When the bridge receives the message, it compares his identity with the bridge ID written in the message. If the response does not come back from the prover within the appropriate time, the witness sends an N-Ack message indicating a Prover-Prover collusion. In the last step, the bridge forwards the message to the verifier over the internet for doing the post signature controls of the earlier steps. In a successful transaction verification, there must be at least a set of transactions not marked as non-N-Ack. There is a reward in the system, which is the amount paid by the prover to the LP approvers in the final step, with a minimum threshold to prevent Prover-Witness collusions. The authors count the percentage of LP requests that successfully pass the P-P collusion detection for different hash key sizes and timeout system parameters in the evaluation tests. For the key sizes 1024, 2048, and 3072, the timeout parameters of 400, 500, and 700 ms are sufficient for successfully detecting most of the collusions. Nonetheless, the proposed solution is weak to the multiple-party collusion attacks.

The same authors proposed another witness-oriented, decentralized approach where witnesses generate the LPs for other mobile users in ad hoc environments [17]. In addition to dealing with Prover-Prover and Prover-Witness collusion attacks, the authors presented the P-TREAD protocol to increase the system's privacy in the implemented prototype, Privacy-Aware and Secure Proof Of pRoximiTy (PASPORT). Although PASPORT moves the control of witness selection from the prover to the verifier, it is still open to three-way/multi-party collusion attacks.

Zafar et al. [19] focus on three-way collusions, which are not resisted by previous studies. In these collusions, only a single party makes the selection of participants, causing collusion attacks probable. To decrease the chance of location manipulation, the researchers implemented a decentralized and

secure consensus protocol called MobChain. The system separates the choosing control of participants with the LP generation steps. The witness and location authority selection is made in a private blockchain where the nodes are peer-to-peer connected. Because the proposed approach offers substantial secure contracts, falsifying the location becomes impractical. In the evaluation tests, MobChain enhances the protection of LPS in a computationally efficient and highly available way compared with state-of-the-art techniques.

Diversely different from prior studies focusing on infrastructural system changes, some researchers draw attention to the advantage of the media for location proofing. Bucher et al. [21] presented a cheap to implement system built on visual features using image recognition with no infrastructural overhead. There are three leading roles in the architecture as follows: (1) LBS Provider like a web application, (2) location owner who owns the place like a restaurant or cafe, and (3) the user client requesting the LP. When a user requests an LP, the LBS provider assigns a task to the user as taking a picture of the given location, similar to the already present image data set saved in the central server. After collecting a sufficient number of pictures for a particular place, the system quickly detects the real and bogus LP requests. The given challenge task may be one of these options: taking a new photo contributing to the image tree, an overlapping copy of an image randomly selected from the tree, or a partially overlapping image like completing half of an existing image. The system results in better performance, especially on crowd-sourced destinations where a service provider confirms the collected data's authenticity. In the evaluation tests, although the prototype cannot prove all of the users from a cryptographic security perspective, the system catches the majority of the attacks in most of the scenarios. The limitations of this approach are that at least an honest user must be contributed to the given places. Completing the given challenge will be feasible for indoor locations such as restaurants, but it will not be easy for large-scale outdoor areas like parks to find the correct part of the place to take the picture defined in the assigned task.

In the video subsection of the media domain, video filtering, video suggestion, and copyright protection are the challenging research problems. Kordopatis-Zilos et al. [24] address the problem of similarity estimation between video pairs. Previous video retrieval approaches embed the entire frame or video into a vector embedding. The implemented prototype, called Fine-grained Spatio-Temporal Video Similarity Learning (ViSiL), considers fine-grained SpatioTemporal relations to consist of intra-frame and inter-frame connections, commonly lost in previous studies. The study shares evaluation comparisons against near-duplicate video retrieval, fine-grained incident video retrieval, event video retrieval, and action video retrieval subtasks of the computer vision domain.

Extracting information from video and visual content has been an active research area since the 2000s [20]. Accordingly, compared to infrastructural system-focused approaches, employing media for location proofing could be used as another totally different solution avenue. In this approach, location proofing is achieved by comparing the visual features of two images or video frames, to check whether the two locations are the same place or not [21]. Hence, this paper proposes location proofing using the video similarity technique, which addresses the challenges mentioned above. Furthermore, it describes a novel location proofing solution based on a comparison of the visual similarities in video pairs to determine the surrounding environment without any infrastructural prerequisites. To the best of our knowledge, there is no work that has utilized video similarity evaluation techniques for location proofing purposes.

2. MATERIAL AND METHODS

Location proofing using video similarity consists of two major parts. Employing the live video streaming ability of web or mobile clients with cameras in the source device, the user records a short panoramic video clip of the indoor environment as proof of existing in the selected location. The second part checks the validity of the recorded video, comparing it with the already collected and approved video files for the proper location. This section firstly provides information about the WebRTC [25] protocol used on the clients for live streaming, followed by the ViSiL [24] framework, which calculates the video similarity scores of multiple video files.

2.1. Web Real-Time Communication (WebRTC)

With the wide use of the internet and the increased popularity of smartphones, video streaming has become a de facto segment of communication applications such as social media, chat platforms, and video conferencing [26]. Although video communication seems straightforward, like data transfer, the most challenging characteristic of the video is that it requires a considerable bandwidth [27].

WebRTC is a state-of-the-art open technology, published by the World Wide Web Consortium (W3C) [28], a standard for end-to-end encrypted real-time communication between Internet browsers for media and data transfer. The main logic of WebRTC is that the client browsers register a common communication service provider website, as shown in Figure 1.

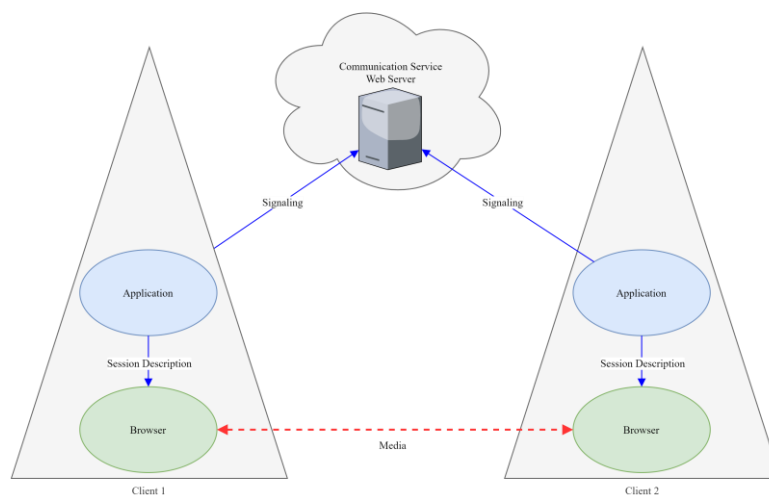


Figure 1. The main architecture of the JSEP protocol.

After the website publishes the browser IDs of the connected clients to the requester client, the client browser can establish a peer-to-peer communication with the target browser directly without knowing the exact IP addresses. To overcome the IP address and port requirement of the P2P networks, WebRTC establishes signaling channels between the website server and the clients using Web Socket technology and JavaScript Session Establishment Protocol (JSEP) [29] to create the offer and answer messages. After the proposal of WebRTC, browser vendors (Google Chrome, Mozilla Firefox, Safari, and Internet Explorer) implemented the WebRTC API for browser-to-browser communication

management and introduced a set of more easy-to-use JavaScript functions for application developers. A specific method named “getUserMedia” is used to access both the client devices’ audio and video input and outputs with the user’s attention for taking approval of the usage. WebRTC has three main functions. RTCPeerConnection is the service provider API for peer-to-peer communication, RTCDataChannel establishes a full-duplex data communication between the clients, and MediaStream denotes audio or video data streams. Only the MediaStream function of the WebRTC protocol is enough for capturing video frames from the client device camera, disabling the audio sources.

2.2. ViSiL: Fine-grained Spatio-temporal Video Similarity Learning

As a result of the increasing popularity of video-sharing services such as YouTube, publicly visible video content on the internet has been boosted to remarkable scales. The video recommendation and copyright reservation systems have become crucial parts of these applications.

ViSiL is a video similarity learning network for handling the similarity calculation and estimation of multiple videos. Traditional approaches group the features of all the video frames into a single video-level vector descriptor, ignoring the spatial and temporal layout of the visual similarity.

On the other side, ViSiL deals with both the spatial (intra-frame) and temporal (inter-frame) structure of the visual content when calculating the similarity to avoid ignoring the regional details. The main architecture of the video similarity calculation process is illustrated in Figure 2. First, the system extracts the feature vectors (output of Figure 2.a) of each frame of the provided video pair by utilizing a pretrained Convolutional Neural Network (CNN). After several normalization and whitening steps, the features are weighted with an attention mechanism. A similarity matrix (output of Figure 2.b) of the video pairs is built with the Tensor Dot (TD) product which computes the pairwise frame-to-frame similarity, followed by a Chamfer Similarity (CS) to calculate the region-to-region similarity without feature aggregation. TD gives the sum of tensor pairs for the given axes. CS is the similarity counter of Chamfer Distance by calculating the average similarity of a set of items for the given property. The similarity matrix (output of Figure 2.c) is the input of another four-layered CNN that has a CS final layer to summarize the video-to-video similarity score. The definitive score has a value between [-1, +1], where negative values indicate irrelevant and positive values denote relevant video pairs.

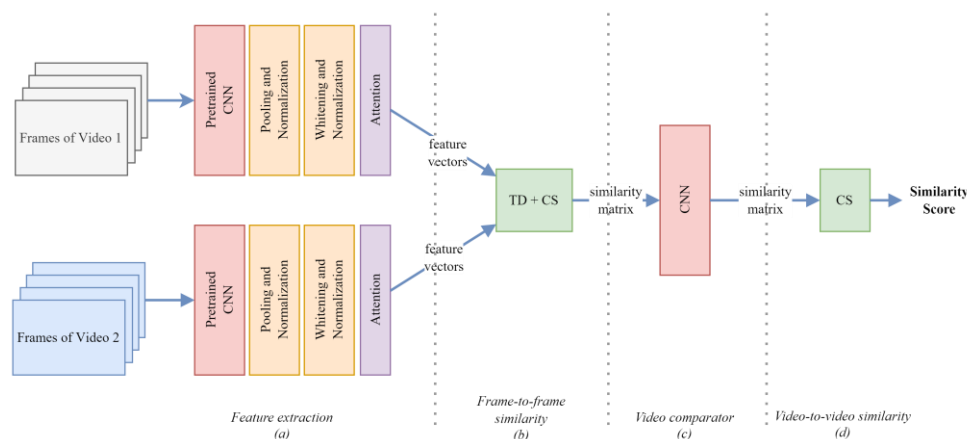


Figure 2. The main architecture of the ViSiL framework.

2.3. System Design

This section discusses and examines the requirements for achieving the necessary functionality of the proposed system.

2.3.1. System analysis

The idea behind the approach is based on the similarity of video pairs recorded in several locations. The mechanism needs an application to serve the user in a mobile environment, a native mobile application, or a website running on mobile browsers like Chrome or Safari.

The video verification task is based on memory-hungry computer vision algorithms. Because the algorithm will compare the recorded video with the other video pairs, the operating environment needs to access the earlier recorded videos of the given location. Hence, the video verification operation could not be completed on the client's mobile device; a central server must handle the task, which has sufficient disk size, CPU, and memory.

An external authentication mechanism is needed to trust and identify the user, requesting the location proof. The unique user ID returned by the authentication service will be used in all the operations. After a successful login, already present locations in the system are displayed to the user for his selection. The user may select one of these options or enter a new location name.

The user's smartphone should have a video input device to record a video as evidence of the location proof. If multiple cameras are attached to the device, the user should select one of these inputs. Modern smartphones have at least two cameras, one is in the front, and one is in the rear. The mechanism should force the rear camera to record a better panoramic video of the environment.

The resolution of the camera is another constraint on the client device. Low-resolution videos will not result in apparent feature vectors. Recorded video on the client device will be sent to the centralized server for verification. Transferring high-resolution videos will take longer and be sensitive to communication errors. So, 640x480 will be the exact resolution supported by the solution. If the client camera does not support this minimum threshold resolution, the recording operation should not be started on the device.

WebRTC is the state-of-art technology used to capture the media streams on client browsers. Most modern browsers natively support WebRTC, but there are some exceptional browsers. The browser on the client device should support the WebRTC protocol to record the video. When the web application calls the `getMediaStream` function of the WebRTC protocol, the browser asks the user to allow accessing the selected camera. The user's attention is required to start the capturing process in this step. In the recording phase, the audio will be muted.

Correctly defining the length of the recorded video is crucial. Longer videos will be sent to the central server in a long time, and also, the computer vision tasks in the verification phase will take much more time. Five-second long video will be sufficient to identify the video's features and calculate the similarity with other videos. If the application captures ten frames each second, there will be 50 frames in total.

While recording the video, the user should slightly swivel the camera toward the left and right for best performance. When the video clip is not recorded in a panoramic view, documenting a narrow area for

5 seconds would result in an image rather than a video, not including temporal data, and would have a weak feature spectrum compared to the video. To eliminate this problem, the algorithm should check the sanity of the videos with a static content filter.

When the location is new and there are no earlier sample videos in the repository, the system may automatically accept the video for the first a specific number of samples. Rather than automatically accepting the initial videos as marking positive samples of the given location, a manual check either be done by the place owner, who is the restaurant, or the café administrator.

Instead of continuously getting new video samples of the locations from the users, some additional controls should be added to the system to increase the security level. A challenge-based approach defined in Bucher et al.'s study may be an example. For the given location, the solution may sometimes get new video samples, or sometimes the application will assign some task to the user to complete as recording a video, including a displayed image or a video slice.

2.3.2. Solution design

The proposed system has two primary and one optional stakeholder; (1) the user who requests a location proof, (2) the location-based service provider running the algorithms in the server, and (3) the optional location owner who is the business administrator of a restaurant or café.

The sequential diagram of the proposed solution is shown in Figure 3. Initially, the user opens the web application served by the LBS provider, deployed on a centralized server. After a successful login operation done by an external authority, the web application lists the earlier locations present in the system. The user may select one of these locations or enter a new location name. Then, the user requests a challenge from the LBS provider for submitting the LP. The LBS provider has two options: request the user to record a new video or, after randomly selecting one of the earlier videos of the selected location, the LBS provider requests the user to record a video including the displayed frame. The user has two minutes to complete the task.

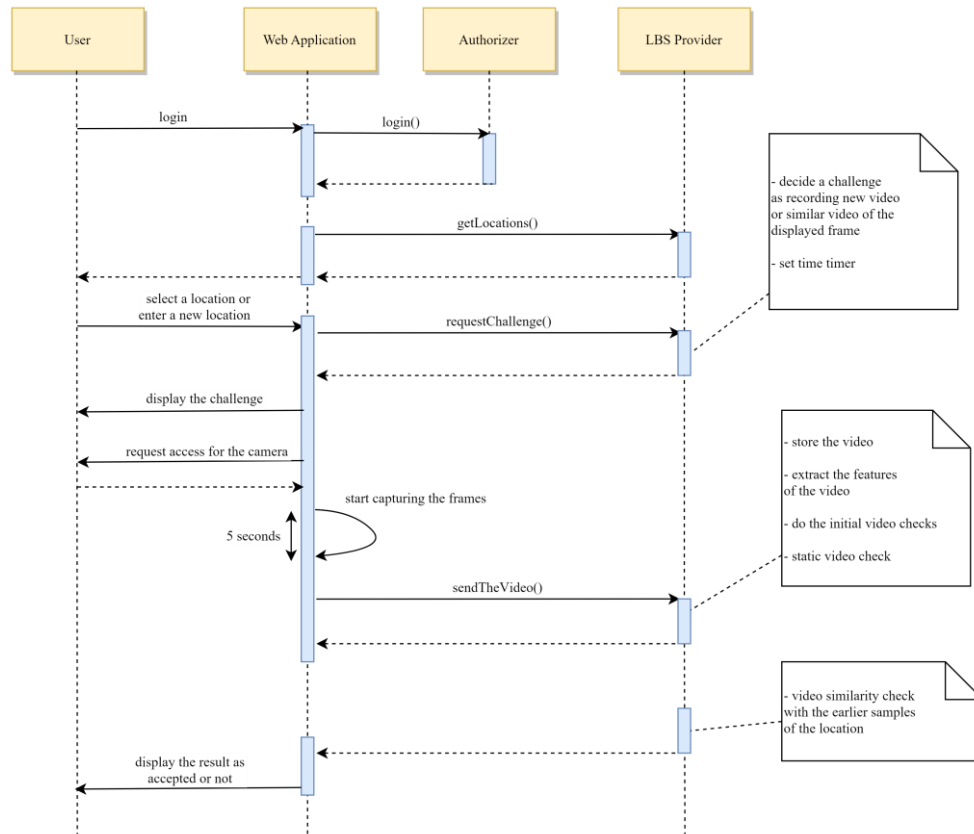


Figure 3. The sequential diagram of the proposed solution.

After defining the challenge to the user, the web application asks the user to select the video input and requests allowing access to the selecting camera. The web application captures fifty frames for five seconds while the user slightly turns the camera in the environment to have a panoramic view. The web application sends the recorded video frames to the LBS provider at the end of the recording. If the challenge is not completed in two minutes, the LBS provider automatically rejects the LP request. When the LBS provider receives the video in the given time interval, it checks the initial sanity of the video by counting the frames, extracting the feature vectors of the video followed by operating the static video filter. Then, the LBS provider saves the video for further video similarity check batch operation.

The recorded video is the evidence of the prover, which is marked as the source video of the LP request in the location. The target videos are stored attachments of already authorized LP requests of the proper location, used as similarity hints by the affinity mechanism of the system. This mechanism examines the video pairs to see if they look like each other by comparing their visual features and detects whether they are recorded in equivalent locations or not. When the similarity check is done, the result of the LP submission is displayed to the user as Accepted or Rejected.

2.3.3. System architecture

The system architecture of the proposed solution is shown in Figure 4. The web application server publishes the web application, which serves on the client's PC or smartphone and communicates with the video input sources of the device over WebRTC technology. The web application communicates with the backend server over the internet and gets services using POST API calls. The backend server contains the LBS provider, responsible for the service operations, and the affinity system operating the video and neural network accelerated operations. Rather than a standalone database server, simple Comma Separated Values (CSV) files are used to store the status of the operations and results. Both the LBS provider and Affinity system share the common file system to store and read the video files; the LBS provider writes the video files, and the affinity system reads these files and stores the extracted feature vectors. The affinity system employs the pretrained neural networks, which extract the feature vectors of the videos and calculate the video similarities.

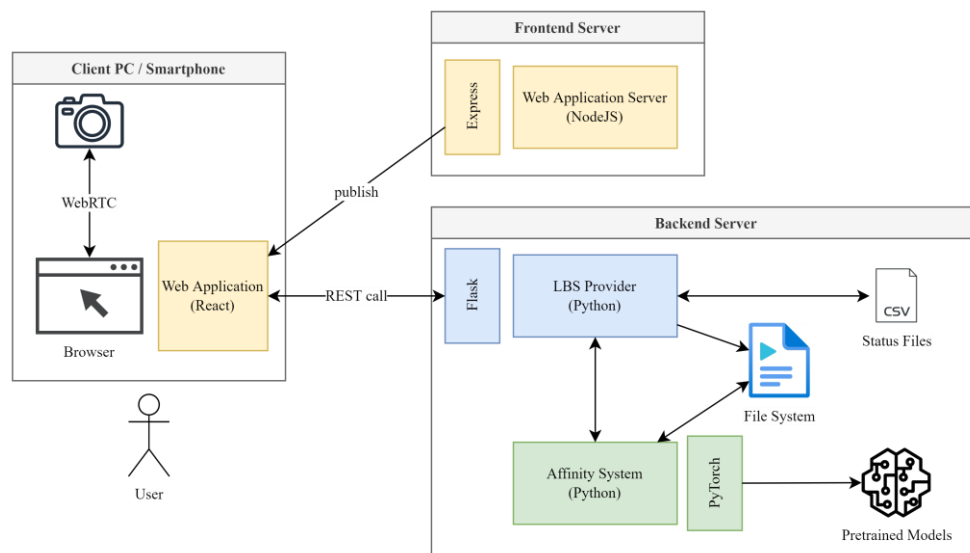


Figure 4. The system architecture of the proposed solution.

2.4. Implementation

The solution has recording and verification phases. In the recording phase, the user logs in to the system, requests a location proof, and records a video to complete the assigned challenge tasks. Next, the LBS prover launches several controls over the process and checks the sanity of the recorded video. In the verification phase, the affinity mechanism runs the video similarity algorithms to approve or reject the LP request. The user can visually track earlier submitted requests and their ongoing or completed statuses from the website's history section.

2.4.1. Recording phase

The LBS provider interacts with the user over a website. The website initially redirects the user to a third-party login page; Google 2.0 Authentication algorithm is selected in the solution. After a successful login operation, the user identifier is attached to the session as the input for further

validations. The user chooses the desired location from the earlier documented locations list or enters a new place name as the location input and requests location proof from the LBS provider.

As part of the challenge assignment step, the system examines whether the location input is present in the database or it is a new location. If a new location is entered, the LBS provider requests the user to record a short panoramic video clip in the given place. If the user selects a place from the locations list, the LBS provider assigns a challenging task to the user, which is randomly selected from the following two options. In option (1), the algorithm requests the user to record a new video in the given place like the previous step. This task aims to enrich the video repository with new video visuals. In option (2), the algorithm randomly selects one of the target location's earlier registered and approved videos, as a candidate video V_C , followed by randomly selecting one of the frames F_C of this candidate video V_C . Next, the system assigns a challenge to the user, and the user has only two minutes to complete the given task. This two-option and timer-based challenge process seek to increase the security level and prevent fake user attacks by uploading bogus videos. Two minutes is long enough to complete the challenge but short to integrate the previously displayed frame into a video for faking the proposed task. When the challenge is assigned to the user, the LBS provider sets up a two minutes timer, generates a unique identifier for the generated challenge, and responds to the user.

In the video recording step, the website displays the candidate frame F_C to the user if option (2) is selected. Then, for using the live media capturing capabilities of the smartphone's browser, the web application requests the user to allow access to the environment camera of the device. If the user device has more than one camera, the system asks the user to select one of these cameras as the source. After the user gives permission, the application starts frame capturing for five seconds. The application records ten frames every second, and 50 frames are collected to build the video. Then, the application stops capturing and sends the video frames back to the server with the challenge and user identifiers.

The LBS provider first checks the status of the timer, and if it has timed out, the system automatically rejects the LP request. Secondly, the algorithm counts the frames and scans their order. After validating the challenge and user identifiers with the submitted ones in the initial LP request, the algorithm extracts the visual features of all the frames and builds a three-dimensional cube vector representing the source video. The static content filter utilizes the frame-to-frame similarity of the ViSiL approach to check if the video has a valid panoramic view. The system calculates the frame similarity of each video frame by comparing it with the rest of the frames one by one. If the average frame-to-frame similarity score exceeds the threshold system parameter, the algorithm rejects the video and marks it as holding static content.

2.4.2. Verification phase

The system sets the recorded video as the source of the similarity algorithm. If the submitted video contains a location that is new and there are no earlier sample videos of this location in the repository, the system automatically accepts the video as the first sample video - out of three. If an existing location is selected from the drop-down menu and option one (1) is picked by the system, the algorithm sets all the earlier recorded samples of the chosen location as target videos. In this way, the system compares the similarity of the latest recorded video with the rest of the earlier samples. If option (2) is picked by the system, then video V_C , which contains the randomly chosen candidate frame F_C , partially or fully is set as the target video. Then, the algorithm only compares the similarity of the recorded video with V_C , which could either be the full length of the video or a part of it. Trials

development phase showed that one-second video is long enough to be sure that the video is recorded in the same place and short enough not to force users to shoot the same video with the V_C .

After defining the source and target videos, the system performs the video similarity check, operating the methods defined in the ViSiL framework. Initially, the visual features are extracted by applying a pretrained Convolutional Neural Network (CNN) to the frames of the video pairs. Initially, for each video in the pair, the visual features are extracted from the frames by involving a pretrained Convolutional Neural Network (CNN). After several normalization steps, the attention mechanism weighs the features. Tensor Dot (TD) product is applied to measure the pairwise frame-to-frame similarity between the source and target videos, which outputs a similarity matrix by summarizing the tensor pairs on proper axes. Next, Chamfer Similarity (CS) employs this similarity matrix and computes the region-to-region similarity by counting the Chamfer Distance without feature aggregation. Chamfer Distance is the average similarity of the items set for the given property. The last step is another four-layered CNN with a CS final layer which obtains the similarity matrix and summarizes the video-to-video similarity score. The conclusive score has a value between $[-1, +1]$, where negative numbers point to irrelevant and positive numbers distinguish relevant video pairs. If there are numerous target videos, the system independently calculates the similarity of each target video with the source video and brings the maximum value as the final decision.

After the affinity mechanism completes the similarity checks of the recorded video, the LBS provider updates the status of the LP request historical record in the system as Accepted or Rejected. For evaluating the sanity of the decision, the web application opens a survey to the user whether the given result is correct or not. These grading results are collected and analyzed in the evaluation results.

2.4.3. Development details

The system has three development components: (1) the web application serving the user, (2) the LBS provider as the backend server, and (3) the affinity system responsible for video operations and similarity checks. The web application is developed with React 4+ and deployed with Express modules on a NodeJS server. React is selected because it natively supports a vast spectrum of modern browsers. LBS provider is developed with Python 3.10 and serves as again a web server using Flask modules. Instead of using a standalone database server, simple CSV files, maintained with Pandas, are used to store the status of the system and the operations. The affinity system is built inside the LBS provider, and the computer vision components are implemented using the Python Pytorch library. The web application communicates with the LBS provider over the internet and gets services over POST API calls. The topology of the system is shown in Figure 5. Because the affinity system is a memory-hungry and computationally costly component, the web application server and LBS provider are separately deployed on different servers. Both LBS provider and affinity system is deployed on the same server to access the same file system which hosts the stored video files and feature vectors.

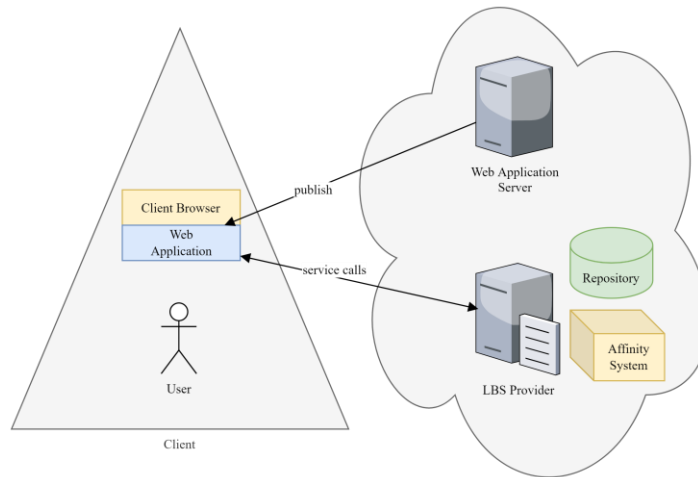


Figure 5. The topology of the proposed solution.

3. RESULTS AND DISCUSSION

3.1. Experimental Setup

The implemented system components are deployed on cloud platforms for evaluation tests. The web application server is deployed on a free dyno of the Heroku service platform, located in the United States, with a slug size of 68.2 MB. The LBS provider is deployed on an e2-medium machine typed Google Cloud compute engine, with one vCPU, 4 GiB memory, Ubuntu 18.04 operating system, located on us-central1-a zone. The clients are located in Istanbul (Turkey) and Bologna (Italy). Apple iPhone 11, iPhone X, iPhone 7 and General Mobile 9 Pro smartphones are used as the clients in the tests. For iOS-based clients, both the Safari and Chrome, and for Android typed phones, only the Chrome browser is operated as the browser.

3.2. Evaluation Results

3.2.1. CPU and memory utilization

In order to evaluate resource usage of the LBS provider, CPU and memory usages are captured from the server where the component is deployed. For an accurate evaluation, only the LBS provider is deployed as a single-process application on the cloud virtual machine to minimize the effect of other threads. The captured CPU and memory usage are shown in Figure 6. There are some peaks in the CPU usage when the affinity system processes are active, like extracting the video features and calculating the video similarity of video pairs. CPU usage significantly drops to 0% when the system is idle. The average CPU usage of the system is 2.214%, with a minimum value of 0% and a maximum value of 89.1%. Unlike CPU, memory usage is not sensitive to the affinity system threads. After the predefined models are loaded during the initialization step of the application, the memory usage is increased to 18.5%. It is increased to 26.7% on active video operation threads. The average memory usage of the system is 23.91%, with a minimum value of 18.5%.

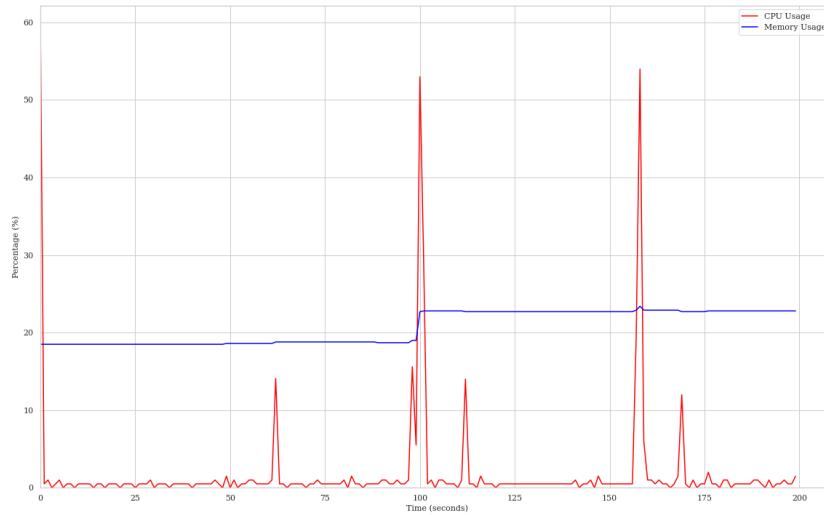


Figure 6. The CPU and Memory usage of the LBS provider.

3.2.2. Processing time of the operations

This section evaluates the processing time of the client and server operations. The most time-consuming operation in the process is uploading the videos from the client to the server. The duration is directly related to the network communication quality between the client and the cloud server location in the U.S. The upload time increases up to 20 seconds when the connection bandwidth is very low. For a 5-seconds long video having a resolution of 480x640, the average upload video time of the client is 9 seconds, with a minimum value of 5.75 and a maximum value of 19.79 seconds. The operation time likewise doubled when the video length is increased from 5 seconds to 10 seconds. There is even a direct positive proportion between the resolution of the video and the uploading time. When the resolution is increased to 768x1024, the time duration is expanded from 9 seconds to 15 seconds.

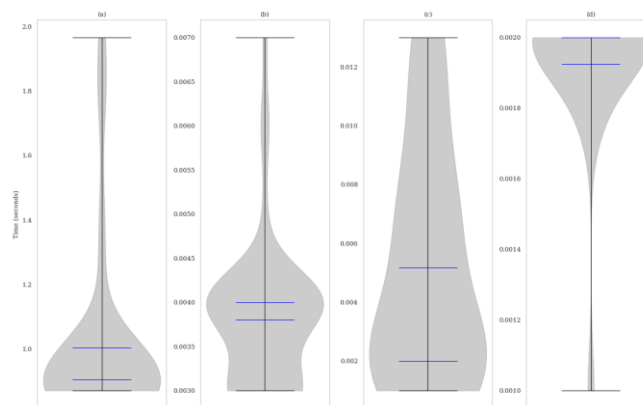


Figure 7. The processing time of operations. (a) Extract features. (b) Static video check. (c) Video similarity check. (d) Video similarity check (normalized).

There are three time-consuming primary operations done on the server-side, shown in Figure 7. The first violin shape illustrates the time taken to extract the features of the videos. In an only CPU environment, the average processing time of extract feature operation is 1.003 seconds, with a minimum value of 0.871 seconds and a maximum value of 1.966 seconds. Compared to the other affinity system jobs, this is the most time-consuming computer vision accelerated step that employs the pretrained CNN module. If the server has a GPU (Tesla V100) and the operation is done with a batch size of eight, the duration significantly drops to 0.5 seconds on average.

The second shape represents the time duration of the static video review operation. For a five-second long video, the operation takes 0.003 seconds on average, with a minimum value of 0.003 seconds and a maximum value of 0.007. The standard deviation of the time is very low compared with the other affinity system processes. Operating GPUs does not result in a significant improvement in the processing time.

The last two violins illustrate the processing time of video similarity operation. There are two types of challenges in the solution. The user may upload a new video to the system, and the affinity system compares the video with all of the other videos already recorded and approved in the given location. In this challenge, the video similarity examination operation is repeated n times, where n is the number of earlier captured videos in the location. In the second option, the client records a video, including the displayed frame, to the user. The video similarity operation is done only once in this scenario. The third violin represents the all-time taken operation for the video similarity check operation, and the last one is the normalized version of the time in which the total time is plotted in (c) is divided by the video count, indicated as n . For a five-second long video, the operation takes 0.005 seconds on average, with a minimum value of 0.001 seconds and a maximum value of 0.013. When the data is normalized, the average time is measured as 0.001 seconds, with a minimum value of 0.001 seconds and a maximum value of 0.002.

3.2.3. Accuracy results of the verification

After displaying the verification result of the location proof operation, the prototype asks the user to grade the response as correct or wrong. Depending on these human testing results, the accuracy of the affinity system is calculated. For the static video review step, the accuracy is measured as 98.2%. The algorithm only fails for the videos when the user moves the smartphone camera more slowly than the expected threshold, during the recording step.

For the first option type of challenge - a user uploading a new video for the given location - if the threshold system parameter is set to 0.8, the algorithm's accuracy is 85.0%. On the other hand, if the threshold parameter is decreased to 0.5, the accuracy increases to 99.5%. For the second option challenges, the accuracy is decreased to 71.4% when the target video is set to a one-second-long sub video, including the displayed candidate frame. The accuracy is significantly increased up to 92.85% when the target video length is set to three seconds and 99.5% when the target video is not cropped. The average accuracy of the video similarity check operation is calculated as 97.05% in summary.

The algorithm fails when the video includes many irrelevant features that mislead the system to identify the location environment, like humans or static visual parts such as empty walls in the rooms. Compared to outdoor environments, the algorithm gives better results in indoor environments. When the prototype is tested on a national park where there are many similar patterns like the lakes, trees, or the grasses, the affinity system video similarity check algorithm accuracy goes down.

4. CONCLUSIONS

This paper presents a novel centralized architecture for location proofing, which contrary to earlier studies, does not need or require any sort of hardware or infrastructure. The proposed approach is based on comparing visual similarities in video pairs to determine the surrounding environment. The affinity system built in the LBS provider has two main parts. Operating the live video streaming ability of web or mobile clients with cameras in the source device, the user records a short panoramic video clip of the indoor environment as proof of existing in the selected location. The second part checks the validity of the recorded video, comparing it with the already collected and approved video files for the proper location. Because the system does not require any additional settings on the client-side and customized network components placed in the locations, it can be easily integrated into daily life location proof required scenarios.

The implemented prototype system can perform with limited CPU needs, where the average CPU use rate is 2.21%, and the maximum use rate is 89.1%. Furthermore, the memory consumption does not go beyond the 26.7% limit, and the time needed for the server to extract the features of a video is 1.003 seconds on average. Extraction time could be even reduced by 0.5 seconds with the use of a GPU. On the other hand, on a client device, it takes on average 9 seconds for a 5-seconds long video with a resolution of 480x640 to be uploaded to the server. Overall, the prototype's similarity check accuracy is 97.05% in an indoor environment. Bearing in mind the above results, it is clear that this type of solution would fit great in a scenario where the user is aiming to prove the location of an indoor environment with no physical networking infrastructure. Considering the latest move from popular streaming services, where they try to prevent their subscribers from accessing content from multiple sites, integrating a user location proving system would be an effective way to achieve this goal. Accordingly, the solution proposed as part of this work can facilitate a control mechanism without requiring any additional software or hardware infrastructure.

Like all other location proofing systems, the proposed method has its shortcomings too. This prototype accepts the first three samples of a newly registered location without conducting any checks and accepts them as is. If a dishonest user creates a new location and uploads an initial couple of bogus videos, there are no additional control mechanisms to prevent this. Also, need to be considered the cases where the user moves the smartphone camera slower than the expected threshold while recording; this results in the static video check algorithm failing. Furthermore, the video similarity algorithm may not perform as required if the video includes notable unrelated features that mislead the system in identifying the location environment - e.g. too many people in a closed environment or blank patterns. As a result of this, compared to outdoor environments, which may be crowded with humans, objects, and blank patterns, the algorithm performs better in indoors. The most noteworthy drawbacks of the system are not having a satisfactory success rate in outdoor environments and automatically accepting the first three samples in a new location without any control. In order to increase the success in outdoor environments, recent computer vision algorithms can be evaluated and adapted to the system, which may improve the overall performance. Considering the inherited issue with this approach, which requires the system to accept the first three videos as authentic, wireless infrastructure or beacon style solutions can be integrated into this so that it will act as a failsafe and provisioning solution. Hence, the existing system will be merged with a network-based approach, and their findings will be shared with academia.

ACKNOWLEDGEMENT

The authors declare that there was no conflict of interest in the course of this study.

REFERENCES

- [1] Saroiu, S., & Wolman, A. (2009, February). Enabling new mobile applications with location proofs. In Proceedings of the 10th workshop on Mobile Computing Systems and Applications, 1-6.
- [2] Ferreira, J., & Pardal, M. L. (2018, November). Witness-based location proofs for mobile devices. In 2018 IEEE 17th International Symposium on Network Computing and Applications (NCA), IEEE, 1-4.
- [3] Kenan, M. (2021, April). Comparative analysis of localization techniques used in lbs. In 2021 5th International Conference on Computing Methodologies and Communication (ICCMC), IEEE, 300-304.
- [4] Martins, P., Abbasi, M., Sa, F., Celiclio, J., Morgado, F., & Caldeira, F. (2019). Intelligent beacon location and fingerprinting. *Procedia Computer Science*, 151, 9-16.
- [5] Alamleh, H., & AlQahtani, A. A. S. (2020, July). A cheat-proof system to validate GPS location data. In 2020 IEEE International Conference on Electro Information Technology (EIT), IEEE, 190-193.
- [6] Saroiu, S., and Wolman, A. (2019, February). Enabling new mobile applications with location proofs. In Proceedings of the 10th workshop on Mobile Computing Systems and Applications, 1-6.
- [7] Wang, X., Pande, A., Zhu, J., and Mohapatra, P. (2016). STAMP: Enabling privacy-preserving location proofs for mobile users. *IEEE/ACM transactions on networking*, 24(6), 3276-3289.
- [8] Zhu, Z., and Cao, G. (2011, April). Applaus: A privacy-preserving location proof updating system for location-based services. In 2011 Proceedings IEEE INFOCOM, IEEE, 1889-1897.
- [9] Javali, C., Revadigar, G., Rasmussen, K. B., Hu, W., and Jha, S. (2016, November). I am alice, i was in wonderland: secure location proof generation and verification protocol. In 2016 IEEE 41st conference on local computer networks (LCN), IEEE, 477-485.
- [10] Davis, B., Chen, H., and Franklin, M. (2012, May). Privacy-preserving alibi systems. In Proceedings of the 7th ACM Symposium on Information, Computer and Communications Security, 34-35.
- [11] Talasila, M., Curtmola, R., and Borcea, C. (2010, December). Link: Location verification through immediate neighbors knowledge. In International Conference on Mobile and Ubiquitous Systems: Computing, Networking, and Services, Springer, Berlin, Heidelberg, 210-223.

- [12] Gambs, S., Killijian, M. O., Roy, M., and Traoré, M. (2014, October). PROPS: A privacy-preserving location proof system. In 2014 IEEE 33rd International Symposium on Reliable Distributed Systems, IEEE, 1-10.
- [13] Hasan, R., and Burns, R. (2011). Where have you been? secure location provenance for mobile devices. arXiv preprint arXiv:1107.1821.
- [14] Logan, L., Davids, C., & Davids, C. (2020, May). Determining the Indoor Location of an Emergency Caller in a Multi-story Building. In 2020 IEEE International Workshop Technical Committee on Communications Quality and Reliability (CQR), IEEE, 1-6.
- [15] Goh, B. S., Mahamad, A. K., Saon, S., Isa, K., Ameen, H. A., Ahmadon, M. A., & Yamaguchi, S. (2020, January). IoT based indoor locating system (ILS) using bluetooth low energy (BLE). In 2020 IEEE international conference on consumer electronics (ICCE), IEEE, 1-4.
- [16] Nosouhi, M. R., Yu, S., Zhou, W., Grobler, M., and Keshtiar, H. (2020). Blockchain for secure location verification. *Journal of Parallel and Distributed Computing*, 136, 40-51.
- [17] Nosouhi, M. R., Sood, K., Yu, S., Grobler, M., and Zhang, J. (2020). PASPORT: A secure and private location proof generation and verification framework. *IEEE Transactions on Computational Social Systems*, 7(2), 293-307.
- [18] Barabas, P., Regnath, E., & Steinhorst, S. (2020). COLAW: Cooperative Location Proof Architecture for VANETs based on Witnessing. In 2020 International Conference on Omni-layer Intelligent Systems (COINS), IEEE, 1-8.
- [19] Zafar, F., Khan, A., Malik, S. U. R., Ahmed, M., Maple, C., and Anjum, A. (2021). MobChain: Three-way collusion resistance in witness-oriented location proof systems using distributed consensus. *Sensors*, 21(15), 5096.
- [20] Gulliver, S. R., Serif, T., and Ghinea, G. (2004). Pervasive and standalone computing: the perceptual effects of variable multimedia quality. *International journal of human-computer studies*, 60(5-6), 640-665.
- [21] Bucher, D., Rudi, D., and Buffat, R. (2018, January). Captcha your location proof—A novel method for passive location proofs in adversarial environments. In LBS 2018: 14th International Conference on Location Based Services, Springer, Cham, 269-291.
- [22] Maia, G. A., and Pardal, M. L. (2019). CROSS: loCation pROof techniqueS for consumer mobile applicationS. INForum. Guimaraes, Portugal.
- [23] Santos, H. F., Claro, R. L., Rocha, L. S., and Pardal, M. L. (2020, October). STOP: A Location Spoofing Resistant Vehicle Inspection System. In International Conference on Ad-Hoc Networks and Wireless, Springer, Cham, 100-113.

- [24] Kordopatis-Zilos, G., Papadopoulos, S., Patras, I., and Kompatsiaris, I. (2019). Visil: Fine-grained spatio-temporal video similarity learning. In Proceedings of the IEEE/CVF International Conference on Computer Vision, 6351-6360.
- [25] (2022, May). WebRTC 1.0: Real-Time Communication Between Browsers. <https://w3c.github.io/webrtc-pc/>
- [26] Suciu, G., Stefanescu, S., Beceanu, C., and Ceaparu, M. (2020, June). WebRTC role in real-time communication and video conferencing. In 2020 Global Internet of Things Summit (GloTS), IEEE, 1-6.
- [27] Rhinow, F., Veloso, P. P., Puyelo, C., Barrett, S., and Nuallain, E. O. (2014, January). P2P live video streaming in WebRTC. In 2014 World Congress on Computer Applications and Information Systems (WCCAIS), IEEE, 1-6.
- [28] <https://www.w3.org/>(2022, May 5). World Wide Web Consortium (W3C).
- [29] Koh, E. (2010, November). Conferencing room for telepresence with remote participants. In Proceedings of the 16th ACM international conference on Supporting group work, 309-310.



RESEARCH ARTICLE

CONFINEMENT EFFECTS on the TRANSPORT PROPERTIES of ROOM TEMPERATURE IONIC LIQUID BASED ELECTROLYTES in SUPERCAPACITORS

Betul URALCAN*

*Bogazici University, Department of Chemical Engineering and Polymer Research Center, betul.uralcan@boun.edu.tr, ORCID: 0000-0002-0669-8441

Receive Date:26.05.2022

Accepted Date: 18.06.2022

ABSTRACT

The study of transport properties in supercapacitors is important for optimizing their power density. Properties that control charging kinetics in supercapacitors include ion self-diffusion coefficients and ionic conductivity which are significantly different at electrode/electrolyte interfaces compared to their bulk counterparts. Here, we use molecular dynamics simulations to elucidate the effect of electrolyte composition and confinement on ion self-diffusion coefficients and ionic conductivity in mixtures of room temperature ionic liquids with organic solvents. Our results reveal that ion diffusion significantly slows down at the electrode/electrolyte interface compared to the bulk. In particular, diffusion coefficients in the dilute regime are found to be several orders of magnitude smaller than their bulk counterparts. This effect is more pronounced when a potential difference is applied between the electrodes. We show that the ionic conductivity of the electrolytes also significantly diminishes due to confinement effects manifested by the decrease in the coordination numbers of ions. Our findings depict that electrolyte composition also plays an important role in ion dynamics: Introduction of an organic solvent to a concentrated ionic solution significantly increases both bulk and interfacial diffusion coefficients while it leads to a maximum in ionic conductivity at intermediate dilution levels. These results reveal that optimizing the solvent content of an ionic liquid-based electrolyte can potentially boost the power density of supercapacitors.

Keywords: *energy storage, supercapacitors, molecular dynamics, diffusivity, conductivity*

1. INTRODUCTION

Supercapacitors are energy storage devices that can deliver bursts of energy at high power densities through storing charges at an electrode/electrolyte interface [1–3]. Despite their lower energy densities compared to conventional electrochemical energy storage devices such as batteries, supercapacitors are already employed in high power applications such as blade angle control systems of wind turbines, battery-assist and regenerative power systems of electric/hybrid cars, and engine starts for construction and industrial equipment [4].

The performance of a supercapacitor is based on two principal metrics: energy density (E) in units (Wh/kg or Wh/cm³) and power density (P) in units (W/kg or W/cm³) [5, 6]. Energy density dictates the ability of a device to store energy per unit mass or volume, and is given by

$$E = \frac{1}{2}CU^2 \quad (1)$$

where C is the capacitance and U is the operating voltage.

In contrast to batteries that involve faradaic reactions, supercapacitors store energy through physical adsorption of ions as a response to an applied potential difference, where electrode charge is balanced by the accumulation of opposite ionic charges at the interface [7, 8]. The physical charge storage mechanism through ion adsorption and desorption facilitates fast charge and discharge kinetics in supercapacitors, and power density describes the charge/discharge rates

$$P = \frac{U^2}{ESR} \quad (2)$$

where ESR is the equivalent series resistance of the device. U and ESR strongly depend on both electrode and electrolyte properties. Consequently, on the electrode side, research on improving power density is focused on synthesizing electrochemically stable (for higher U) and electrically conductive (for smaller ESR) carbon-based materials with large surface area and optimized pore structure [8]. Meanwhile, on the electrolyte side, the ultimate goal is to deliver electrolyte materials with high electrochemical stability and ionic conductivity. Consequently, optimizing power density in supercapacitors requires elucidating how ion diffusion at an electrode/electrolyte interface is affected from electrolyte composition [9–11].

In supercapacitors, dilute electrolytes comprised of salts dissolved in organic solvents (e.g., tetraethylammonium tetrafluoroborate in acetonitrile) are commonly used as electrolytes [12]. These electrolytes offer relatively high electrochemical stability at operating voltages around ~ 2.5 V and high ionic conductivities at room temperature (up to ~ 60 mS/cm) [13]. Aqueous electrolytes provide even higher conductivities (exceeding 100 mS/cm) and are cost effective, yet, unless cost is the primary factor, they can not compete with organic electrolytes as their electrochemical stability window is limited to ~ 1 V [12, 13]. Room temperature ionic liquids (RTILs) emerge as electrochemically stable electrolytes (~ 4 V) that deliver high energy densities (Equation 1) [14]. However, the enhanced energy density of RTIL-based supercapacitors comes at a cost, namely low power density associated with the diminished ionic conductivity and slow ion transport at room temperature. Consequently, elucidating the charge storage mechanisms and kinetics of supercapacitors is critical in optimizing transport properties in supercapacitors to boost power performance [2, 8, 15–19].

While a wide literature exists on bulk electrolyte properties, interfacial transport properties of RTIL-based electrolytes at charged electrode/electrolyte interfaces remain to be explored. Previous studies have shown that diffusion properties of confined liquids are significantly different from their bulk counterparts [20–22]. In particular, computational studies have shown anomalies in the diffusion coefficients of hard sphere fluids, water, oxygen and alkanes under confinement [23–25] that behave significantly different than they do in bulk. These findings have been of interest in applications that include ion transport through desalination membranes and drug delivery [23]. However, kinetics of concentrated ionic solutions under confinement and near charged interfaces remain to be explored. For this purpose, experimental techniques including NMR spectroscopy [26], scattering approaches [27], electrochemical quartz crystal microbalance [28] and IR spectroscopy [29] are used to show that charging properties of supercapacitors are sensitive to electrode and electrolyte materials

combinations. Nevertheless, experiments lack the spatiotemporal resolution to fully elucidate charge storage mechanisms and kinetics at the atomistic level. Here, molecular modeling becomes significant in studying the effect of electrolyte properties on charging kinetics.

In this work, we study the relationship between solvation, electrolyte diffusion and ionic conductivity at an electrode/electrolyte interface. The rest of this paper is organized as follows. First, we describe the simulation system and introduce the model parameters that we use to set up the simulation systems. Then, we establish connections between the local structuring of confined electrolytes and the anomalous behavior of self-diffusivities. We show confinement slows down ion transport, and this effect is enhanced near charged surfaces. We then depict how a maximum in ionic conductivity emerges due to the presence of competing forces associated with solvation. To the best of our knowledge, self-diffusion and ionic conductivity in RTIL-based electrolytes under confinement has not been studied before. Finally, we provide concluding remarks and potential future directions.

2. COMPUTATIONAL DETAILS

2.1. Simulation Setup for Bulk Electrolyte

Bulk electrolytes are comprised of molecular simulation models of the ionic liquid 1-butyl-3-methylimidazolium hexafluorophosphate ([BMIM⁺][PF₆⁻]) [30] and organic solvent acetonitrile (ACN) [31]. These simulations are used to compute the bulk density of the electrolytes used in Section 2.2. In particular, seven different electrolytes are prepared: pure [BMIM⁺][PF₆⁻] and its corresponding ion fraction (ρ) = 0.03, 0.12, 0.26, 0.36, 0.47 and 0.67 solutions with ACN. For all electrolyte species, parameters of the coarse-grained models with site-site Lennard-Jones and Coulombic interactions are given in Table 1. The cross-parameters are computed using the standard Lorentz-Berthelot combination mixing rules. The solvent and cation are kept rigid using the SHAKE algorithm for computational efficiency [32]. The simulations are conducted in a cubic box. The isobaric-isothermal ensemble simulations at 5 atm and 400 K are done with the LAMMPS software [33] using the Nosé-Hoover thermostat and barostat. For the Lennard-Jones interactions, a 16 Å cut-off was used which corresponds to the half of the simulation box length. The particle-particle particle-mesh solver is employed for Coulombic interactions [34]. Equilibration simulations were run for 5 ns. Additional 5 ns production runs are carried out and the trajectories are used to compute bulk densities.

Table 1. Force field parameters for PF₆⁻ (A) [30], BMIM⁺ (C1, C2, C3) [30], acetonitrile (ME, CA, N) [31] and electrodes (C) [35].

Particle ID	A	C1	C2	C3	ME	CA	N	C
<i>MW</i> (g/mol)	144.96	67.07	15.04	57.12	15.04	12.01	14.01	12.01
<i>q</i> (e)	-0.78	0.4374	0.1578	0.1848	0.269	0.129	-0.398	-
σ (Å)	5.06	4.38	3.41	5.04	3.60	3.40	3.30	3.37
ϵ (kcal/mol)	1.126	0.612	0.086	0.437	0.38002	0.10038	0.10038	0.055

2.2. Simulation Setup for Supercapacitor Systems

Supercapacitor models are comprised of the electrolytes with ρ values given in Section 2.1, confined by flat electrodes representing graphene sheets modelled as three layers of carbon atoms arranged in a honeycomb lattice. Electrode model parameters are adopted from Cole et al. [35] and reported in

Table 1. The cross parameters between electrodes and electrolyte molecules are computed using the Lorentz-Berthelot rules. The force-field combination in Table 1 has been previously used in modelling ionic solutions both in bulk and under confinement, and has shown good agreement with experiments [8, 36–39]. Isochoric-isothermal ensemble simulations are conducted using the Nosé–Hoover thermostat. Periodic boundary conditions are employed in the directions parallel to the electrode surface, while boundaries are fixed in the direction normal to electrodes. Simulation systems are set up so that the bulk electrolyte mass densities (computed in Section 2.1) are reproduced in the bulk electrolyte region (Ω_b) of the supercapacitor systems (Figure 1). This is achieved by tuning the location of the electrodes in the z-direction and conducting 0.5 ns equilibration runs until the target density is reached. Once the target density is reached, systems are further equilibrated for 2 ns, followed by 10 ns production runs at zero charge. The production data is used to compute transport and structural properties of the systems with uncharged electrodes. Afterwards, electrodes are charged to maintain a 1.5 V potential difference between the electrodes. 1.5 V corresponds to potential difference limit under which an RTIL-based electrolyte in an organic solvent remains electrochemically stable [12, 14]. 10 ns simulations of the charged systems are carried out for equilibration, followed by additional 10 ns production runs at constant charge. The equilibration simulations are run long enough to maintain the equilibrium charge ordering at the electrode/electrolyte interface. The production runs are extended until the convergence of kinetic properties are ensured (see Section 2.3 for details.)

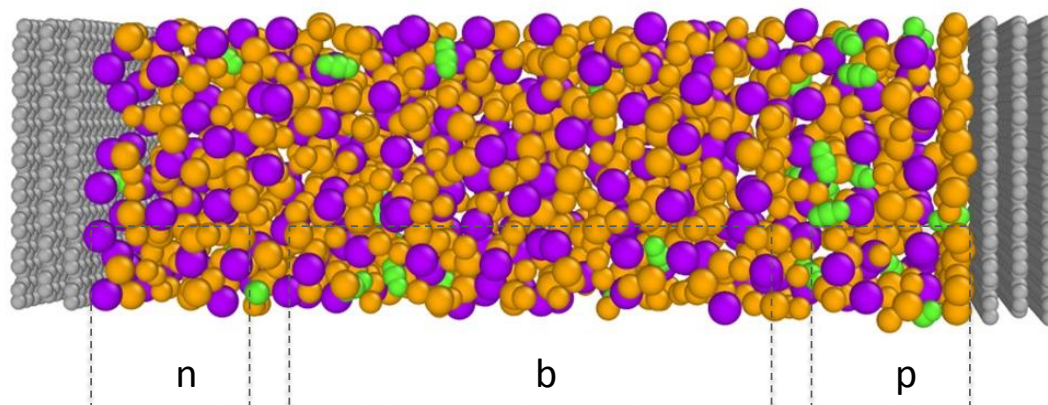


Figure 1. Simulated supercapacitor consists of a room temperature ionic liquid (orange for $[\text{BMIM}^+]$ and purple for $[\text{PF}_6^-]$) - organic solvent (green for ACN) electrolyte sandwiched between two electrodes modelled as three layers of hexagonal carbon lattices. Three regions are defined within the system, namely the bulk electrolyte (Ω_b) and interfacial regions (Ω_n and Ω_p). The electrolyte has $\rho = 0.67$.

2.3. Self-diffusion Coefficient and Conductivity Calculations

Self-diffusion is a measure of the average displacement of a molecule from its initial position due to thermal molecular motion. It describes how fast a material can diffuse through a medium. Self-diffusion coefficients for the bulk electrolytes are computed using the Einstein relation where the mean-square displacement (MSD) of molecules is computed as a function of time and the linear regime of the MSD profile is used to compute the self-diffusion coefficient D_i

$$D_i = \lim_{t \rightarrow \infty} \frac{\langle (r_i(t) - r_i(0))^2 \rangle}{6t} \quad (3)$$

with $r_i(t)$ as the instantaneous center of mass of ion type i and $\langle \dots \rangle$ as the average over all type i ions in the ensemble. Diffusion coefficients are computed from the production run trajectories block-averaged in 1 ns long sections. The position-dependent self-diffusion coefficients are computed for the ions in bulk (Ω_b) and at the electrode/electrolyte interface (Ω_n and Ω_p) following Zhang et al. [40]. Since ions can penetrate in and move out of the interface during a simulation, only the ions that remain in the defined regions during 1 ns blocks are considered to compute D_i . Electrolyte ionic conductivity (κ) is calculated using the Nernst-Einstein equation via the weighted sum of the ion self-diffusion coefficients.

3. RESULTS and DISCUSSION

Diffusion in confined liquids differ from diffusion in bulk. In particular, diffusion near walls is influenced by liquid-solid interactions which results in density fluctuations at the interface [23]. In order to compute the bulk and interfacial ion self-diffusion coefficients for the simulation system presented in Figure 1, three regions are defined within the system, namely the bulk electrolyte 25 Å away from the electrode surface (Ω_b) and interfacial regions encompassing the first two solvation layers of the ions near the electrode (Ω_n and Ω_p).

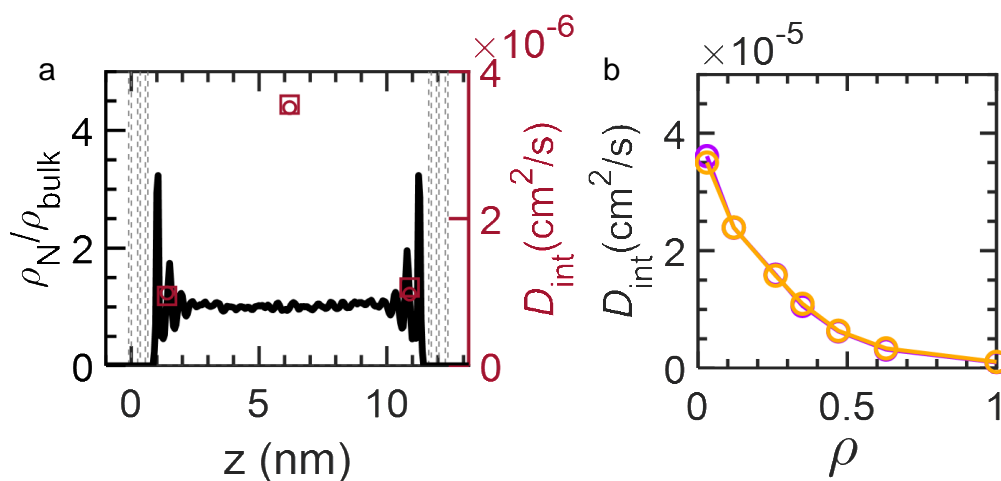


Figure 2. (a) Position dependent number density profile of the electrolyte parallel to the basal plane of the electrodes (ρ_N) normalized by the bulk number density (ρ_{bulk}) in Figure 1. Near the electrode surfaces (Ω_n and Ω_p), there is a non-uniform particle distribution. In particular, electrolyte that is close to the electrodes shows large density fluctuations due to strong electrode/electrolyte interactions that restrict

coefficients for Ω_n , Ω_p and Ω_b (right axis) for the system with $\rho = 0.67$, (b) Self-diffusion coefficients of cation (orange) and anion (purple) as a function of ion fraction near uncharged electrodes.

Figure 2a shows the number density profile of the electrolyte confined between the uncharged electrodes (ρ_N) normalized by the bulk number density (ρ_{bulk}) in Figure 1. Near the electrode surfaces (Ω_n and Ω_p), there is a non-uniform particle distribution. In particular, electrolyte that is close to the electrodes shows large density fluctuations due to strong electrode/electrolyte interactions that restrict

kinetics. Meanwhile, at the center of the pore (Ω_b), the confinement effect vanishes. Hence, while the self-diffusion coefficients in the bulk are on the order of $4.5 \cdot 10^{-6}$ cm²/s, near the electrodes they are only around $1.2 \cdot 10^{-6}$ cm²/s as confinement slows down the dynamics (Figure 2a). The difference between

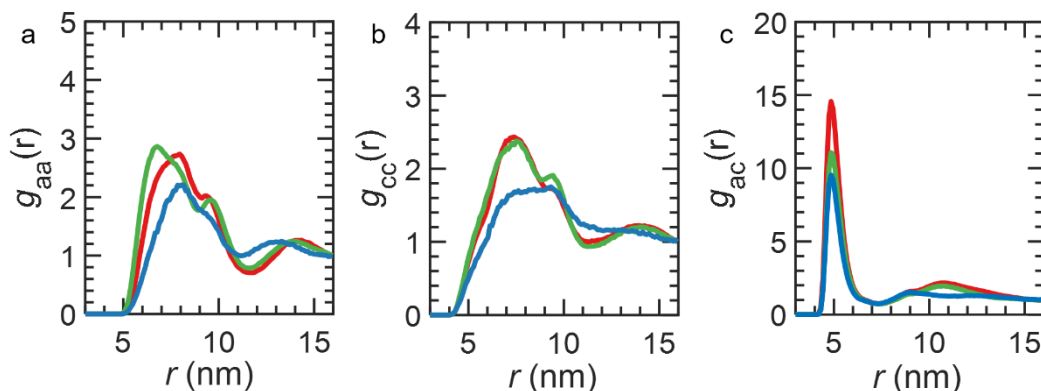


Figure 3. Composition dependence of pairwise radial distribution profiles for (a) anion-anion, (b) cation-cation, and (c) anion-cation interactions. Blue, green and red represent $\rho = 0.26, 0.67$ and 1.0 , respectively.

the interfacial and bulk diffusion coefficients entails a pure confinement effect: In particular, the structuring of the ions within the first two adsorbed layers near the electrodes depicted by the peaks of the number density profile (Figure 2a) slows down ion kinetics.

The question that is next to be addressed is how this surface effect depends on the dilution of the ionic liquid by a solvent. In particular, Figure 2b shows the diffusion coefficients near the uncharged electrode surfaces when [BMIM⁺] [PF₆⁻] is diluted with the organic solvent ACN. At the interface, introduction of the solvent significantly increases the self-diffusion coefficients for the anion and the cation (Figure 2b). In particular, decreasing the ion fraction from $\rho = 1$ to $\rho = 0.03$ enhances the ion self-diffusion coefficients by more than an order of magnitude.

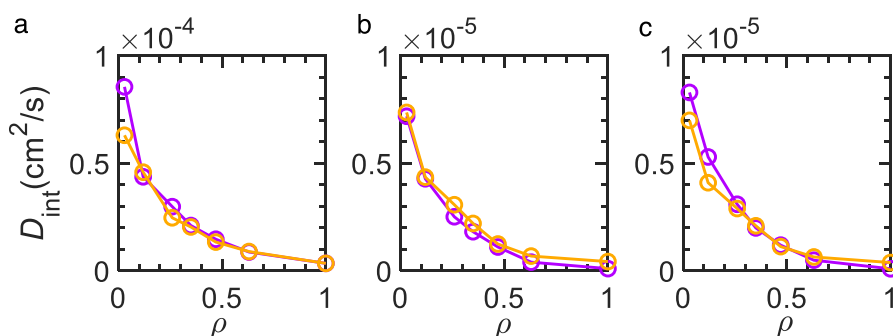


Figure 4. Composition dependence of self-diffusion coefficients for anion (purple), cation (orange) (a) in the bulk, (b) near the negative electrode, and (c) near the positive electrode.

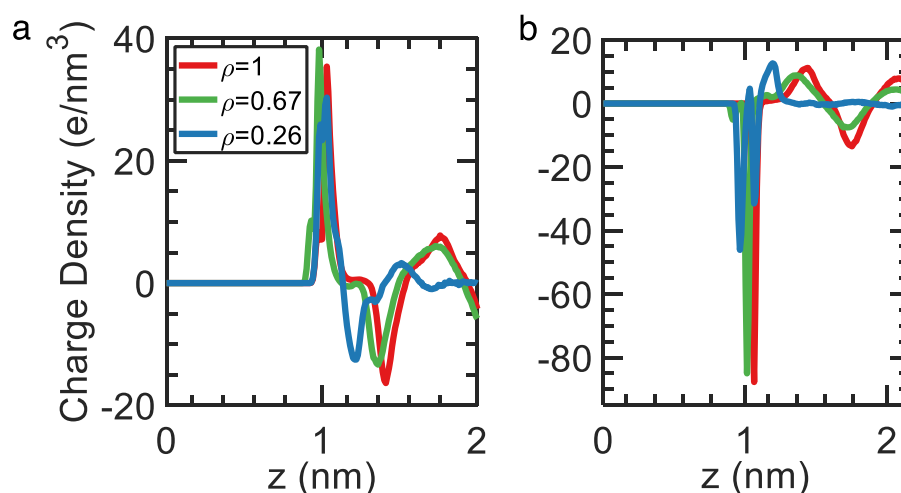


Figure 5. Charge density profile as a function of distance from the (a) negative and (b) positive electrode surface for $\rho = 0.26$ (blue), 0.67 (green) and 1.0 (red).

Interestingly, Figure 2 also shows that the anion and cation self-diffusion coefficients are significantly close to each other throughout the entire concentration regime, indicating that cations and anions remain strongly correlated even when they are solvated, indicated by Figure 3c with the pronounced first peaks of the anion-cation radial distribution profiles normalized by the number in bulk (i.e., when the molecules are further apart and uncorrelated). The pairwise radial distribution functions (RDFs) suggest a preferential interaction should result in a higher peak in the radial distribution functions: In Figure 3, the first peak height is the highest for anion-cation interactions. This indicates that anions are preferentially located around cations in the electrolyte. The broader and lower first peaks in the anion-anion ($g_{aa}(r)$) and cation-cation ($g_{cc}(r)$) profiles indicate that co-ions interact weakly. The RDFs of the anion around the cation indicate the first peak is near 5 Å. The peak distance is not correlated with solvent composition as the peak does not shift with dilution (Figure 3c), but the peak height decreases with increasing solvent concentration. This indicates that cation-anion correlations decrease with solvation. Figure 3a-b show that, although the effect of solvation is not significant when the electrolyte concentration changes from $\rho = 1$ to $\rho = 0.67$, when the electrolyte is diluted to $\rho = 0.26$, the first peak heights of $g_{aa}(r)$ and $g_{cc}(r)$ decrease with dilution. Furthermore, the first peak shifts to larger distances when the pure ionic liquid is diluted from $\rho = 1$ to $\rho = 0.26$. This indicates that correlations between ions of the same charge weaken with solvation and ion pairs become more separated improving diffusion kinetics.

We next investigate the diffusion kinetics of the electrolytes near charged electrode surfaces under equilibrium. The difference between diffusion coefficients in the bulk and at the interface further increases when the system is charged, i.e., a potential difference is applied between the electrodes. Figure 4 shows the ion self-diffusion coefficients in the bulk and near the positively and negatively charged electrodes as a function of ionic liquid fraction. Compared to the bulk (Figure 4a) and noncharged interfaces (Figure 2b), confinement at a charged interface significantly slows down ion

kinetics (Figure 4b-c). The charge density profiles in Figure 5 sheds light onto this behavior. Near the charged electrodes, the electrolyte is highly charge-ordered as shown in Figure 5. This is due to the

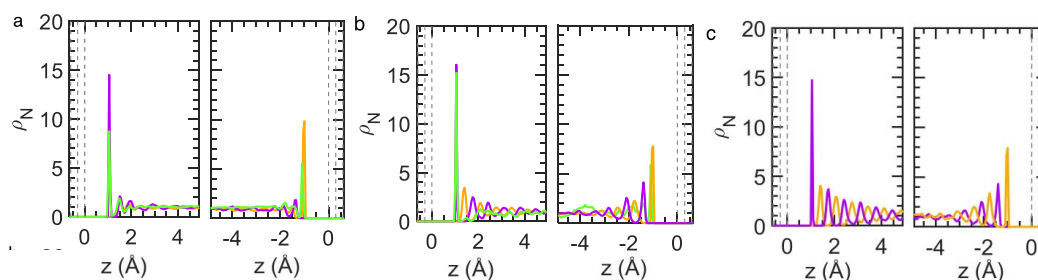


Figure 6. Number density profiles for anion (purple), cation (orange) and solvent (green) molecules as a function of distance from the positive (left) and negative (right) electrodes for (a) $\rho = 0.26$, (b) $\rho = 0.67$ and (c) $\rho = 1.0$.

layering of the ions (Figure 6) to screen the electrode charges. In particular, since the electric field stabilizes the ions in the direction normal the basal plane of the electrodes, confined electrolytes at charged surfaces have an order of magnitude slower kinetics than their bulk counterparts.

When the electrolyte near a charged surface is diluted, charge ordering weakens, and ions can move more freely enhancing diffusion kinetics. This is shown by the dampening of the charge density profile peaks with dilution in Figure 5. When the electrolyte is pure ionic liquid, charge ordering at the interface is highly structured as anions and cations are significantly correlated and this leads to overscreening and crowding effects [41–43]. When the electrolyte is diluted, anion-cation interactions weaken hence the peak heights of the charge density profile dampens leading to improved kinetics depicted by the diffusion coefficient profiles in Figure 4b-c.

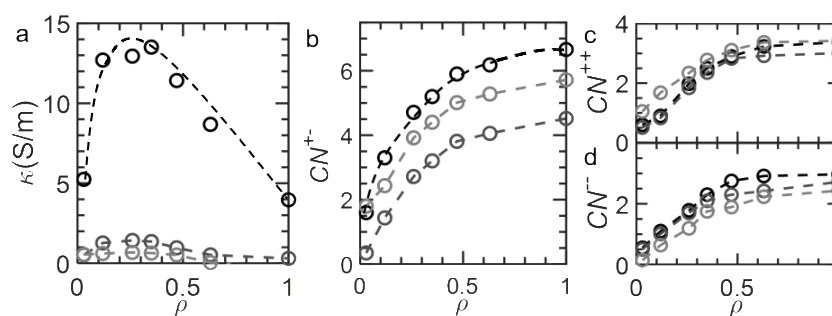


Figure 7. Composition dependence of ion dynamics in the electrolyte. (a) Ionic conductivity (κ), (b) cation-anion coordination number (CN^{+}), (c) cation-cation coordination number (CN^{++}), (d) anion-anion coordination number (CN^{-}) as a function of electrolyte ion fraction. Black, dark gray and light gray circles represent the bulk electrolyte and the electrolyte near the negative and positive electrodes, respectively. Lines are guides to the eye.

The ionic conductivity profiles of the electrolyte in bulk and near charged surfaces as a function of ion content (Figure 7a) shows how ionic conductivity is affected from dilution. The electrolyte composition dependence of κ in bulk (black circles) is in qualitative agreement with experimental measurements [44-45]. In the dilute regime, solvation decreases ionic conductivity. This is attributable to the decrease in the number of free ions in bulk with solvation. To illustrate this point, Figure 7b-d shows how the coordination number of ions around each other (CN^{+-} for anions around cations and CN^{++} (CN^-) for cations around cations (anions around anions)) changes with concentration. Both in bulk and at the interface, solvation decreases the number of ions around each other. In particular, bulk CN^{+-} decreases from 6.8 to 1.6 as the electrolyte is diluted down to $\rho = 0.03$. In agreement with the Nernst-Einstein theory, the effect of decreasing free ions becomes dominant at high dilution, leading to a drop in ionic conductivity. In the concentrated regime, on the other hand, the dominant factor is solvent's ability to enhance ion mobility, thus solvation improves conductivity by increasing ion diffusivities. Consequently, these two competing forces, namely the trade-off between decreasing ion content with solvation dominant in the dilute regime and improved diffusivity with dilution dominant in the concentrated regime, results in a maximum in conductivity at intermediate dilution levels. As a result of this competition, for [BMIM⁺][PF₆⁻] in ACN, the maximum in ionic conductivity is observed near $\rho = 0.26$ at 13.9 S/m. We note that a similar nonmonotonic behavior is also observed near the charged and uncharged interfaces albeit with nearly an order of magnitude smaller ionic conductivity values (Figure 7a). CNs are slightly smaller at interfacial regions Ω_n and Ω_p due to the presence of carbon electrode/electrolyte interactions. Yet, qualitatively similar CN profiles are obtained near charged and uncharged surfaces as a function of solvation (Figure 7b-d). While total CN values ($CN^{++} + CN^- + CN^{+-}$) are similar in magnitude both near charged and uncharged electrodes, near the charged surfaces counter-ions are replaced by co-ions as seen from the decrease in CN^{+-} and increase in CN^{++} and CN^- profiles upon charging (Figure 7c-d). This is reflected in the small decrease in interfacial conductivity upon charging due to the strong charge ordering of the ions, as reflected in Figure 7a.

4. CONCLUSION

Transport properties of room temperature ionic liquids and their solutions in ACN are investigated using molecular dynamics simulations. The simulations reveal that ion kinetics under confinement significantly differ from the kinetics of their bulk counterparts. Bulk simulations indicate that the introduction of the solvent enhances ion self-diffusion coefficients while weakening the correlations between ions. The same solvation effect is also observed at the charged interfaces, but the magnitude of the diffusion coefficients at the interface are significantly lower than the ones in bulk. This is attributable to the charge ordering at the interface due to the layering of the ions to balance the electrode charges. Our results show introduction of the solvent drastically improves ion kinetics at the interface. The simulations also reveal that dilution imposes two competing effects on conductivity both in bulk and at the interface. At the concentrated regime, conductivity is improved with dilution as solvent dampens ion correlations and charge ordering. Meanwhile, in the dilute regime, diluting the electrolyte further decreases the conductivity due to decreasing free ion concentration. This competition results in a conductivity maximum both at the interface and in bulk. Our work demonstrates the kinetics of supercapacitors can be improved by tailoring electrolyte properties with the support of molecular modelling to facilitate supercapacitor design with improved power density. Extending the findings of this work to supercapacitor models with more complex electrode structures can facilitate designing supercapacitors with improved energy storage performance.

ACKNOWLEDGEMENTS

This work was supported by The Scientific and Technological Research Council of Turkey (TUBITAK) under BIDEB 2232-A (Project Number T118C220) and Bogazici University Research Fund (Project Number 17841).

REFERENCES

- [1] Béguin, F., Presser, V., Balducci, A., Frackowiak, E., (2014), Carbons and Electrolytes for Advanced Supercapacitors. *Advanced Materials*, 26, 2219-2251.
- [2] Simon, P., Gogotsi, Y., (2013), Capacitive Energy Storage in Nanostructured Carbon–Electrolyte Systems. *Accounts of Chemical Research*, 46, 1094-1103.
- [3] Stoller, M. D., Park, S., Zhu, Y., An, J., Ruoff, R. S., (2008), Graphene-Based Ultracapacitors. *Nano Letters*, 8(10), 3498-3502.
- [4] Wong, S. I., Sunarso, J., Wong, B. T., Lin, H., Yu, A., Jia, B., (2018), Towards enhanced energy density of graphene-based supercapacitors: Current status, approaches, and future directions. *Journal of Power Sources*, 396, 182- 206.
- [5] Aslyamov, T., Sinkov, K., Akhatov, I., (2022), Relation between Charging Times and Storage Properties of Nanoporous Supercapacitors. *Nanomaterials*, 12, 587.
- [6] Liu, T., Zhang, F., Song, Y., Li, Y., (2017), Revitalizing carbon supercapacitor electrodes with hierarchical porous structures. *Journal of Materials Chemistry A*, 5, 17705-17733.
- [7] Péan, C., Merlet, C., Rotenberg, B., Madden, P. A., Taberna, P.-L., Daffos, B., Salanne, M., Simon, P., (2014), On the Dynamics of Charging in Nanoporous Carbon-Based Supercapacitors. *ACS Nano*, 8(2), 1576-1583.
- [8] Pean, C., Rotenberg, B., Simon, P., Salanne, M., (2016), Understanding the different (dis)charging steps of supercapacitors: influence of potential and solvation. *Electrochimica Acta*, 206, 504-512.
- [9] Uralcan, B., Aksay, I. A., Debenedetti, P. G., Limmer, D. T., (2016), Concentration Fluctuations and Capacitive Response in Dense Ionic Solutions. *The Journal of Physical Chemistry Letters*, 7(13), 2333-2338.
- [10] Bozym, D. J., Uralcan, B., Limmer, D. T., Pope, M. A., Szamreta, N. J., Debenedetti, P. G., Aksay, I. A., (2015), Anomalous Capacitance Maximum of the Glassy Carbon-Ionic Liquid Interface through Dilution with Organic Solvents. *The Journal of Physical Chemistry Letters*, 6(13), 2644-2648.

- [11] Uralcan, B., Uralcan, I. B., (2022), Origin of Enhanced Performance in Nanoporous Electrical Double Layer Capacitors: Insights on Micropore Structure and Electrolyte Composition from Molecular Simulations. *ACS Applied Materials & Interfaces*, 14(14), 16800-16808.
- [12] Pal, B., Yang, S., Ramesh, S., Thangadurai, V., & Jose, R., (2019), Electrolyte selection for supercapacitive devices: a critical review. *Nanoscale Advances*, 1(10), 3807-3835.
- [13] Cheng, Z., Yida D., Wenbin, H., Daoming, S., Jinli, Q., Jiujun, Z., (2016), *Electrolytes for Electrochemical Supercapacitors*. Routledge & CRC Press.
- [14] Yu, L., Chen, G. Z., (2019), Ionic Liquid-Based Electrolytes for Supercapacitor and Supercapattery. *Frontiers in Chemistry*, 7.
- [15] Lian, Z., Chao, H., Wang, Z.-G., (2021), Effects of Confinement and Ion Adsorption in Ionic Liquid Supercapacitors with Nanoporous Electrodes. *ACS Nano*, 15(7), 11724-11733.
- [16] Lin, R., Huang, P., Ségalini, J., Largeot, C., Taberna, P. L., Chmiola, J., Gogotsi, Y., Simon, P., (2009), Solvent effect on the ion adsorption from ionic liquid electrolyte into sub-nanometer carbon pores. *Electrochimica Acta*, 54(27), 7025-7032.
- [17] Feng, G., Qiao, R., Huang, J., Sumpter, B. G., Meunier, V., (2010), Ion Distribution in Electrified Micropores and Its Role in the Anomalous Enhancement of Capacitance. *ACS Nano*, 4(4), 2382-2390.
- [18] Oyarzun, D. I., Zhan, C., Hawks, S. A., Cerón, M. R., Kuo, H. A., Loeb, C. K., Aydın, F., Pham, T. A., Stadermann, M., Campbell, P. G., (2021), Unraveling the Ion Adsorption Kinetics in Microporous Carbon Electrodes: A Multiscale Quantum-Continuum Simulation and Experimental Approach. *ACS Applied Materials & Interfaces*, 13(20), 23567-23574.
- [19] Lahrar, E. H., Deroche, I., Matei Ghimbeu, C., Simon, P., Merlet, C., (2021), Simulations of Ionic Liquids Confined in Surface-Functionalized Nanoporous Carbons: Implications for Energy Storage. *ACS Applied Nano Materials*, 4(4), 4007-4015.
- [20] Walton, J. P. R. B., Quirke, N., (1989), Capillary Condensation: A Molecular Simulation Study. *Molecular Simulation*, 2(4- 6), 361-391.
- [21] Mu, R., Malhotra, M. V., (1991), Effects of surface and physical confinement on the phase transitions of cyclohexane in porous silica. *Physical Review. B, Condensed Matter*, 44(9), 4296-4303.
- [22] Gelb, L. D., Gubbins, K. E., Radhakrishnan, R., Sliwinski-Bartkowiak, M., (1999), Phase separation in confined systems. *Reports on Progress in Physics*, 62(12), 1573-1659.
- [23] Spera, M. B. M., Franco, L. F. M., (2020), Surface and confinement effects on the self-diffusion coefficients for methane-ethane mixtures within calcite nanopores. *Fluid Phase Equilibria*, 522, 112740.

- [24] Wang, G. J., & Hadjiconstantinou, N. G. (2018). Layered Fluid Structure and Anomalous Diffusion under Nanoconfinement. *Langmuir*, 34(23), 6976-6982.
- [25] Leoni, F., Calero, C., Franzese, G., (2021), Nanoconfined Fluids: Uniqueness of Water Compared to Other Liquids. *ACS Nano*, 15(12), 19864-19876.
- [26] Griffin, J. M., Forse, A. C., Wang, H., Trease, N. M., Taberna, P.-L., Simon, P., Grey, C. P., (2015), Ion counting in supercapacitor electrodes using NMR spectroscopy. *Faraday Discussions*, 176(0), 49-68.
- [27] Boukhalfa, S., He, L., Melnichenko, Y. B., Yushin, G., (2013), Small-angle neutron scattering for in situ probing of ion adsorption inside micropores. *Angewandte Chemie (International Ed. in English)*, 52(17), 4618-4622.
- [28] Levi, M. D., Salitra, G., Levy, N., Aurbach, D., Maier, J., (2009), Application of a quartz-crystal microbalance to measure ionic fluxes in microporous carbons for energy storage. *Nature Materials*, 8(11), 872-875.
- [29] Richey, F. W., Dyatkin, B., Gogotsi, Y., Elabd, Y. A., (2013), Ion Dynamics in Porous Carbon Electrodes in Supercapacitors Using in Situ Infrared Spectroelectrochemistry. *Journal of the American Chemical Society*, 135(34), 12818-12826.
- [30] Roy, D., Patel, N., Conte, S., Maroncelli, M., (2010), Dynamics in an Idealized Ionic Liquid Model. *The Journal of Physical Chemistry B*, 114(25), 8410-8424.
- [31] Edwards, D. M. F., Madden, P. A., McDonald, I. R., (1984), A computer simulation study of the dielectric properties of a model of methyl cyanide. *Molecular Physics*, 51(5), 1141-1161.
- [32] Ryckaert, J.-P., Ciccotti, G., Berendsen, H. J. C., (1977), Numerical Integration of the Cartesian Equations of Motion of a System with Constraints: Molecular Dynamics of n-Alkanes. *Journal of Computational Physics*, 23, 327-341.
- [33] Thompson, A. P., Aktulga, H. M., Berger, R., Bolintineanu, D. S., Brown, W. M., Crozier, P. S., in 't Veld, P. J., Kohlmeyer, A., Moore, S. G., Nguyen, T. D., Shan, R., Stevens, M. J., Tranchida, J., Trrott, C., Plimpton, S.J., (2022), LAMMPS - a flexible simulation tool for particle-based materials modeling at the atomic, meso, and continuum scales. *Computer Physics Communications*, 271, 108171.
- [34] Hockney, R. W., Eastwood, J. W., (2021), *Computer Simulation Using Particles*. CRC Press.
- [35] Cole, M. W., Klein, J. R., (1983), The interaction between noble gases and the basal plane surface of graphite. *Surface Science*, 124(2- 3), 547-554.
- [36] Merlet, C., Rotenberg, B., Madden, P. A., Salanne, M., (2013), Computer simulations of ionic liquids at electrochemical interfaces. *Physical Chemistry Chemical Physics*, 15(38), 15781-15792.

- [37] Merlet, C., Péan, C., Rotenberg, B., Madden, P. A., Daffos, B., Taberna, P.-L., Simon, P., Salanne, M., (2013), Highly confined ions store charge more efficiently in supercapacitors. *Nature Communications*, 4, 2701.
- [38] Merlet, C., Péan, C., Rotenberg, B., Madden, P. A., Simon, P., Salanne, M., (2013), Simulating Supercapacitors: Can We Model Electrodes As Constant Charge Surfaces? *The Journal of Physical Chemistry Letters*, 4(2), 264-268.
- [39] Péan, C., Merlet, C., Rotenberg, B., Madden, P. A., Taberna, P.-L., Daffos, B., ... Simon, P., (2014), On the Dynamics of Charging in Nanoporous Carbon-Based Supercapacitors. *ACS Nano*, 8(2), 1576-1583.
- [40] Zhang, Y., Cummings, P. T., (2019), Effects of Solvent Concentration on the Performance of Ionic-Liquid/Carbon Supercapacitors. *ACS Applied Materials & Interfaces*, 11(45), 42680-42689.
- [41] Kondrat, S., Kornyshev, A., (2010), Superionic state in double-layer capacitors with nanoporous electrodes. *Journal of Physics: Condensed Matter*, 23(2), 022201.
- [42] Kornyshev, A. A., (2007), Double-Layer in Ionic Liquids: Paradigm Change? *The Journal of Physical Chemistry B*, 111(20), 5545-5557.
- [43] Bazant, M. Z., Storey, B. D., Kornyshev, A. A., (2011), Double layer in ionic liquids: overscreening versus crowding. *Physical Review Letters*, 106(4), 046102.
- [44] Zhu, A., Wang, J., Han, L., Fan, M., (2009), Measurements and correlation of viscosities and conductivities for the mixtures of imidazolium ionic liquids with molecular solutes. *Chemical Engineering Journal*, 147(1), 27-35.
- [45] Roy, D., Maroncelli, M., (2010), An Improved Four-Site Ionic Liquid Model. *The Journal of Physical Chemistry B*, 114(39), 12629-12631.



RESEARCH ARTICLE

THE EFFECT of MINOR Ti and Sr ADDITION on the MICROSTRUCTURAL, MECHANICAL, and CORROSION PROPERTIES of a BIODEGRADABLE Mg-5Sn-3Al ALLOY

Selma ÖZARSLAN*

*Hatay Mustafa Kemal University, Faculty of Arts and Sciences, Department of Physics, selmaozarslan@gmail.com,
ORCID: 0000-0002-7225-1613

Receive Date: 29.03.2022

Accepted Date: 09.06.2022

ABSTRACT

In this study, the microstructural, mechanical, and corrosion properties of the alloys obtained by adding Al-15Ti and Al-15Sr master alloys to the Mg-5Sn alloy were investigated. Microstructural properties of the alloys were investigated by X-ray diffraction (XRD), scanning electron microscopy (SEM), and optical microscopy (OM). The mechanical properties of the alloys were analyzed by performing tensile tests, macrohardness tests, and nanoindentation tests. Corrosion behavior of both alloys was investigated by determining the corrosion rates with both electrochemical techniques and immersion techniques in Hanks Balanced Salt Solution (HBSS). When the microstructure results were examined, it was observed that minor Ti and Sr have a significant effect on reducing magnesium grain size, with Ti being more effective in grain refining. When compared to Al-15Sr, the addition of Al-15Ti to Mg-5Sn improves both mechanical and corrosion properties more effectively.

Keywords: *Biomaterials, Magnesium alloys, Corrosion behavior, Mechanical properties*

1. INTRODUCTION

The use of magnesium as a biomaterial dates back many years ago, and it has again found a field of application along with the development of technology. In the field of health, magnesium, which was discovered by Humphrey Davy in 1808, is used in implant applications due to its biodegradable property. Mg wires were initially used by Dr. Edward C. Huse in 1878 to join the veins in order to stop the bleeding of patients [1-3]. Later, it was decided to abstain from using pure magnesium as a biomaterial due to its weak mechanical property and high corrosion rate, and stainless steel has begun to be used [2,4]. But by the studies conducted, it was observed that the weak mechanical properties and high corrosion rate of magnesium were improved by the addition of alloy elements, and for about 20 years, it has found an extensive field of application in the health sector as a biodegradable metallic alloy [5].

Magnesium alloys exhibit superior properties in many aspects compared to other biodegradable metallic alloys (like iron and zinc-based alloys). Even though Fe, and Fe-based alloys have high strength and high biocompatibility, their elastic modulus is much higher than the elastic modulus of human bone, and this status causes the fact of stress concentration frequently encountered in metallic

implants. Thus, the area of use of Fe and Fe-based alloys is limited [6]. Similarly, the corrosion rate of zinc, which is a biodegradable metallic material, has a value between the Fe and Mg-based alloys. But as the intake of zinc of more than 100-300 mg per day causes severe health problems, it requires the selection of alloy to be made carefully [7]. The corrosion resistance of pure magnesium is able to be improved by the addition of various alloy elements [4]. However, care must be taken to ensure that the alloy elements are especially biocompatible and do not have toxic effects [7-8]. As tin (Sn) is among the main elements present in the human body, its use in the field of biomaterials has become widespread [9]. Thus, Mg-Sn has been determined as the main alloy in this study. When the studies conducted on Mg-Sn alloy, as a biodegradable alloy, were examined, Gu et al. [7] examined the corrosion and biocompatibility of Mg-1Sn alloy and asserted that Sn may be a good alloy element for magnesium alloys. And in a study conducted on the addition of different weight rates of Sn to magnesium, it was found that the Mg-5Sn alloy has the best mechanical properties [10]. For this reason, Sn was used at a rate of 5% by weight in this study.

When the studies conducted were examined, it was observed that the studies for improving the properties of biodegradable Mg-based alloys had concentrated on the AZ series (with aluminum and zinc as alloy elements). As the addition of Al to magnesium increases the tensile strength and forms an Al_2O_3 oxide layer on the surface of the alloy as it reduces the grain size of the alloy, it was observed that it also increases the corrosion resistance [11-12]. Moreover, it was reported that a small amount of aluminum continuously released along with the degradation process in the body could be tolerated [13-15]. Huang et al. [16], in their study conducted on Mg-Sn-Al alloys, found that Mg-3.52Sn-3.32Al alloy exhibits better mechanical properties compared to AZ31B, and that Mg-6.54Sn-4.78Al alloy exhibits better mechanical properties compared to ZK60. Moreover, in their study, Bowles et al. [17] presented a preliminary examination with respect to the Mg-Sn(-Al) alloy system. As the Mg-Sn-based alloys have good creep properties and high corrosion resistance, and as tin is a very cheap alloy element and has a low melting point and increases castability, it was observed that the studies concentrated on this main alloy.

In this study, Al-5Ti and Al-15Sr master alloys, functioning as grain refiners, were used for the addition of Al to Mg-5Sn alloys. Thus, the effect of the addition of minor Ti and Sr to Mg-5Sn-3Al alloys on microstructural, mechanical, and corrosion properties was investigated. Koltygin et al. [18] added Al-5Ti-1B to the AZ91 alloy and examined its effect on the mechanical properties of the alloy. The results showed that the Al-5Ti-1B master alloy improves the mechanical properties of the AZ91 magnesium alloy. The production of Mg-5Sn-3Al-0,3Ti (TA-Ti) and Mg-5Sn-3Al-0,4Sr (TA-Sr) alloys obtained by the addition of Al-6Ti and Al-15Sr master alloys to Mg-5Sn alloy was performed by the use of die casting machine. By this production technique, the performance of fine grain size, high-strength and very thin-walled castings becomes possible [19-20]. Thus, the improvement of both the mechanical properties and corrosion resistance of fine-grained alloys is enabled [21-23]. In this study, it was intended to examine the microstructural, mechanical, and corrosion properties of new alloys produced using two different master alloys, and to determine the alloy having better mechanical and corrosion properties.

2. MATERIAL AND METHOD

2.1. Production of the Materials

To produce Mg-5Sn-3Al-0,3Ti (TA-Ti) and Mg-5Sn-3Al-0,4Sr (TA-Sr) alloys, high purity Al-5Ti and Al-15Sr master alloys were added to molten Mg-5Sn by calculating mass weight ratios. Both

alloys were produced using the high pressure die casting (HPDC) technique. The production of alloys used in this study was performed using 96% CO₂ and 4% SF₆ gas mixture in a silicon carbide melting pot in an induction melting furnace having a power of 1.5 kW. In the production of the alloys, Mg with a purity of 99.8%, Sn with a purity of 99.8%, and as a grain refiner, the Al-15Ti and Al-15Sr master alloys of 3% by weight were used. For each alloy, the solution was held at a temperature of 750 °C for 10 minutes. After holding, mixing was performed in a shielding gas environment, and the production was performed in a cold chamber die casting machine with a 100-ton capacity and cold chamber high-pressure die-cast machine with 76kN injection force.

For the whole analyses, the samples produced were removed from the casting centers with wire erosion in the form of cylinder with a diameter of 10 mm and a thickness of 2 mm. Before all the microstructure analyses, the surfaces of the alloys were first subjected to grinding operations with 800, 1200, 2500, and 4000 grit papers, and then to polishing operations with 1µm alumina wax. Right after the polishing operation, the surfaces of the samples were washed with pure water and alcohol, then dried. For the grain structures of the alloys and arising intermetallic phases to become apparent, the surfaces of the samples were seared with Nital (2% nitric acid and 98% ethyl alcohol).

2.2. Microstructure Characterization

Microstructure analyses of alloys produced by the HPDC method were performed by the use of optical microscopy (OM), scanning electron microscopy (SEM) analysis, and X-ray diffraction (XRD) analysis. XRD analyses were performed by the use of a Rigaku brand Smartlab model X-ray diffractometer under Cu-K α radiation, 40 kV voltage, and 30 mA current with a 1 degree/min. measurement rate in the range of 0 and 90 degrees, and phase identification was carried out according to the ICDD database. An Olympus brand BX51 model OM device was used for the microstructure images of the samples, whose metallographic sample preparation operations were completed. AnalySIS Pro Software (Olympus Soft Imaging Solutions, Germany) was used for grain size measurements.

2.3. Mechanical Characterization

In the hardness calculation of the samples, nanoindentation and macrohardness tests were performed. As a result of the nanoindentation tests of the alloys, reduced elastic modulus (E_r) and nanohardness (H_N) values were determined. Hysitron TI 950 TriboIndenter device was used for the tests. Following the nanoindentation measurement, the images of the surface were recorded as before and after the hardness test by the scanning probe microscopy (SPM) for the surface analysis. Diamond Berkovich was used as hardness tip. The tests were performed in load-controlled feedback mode, and through the application of 6 units of load on a matrix of 3x2 formed on the surface under a force of maximum 5 mN, and in 5 seconds of loading and unloading periods, and 2 seconds of waiting periods. The applied load and displacement data obtained after the measurement was analyzed according to the Oliver-Pharr method. By this method, the samples' nanohardness and elastic modulus values are able to be determined from the loading and unloading curve [24]. And the macrohardness measurements of the materials were performed with the Brinell hardness device. In order to determine the hardness, the sample's Brinell hardness value was calculated by measuring the diameter of the mark formed on the sample's surface by the tip.

The alloys' tensile tests were performed with RAAGEN brand universal tensile machine. The tensile tests of each alloy were performed by averaging over 4 samples. The tensile tests, using rectangular

test specimens in accordance with ASTM standard E8/E8M were performed at a body temperature of 36.5 °C and at a pulling speed of 0.2 mm/min.

2.4. Corrosion Tests

Both electrochemical and immersion tests were performed to examine the corrosion behavior of the alloys. Electrochemical corrosion tests were performed with a potentiostat/galvanostat device (CH Instruments). The tests were performed with the use of the samples in which three electrode systems were used, namely the Ag/AgCl reference electrode, the platinum counter electrode, and the working electrode. All the corrosion tests were performed in 100 ml of HBSS prepared by simulating the body fluid. Some corrosion parameters were obtained by fitting the Tafel curves obtained from electrochemical tests, and corrosion rates were calculated. As a result of the immersion tests of the alloys, the measured mass loss weights and degradation rates were calculated. The immersion tests were performed again in 100 ml of HBSS with measurements at specific time intervals.

3. RESULTS

Figure 1 shows the (a) OM and (b) SEM microstructures and grain sizes of TA-Ti and TA-Sr alloys. As observed in Figure 1, the grain size of the titanium added alloy was measured as 13.7 μm , and the grain size of the strontium added alloy was measured as 23.6 μm . Through both the grain size measurements and SEM and OM images, it may be said that the titanium element is more effective in grain refining. When the XRD graph of TA-Ti and TA-Sr alloys given in Figure 2 is examined, Mg_2Sn eutectic phase has formed on the grain boundaries observed in SEM images of the alloys as well as the primary $\alpha\text{-Mg}$. The microstructure of both alloys indicated that the grains and secondary phases (Mg_2Sn) had showed a homogenous distribution. As shown in Figure 1 (b), residues were observed at grain borders verified by X-ray diffraction analysis. As Al decomposes in $\alpha\text{-Mg}$ matrix due to trace addition of Ti and Sr, and due to the addition of Al of less than 3% by weight, the formation of a new phase is not expected. Considering the Mg-Al binary equilibrium diagram, the decomposition rate of Al in Mg is 25 at room temperature [25]. As the production method ensures rapid solidification, the formation of a beta phase is not expected. This status was also revealed by the XRD analysis.

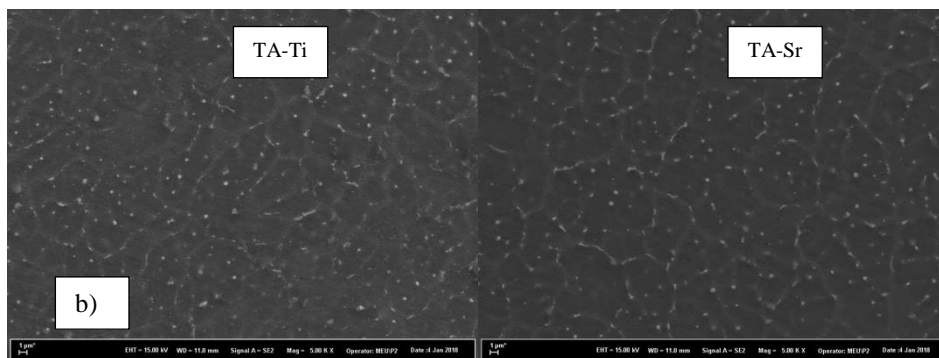
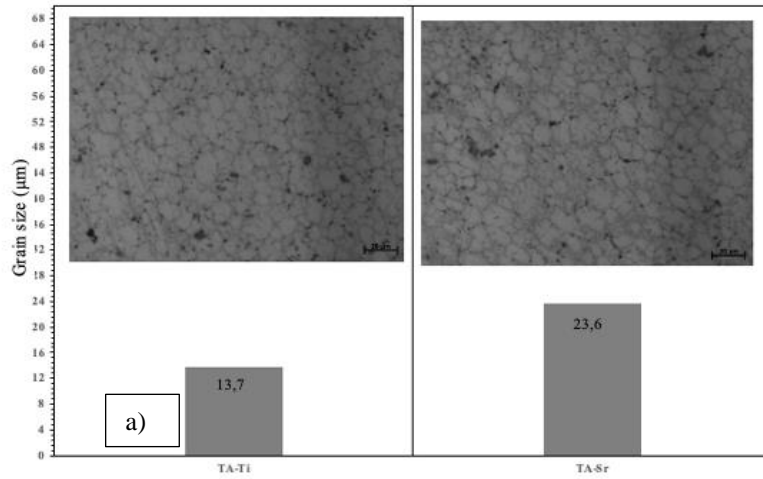


Figure 1. (a) Grain size distribution graph and OM images; (b) SEM images of TA-Ti and TA-Sr magnesium alloys.

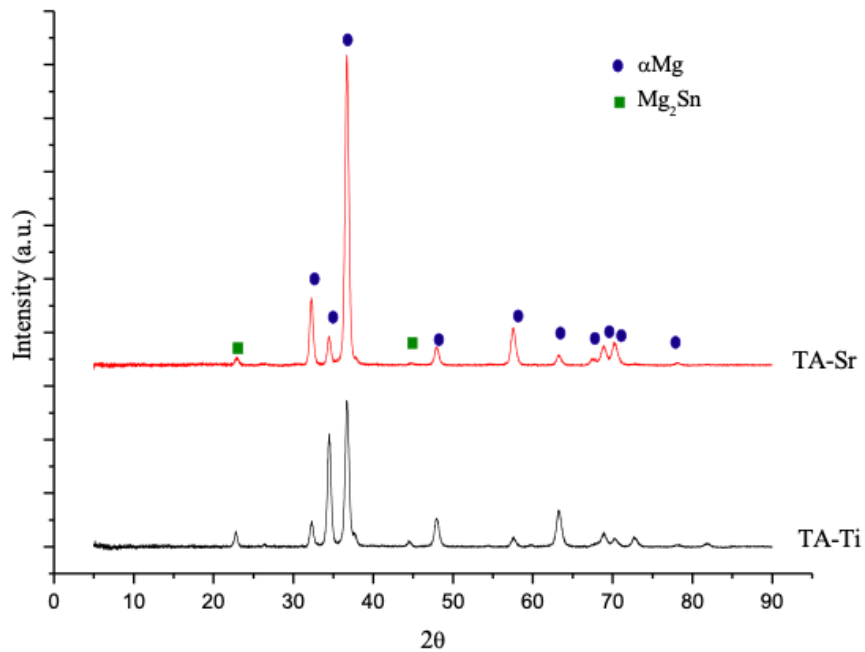


Figure 2. XRD analysis of TA-Ti and TA-Sr magnesium alloys.

In Figure 3, percentage elongation, tensile strength, yield strength, and hardness values of TA-Ti and TA-Sr alloys are observed. The percentage elongation, yield strength, tensile strength, and macrohardness values of TA-Ti alloys are 15.2, 150 MPa, 203 MPa, and 50 HB, respectively, and they are 10.4, 135 MPa, 197 MPa, and 50 HB, respectively, for the TA-Sr alloy. The demonstration of better mechanical properties by the TA-Ti alloy may be associated with the more effective grain size reduction by the addition of titanium. Because the reduction of grain size is one of the mechanisms that increases strength [26]. With the reduction of grain size, the amount of grain boundary increases. In this case, it causes the formation of an impediment, which limits the movements of the dislocations. When the grain size graph in Figure 1(a) and the macrohardness values in Figure 3 are compared, it is observed that the alloy in which Ti was added exhibits higher mechanical properties. Ti is known as a strong structural cooling element. Ti atoms limit the growth of α -Mg and cause the formation of a finer-grained microstructure, and in addition, when Ti is used as the active component of the refiner, it accelerates the nucleation [27, 28]. Moreover, the homogenous precipitation of secondary particles contributes to high macrohardness [29].

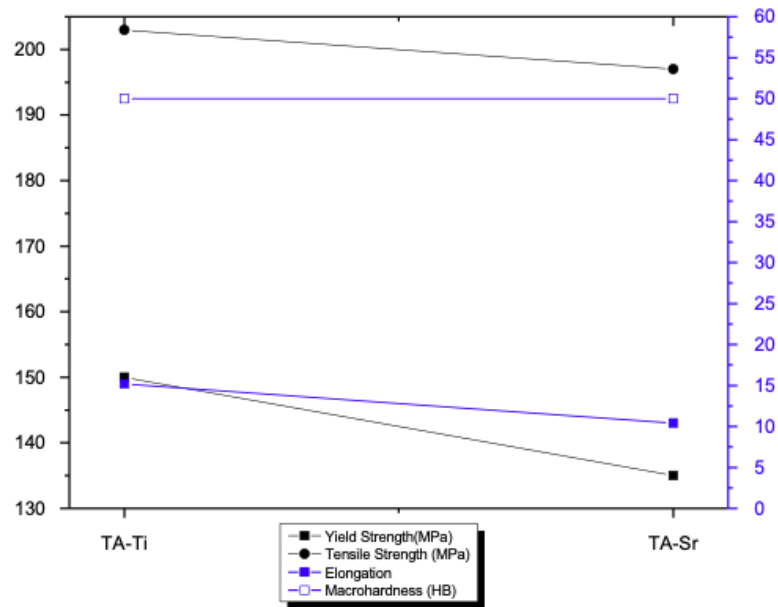


Figure 3. Percentage elongation, tensile strength, yield strength, and macrohardness graph of TA-Ti and TA-Sr alloys.

In Figure 4, the load-displacement curves applied on TA-Ti and TA-Sr alloys are given. As observed from the OM images of the alloys, the fact of *pop-in* is not observed in the curves due to the homogenous structure of the alloys. By the calculations obtained from the load-displacement curves, the average nanohardness and elastic modulus values for the TA-Ti alloy were found to be 46 GPa and 1.19 GPa, respectively, and they were found to be 45.6 GPa and 1.12 GPa for the TA-Sr alloy. Considering these values, it was observed that the nanohardness and elastic modulus were barely increased by the addition of Ti. The increase in the nanohardness value may be directly attributed to the change in microstructure. The increase in nanohardness value by the addition of Ti might have arisen due to the limiting effect of the reduction in grain size on the dislocation movement. On the other hand, it may not be possible to associate the cause of the change in elastic modulus directly with the change in microstructure [30, 31]. The studies performed didn't show that the alloy elements being present in small or trace amounts in the matrix of such alloys affect the magnesium towards higher elastic modulus values [32].

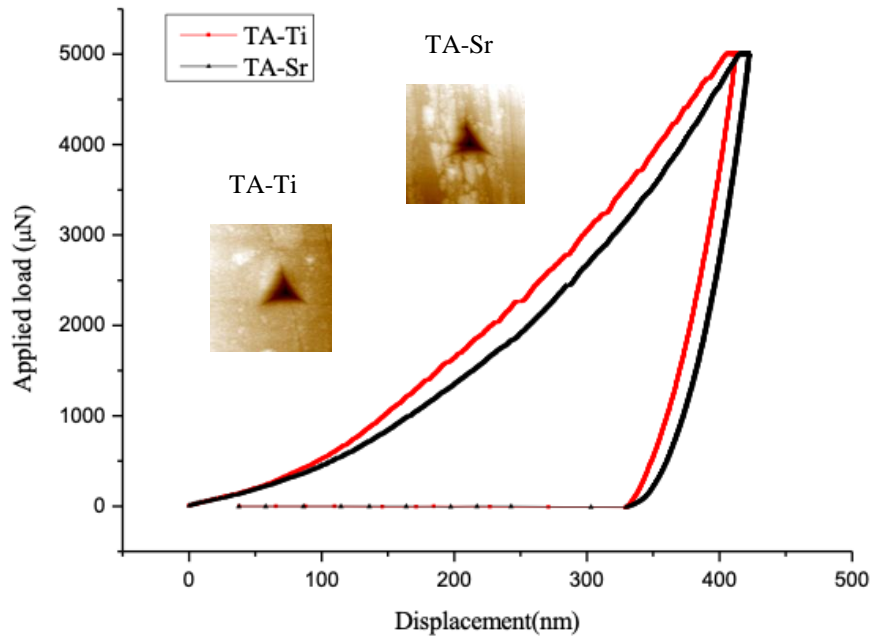


Figure 4. Load-displacement curves of TA-Ti and TA-Sr magnesium alloys.

In Figure 5, the Tafel curves of TA-Ti and TA-Sr alloys obtained from the potentiodynamic polarization test performed in HBSS are given. The addition of Al-15Sr as 3% by weight to the Mg-5Sn alloy caused the alloy's corrosion potential value to move more in a positive direction compared to addition of Al-15Ti as 3% by weight. In Table 1, the corrosion parameters obtained from the Tafel curves of the alloys are given. When Table 1 is examined, the current density values of TA-Ti and TA-Sr alloys were measured as $4.45 \mu\text{A}\cdot\text{cm}^{-2}$ and $6.80 \mu\text{A}\cdot\text{cm}^{-2}$, respectively, and their corrosion rates were measured as 3.8 mm/yr and 5.8 mm/yr. In this case, it was observed that the addition of Ti is more effective in increasing the corrosion resistance of the TA main alloy.

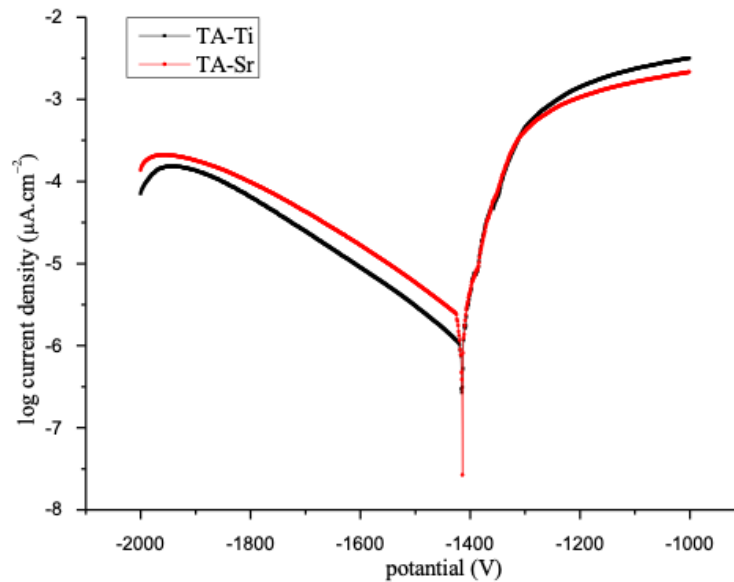


Figure 5. Tafel graphs of TA-Ti and TA-Sr magnesium alloys.

Figure 6 shows the degradation rate graph of TA-Ti and TA-Sr alloys whose degradation rates were calculated by the mass loss method following immersion test. When the graph is examined, it is observed that the degradation rates become stable after about 50 hours. The degradation rate values of the alloys are given in Table 1. As also observed from Table 1, the degradation rate of the TA-Ti alloy (0.18 mm/yr) has a lower value compared to the degradation rate of the TA-Sr alloy (0.24 mm/yr). When the Tafel graph obtained from the electrochemical measurements and the degradation rate graph obtained from the mass loss measurements following the immersion test are examined together, it can be said that both graphs are compatible. The reason for the value of the degradation rate being smaller compared to the value of the corrosion rate is the inability to completely clean the corrosion products remaining within the surface, which transforms into a porous structure during the degradation.

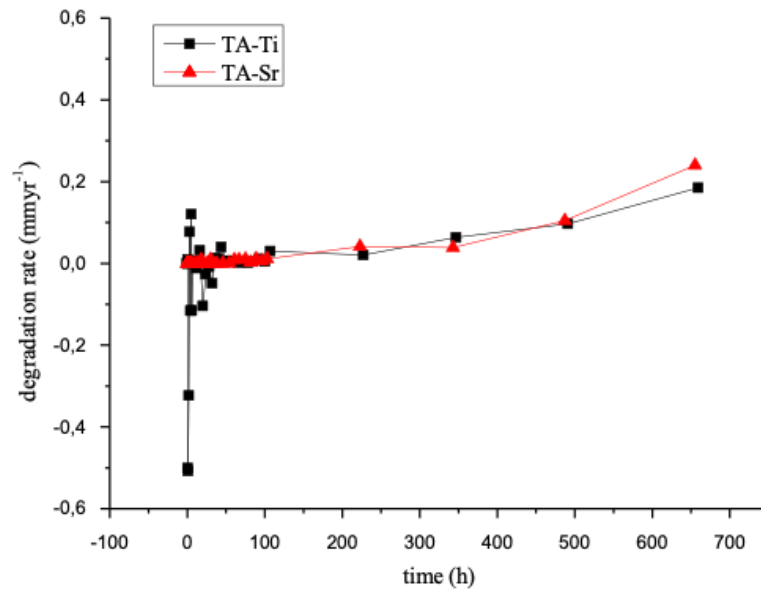


Figure 7. Tafel graphs of TA-Ti and TA-Sr magnesium alloys.

Table 1. Some corrosion parameters of magnesium alloys.

Alloy	E_{corr} (V)	I_{corr} ($\mu A.cm^{-2}$)	Corrosion rate (mm/yr)	Degradation rate (mm/yr)
TA-Ti	-1.415	4.45	3.8	0.18
TA-Sr	-1.414	6.80	5.8	0.24

It is well known that the changes in the microstructure of an alloy affect the alloy's corrosion properties as well as directly affect the alloy's mechanical properties [33-34]. The reduction in grain size by the addition of Ti might have caused the formation of a more passive film and its role in preventing corrosion [35]. As a result of the electrochemical and immersion tests performed, it was observed that the addition of both alloys had the effect of increasing the corrosion resistance of magnesium, but that the addition of Ti was more effective in enhancing the corrosion.

4. DISCUSSION

The microstructural, mechanical, and corrosion properties of TA-Ti and TA-Sr alloys, produced using the high pressure die casting technique, were investigated. As a result of microstructure examinations, it was observed that the addition of Al-15Ti and Al-15Sr master alloys effectively reduced the grain

size of the Mg-5Sn alloy, and that the addition of Ti was more effective in the reduction of grain sizes compared to the addition of Sr. The alloys were found to be composed of α -Mg phase and Mg₂Sn intermetallic phases. When the mechanical properties were examined, it was observed that the addition of Ti increased the yield strength, tensile strength, percentage elongation, macrohardness, nanohardness, and elastic modulus values more compared to the addition of Sr. It can be stated that both the corrosion and degradation rates obtained as a result of electrochemical and immersion tests decreased with the addition of Ti, in other words the TA-Ti alloy was more resistant to corrosion compared to the addition of TA-Sr.

ACKNOWLEDGEMENT

There is no funding body the author could acknowledge.

REFERENCES

- [1] Witte, F., Hort, N., Vogt, C., Cohen, S., Kainer, K.U., Willumeit, R., Feyerabend, F., (2008), Degradable biomaterials based on magnesium corrosion, *Curr. Opin. Solid State Mater. Sci.*, 12, 63 -72.
- [2] Moravej, M. and Mantovani, D., (2011), Biodegradable metals for cardiovascular stent application: interests and new opportunities,” *International journal of molecular sciences*, 12 (7), 4250-4270.
- [3] Kirkland, N.T., Birbilis, N. and Staiger, M.P., (2012), Assessing the corrosion of biodegradable magnesium implants: a critical review of current methodologies and their limitations. *Acta biomaterialia*, 8 (3), 925-936.
- [4] Staiger, M.P., Pietak, A.M., Huadmai, J. and Dias, G., (2006), Magnesium and its alloys as orthopedic biomaterials: a review, *Biomaterials*, 27 (9), 1728-1734.
- [5] Uddin, M.S., Hall, C., Murphy, P. (2015), Surface treatments for controlling corrosion rate of biodegradable Mg and Mg-based alloy implants,” *Science and technology of advanced materials*, 16 (5), 053501.
- [6] Johnson, A.R., Munoz, A., Gottlieb J.L. and Jarrard, D.F., (2007), High dose zinc increases hospital admissions due to genitourinary complications, *The Journal of urology*, 177 (2), 639-643.
- [7] Gu, X., Zheng, Y., Cheng, Y., Zhong, S. and Xi, T., (2009), In vitro corrosion and biocompatibility of binary magnesium alloys, *Biomaterials*, 30 (4), 484-498.
- [8] Song, G., Control of biodegradation of biocompatible magnesium alloys (2007), *Corrosion science*, 49 (4), 1696-1701.
- [9] Liu, X., Sun, J., Yang, Y., Pu, Z., Zheng, Y., (2015), In vitro investigation of ultra-pure Zn and its mini-tube as potential bioabsorbable stent material, *Mater. Lett.*, 161, 53-56.

- [10] Liu, H., Chen, Y., Tang, Y., Wei, S. and Niu, G., (2007), The microstructure, tensile properties, and creep behavior of as-cast Mg-(1–10)% Sn alloys, *Journal of Alloys and Compounds*, 440 (1-2). 122-126.
- [11] Marya, M., Hector, L.G., Verma, R., Tong, W., (2006), Microstructural effects of AZ31 magnesium alloy on its tensile deformation and failure behaviors, *Mater. Sci. Eng., A*, 418, 341-356.
- [12] Zheng, Y.F., Gu, X.N., Witte, F., (2014), Biodegradable metals, *Mater. Sci. Eng. R. Rep.*, 77, 1-34.
- [13] Homayun, B. Afshar, A., (2014), Microstructure, mechanical properties, corrosion behavior and cytotoxicity of Mg–Zn–Al–Ca alloys as biodegradable materials, *J. Alloys Compd.*, 607, 1-10.
- [14] Sunil, B.R., Kumar, T.S.S., Chakkingal, U., Nandakumar, V., Doble, M., et al. (2016), In vitro and in vivo studies of biodegradable fine grained AZ31 magnesium alloy produced by equal channel angular pressing, *Mater. Sci. Eng. C*, 59, 356-367.
- [15] Sun, W., Zhang, G, Tan, L., Yang, K., Ai, H., (2016), The fluoride coated AZ31B magnesium alloy improves corrosion resistance and stimulates bone formation in rabbit model, *Mater. Sci. Eng. C*, 63, 506-511.
- [16] Huang, Z.H., Zhou, N., Xu, J., Li, Y.D. and Li, W.R., (2017), Microstructure and Mechanical Property of Mg-Sn-Al Wrought Magnesium Alloys, In *Materials Science Forum Trans Tech Publications Ltd.*, 898, 97-103.
- [17] Bowles, A.L., Blawert, C., Hort, N. and Kainer, K.U., (2004), Microstructural investigations of the Mg-Sn and Mg-Sn-Al alloy systems, *Magnesium Technology*, ss.307-310.
- [18] Koltygin, A., Bazhenov, V. and Mahmadiyrov, U., (2017), Influence of Al–5Ti–1B master alloy addition on the grain size of AZ91 alloy, *Journal of magnesium and alloys*, 5(3), 313-319,
- [19] Luo, A.A., (2013), Magnesium casting technology for structural applications, *Journal of Magnesium and Alloys*, 1 (1), 2-22.
- [20] Banerjee, A., (2013), Process-Structure Relationships of Magnesium Alloys, The University of Western Ontario Graduate Program in Mechanical and Materials Engineering Master thesis.
- [21] Ralston, K.D. and Birbilis, N., (2010), Effect of grain size on corrosion: a review, *Corrosion*, 66 (7), 075005-075005.
- [22] Bahmani, A., Arthanari, S. and Shin, K.S., (2020), Formulation of corrosion rate of magnesium alloys using microstructural parameters, *Journal of Magnesium and Alloys*, 8 (1), 134-149.

- [23] Chao, H.Y. Yang, Y. Wang, X. and Wang, E.D., (2011), Effect of grain size distribution and texture on the cold extrusion behavior and mechanical properties of AZ31 Mg alloy, *Materials Science and Engineering: A*, 528 (9), 3428-3434.
- [24] Oliver, W. C. and Pharr, G. M., (2004), Measurement of hardness and elastic modulus by instrumented indentation: Advances in understanding and refinements to methodology, *Journal of materials research*, 19 (1), 3-20.
- [25] Murray, J.L., (1982), The Al- Mg (aluminum- magnesium) system. *Journal of Phase Equilibria*, 3 (1), 60-74.
- [26] Dieter, G.E. and Bacon, D.J., (1986), *Mechanical metallurgy (Vol. 3)*. New York: McGraw-hill.
- [27] Wang, Y., Zeng, X., Ding, W., Luo, A. A., Sachdev, A. K., (2007), Grain refinement of AZ31 magnesium alloy by titanium and low-frequency electromagnetic casting. *Metallurgical and Materials Transactions A*, 38(6), 1358-1366.
- [28] Chen, T. J., Wang, R. Q., Ma, Y., Hao, Y., Grain refinement of AZ91D magnesium alloy by Al-Ti-B master alloy and its effect on mechanical properties. *Materials & Design*, 34, 637-648.
- [29] Naik, G. M., Gote, G. D., Narendranath, S., Kumar, S. S., (2012), Effect of grain refinement on the performance of AZ80 Mg alloys during wear and corrosion. *Advances in Materials Research*, 7(2), 105, 2018.
- [30] Kaya, A.A., Çelik, Ç., Türe, Y., Ataman, A., Arkin, E., Palumbo, G., Sorgente, D. and Turan, D., (2017), Elasticity modulus and damping in some novel magnesium alloys, In *Proceedings of the 6th International Conference on Magnesium*.
- [31] Kaya, A.A., Çelik, Ç., Türe, Y., Ataman, A., Arkin, E., Palumbo, G., Sorgente, D. and Turan, D., (2017), New Magnesium Alloys with High Elastic Modulus, *International Materials Technologies and Metallurgy Conference Istanbul*.
- [32] Özarslan, S., Şevik, H. and Sorar, İ., (2019), Microstructure, mechanical and corrosion properties of novel Mg-Sn-Ce alloys produced by high pressure die casting, *Materials Science and Engineering: C*, 105, 110064.
- [33] Cui, Q., Ti, D., Wang, H., Zhang, J., Xu, J., Wang, B., (2019), Effects of grain size and secondary phase on corrosion behavior and electrochemical performance of Mg-3Al-5Pb-1Ga-Y sacrificial anode, *J. Rare Earths*.
- [34] Aung, N.N. Zhou, W., (2010), Effect of grain size and twins on corrosion behaviour of AZ31B magnesium alloy, *Corros. Sci.*, 52, 589.
- [35] Öteyaka, M. Ö., Ghali, E., & Tremblay, R. (2012), Corrosion behaviour of AZ and ZA magnesium alloys in alkaline chloride media, *International Journal of Corrosion*.



RESEARCH ARTICLE

**OPTIMIZATION of ATMOSPHERIC PLASMA SPRAY PROCESS PARAMETERS for
DEPOSITION of THERMAL BARRIER COATINGS**

Savaş ÖZTÜRK*

*Manisa Celal Bayar University, Engineering Faculty, Department of Metallurgical and Materials Engineering,
savas.ozturk@cbu.edu.tr ORCID: 0000-0003-2661-4556

Receive Date:09.03.2022

Accepted Date: 29.06.2022

ABSTRACT

In the production of thermal barrier coating (TBC) with the atmospheric plasma spray coating system, the process parameters directly affect the production cost and performance of the coatings. In this study, a comprehensive modeling-design-optimization study was conducted to improve the analytical performance of TBC. For this purpose, the data were taken from a literature study that included an extensive experimental design application. The modeling study prepared first, second, and third-order polynomial, trigonometric, and logarithmic-based models for each process output. Model selections were made with neuro-regression and a statistical method. The selected models were run on four different stochastic optimization algorithms for the coatings' deposition efficiency, bond strength, porosity, and hardness value outputs. Thirty-six neuro-regression models prepared in the modeling study have high R^2_{training} values. The second-order logarithmic nonlinear (SOLN) models were successful in the coatings' deposition efficiency and bond strength, and the polynomial nonlinear models were successful for the four process outputs. Therefore, they were chosen as the objective functions of the optimization algorithms. In addition, the selected models were run at the parameters determined by numerical optimization in the reference publication, and the prediction abilities of the models in the two studies were compared. SOLN models for deposition efficiency and bond strength values, second-order nonlinear model for hardness value, and reference study' model predicted more closely to the validation test result for porosity values of coating. In the optimization studies, three or more algorithms suggested the same results with the same parameter sets for the deposition efficiency and hardness values. The optimization results show that these points can be a global optimum point for optimizing these two coating properties.

Keywords: *Plasma spray coating, Thermal barrier coating, Neuro-regression, Optimization*

1. INTRODUCTION

Gas turbine engines are widely used in power plants and aircraft engines. Turbine engines used in power plants operate for extended periods (100-500 days) at high temperatures under constant thermal stresses. Although the ones used in aircraft engines work for shorter periods, they operate under variable thermal stresses due to different conditions intake off-landing and flight [1]. More dynamic and stable flight of airplanes is ensured by having a sizeable thrust-weight ratio. Increasing the turbine inlet temperature is an efficient approach to increase the thrust-weight ratio. However, increasing the

temperature will also increase the condition of the turbine components to undergo hot corrosion, high stresses, and oxidation. The most effective method to eliminate this problem is to coat turbine engine components with ceramic TBC with low thermal conductivity [1-3]. TBC are deposited in the form of a metallic bond coating and a ceramic top coating on nickel-based superalloy parts that are resistant to the operating conditions of turbine engines. The bond coating provides oxidation and corrosion resistance to the structure and balances the thermal properties and tensions between the ceramic coating and the substrate. The ceramic top coating provides thermal insulation, strain tolerance, and thermal shock resistance for hot components by reducing heat transfer. Generally, in TBC, 40-200 μm thick MCrAlY (M= Ni, Co) is used as the bond coating, while 100-400 μm thick yttrium-stabilized zirconia (YSZ) is used as the top coating [1, 2, 4].

TBCs are mainly produced using either electron beam physical vapor deposition (EB-PVD) or atmospheric plasma spraying (APS) [5, 6]. In EB-PVD, the raw materials are deposited on the substrate surface after heated and evaporated with a high-energy electron beam. Coatings are deposited as columnar grains containing closed and open pores perpendicular to the substrate in a typical EB-PVD system. Microstructures of PVD coatings have good strain tolerance due to their low elastic modulus. In this way, the thermal cycle life of the coated engine components is extended. However, the EB-PVD technique is more complex and costly than other coating techniques [5]. Metallic or ceramic coating powders in APS coatings are injected into the plasma jet with a carrier gas. The coating powders are converted into semi-molten form by heating in the plasma, and at the same time, they are accelerated and sprayed onto the substrate surface. When semi-molten powders hit the substrate surface, they spread on the surface and form coating layers called splats. Therefore, APS coatings are relatively less costly and have lower thermal conductivity than EB-PVD coatings [1, 2, 5, 6].

Optimization of APS coatings begins with the mathematical modeling of process parameters and responses. Many microstructural and physical properties of TBC, such as the amount of porosity, bond strength, and hardness, are affected by more than fifty factors such as plasma characteristics, substrate properties, coating powder properties, atmosphere, device and user properties [7]. These parameters can affect the properties of coatings both individually and together. Many researchers have studied various experimental and statistical methods to optimize these effects of parameters. Chen et al. investigated the effects of plasma power, process gas flow values, and coating distance on the thermal shock resistance of the coating by using Range analysis [8]. Bertrand et al. statistically investigated the effects of plasma power, coating distance, gas flow rates, speed, and angle of movement of the coating gun on the surface roughness, deposition efficiency, amount of porosity, and thermal conductivity properties of coatings [9]. Ning et al. investigated the effects of process parameters on thermal stress estimation of coatings using Artificial Neural Networks (ANN) [10]. Ramachandran et al. investigated the effects of primary and carrier gas flow rates, plasma power, coating distance, and powder feed rate on coatings' deposition efficiency and bond strength by response surface analysis (RSA) [11]. Kim et al. investigated the change of oxide growth in the bond layer of TBC with thermal cycle tests and process temperature and time with regression analysis (RA) [12]. Karthikeyan et al. investigated the effects of plasma power, coating distance, and powder feed rate on their coatings' porosity and hardness values with RSA. They modeled the data with RA [13].

Optimization of the physical, mechanical, and thermal properties of APS coatings has been investigated by many researchers using various optimization algorithms [4, 14-18]. Lin et al. obtained the optimal plating distance, plasma current, argon, and hydrogen gas flow rates using an ANN and

Genetic Algorithm (GA). They performed validation tests using these parameters and obtained approximately 40% reduction in the porosity value of the coatings, high-temperature stability, and high hardness [4]. Tonkonogy et al. investigated the effects of grinding parameters on the surface properties of coatings by using ant colony, particle swarm, scatter search, and genetic algorithm. They stated that the surfaces of the coatings deposited with the parameters suggested by the genetic algorithm would have lower surface defects and roughness [17]. Ye et al. investigated the microstructural properties of coatings such as porosity, pore-crack ratio, and maximum ferret diameter with the Cuckoo Search Algorithm. They noted that there was no significant relationship between porosity, pore-crack ratio, maximum Feret diameter, and aspect ratio, but the coating powder size had a significant effect on the microstructure properties of the coatings [18]. Shi et al. investigated the effects of the microstructural properties of the coatings on the thermal diffusivity behavior with Random Generation Algorithm. They suggested that the best thermal insulation achieved in a 50 μm coating with porosity widths from 0.54 μm to 2.56 μm [15]. Sankar et al. investigated the effects of coating thickness on thermal conductivity with GA and suggested the optimum coating thickness as 125 μm [16]. Rajesh et al. used Teaching Learning Based Optimization Algorithm to obtain optimum microhardness, porosity, wear and surface roughness values of their coatings. They determined that parameters such as carrier gas flow rate, coating distance, arc current, and powder feed rate are directly related to coating properties [14].

The APS process optimization studies are examined, it is seen that only one first or second-order regression model is used in the preparation of the objective functions. In these studies, the data obtained with the process parameters were estimated by the models prepared with the same parameters. The ability of the models to predict the actual values was checked with the R^2 calculation. After this evaluation, models with high R^2 values were stated as successful. However, in this approach, while the models successfully predict the results obtained only in those parameters, they may not predict the whole process correctly. Such problems have been somewhat resolved with ANN-based modeling and optimization studies [4]. Another critical issue is the limitation of models as objective functions. System parameters can be used within a certain operating range in engineering applications. This situation requires that the functions that define the systems also have boundaries. In addition, the security, sensitivity, and robustness of the algorithm used in stochastic search systems should also be considered [19].

In this study, a modeling-design-optimization technique was conducted to optimize the process parameters in the production of TBCs with the APS system. This method was organized using data from a literature study [11], which organized the experimental work with a factorial experimental design set to optimize the deposition efficiency, tensile bond strength, hardness, and porosity of the coatings. Firstly, in modeling and optimization studies, neuro-regression models in different forms (linear, polynomial, trigonometric and logarithmic) were made. Secondly, the prepared models were selected for each process output by checking the statistical analyzes and limit values. Finally, Differential Evolution (DE), Nelder-Mead (NM), Random Search (RS), and Simulated Annealing (SA) stochastic optimization algorithms were run with selected models to solve the same problems. In this way, optimum operating parameters for the APS process were obtained.

2. MATERIAL AND METHOD

2.1. Modelling

In the modeling stage, a hybrid method combining the benefits of RA and ANN was used to test the accuracy of the predictions. In this method, four-fifths of all data are randomly allocated for training. The rest is used for testing. The purpose of the training process is to minimize the difference between the experimental and predicted values by adjusting the regression models and coefficients listed in Table 1. Finally, in the testing phase, the ability of the models prepared with the training data to predict the test data is checked.

Statistical analyses of the coefficient of determination (R^2_{training} , R^2_{testing}), root mean square error (RMSE), mean absolute error (MAE), and model efficiency (ME) of training and test data for each model were used to determine the relationships between neuro-regression models and experimental data (see Eq. 1-4). In addition, the lowest and highest predictive values of all models were calculated under experimental limit conditions.

$$R^2 = 1 - \frac{\sum_{i=1}^n (X_{A,i} - X_{P,i})^2}{\sum_{i=1}^n X_{P,i}^2} \quad (1)$$

$$RMSE = \sqrt{\frac{1}{n} \sum_{i=1}^n (X_{A,i} - X_{P,i})^2} \quad (2)$$

$$MAE = \frac{1}{n} \sum_{i=1}^n (X_{A,i} - X_{P,i}) \quad (3)$$

$$ME = 1 - \frac{\sum_{i=1}^n (X_{A,i} - X_{P,i})^2}{\sum_{i=1}^n (X_{A,i} - \bar{X}_{P,i})^2} \quad (4)$$

where X_A is the actual value and X_P is the estimated value.

To determine the objective functions in the optimization algorithms, the statistical calculations and limit values of the nine neuro-regression models were calculated, and model selections were made. Model selection is carried out in three steps. In the first step, R^2_{training} and R^2_{testing} values are checked, and those with values greater than 0.9 will be selected. In the second step, the limit values of the models are checked, and the models with less than 100% difference to the experimental data will be selected. In the third step, the models' RMSE, MA, and ME values are checked. Models with RMSE and MA values close to zero and ME values close to one will be determined as target functions.

Table 1. Multiple regression model forms.

Models	Nomenclature	Formula
First Order Multiple linear	FOL	$Y = \sum_{i=1}^3 (a_i x_i) + c$
Second order multiple nonlinear	SON	$Y = \sum_{k=1}^3 \sum_{j=1}^3 (a_j x_j x_k) + \sum_{i=1}^3 (a_i x_i) + c$
Third order multiple nonlinear	TON	$Y = \sum_{l=1}^3 \sum_{m=1}^3 \sum_{p=1}^3 (\beta_l x_l x_m x_p) + \sum_{k=1}^3 \sum_{j=1}^3 (a_j x_j x_k) + \sum_{i=1}^3 (a_i x_i) + c$
First order trigonometric multiple nonlinear	FOTN	$Y = \sum_{i=1}^3 (a_i \sin[x_i] + a_i \cos[x_i]) + c$
Second order trigonometric multiple	SOTN	$Y =$

nonlinear		$\sum_{i=1}^3 (a_i \sin[x_i] + a_i \cos[x_i]) + \sum_{j=1}^3 (\beta_j \sin^2[x_j] + \beta_j \cos^2[x_j]) + c$ $Y =$
Third order trigonometric multiple nonlinear	TOTN	$\sum_{i=1}^3 (a_i \sin[x_i] + a_i \cos[x_i]) + \sum_{j=1}^3 (\beta_j \sin^2[x_j] + \beta_j \cos^2[x_j]) + \sum_{k=1}^3 (\gamma_k \sin^3[x_k] + \gamma_k \cos^3[x_k]) + c$ $Y =$
First order logarithmic multiple nonlinear	FOLN	$Y = \sum_{i=1}^3 (a_i \log[x_i]) + c$ $Y =$
Second order logarithmic multiple nonlinear	SOLN	$\sum_{k=1}^3 \sum_{j=1}^3 (a_j \log[x_j x_k]) + \sum_{i=1}^3 (a_i \log[x_i]) + c$ $Y = \sum_{l=1}^3 \sum_{m=1}^3 \sum_{p=1}^3 (\beta_l \log[x_l x_m x_p]) +$
Third order logarithmic multiple nonlinear	TOLN	$\sum_{k=1}^3 \sum_{j=1}^3 (a_j \log[x_j x_k]) + \sum_{i=1}^3 (a_i \log[x_i]) + c$

2.2. Optimization

Structural optimization is defined as reaching the optimum value by minimizing or maximizing the specified single or multiple targets, considering all constraints. For this purpose, two types of optimization techniques called traditional and non-traditional are used. Traditional optimization techniques only work for continuous and differentiable functions. However, some engineering design problems have characteristic properties that conventional optimization techniques, which only work for continuous and differentiable functions, cannot be used. For this reason, only non-traditional methods can be used to solve these problems. For this purpose, many optimization algorithms such as Ant Colony, Particle Swarm, and Genetic Algorithm were developed and used in many engineering applications [17, 20, 21]. However, since the exact solution cannot be reached with stochastic methods, it is beneficial to use more than one algorithm with various technical infrastructure for the same optimization problem solution to increase the reliability of the result [19].

Some objective function-based problems can be encountered in solving mathematical optimization problems by stochastic algorithms. The problems of objective functions are expressed in general titles as non-multilinearity, having many local optimum points, mixed-integer design variables, and nonlinear constraints [19]. In this study, DE, NM, SA, and RS optimization algorithms, which have been successfully applied in many engineering applications, were used to solve the same APS coating problems to overcome the difficulties encountered in the optimization study. Detailed information and operating parameters of these algorithms are available in [19, 20].

2.3. Problem Definition

In this study, the deposition efficiency, bond strength, porosity, and set values of TBC produced by the APS process were optimized. Firstly, the data used to determine the objective functions were taken from the literature study [11]. The data including coating process inputs (Input Power (P), Primary Gas Flow Rate (PGFR) Coating Distance (D), Powder Feed Rate (PFR), Carrier Gas Flow Rate (CGFR) and outputs (Deposition Efficiency (E), Bond Strength (BS), Porosity (P), Hardness (H)) are presented in Table 2. Next, nine candidate functional structures are proposed to express the relationship between each process output and inputs mathematically. Then, the selection of the most suitable model for each output was made in two steps: the calculation of the R^2_{training} , R^2_{testing} , RMSE,

MAE, ME, limit values of the models, and the selection of those that satisfy the conditions. Finally, all coating problems are solved by four different direct search algorithms with the selected models.

In this optimization study, the objective functions define the deposition efficiency, bond strength, porosity, and hardness values of the coating of YSZ powder as TBC in the APS system. The objectives of the optimization study are to maximize the deposition efficiency, bond strength, and hardness values and minimize the porosity value. The search space is continuous in the optimization setup, and the design variables are integers. Design values for this process were determined as $22 \text{ kW} \leq P \leq 30 \text{ kW}$, $25 \text{ lpm} \leq \text{PGFR} \leq 45 \text{ lpm}$, $90 \text{ mm} \leq D \leq 130 \text{ mm}$, $15 \text{ gpm} \leq \text{PFR} \leq 35 \text{ gpm}$, and $3 \text{ lpm} \leq \text{CGFR} \leq 11 \text{ lpm}$.

Table 2. Process parameters and responses in the factorial experimental design set of thermal barrier coatings [11].

Run	Process parameters					Responses			
	P (kW)	PGFR(lpm)	D (mm)	PFR(gpm)	CGFR(lpm)	E (%)	BS(MPa)	P (%)	H (Hv _{0.3})
1	24	30	100	15	9	44	9	20	710
2	28	30	100	15	5	59	17	8	954
3	24	40	100	15	5	49	7	11	792
4	28	40	100	15	9	67	21	4	1082
5	24	30	40	15	5	42	5	25	675
6	28	30	40	15	9	39	7	22	683
7	24	40	40	15	9	47	10	23	757
8	28	40	40	15	5	60	14	11	966
9	24	30	100	30	5	42	4	25	675
10	28	30	100	30	9	58	13	14	943
11	24	40	100	30	9	47	9	19	757
12	28	40	100	30	5	63	16	9	1024
13	24	30	40	30	9	32	4	25	512
14	28	30	40	30	5	40	5	24	652
15	24	40	40	30	5	41	6	25	663
16	28	40	40	30	9	45	8	17	733
17	22	35	110	25	7	41	6	23	663
18	30	35	110	25	7	64	19	6	1036
19	26	25	110	25	7	38	8	23	617
20	26	45	110	25	7	53	15	11	861
21	26	35	90	25	7	66	16	7	1071
22	26	35	130	25	7	48	7	23	780
23	26	35	110	15	7	58	18	12	943
24	26	35	110	35	7	48	13	21	780
25	26	35	110	25	3	58	10	13	943
26	26	35	110	25	11	53	11	14	861
27	26	35	110	25	7	70	23	5	1129
28	26	35	110	25	7	72	22	4	1164
29	26	35	110	25	7	70	23	5	1129
30	26	35	110	25	7	71	22	4	1140
31	26	35	110	25	7	70	23	5	1129

32 26 35 110 25 7 72 22 4 1164

3. RESULTS AND DISCUSSION

In the reference study [11], the experimental setup of TB production with the APS system was organized according to the factorial experimental design set:

I. The results were modeled by RA.

II. They obtained the optimum values graphically with response surface analysis and numerically via the models. In both calculations, the input power 26.3 kW, coating distance 110.5 mm, carrier gas flow rate 36.15 lpm, powder feed rate 23.35 gpm, and carrier gas flow rate 7.8 lpm were found as optimum values of process parameters. They determined the deposition efficiency as 71.0825%, the bond strength as 22.999 MPa, the porosity as 4.0009%, and the hardness as 1148.92 HV_{0.3} via graphical optimization.

III. They calculated the deposition efficiency as 71.0837%, the bond strength as 22.9997 MPa, the porosity as 4.0001%, and the hardness as 1148.94 HV_{0.3} via numerical optimization.

The statistical results and limit values of neuro-regression models of deposition efficiency, bond strength, porosity, and hardness values of TBC produced with the APS system are given in Table 3-6, respectively. The objective functions for each coating response were selected by examining these values.

Table 3. Results of Neuro-Regression models prepared for deposition efficiency of coatings.

Models	R ² _{training}	R ² _{testing}	RMSE	MAE	ME	Maximum (%)	Minimum (%)
FON	0.982	0.0575	7.2345	5.9144	0.5966	81.4711	32.8749
SON	0.9977	0.8176	2.5516	1.8566	0.9498	81.8114	9.2366x10 ⁻⁷
TON	0.9999	0.9599	0.3202	0.1025	0.9992	81.313	19.3512
FOTN	0.9853	0.4183	6.537	4.7106	0.6706	114.393	4.2758x10 ⁻⁶
SOTN	0.9999	0.1365	0.3202	0.1025	0.9992	76.1162	10.4223
TOTN	0.9999	-0.404	0.3202	0.1025	0.9992	62	1.1014 x10 ⁻¹²
FOLN	0.9827	0.1407	7.0935	5.76	0.6121	78.7856	32.1459
SOLN	0.9975	0.9122	1.6487	0.9137	0.9459	86.798	21.1729
TOLN	0.9999	0.687	0.3202	0.1025	0.9992	117.494	9.1199 x10 ⁻¹¹

All models had R²_{training} values greater than 0.98 as shown in Table 3. However, only the TON and SOLN models have R²_{testing} values greater than 0.9. The maximum and minimum values are 81.313%, 19.3512% for TON and 86.798%, and 21.1729% for SOLN. Therefore, it was determined that the limit values of both models were compatible with the experimental results. In the final model selection step, it was seen that both models met the criteria for RMSE, MAE, and ME values. Therefore, the TON and SOLN models, which were successful in all evaluations, were chosen as objective functions for the optimization of the deposition efficiency of the coatings.

Table 4. Results of Neuro-Regression models for bond strength value of coatings.

Models	R ² _{training}	R ² _{testing}	RMSE	MAE	ME	Maximum (MPa)	Minimum (MPa)
--------	------------------------------------	-----------------------------------	------	-----	----	---------------	---------------

FON	0.9264	-0.0812	3.7064	2.9298	0.6312	28.2771	0.7685
SON	0.9941	0.9192	1.0416	0.798	0.9708	26.6069	1.1248
TON	0.9998	0.6835	0.1601	0.0512	0.9993	27.8997	3.4416 x10 ⁻⁷
FOTN	0.9511	0.352	3.0225	2.0048	0.7547	56.6733	8.0577 x10 ⁻¹¹
SOTN	0.9998	0.3426	0.1601	0.0512	0.9933	27.0203	1.1242 x10 ⁻⁸
TOTN	0.9998	0.4154	0.1802	0.0633	0.9993	11.0614	2.1811 x10 ⁻⁷
FOLN	0.9269	-0.0078	3.6955	2.9044	0.6334	27.0397	0.679
SOLN	0.9924	0.9325	1.1858	0.9116	0.9626	28.5923	1.8785
TOLN	0.9998	0.5425	0.1601	0.0511	0.9993	41.3351	8.1877 x10 ⁻⁸

Table 4 shows the statistical results and limit values for the neuro regression models prepared for the bond strength of the coatings. It is seen that the R^2_{training} values of all models are greater than 0.92, and even the 2nd and 3rd-degree models are greater than 0.99. However, only the R^2_{testing} values of the SON and SOLN models were greater than the limit value of 0.9 (0.9192 and 0.9325). These two models also satisfied the other two criteria and were chosen as objective functions for optimizing the bond strength of the coatings.

Table 5. Results of Neuro-Regression models for porosity value of coatings.

Models	R^2_{training}	R^2_{testing}	RMSE	MAE	ME	Maximum (%)	Minimum (%)
FON	0.9579	0.0221	3.5559	2.7711	0.7768	31.5121	1.8892 x10 ⁻⁷
SON	0.9929	0.7831	1.4061	0.89	0.965	42.7176	9.4926 x10 ⁻¹¹
TON	0.9999	0.9358	0.1601	0.0512	0.9995	36.562	0.8587
FOTN	0.9546	0.0927	3.5683	2.2883	0.7752	57.9335	1.2801 x10 ⁻⁷
SOTN	0.9999	0.3032	0.1601	0.0512	0.9995	30.9089	1.9072 x10 ⁻⁷
TOTN	0.9999	-0.3731	0.1601	0.0512	0.9995	27.925	5.7252 x10 ⁻⁸
FOLN	0.99525	0.1219	3.6484	2.8352	0.765	31.0363	1.7474 x10 ⁻⁸
SOLN	0.993	0.8218	1.3967	0.8633	0.9655	47.5996	3.6005
TOLN	0.9999	-0.1294	0.1601	0.0512	0.9995	91.9325	2.0571 x10 ⁻⁷

Table 5 shows the statistical results and limit values for the neuro-regression models for the porosity values of the coatings. It is seen that the R^2_{training} values of all models are greater than 0.95, but only the R^2_{testing} value 0.9358 of the TON model is greater than the limit value of 0.9. Therefore, the maximum and minimum values that can be reached with the TON model are 36.562% and 0.8587%, respectively, which meet the limit criteria. Finally, the RMSE, MAE, and ME values were examined. It was seen that the RMSE and MAE values were close to zero (0.1601 and 0.0512), and the ME values were close to 1 (0.9995). Therefore, the TON model met all the criteria and was chosen as the objective function for optimizing the porosity of the coatings.

Table 6. Results of Neuro-Regression models for hardness value of coatings.

Models	R^2_{training}	R^2_{testing}	RMSE	MAE	ME	Maximum (HV _{0.3})	Minimum (HV _{0.3})
FON	0.9871	0.042	8.876	78.4129	0.6553	1358.58	487.096
SON	0.9991	0.9694	3.7793	2.4316	0.9792	1238.91	280.1352
TON	0.9999	0.4552	5.6044	1.7948	0.999	1410.46	301.154
FOTN	0.9918	0.4106	78.9978	49.7294	0.8055	2091.45	5.088 x10 ⁻⁶
SOTN	0.9999	-0.0912	5.6044	1.7948	0.999	1248.3	178.491

TOTN	0.9999	0.796	5.6044	1.7948	0.999	1193.6	15.2357 x10 ⁻⁶
FOLN	0.9866	0.1243	100.966	80.0364	0.6823	1312.47	498.078
SOLN	0.9989	0.043	28.2528	17.5079	0.9751	1313.19	3.6379 x10 ⁻¹²
TOLN	0.9999	0.522	5.6044	1.7948	0.999	1760.2	2.8323 x10 ⁻⁸

Table 6 shows the statistical results and limit values for the neuro-regression models for the hardness values of the coatings. It is seen that the R^2_{training} values of all models are greater than 0.98, but only the R^2_{testing} value 0.9694 of the SON model is greater than the limit value of 0.9. Therefore, the SON model also satisfied the other two criteria and was chosen as objective functions to optimize the hardness of the coatings. As a result of the model selections, TON and SOLN models for deposition efficiency, SON and SOLN models for bond strength, TON model for porosity values, and SON model for hardness value were selected as the objective functions in the optimization of the coatings.

In the reference study, regression models were prepared for each coating process response, and then a numeric optimization study was carried out using these models. For all coating process responses, an optimum experimental set was determined as input power 26.3 kW, primary gas flow rate 36.15 lmp, coating distance 110.5 mm, powder feed rate 23.35 gpm, and carrier gas flow rate 7.8 lpm. The results of validation tests, the predicted values of the regression models of the reference, and current studies are given in Table 7.

Table 7. Comparison of Neuro-Regression model results with reference study.

Responses	Validation	Reference Study	Current Study	
			Objective functions TON	SOLN
Deposition efficiency (%)	72	71.0837	73.0561	71.2686
Bond strength (MPa)	21	22.9997	24.1362	22.3709
Porosity (%)	4	4.0001	3.9404	
Hardness (HV_{0.3})	1153	1148.94	1149.37	

When Table 7 is examined, it is seen that the estimated values of regression models of both the reference and the current studies have very close to the validation results. For example, while the error rates in the estimations of the deposition efficiency of coatings were 1.72% in the reference study, it was 1.466 % with the TON model and 1.025 % with the SOLN model in the current study. These values for the bond strength of the coatings were 9.522% in the reference study, 14.934% with the SON model, and 6.528% with the SOLN model in the current study. For the porosity and hardness values of the coatings, the rates were 0.0025% and 0.3521% in the reference study and 1.49% and 0.314% in the current study, respectively.

Four different optimization algorithms were used to maximize the deposition efficiency, bond strength, and hardness values and minimize the coatings' porosity value. Table 8 shows the objective functions, optimization constraints, suggested process parameters, and estimated values of algorithms for each coating response.

Table 8. Optimization results of thermal barrier coating.

Responses	Objective	Constraints	Opt.	Suggested	Suggested Design Parameters
-----------	-----------	-------------	------	-----------	-----------------------------

Functions		Algorithms	Values	
Deposition efficiency (%)	TON	DE	$X_1= 28.6369 \text{ kW}, X_2= 39.4152 \text{ lpm}, X_3=99.4844 \text{ mm}, X_4=22.3357 \text{ gpm}, X_5= 8.1161 \text{ lpm}$	
		SA	81.312	
		NM		
		RS	124.755	
SOLN	SON	DE	$X_1= 27.4608 \text{ kW}, X_2= 36.0565 \text{ lpm}, X_3=90 \text{ mm}, X_4=21.3869 \text{ gpm}, X_5=7.1047 \text{ lpm}$	
		SA	86.798	
		NM		
		RS		
Bond strength (MPa)	SON	DE	$X_1= 29.0027 \text{ Kw}, X_2= 40.6943 \text{ lpm}, X_3= 105.441 \text{ mm}, X_4=21.2947 \text{ gpm}, X_5=7.1047 \text{ lpm}$	
		NM	27.8997	
		RS		
		SA	73.5196	
	SOLN	22 kW<P<30 kW 25lpm<PGFR<45 lpm mm<D<130 mm 15 gpm<PFR< 35 gpm lpm<CGFR<11 lpm	DE	$X_1= 27.8652 \text{ Kw}, X_2= 36.711 \text{ lpm}, X_3= 90 \text{ mm}, X_4=19.6789 \text{ gpm}, X_5=6.2139 \text{ lpm}$
			NM	28.5923
			RS	47.3729
			SA	40.0992
Porosity (%)	TON	DE	$X_1= 27.3598 \text{ kW}, X_2= 36.5172 \text{ lpm}, X_3= 93.8257 \text{ mm}, X_4=15.6061 \text{ gpm}, X_5=6.1185 \text{ lpm}$	
		SA	1.1018	
		NM	0.8881	
		RS	2.0694	
			$X_1= 27.9016 \text{ kW}, X_2= 34.893 \text{ lpm}, X_3=105.305 \text{ mm}, X_4=15.0098 \text{ gpm}, X_5=3 \text{ lpm}$ $X_1= 27.6482 \text{ kW}, X_2= 37.0504 \text{ lpm}, X_3=106.634 \text{ mm}, X_4=22.8431 \text{ gpm}, X_5=6.6352 \text{ lpm}$ $X_1= 29.8778 \text{ kW}, X_2= 42.2386 \text{ lpm}, X_3= 95.307 \text{ mm}, X_4=23.7204 \text{ gpm}, X_5=5.3439 \text{ lpm}$	
Hardness (HV _{0.3})	TON	DE	$X_1= 27.8464 \text{ kW}, X_2= 36.755 \text{ lpm}, X_3= 90 \text{ mm}, X_4=20.2408 \text{ gpm}, X_5=5.7636 \text{ lpm}$	
		SA	1313.19	
		NM		
		RS		

*(X_1 :Input Power, X_2 :Primary Gas Flow Rate, X_3 : Coating Distance, X_4 : Powder Feed Rate, X_5 : Carrier Gas Flow Rate)

When Table 8 is examined, the highest value for maximizing the deposition efficiency of the coatings was predicted as 124.755% by the TON model with the RS algorithm. However, this value was

considered an unrealistic result. Other algorithms of the TON model predicted as 81.312% with the same design parameters ($X_1=28.6369$ kW, $X_2=39.4152$ lpm, $X_3=99.4844$ mm, $X_4=22.3357$ gpm, $X_5=8.1161$ lpm). Similarly, by the SOLN model, the four algorithms predicted as 86.798% with same design parameters ($X_1=27.4608$ kW, $X_2=36.0565$ lpm, $X_3=90$ mm, $X_4=21.3869$ gpm, $X_5=7.1047$ lpm). The fact that more than three algorithms give the same result with the same parameters for the deposition efficiency of the coatings is interpreted as that the objective functions are consistent and that these parameter sets can have local maximum points. In the maximization studies, the bond strength values of the coatings were predicted as 27.8997 MPa by DE and NM algorithms in the TON model with the parameters set as $X_1=29.0027$ kW, $X_2=40.6943$ lpm, $X_3=105.441$ mm, $X_4=21.2947$ gpm, and $X_5=7.1047$ lpm. In the same model, it was predicted as 73.5196 MPa by the RS and SA algorithms with the parameters $X_1=30$ kW, $X_2=25$ lpm, $X_3=130$ mm, $X_4=35$ gpm, and $X_5=3$ lpm. Nevertheless, this value was considered an unrealistic result. The DE and NM algorithms of the SOLN model estimated 28.5923 MPa with the parameter set $X_1=27.8652$ kW, $X_2=36.711$ lpm, $X_3=90$ mm, $X_4=19.6789$ gpm, $X_5=6.2139$ lpm. The values estimated by the RS and SE algorithms are 47.3729 MPa and 40.0992 MPa, about twice the maximum experimental result, so they did not meet the criterion. To minimize the porosity value of the coatings, DE, SA, NM, and RS algorithms were run with the TON model and predicted as 2.0568%, 1.1018%, 0.8881%, and 2.0694%, respectively. To maximize the hardness values of the coatings, four algorithms were run with the TON model and predicted as 1313.19 HV_{0.3} with the same design parameters ($X_1=27.8464$ kW, $X_2=36.755$ lpm, $X_3=90$ mm, $X_4=20.2408$ gpm, $X_5=5.7636$ lpm). It is interpreted that these parameters, which are suggested to give the same result by all four algorithms, can indicate a global optimum point. The optimization results of the TBC are evaluated in general, both polynomial and logarithmic models were successful, but trigonometric models were not.

4. CONCLUSIONS

The deposition efficiency, adhesion strength, porosity, and hardness values are the properties that affect both the production costs and the performance of TBCs. The optimization studies of TBC were carried out in two steps in the study. In the first step, first, second, and third-order polynomial, logarithmic and trigonometric regression models were prepared by fitting from the coating process data. Then, model selection was made for each coating output. The selected models were run with four different optimization algorithms for the same problem solutions in the second step. Based on the studies carried out, the following results have been obtained:

- R^2_{training} values of thirty-six models prepared for four different process outputs are greater than 0.92. However, only six models have R^2_{testing} values greater than 0.9. This situation shows the inadequacy of the classical R^2 calculation.
- In the regression model selections, 2nd and/or 3rd-order nonlinear polynomial and logarithmic models successfully described the process, while trigonometric models were not successful in solving any problem.
- A design parameter set was proposed for the optimum values of all coating outputs in the reference study, and a validation test was performed according to the parameter set. Calculations were made using this proposed design set with the regression models in both the reference study and the current study. The closeness of the results in the two studies to the validation test results was compared. The

present study models gave better results for the deposition efficiency, adhesion strength, and hardness values.

- In the optimization studies, the same result was estimated for the deposition efficiency value with the same design parameters by three algorithms with the TON model and four algorithms with the SOLN model. Similarly, for the hardness value of the coatings, the four algorithms predicted the same result with the same design parameters. Therefore, these results are interpreted as showing the global optimum of the proposed parameters for the two outputs.

ACKNOWLEDGMENT

The author thanks reviewers for constructive comments and suggestions that helped to improve the quality of the article.

REFERENCES

- [1] Boyce, M.P., (2011), Gas turbine engineering handbook, Elsevier.
- [2] Darolia, R., (2013), Thermal barrier coatings technology: critical review, progress update, remaining challenges and prospects, *International Materials Reviews*, 58(6), 315-348.
- [3] Mutasim, Z. and Brentnall, W., (1997), Thermal barrier coatings for industrial gas turbine applications: An industrial note, *Journal of Thermal Spray Technology*, 6(1), 105-108.
- [4] Lin, C.M., Yen, S.H. and Su, C.Y., (2016), Measurement and optimization of atmospheric plasma sprayed CoMoCrSi coatings parameters on Ti-6Al-4V substrates affecting microstructural and properties using hybrid abductor induction mechanism, *Measurement*, 94, 157-167.
- [5] Guo, H., Gong, S., Khor, K.A. and Xu, H., (2003), Effect of thermal exposure on the microstructure and properties of EB-PVD gradient thermal barrier coatings, *Surface and Coatings Technology*, 168(1), 23-29.
- [6] Liu, Q., Huang, S. and He, A., (2019), Composite ceramics thermal barrier coatings of yttria stabilized zirconia for aero-engines, *Journal of Materials Science And Technology*, 35(12), 2814-2823.
- [7] Matejka, D. and Benko, B., (1989), Plasma spraying of metallic and ceramic materials, John Wiley and Sons.
- [8] Chen, H., Hao, Y., Wang, H. and Tang, W., (2010), Analysis of the microstructure and thermal shock resistance of laser glazed nanostructured zirconia TBCs, *Journal of Thermal Spray Technology*, 19(3), 558-565.

- [9] Bertrand, G., Bertrand, P., Roy, P., Rio, C. and Mevrel, R., (2008), Low conductivity plasma sprayed thermal barrier coating using hollow psz spheres: Correlation between thermophysical properties and microstructure, *Surface and Coatings Technology*, 202(10), 1994-2001.
- [10] Ning, L., Cai, Z., Zhao, X., Liu, Y. and Wang, W., (2021), Fast stress evaluation of the top coat of thermal barrier coatings under CaO–MgO–Al₂O₃–SiO₂ penetration based on image recognition and an artificial neural network, *Ceramics International*, 47(13), 18252-18261.
- [11] Ramachandran, C., Balasubramanian, V. and Ananthapadmanabhan, P., (2011), Multiobjective optimization of atmospheric plasma spray process parameters to deposit yttria-stabilized zirconia coatings using response surface methodology, *Journal of Thermal Spray Technology*, 20(3), 590-607.
- [12] Kim, K., Kim, D., Park, K., Yun, J., Jun, N. and Seok, C.S., (2021), A cumulative oxide growth model considering the deterioration history of thermal barrier coatings, *Corrosion Science*, 182, 1-8.
- [13] Karthikeyan, S., Balasubramanian, V. and Rajendran, R., (2014), Developing empirical relationships to estimate porosity and microhardness of plasma-sprayed YSZ coatings, *Ceramics International*, 40(2), 3171-3183.
- [14] Rajesh, T.S. and Rao, R.V., (2016), Parameter Optimization of Amalgamated Al₂O₃-40%TiO₂ Atmospheric Plasma Spray Coating on SS304 Substrate Using TLBO Algorithm, *Journal of Surface Engineered Materials and Advanced Technology*, 6(03), 89-105.
- [15] Shi, H., Zhao, C. and Wang, B., (2016), Modeling the thermal radiation properties of thermal barrier coatings based on a random generation algorithm, *Ceramics International*, 42(8), 9752-9761.
- [16] Sankar, V., Thampi, B.G. and Panicker, M.R., (2020), Optimization of thermal barrier coatings in a single cylinder diesel engine using thermal analysis and genetic algorithm, *Journal of Physics: Conference Series*, IOP Publishing.
- [17] Tonkonogyi, V., Dasic, P., Rybak, O. and Lysenko, T., (2019), Application of the modified genetic algorithm for optimization of plasma coatings grinding process, *International Conference New Technologies, Development and Applications*, Springer.
- [18] Ye, D., Wang, W., Xu, Z., Yin, C., Zhou, H. and Li, Y., (2020), Prediction of thermal barrier coatings microstructural features based on support vector machine optimized by cuckoo search algorithm, *Coatings*, 10(7), 1-13.
- [19] Aydin, L., Artem H.S. and Oterkus, S., (2020), *Designing engineering structures using stochastic optimization methods*, CRC Press, Taylor & Francis Group.
- [20] Ozturk, S., Aydin, L. and Celik, E., (2018), A comprehensive study on slicing processes optimization of silicon ingot for photovoltaic applications, *Solar Energy*, 161, 109-124.

- [21] Ozturk, S., Aydin, L., Kucukdogan, N., and Celik, E, (2018), Optimization of lapping processes of silicon wafer for photovoltaic applications, *Solar Energy*, 164, 1-11.



REVIEW ARTICLE

**PROTON TRANSFER SALTS and THEIR COMPLEXES and MIXED-LIGAND
COMPLEXES of PYRIDINE DICARBOXYLIC ACIDS and PIPERAZINES: A SHORT
REVIEW**

Nurgün BÜYÜKKIDAN*

*Kütahya Dumlupınar University, Arts and Science Faculty, Chemistry Department, nurgun.buyukkidan@dpu.edu.tr, ORCID:
0000-0001-6879-9355

Receive Date: 28.01.2022

Accepted Date: 24.06.2022

ABSTRACT

In this study, a short review covering the years 2009-2021 was made about the proton transfer salts obtained from the reaction of pyridine-acids, which are accepted as suitable proton donors, and piperazines, which are proton acceptors, and their metal complexes and mixed ligand metal complexes. In some complexes studied, both initial ion pairs bind to the metal, while in others they contain only one of the cationic and anionic moieties as ligands.

Keywords: *Proton transfer salt, Piperazine, Pyridine, Mixed ligand, Metal complexes*

1. INTRODUCTION

Heterocyclic compounds have a large range of uses in industry and various areas of chemistry [1]. Piperazine among heterocyclic rings containing nitrogen atoms has different application areas such as materials, agricultural chemicals and pharmaceutical chemistry. Studies have shown that piperazine and its derivatives have the following biological activities: anti-fungal [2], anti-depressant [3], anti-malarial [4], anti-migraine [5], anti-diabetic [6], anti-aggregating [7], anti-tumor [8, 9], anti-inflammatory [10], anti-obesity [11], and cardio-vascular [12]. As piperazine derivatives have many biological applications, there is an increasing interest in the synthesis of these compounds. In recent years, reaction mechanisms based on the proton transfer system were used in the preparation of metal complexes [13-15]. The very different geometries of the complexes are due to the coordinated covalent bonds between metals (transition, lanthanide and main group) and ligands. Supramolecular metal compounds, called metal-organic frameworks (MOF) [16], can be obtained from the formation of supramolecular proton transfer salts from a good proton donor-acceptor system and their reaction with s, p, d block and even f block metals. Supramolecular structures contain intramolecular or intermolecular interactions as O-H...O, O-H...N, N-H...O, N-H...N [17-19]. Pyridine carboxylic acids, which are found in natural products like alkaloids, coenzymes and vitamins, have great importance in medicinal chemistry due to their various physiological properties [20]. It has been reported that pyridine-2,4-dicarboxylic acid protects certain enzymes from heat inactivation [21], while 2,5- and 2,6-pyridinedicarboxylic acids activate or inhibit certain metalloenzymes [22, 23]. Pyridine dicarboxylates are among the most versatile ligands known, containing different functional groups that can coordinate to metal atoms.

This study aims to describe the reactions of piperazine and its derivatives with pyridine-di carboxylic acids, the synthesis of their metal complexes and their spectral and structural properties. In this work, proton transfer salts and their complexes and mixed ligand complexes obtained from piperazines and pyridine-dicarboxylic acids between 2009-2021 are presented. The pyridine-dicarboxylic acids for proton donors are: pyridine-2,3-dicarboxylic acid (Py-2,3-H₂Dc), pyridine-2,5-dicarboxylic acid (Py-2,5-H₂Dc) and pyridine-2,6-dicarboxylic acid (Py-2,6-H₂Dc). Bases used as proton acceptors are: Piperazine (Ppz), 2-(piperazin-1-yl)ethanol (HOEtPpz) and 2-piperazin-1-yl-ethanamine (PpzEa).

2. SYNTHESIS

The metal complexes reported in this study were synthesized either from the proton transfer salt formed by pyridine dicarboxylic acids and piperazines, or from mixed-ligands under hydrothermal conditions.

2.1. Proton Transfer Reaction

The reaction or reaction mechanism in which a proton (H⁺) is separated from one species such as an acid and accepted by another species such as a base is called a proton transfer reaction. The stability of proton transfer types relies on many agents, such as the attractive and repulsive forces of opposite charges, the nature of the solvent, the geometry and topology of the acid and base. In the preparation of an effective ion pair that forms the components of the proton transfer salt and accelerates the formation of the metal complex, it may be useful to consider the following aspects [24-26]: i. Selection of functional acids and bases that can act as polydentate ligands in the formation of complexes, ii. Selection of donors and acceptors sensitive to intermolecular H-bonding and π - π stacking, iii. Selection of convenient acceptors and donors, taking into account the acidity and basicity constants, to ensure exact H-transfer. Proton transfer salts and their metal compound are of biological interest to chemists [27, 28].

2.2. Hydrothermal Synthesis

The synthesis of substances in a closed heated solution above ambient pressure and temperature is called hydrothermal synthesis. Hydrothermal method, which is a liquid phase preparation technology, has been developing rapidly in recent years [29]. It includes the development of new synthetical methods and techniques for the preparation of new materials. Hydrothermal technology is used in many branches of science such as earth science, materials science, physics, metallurgy, biology and chemistry [30-33]. Hydrothermal *in situ* ligand synthesis, such as hydrolyation or decarboxylation of carboxyl groups, has become a very important method in the synthesis of organic ligands and their metal complexes, and in coordination engineering. This method is very useful for the synthesis of MOFs that are difficult to obtain at room conditions. Many coordination polymers synthesized by this method have been reported in the literature [16-19, 34-36].

2.3. Pyridine-dicarboxylic Acids

The isomers of pyridine-dicarboxylic acid (2,3-, 2,4-, 2,5-, 2,6-, 3,4- and 3,5-dicarboxylic acid) (Figure 1) have different coordination patterns with transition metals [37,38], main group elements [39, 40], and inner transition elements [41-43].

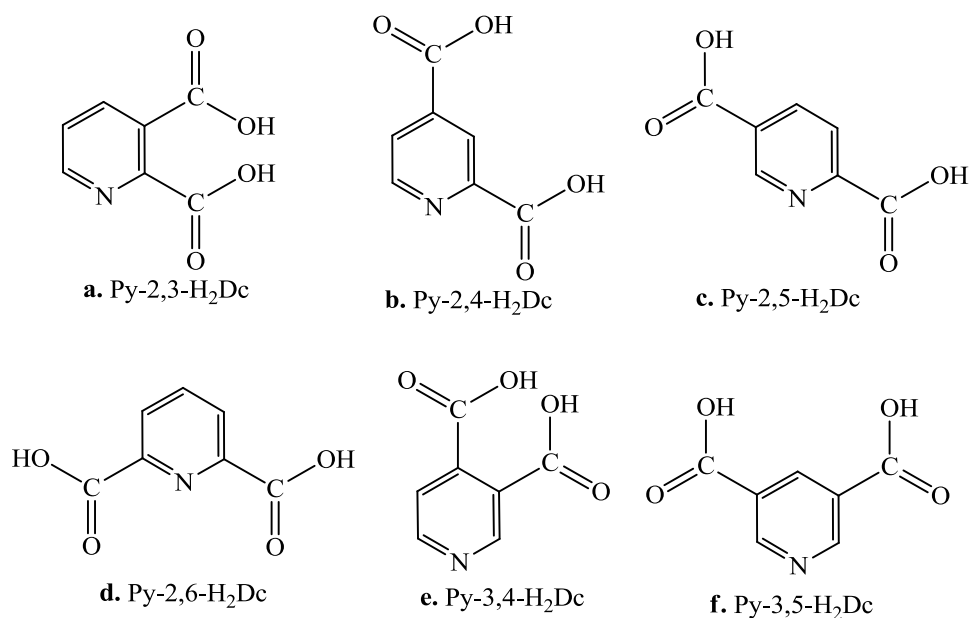


Figure 1. Isomers of pyridine-dicarboxylic acid.

2.3.1. Pyridine-2,3-dicarboxylic acid (Py-2,3-H₂Dc)

Py-2,3-H₂Dc (Figure 1a) can be highly neurotoxin and cell death may occur as a result of overstimulation of nerve cells. Brain toxicity caused by quinolinic acid has been associated with diseases such as autism, depression, dementia, stroke, Alzheimer's, and schizophrenia [44]. Different coordination modes of Py-2,3-HDc⁻ and Py-2,3-Dc²⁻ anions with various metal ions have been reported in the literature. The presence of versatile and different coordination motifs of Py-2,3-H₂Dc is quite remarkable in the construction of polymeric structures [45]. The different binding modes of the Py-2,3-Dc²⁻ ion allow it to act as a monodentate, tridentate, tetradentate, and quintuple ligand [46, 47] (Figure 2).

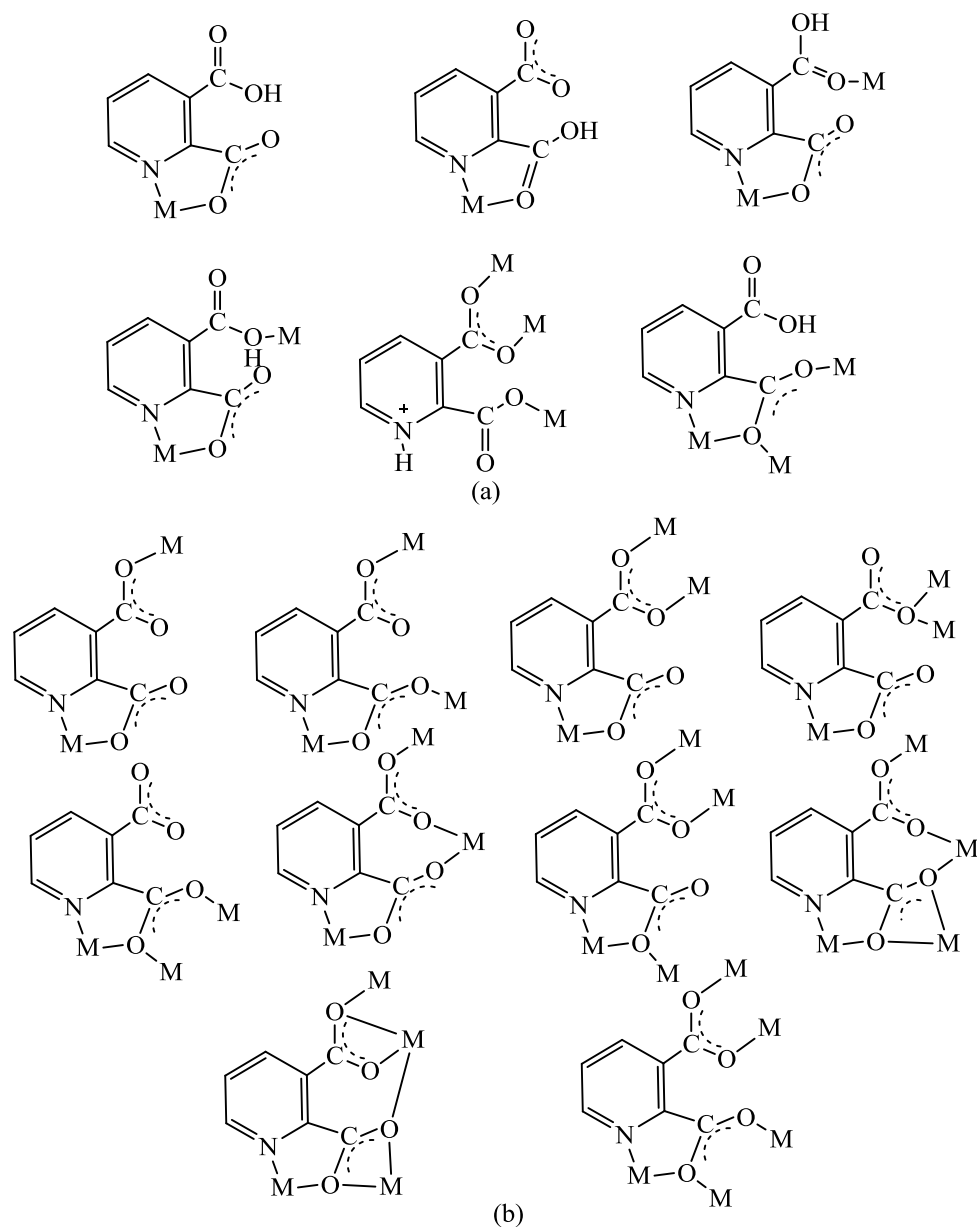


Figure 2. Coordination forms of (a) Py-2,3-HDc⁻ anion (b) Py-2,3-H₂Dc²⁻ anion.

2.3.1.1. Proton transfer salt, (H₂Ppz)²⁺(Py-2,3-HDc)₂⁻ (1) and its metal complexes 2 and 3

The proton transfer salt **1** (Figure 3), (H₂Ppz)²⁺(Py-2,3-Dc)₂⁻, was prepared from the Py-2,3-H₂Dc and Ppz [48].

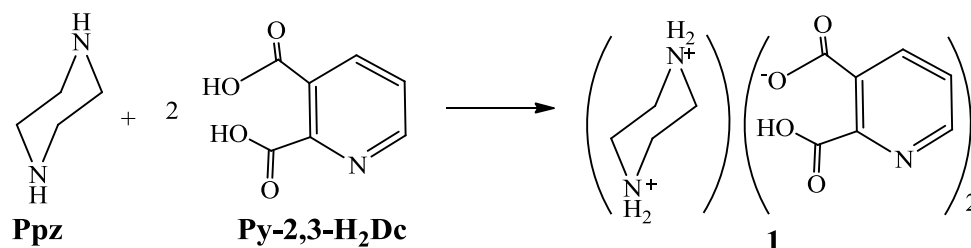


Figure 3. Synthesis of $(\text{H}_2\text{Ppz})^{2+}(\text{Py-2,3-HDc})_2^-$ (**1**).

The fact that Py-2,3-H₂Dc has variable and different coordination motifs makes it interesting in terms of forming polymeric architecture. Polymeric MOF compounds $\{(\text{H}_2\text{Ppz})[\text{Mn}(\text{Py-2,3-Dc})_2] \cdot 7.75\text{H}_2\text{O}\}_n$ (**2**), and $\{(\text{H}_2\text{Ppz})[\text{Hg}_4\text{Cl}_{10}]\}_n$ (**3**) [49] (Figure 4) were obtained from the proton transfer salt, $(\text{H}_2\text{Ppz})(\text{Py-2,3-HDc})_2$ (**1**), with corresponding metal salts. The analyses, space groups and crystal systems of the compounds **1-4** are given in Table 1.

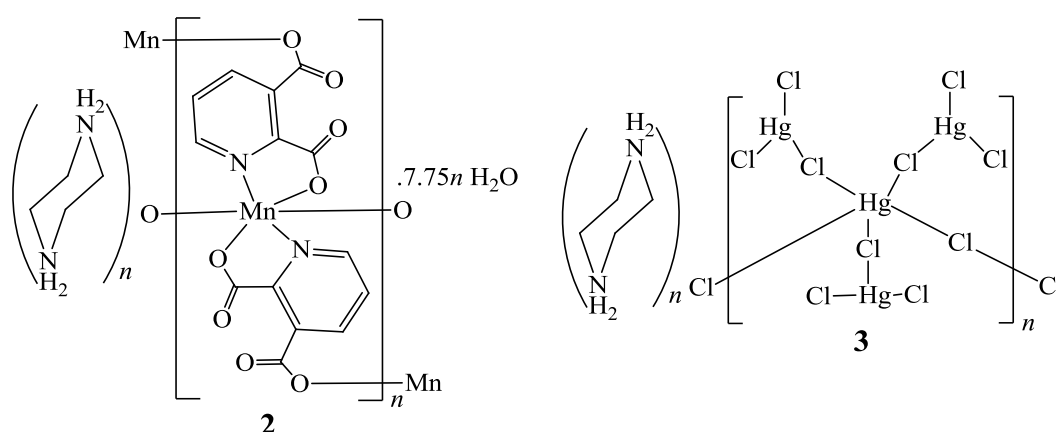


Figure 4. The structures of compounds **2** and **3**.

Table 1. The analyses, space groups and crystal systems of the compounds **1-4**.

Ref. No	Analyses	Proton Transfer Complexes	Salts and	Space Group	Crystal system
48	X-ray	$(\text{H}_2\text{Ppz})^{2+}(\text{Py-2,3-HDc})_2^-$ (1)		$P2_1/c$	Monoclinic
49	NMR, IR and X-ray	$\{(\text{H}_2\text{Ppz})[\text{Mn}(\text{Py-2,3-Dc})_2] \cdot 7.75\text{H}_2\text{O}\}_n$ (2)		$P2_1/c$	Monoclinic
49	NMR, IR and X-ray	$\{(\text{H}_2\text{Ppz})[\text{Hg}_4\text{Cl}_{10}]\}_n$ (3)		$C2/c$	Monoclinic
52	X-ray	$(\text{H}_2\text{Ppz})^{2+}(\text{Py-2,3-Dc})_2^- \cdot \text{CH}_3\text{OH}$ (4)		$P2_1/n$	Monoclinic

The molecular structure of the Mn(II) (**2**) complex (Figure A1) includes two distinct Mn²⁺ ions, each located at the middle of a parallel 1-D chain. One of the Mn²⁺ ions (Mn1) binds to the O1, N1, O5 and N2 atoms of the two Py-2,3-Dc²⁻ ligands and to the O4 and O8 atoms of the other two Py-2,3-Dc²⁻ ligands, forming the six-coordinated structure. The other Mn²⁺ ion (Mn2) binds to the O9, N3, O13 and N4 atoms of the two Py-2,3-Dc²⁻ ligands and to the O12 and O16 atoms of the other two Py-2,3-Dc²⁻ ligands to form the six coordinated structure. The bond angles of O1–Mn1–O5 and O9–Mn2–O13 are 164.9 (1)° and 163.8 (1)°, respectively. These values show that the bond angles around both Mn²⁺ ions deviate from linearity and have a distorted octahedral geometry. When the Hg(II) (**3**) compound is compared with the Zn(II) [50] and Cd(II) [51] complexes, it is seen that it has a different structure. In the Zn(II) compound, two Py-2,3-Dc²⁻ ligands are coordinated to the metal, while H₂Ppz²⁺ remains as a complementary ion. The Cd²⁺ ion is coordinated by three aqua and a Py-2,3-Dc²⁻ ligand, while the H₂Ppz²⁺ cation is absent in the structure. It was found that the Hg(II) (**3**) compound, in which an endless network of chlorine and mercury atoms balanced with H₂Ppz²⁺ cation fragments, has a different structure compared to **2**, Zn(II) and Cd(II) (Figure 5).

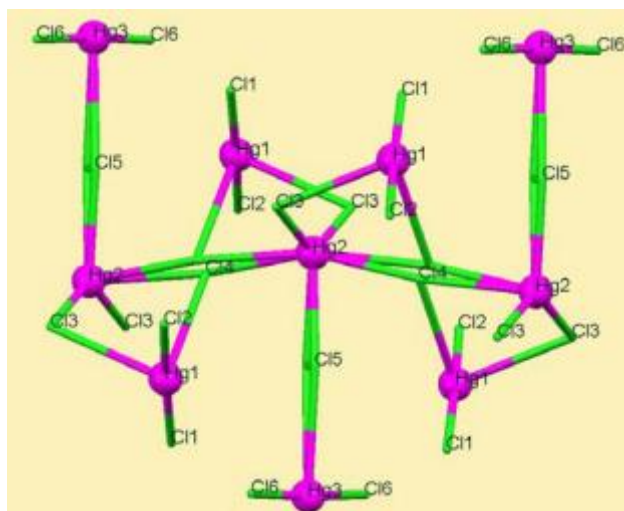


Figure 5. Coordination medium of Hg²⁺ ions in the Hg-Cl network of {(H₂Ppz)[Hg₄Cl₁₀]}_n (**3**), H₂Ppz²⁺ is omitted.

2.3.1.2. Proton transfer salt (H₂Ppz)²⁺(Py-2,3-Dc)²⁻·CH₃OH (**4**)

The moieties in the proton transfer salt, (H₂Ppz)²⁺(Py-2,3-Dc)²⁻·CH₃OH (**4**) [52] (Figure 6) obtained from the reaction of Ppz and Py-2,3-H₂Dc in methanol form the 3-D structure by connecting with H-bonds O–H···O, N–H···O and C–H···O. The asymmetric unit of proton transfer salt (**4**) has one (H₂Ppz)²⁺ cation, one (Py-2,3-Dc)²⁻ anion and one CH₃OH with two H-bonds.

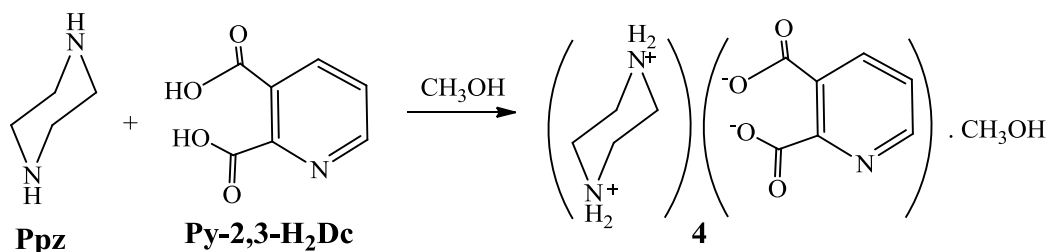


Figure 6. Synthesis of proton transfer salt, (H₂Ppz)(Py-2,3-Dc)·MeOH (4).

The C–O···π and C–H···π stackings are observed between the C6–O2 and N1/C1–C5 ring (3.5240 (9) Å) and between the C12–H1A and N1/C1–C5 ring (2.791 (1) Å) [52], respectively (Figure 7).

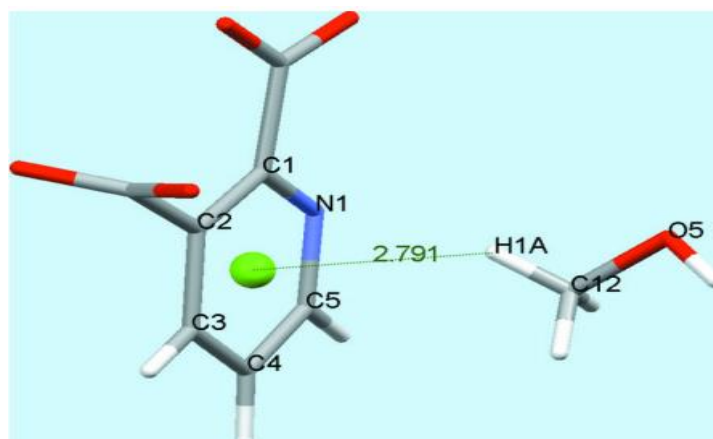


Figure 7. The C–H···π stacking of (4).

2.3.2. Pyridine-2,5-dicarboxylic acid (Py-2,5- H₂Dc) and it's complexes (5-13)

Py-2,5-H₂Dc (Figure 1c) is known as isosicomeronic acid. Py-2,5-HDc⁻ and Py-2,5-Dc²⁻ anions are versatile ligands coordinated to transition metals with nitrogen and four oxygen atoms, and numerous polymeric complexes of these have been reported. [53-55]. The coordination forms of Py-2,5-H₂Dc are shown in Figure 8. It has been stated that derivatives of Py-2,5-H₂Dc show inhibitory effect against hepatitis B virus [56], and metal complexes have many applications such as enzyme inhibition [57], antibacterial activity [58], magnetism [59], catalysis [60], surface chemistry [61], aqueous solution chemistry [62]. Since 2009, proton transfer salts of Py-2,5-H₂Dc and metal complexes obtained from these salts have not been encountered. The complexes (5-13) of Py-2,5-H₂Dc in the literature are metal salts obtained under hydrothermal conditions with mixed ligands. The analyses, space groups and crystal systems of the compounds 5-13 are given in Table 2.

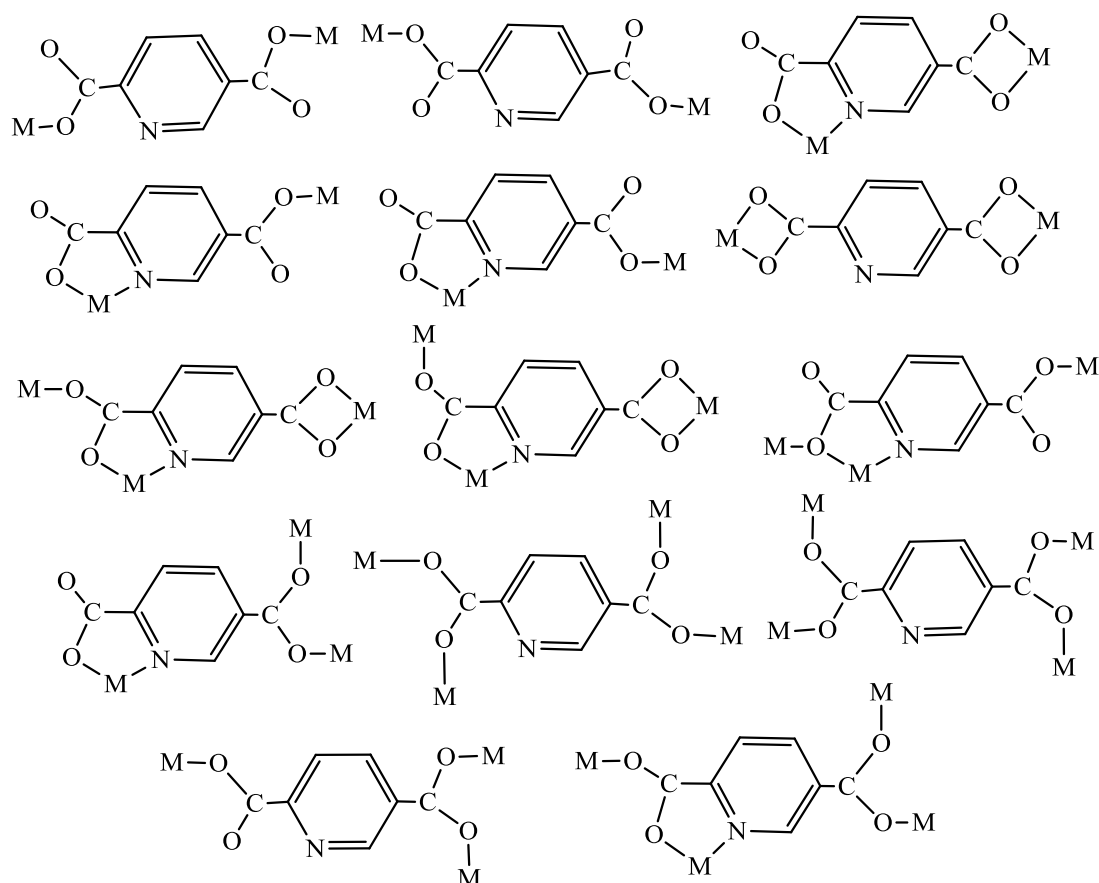


Figure 8. Coordination forms of Py-2,5-H₂Dc.

Table 2. The analyses, space groups and crystal systems of the mixed ligand complexes **5-13**.

Ref. No	Analyses	Complexes	Space Group	Crystal system
63	X-ray, UV, IR, TGA, Elemental analysis	[Co(Py-2,5-Dc) ₂ (H ₂ O)]·(Ppz)·2H ₂ O (5)	<i>P2₁/c</i>	Monoclinic
64	UV, SPS, X-ray	[Ni(Py-2,5-Dc) ₂ (HPpz) ₂]·H ₂ O (6)	<i>C2/c</i>	Monoclinic
66	X-ray, PXRD, IR, TGA, FESEM, Elemental analysis	[Ce(Py-2,5-Dc)(Ppz) _{1/2} (H ₂ O)] (7)	<i>P2₁/c</i>	Monoclinic
66	X-ray, PXRD, IR, TGA, FESEM, Elemental analysis	[Pr(Py-2,5-Dc)(Ppz) _{1/2} (H ₂ O)] (8)	<i>P2₁/c</i>	Monoclinic
69	X-ray, PXRD, IR, UV, TGA and photoluminescence measurements	{(H ₂ Ppz)[Mn(Py-2,5-Dc) ₂ (H ₂ O)]·2H ₂ O} (9)	<i>P2₁/c</i>	Monoclinic

70	IR, PXRD, SEM, TGA and EDX elemental mapping analysis.	{(H ₂ Ppz)[Zn _{1/3} Fe _{2/3} (Py-2,5-Dc) ₂ (H ₂ O)]·2H ₂ O} (10)	-	-
70	X-ray	{(H ₂ Ppz)[Fe(Py-2,5-Dc) ₂ (H ₂ O)]·2H ₂ O} (11)	P2 ₁ /c	Monoclinic
71	IR, PXRD, SEM, TGA and EDX elemental mapping analysis.	{(H ₂ Ppz)[Co _{1/3} Fe _{2/3} (Py-2,5-Dc) ₂ (H ₂ O)]·2H ₂ O} (12)	-	-
72	IR, PXRD, SEM, TGA and EDX elemental mapping analysis	{(H ₂ Ppz)[Zn _{1/3} Co _{2/3} (Py-2,5-Dc) ₂ (H ₂ O)]·2H ₂ O} (13)	-	-

2.3.2.1. Mixed-ligand complex [Co(Py-2,5-Dc)₂(H₂O)]·(Ppz)·2H₂O_n (**5**)

The asymmetric unit of hydrothermally synthesized complex, [Co(Py-2,5-Dc)₂(H₂O)]·(Ppz)·2H₂O_n (**5**) [63], consists of a Co(II) cation, two Py-2,5-Dc²⁻, an aqua ligand, two lattice water and an uncoordinated Ppz. The Py-2,5-Dc²⁻ moieties bind to Co(II) ions in two different ways. In the first of these, the nitrogen atom of the Py-2,5-Dc²⁻ and one oxygen atom of the neighboring carboxylate group coordinate to a Co(II) ion and the other carboxylate group to the other Co²⁺ ion. In the second, the neighboring carboxylate group and a nitrogen atom coordinate to a Co²⁺ ion, while the other carboxylate group does not participate in the coordination. In its crystal structure, initially, Co(II) ions bind to Py-2,5-Dc²⁻ groups, forming a 1-D chain along the b-axis (Figure A2a). Next, the 1-D chains are linked by H-bonds between the coordinated H₂O molecules and the uncoordinated carboxylate oxygen atoms of the two Py-2,5-Dc²⁻ rings along the c-axis and an H-bonded 2-D structure is created in the bc plane (Figure A2b).

2.3.2.2. Mixed-ligand complex [Ni(Py-2,5-Dc)₂(HPpz)₂]·H₂O (**6**)

The mononuclear [Ni(Py-2,5-Dc)₂(HPpz)₂]·H₂O (**6**) with six coordinated, distorted octahedral geometry, was hydrothermally obtained [64]. The compound contains a Ni²⁺ cation, two Py-2,5-Dc²⁻ anions, two HPpz²⁺ cations, and a lattice H₂O molecule (Figure A3). The Ni²⁺ cation was coordinated to O1, O1A, N1 and N1A atoms of two Py-2,5-Dc²⁻ anions in equatorial plane and to N2 and N2A atoms of HPpz⁺ cation in axial positions. Although the bond lengths of Ni–N (2.0398(14) and 2.2033(15) Å) and Ni–O (2.0664(13) Å) are slightly longer than those reported for Py-2,5-Dc-Ni complexes, they are still within normal limits [61]. The C–O bond lengths of the two Py-2,5-Dc²⁻ ligands are 1.274(2), 1.234(2), 1.256(2) and 1.244(2) Å, indicating that the both carboxylic groups are deprotonated. In HPpz⁺ fragment, one of the N-atoms coordinates to the Ni(II) ion, while the other N-atom is protonated and turns into NH²⁺ [65]. The compound forms a network within a 3-D supramolecule through intermolecular N–H···O H-bonds.

2.3.2.3. Mixed-ligand complexes [Ce(Py-2,5-Dc)(Ppz)_{1/2}(H₂O)] (**7**) and [Pr(Py-2,5-Dc)(Ppz)_{1/2}(H₂O)] (**8**)

The solution of Ln(NO₃)₃·6H₂O, (Ln = Ce and Pr), Py-2,5-H₂Dc and Ppz in H₂O (5 mL) with the molar ratio of 1:3:1 was heated at 160 °C. After 3 days the yellow [Ce(Py-2,5-Dc)(Ppz)_{1/2}(H₂O)] (**7**) (Ppz = 2,5-piperazinedicarboxylic acid) and the green [Pr(Py-2,5-Dc)(Ppz)_{1/2}(H₂O)] (**8**) complexes were obtained [66]. A ligand was synthesized in the presence of piperazine and pyridine-2,5-

dicarboxylic acid by hydrothermal *in situ* ligand synthesis method such as hydrolyation or decarboxylation of carboxyl groups, where ligand synthesis is rarely observed [67, 68]. Both of the carboxyl groups of the Py-2,5-Dc²⁻ ligand were separated and bound to the 2- and 5-positions of the piperazine ring, producing 2,5-piperazinedicarboxylic acid. The coordination polymers **7** and **8** formed by bridging mixed ligands are isostructural have interesting 3-D frameworks. 3-D structure of **8** is shown in Figure A4. In complexes **7** and **8** the coordination number of both Pr and Ce atoms are nine. Each asymmetric unit of compounds (**7** and **8**) includes one metal ion, half of Ppz, one Py-2,5-Dc²⁻, and one aqua ligand. The geometry of the Pr(III) and Ce(III) ions are monocapped square-antiprism [66].

2.3.2.4. Mixed-ligand complex {(H₂Ppz)[Mn(Py-2,5-Dc)₂(H₂O)]·2H₂O} (**9**)

Hydrothermally synthesized metal-organic coordination polymer {(H₂Ppz)[Mn(Py-2,5-Dc)₂(H₂O)]·2H₂O} (**9**) [69] is soluble in water. The asymmetric unit of the Mn(II) complex contains one Mn(II) ion, two Py-2,5-Dc²⁻ ligands, one H₂Ppz²⁺ cation, one water molecule, and two uncoordinated water molecules (Figure A5). The Mn²⁺ ion binds to both carboxylate oxygen atoms of one of the two Py-2,5-Dc²⁻ ligands, while it coordinates to only one carboxylate oxygen of the other Py-2,5-Dc²⁻ ligand. It also binds to one water molecule and the nitrogen atoms of both Py-2,5-Dc²⁻ ligands. Thus, there are a total of six coordinated groups around the Mn²⁺ ion. The average bond lengths of Mn–O and Mn–N are 2.17 and 2.25 Å, respectively. The bond angles of O–Mn–O/N–Mn–N are in the range 75.49(7)–172.89(7)°. H-bond interaction was formed between the hydrogens of the coordinated H₂O molecule (H1A and H1B) and the O(3) and O(8) atoms of the two Py-2,5-Dc²⁻ ligands. 2-D structures connected by two lattice water molecules and Ppz²⁺ cation *via* N–H···O and O–H···O H-bond interactions form a 3-D supramolecular structure [69].

2.3.2.5. Mixed-ligand complexes {(H₂Ppz)[Zn_{1/3}Fe_{2/3}(Py-2,5-Dc)₂(H₂O)]·2H₂O} (**10**), {(H₂Ppz)[Fe(Py-2,5-Dc)₂(H₂O)]·2H₂O} (**11**), {(H₂Ppz)[Co_{1/3}Fe_{2/3}(Py-2,5-Dc)₂(H₂O)]·2H₂O} (**12**) and {(H₂Ppz)[Zn_{1/3}Co_{2/3}(Py-2,5-Dc)₂(H₂O)]·2H₂O} (**13**)

The isostructural Fe compound, {(H₂Ppz)[Fe(Py-2,5-Dc)₂(H₂O)]·2H₂O} (**11**), with hydrothermally obtained mixed metal coordination polymers {(H₂Ppz)[Zn_{1/3}Fe_{2/3}(Py-2,5-Dc)₂(H₂O)]·2H₂O} [70] (**10**) and {(H₂Ppz)[Co_{1/3}Fe_{2/3}(Py-2,5-Dc)₂(H₂O)]·2H₂O} [71] (**12**) was synthesized to confirm the structures of these mixed metal compounds (**10** and **12**). Heterobimetallic coordination polymer (**12**) has been used as the sole source precursor for the synthesis of nano-sized CoFe₂O₄ by thermal decomposition [71]. Also, to confirm the structure of MOF compound, {(H₂Ppz)[Zn_{1/3}Co_{2/3}(Py-2,5-Dc)₂(H₂O)]·2H₂O} (**13**) [72], the isostructural Co complex {(H₂Ppz)[Co(Py-2,5-Dc)₂(H₂O)]·2H₂O} (**5**) [63] was used. Decomposition of **13** at 400 °C results in nano-size ZnCo₂O₄ [72].

2.3.3. Pyridine 2,6-dicarboxylic acid (Py-2,6-H₂Dc)

Py-2,6-H₂Dc (Figure 1d) which coordinates to the metal with N and O donor atoms and is known as dipicolinic acid, is a pyridine dicarboxylic acid that has been extensively studied because of its various coordination motifs. Py-2,6-H₂Dc and Ppz form a good binary system as proton donor-acceptor. Many ion pairs were reported from the reaction of Py-2,6-H₂Dc with different amines [73-75] and piperazines with different acids [48, 76, 77]. The coordination chemistry of Py-2,6-H₂Dc attracts more attention because it is a convenient ligand for the preparation of pharmacologically active compounds due to its low toxicity, different biological properties and amphiphilic nature [78,79]. It has been reported that metal ions have stronger interaction with target molecules and show more antimicrobial activity than free ligand [80]. Py-2,6-H₂Dc has a wide variety of coordination modes [81, 82] and it

can coordinate to metal as a monodentate, bidentate, tridentate and bridging ligand as shown in Figure 9.

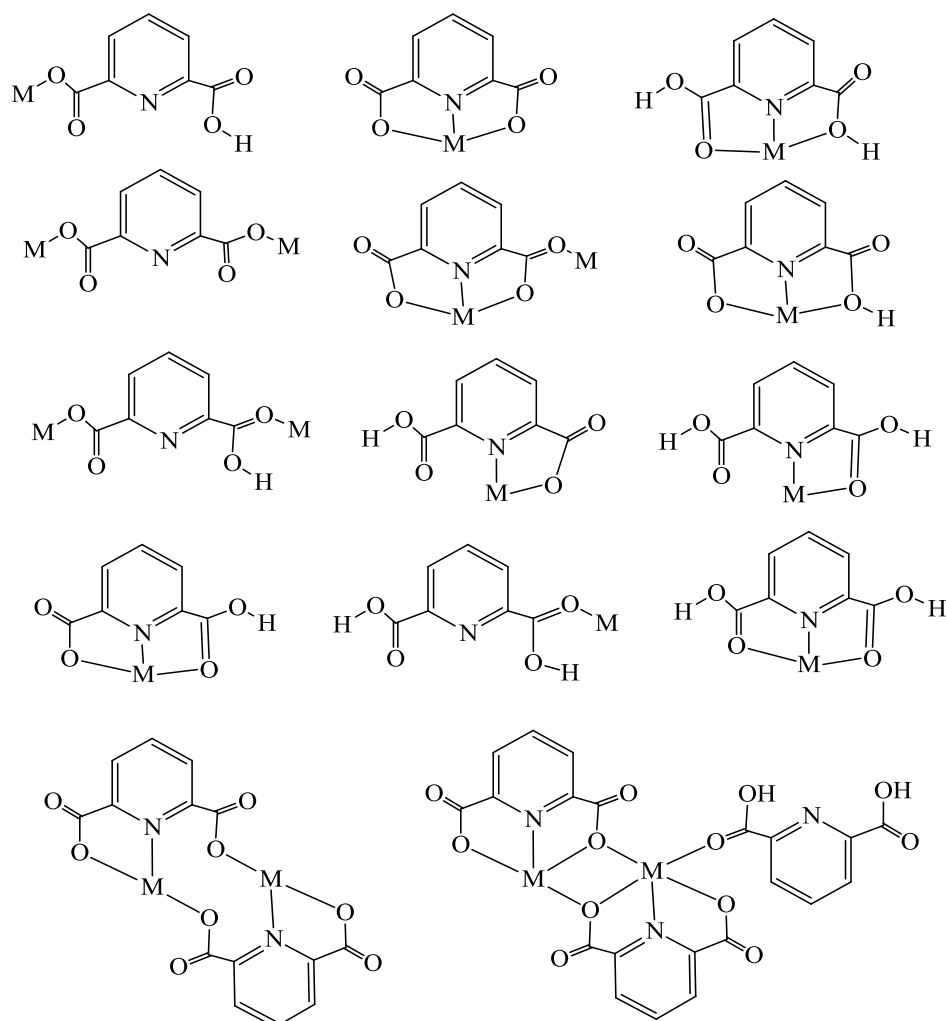


Figure 9. Versatile coordination forms of Py-2,6-H₂Dc.

2.3.3.1. Proton transfer salts and metal complexes

The analyses, space groups and crystal systems of proton transfer salts (**14**, **17** and **22**) and their metal complexes (**15** and **16**, **18-21** and **23-26**) are given in Table 3.

Table 3. The analyses, space groups and crystal systems of **14-26**.

Ref. No	Analyses	Proton Transfer Complexes	Salts	and	Space Group	Crystal system
---------	----------	---------------------------	-------	-----	-------------	----------------

83	X-ray, NMR, IR, and elemental analysis	(H ₂ Ppz)(Py-2,6-Dc) (14)	<i>Pbcn</i>	Orthorhombic
84	X-ray, NMR, IR, and elemental analysis	(H ₂ Ppz)[Cd(pydc) ₂]·6H ₂ O (15)	<i>P1</i>	Triclinic
87	X-ray, NMR, IR, and elemental analysis	(H ₂ Ppz)[Sb ₂ (Py-2,6-Dc) ₄]·2H ₂ O (16)	<i>P1</i>	Triclinic
89	X-ray and elemental analysis	(H ₂ Ppz) _{1.5} (Py-2,6-Dc H) ₃ ·3.7H ₂ O (17)	<i>C2/c</i>	Monoclinic
89	X-ray, NMR, IR, and elemental analysis	(H ₂ Ppz)[Zr(Py-2,6-Dc) ₃]·8H ₂ O (18)	<i>P1</i>	Triclinic
89	X-ray, NMR, IR, and elemental analysis	(H ₂ Ppz)[Ce(Py-2,6-Dc) ₃]·8H ₂ O (19)	<i>P1</i>	Triclinic
91	X-ray, IR and elemental analysis	(H ₂ Ppz)[Sr(Py-2,6-Dc) ₂ (H ₂ O) ₂]n·4H ₂ O (20)	<i>P2₁/n</i>	Monoclinic
91	X-ray, IR and elemental analysis	[Ce(Py-2,6-Dc) ₂ (H ₂ O) ₂]n·4H ₂ O (21)	<i>P2₁/c</i>	Monoclinic
97	NMR, IR and UV-Vis and elemental analysis	(HOEtH ₂ Ppz) ²⁺ (Py-2,6-HDc) ₂ ⁻ (22)	-	-
97	X-ray, NMR, IR and UV-Vis, TG and elemental analyses	(H ₂ Ppz)[Cu(Py-2,6-Dc) ₂]·6H ₂ O (23)	<i>P2₁/c</i>	Monoclinic
98	X-ray, NMR, IR and UV-Vis, TG and elemental analyses	(H ₂ Ppz)[Co(Py-2,6-Dc) ₂]·6H ₂ O (24)	<i>P2₁/c</i>	Monoclinic
98	X-ray, NMR, IR and UV-Vis, TG and elemental analyses	(H ₂ Ppz)[Ni(Py-2,6-Dc) ₂]·6H ₂ O (25)	<i>P2₁/c</i>	Monoclinic
98	X-ray, NMR, IR and UV-Vis, TG and elemental analyses	(H ₂ Ppz)[Zn(Py-2,6-Dc) ₂]·6H ₂ O (26)	<i>P2₁/c</i>	Monoclinic

2.3.3.1.1. Proton transfer salt (H₂Ppz)²⁺(Py-2,6-Dc)²⁻ (**14**) and metal complexes **15** and **16**

The proton transfer salt **14** reported in the literature was obtained [83] from a 1:1 molar ratio of a mixture of Py-2,6-H₂Dc and piperazine in THF (Figure 10).

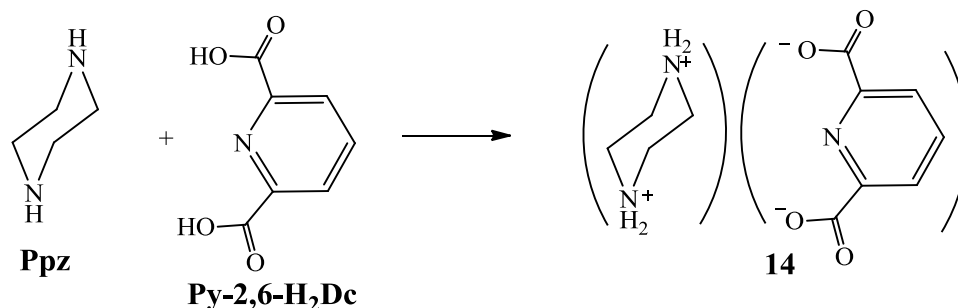


Figure 10. Synthesis of compound **14**.

The compound $(\text{H}_2\text{Ppz})[\text{Cd}(\text{Py-2,6-Dc})_2] \cdot 6\text{H}_2\text{O}$ (**15**) [84] (Figure 11) was synthesized from the proton transfer salt (**14**) [83].

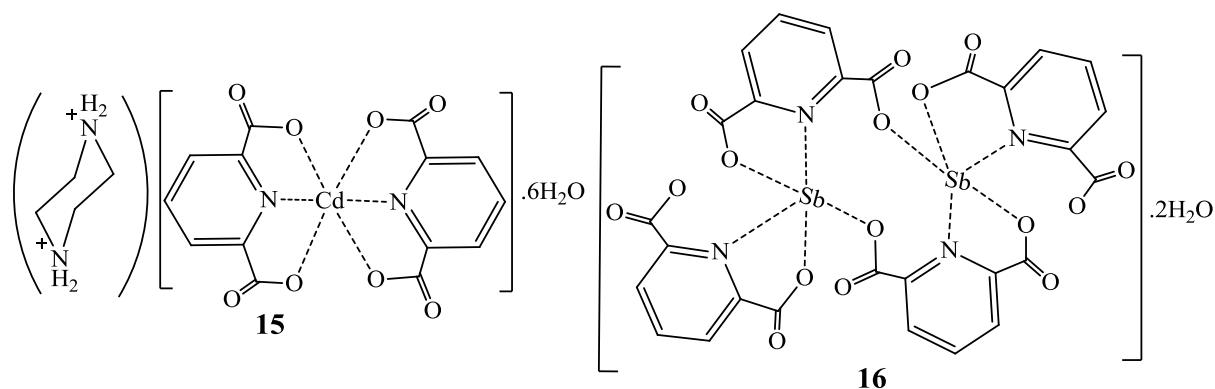


Figure 11. Structures of **15** and **16**.

In this complex, there are six uncoordinated water molecules that form hydrogen bonds with both $(\text{H}_2\text{Ppz})^{2+}$ and $[\text{Cd}(\text{Py-2,6-Dc})_2]^{2-}$ ions with a piperazinium ion as the counter ion. Complexes of metal ions Zn(II) [85] and Hg(II) [86], which are in the same group as Cd(II), obtained from the same proton transfer salt $(\text{H}_2\text{Ppz})^{2+}(\text{Py-2,6-Dc})^{2-}$ (**14**) have the same coordination environment. An increase in the order of $\text{Hg}(\text{II}) > \text{Cd}(\text{II}) > \text{Zn}(\text{II})$ was observed when the M–O bond lengths of the compounds were compared. It was found that the M–N bond in the Zn(II) complex was shorter than the others, but the Hg–N bond was also unexpectedly shorter than the Cd–N bond. In the anionic part of the complex, the $\text{N1}'\text{-Cd1}\text{-N1}$ angle was measured as $174.05(5)^\circ$ and it was observed that it deviated from linearity. It is understood that the two $(\text{Py-2,6-Dc})^{2-}$ rings are not perpendicular to each other since the torsion angles of $\text{O3}'\text{-Cd-O3-C7}$ and $\text{O3}'\text{-Cd-O2-C6}$ are $105.52(9)^\circ$ and $96.32(9)^\circ$, respectively. These data showed that the geometry of the complex is distorted octahedral around the six-coordinate Cd(II) ion (Figure 12).

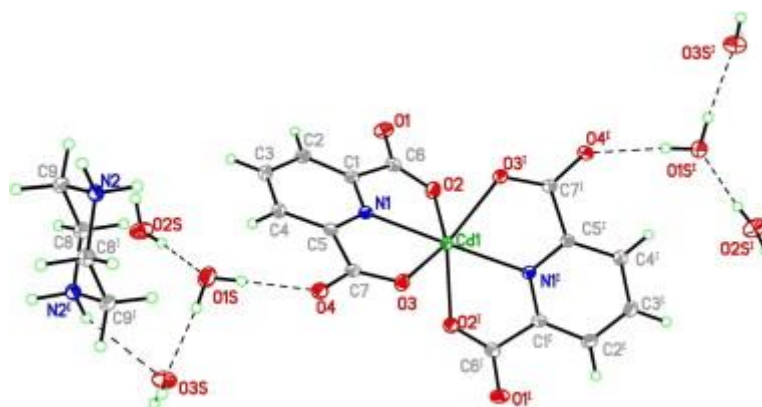


Figure 12. Molecular structure of $(\text{H}_2\text{Ppz})[\text{Cd}(\text{Py-2,6-Dc})_2] \cdot 6\text{H}_2\text{O}$ (**15**).

The compound $(\text{H}_2\text{Ppz})[\text{Sb}_2(\text{Py-2,6-Dc})_4]\cdot 2\text{H}_2\text{O}$ (**16**) [87] (Figure 11) was synthesized by the reaction of proton transfer compound **14** with the related metal salt. The ^1H NMR spectrum of $(\text{H}_2\text{Ppz})[\text{Sb}_2(\text{Py-2,6-Dc})_4]\cdot 2\text{H}_2\text{O}$ (**16**) exhibits two sets of peaks: signals at 3.33 ppm and at 8.42-8.25 ppm were attributed to the protons of $(\text{H}_2\text{Ppz})^{2+}$ and $(\text{Py-2,6-Dc})^{2-}$ moieties, respectively. Two of the four Py-2,6-Dc^{2-} anions in the binuclear Sb(III) complex bind to a metal center as tridentate and the other two as bidentate ligands to the other metal center. The angle between the N1/C2-C6 and N2/C9-C13 rings is 86.56° , indicating that the two Py-2,6-Dc^{2-} groups attached to the each metal center are nearly perpendicular to each other. From the crystallographic data, it is seen that the $\text{Sb1-N1}(2.393(3) \text{ \AA})$ and $\text{Sb1-O3A}(2.464(3) \text{ \AA})$ bonds are longer than the others ($2.088(2)$ - $2.282(3) \text{ \AA}$). The bond angles around the Sb(III) ion show the distorted trigonal bipyramid in which the O1 and O3 atoms lie in the axial position. Compared with the similar complex of Bi(III) ion, $\{(\text{H}_2\text{Ppz})[\text{Bi}_2(\text{Py-2,6-Dc})_4(\text{H}_2\text{O})]\cdot \text{H}_2\text{O}\}_n$, which is in the same group as Sb(III) , it was determined that Sb-N bond lengths were slightly shorter than Bi-N bond lengths, and Sb-O bond lengths were longer than Bi-O [88].

2.3.3.1.2. Proton transfer salt $(\text{H}_2\text{Ppz})_{1.5}(\text{Py-2,6-HDc})_3\cdot 3.7\text{H}_2\text{O}$, (**17**) and it's complexes **18-21**

Pale yellow proton transfer salt **17**, $(\text{H}_2\text{Ppz})_{1.5}(\text{Py-2,6-HDc})_3\cdot 3.7\text{H}_2\text{O}$, was synthesized by the reaction of $\text{Py-2,6-H}_2\text{Dc}$ and Ppz in THF [89] (Figure 13).

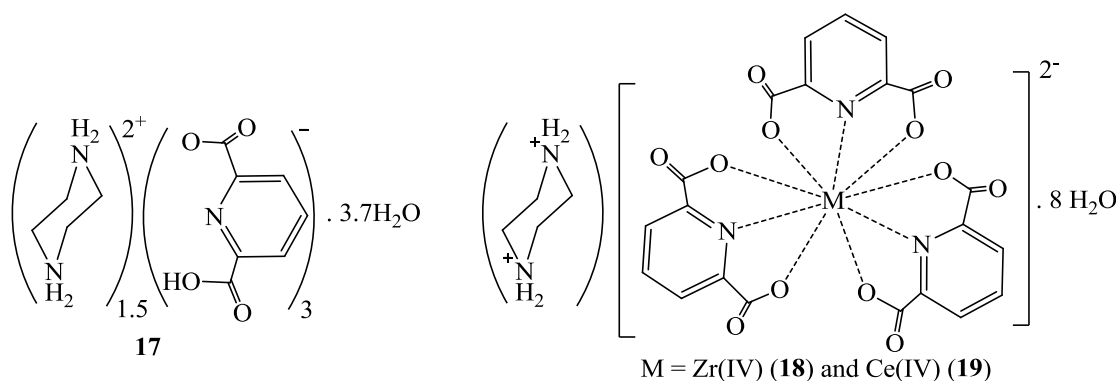


Figure 13. Proton transfer salt **17** and it's complexes **18** and **19**.

Only one of the hydrogens of the carboxylic acid was removed in complex **17**. The asymmetric units of the proton transfer salt **17** have three Py-2,6-Dc^{2-} rings and one and a half H_2Ppz ions to balance the charge. The strongest H-bond was observed as $\text{O1C-H1C}\cdots\text{O3B}$ ($2.4700(14)\text{ \AA}$) in the crystal structure of proton transfer salt **17**. In the molecular structure of **17**, π - π stacking was also observed as an intermolecular interaction between aromatic rings with the distance of $3.669(8) \text{ \AA}$ (Figure A6). The nine coordinated complexes Zr(IV) (**18**) and Ce(IV) (**19**) (Figure 13) were synthesized from the proton transfer salt **17** [89]. The asymmetric unit of complexes $(\text{H}_2\text{Ppz})[\text{Zr}(\text{Py-2,6-Dc})_3]\cdot 8\text{H}_2\text{O}$ (**18**) and $(\text{H}_2\text{Ppz})[\text{Ce}(\text{Py-2,6-Dc})_3]\cdot 8\text{H}_2\text{O}$ (**19**) contains three Py-2,6-Dc^{2-} ions as tridentate ligands, one $\text{H}_2\text{Ppz}^{2+}$ and eight-uncoordinated H_2O . The Zr(IV) and Ce(IV) ions in each complex bind to the three N and six O atoms of the three Py-2,6-Dc^{2-} ligands [89]. In the molecular structure of **18** (Figure 14) the Zr-O (O1 , O3 , O5 , O7 , O9 , O11) bond lengths are very close to each other and the Zr-N bond lengths are almost equal. The sum of the N1-Zr-N2 , N2-Zr-N3 and N3-Zr-N1 bond angles is $360.00(8)^\circ$, indicating that the Zr(IV) ion is in the center of the N1-N2-N3 plane. When the crystal

structure of **18** is compared with $(\text{HPyDa})_2[\text{Zr}(\text{Py-2,6-Dc})_3] \cdot 5\text{H}_2\text{O}$ (PyDa = pyridine-2,6-diamine) [90], it is seen that the bond lengths and bond angles surrounding the Zr(IV) ion are similar in both complexes. In the crystal structure of **18**, inter and intramolecular N–H \cdots O, O–H \cdots O, and C–H \cdots O H-bonds have values ranging from 2.718(3) to 3.464(4) Å.

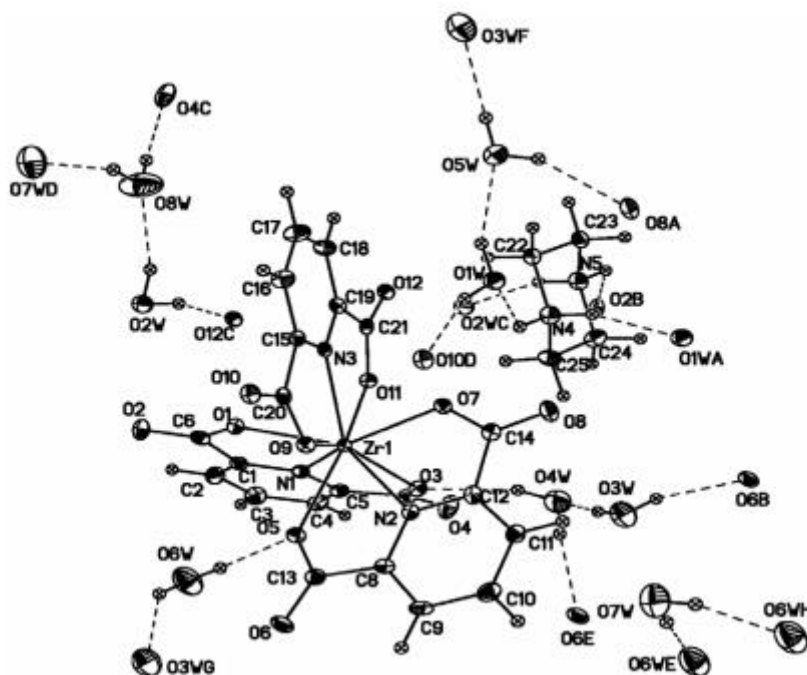


Figure 14. Molecular structure of **18**.

The geometry of $(\text{H}_2\text{Ppz})[\text{Ce}(\text{Py-2,6-Dc})_3] \cdot 8\text{H}_2\text{O}$ (**19**) is a distorted three-headed triangular prism with six oxygen atoms and three caps on its faces. The Ce(IV) complex has intramolecular and intermolecular H-bonds in its crystal structure, N–H \cdots O, O–H \cdots O, and C–H \cdots O, with values ranging from 2.711(5) to 3.448(5) Å [89]. Complexes $(\text{H}_2\text{Ppz})[\text{Sr}(\text{Py-2,6-Dc})_2(\text{H}_2\text{O})_2]_n \cdot 4\text{H}_2\text{O}$ (**20**) and $[\text{Ce}(\text{Py-2,6-Dc})_2(\text{H}_2\text{O})_2]_n \cdot 4\text{H}_2\text{O}$ (**21**) were obtained [91] from the proton transfer salt **17** [89]. These complexes show characteristic bands in their IR spectra. The bands observed in the range of 3600–3200 cm^{-1} belong to the C–H, N–H and O–H stretching vibrations originating from the piperazine cation, pyridine-2,6-dicarboxylate and lattice water molecules [92]. Asymmetrical and symmetrical carboxylate vibrations were observed at 1680–1700 cm^{-1} and 1580 cm^{-1} , respectively. A $\Delta\nu$ value of 120 cm^{-1} for complexes **20** and **21** indicates polybinding of the carboxylate to the metal [93]. In Sr(II) compound, the Sr(II) ion is bonded to one oxygen atom of the bridge Py-2,6-Dc $^{2-}$ ion, two water molecules, and four oxygens and two nitrogens of two pyridine-2,6-dicarboxylates [91]. Intermolecular H-bonds and Sr–Py-2,6-Dc–Sr distances of **20** are of great importance in the formation of its 2-D supramolecular structure. The chair-form piperazine cations are very good H-bond donors and also act as complementary ions [94–96]. The $[\text{Ce}(\text{Py-2,6-Dc})_2(\text{H}_2\text{O})_2]_n \cdot 4\text{H}_2\text{O}$ (**21**) complex has a 3-D polymeric structure. The Ce(IV) ion is coordinated to the four oxygens and two nitrogens of the two Py-2,6-Dc $^{2-}$ anion, two oxygen atoms of the two H $_2$ O molecules, and the one oxygen atom of the

Py-2,6-Dc²⁻ ion [91] (Figure 15). Sr(II) and Ce(IV) ions both have a distorted tricapped trigonal prism geometry.

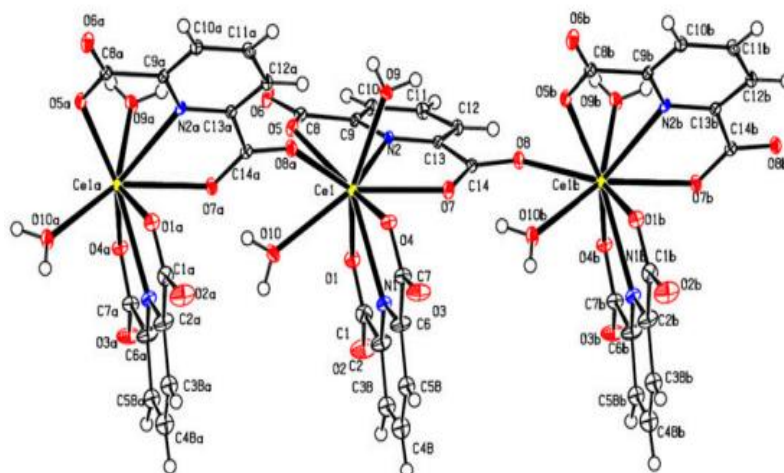


Figure 15. Polymeric structure of $[Ce(Py-2,6-Dc)_2(H_2O)_2]_n \cdot 4H_2O$ (**21**).

2.3.3.1.3. Proton transfer salt $(HOEtH_2Ppz)^{2+}(Py-2,6-HDc)_2^-$ (**22**) and its complexes (**23-26**)

Proton transfer salt $(HOEtH_2Ppz)^{2+}(Py-2,6-HDc)_2^-$ (**22**) ($HOEtH_2Ppz = 1-(2\text{-hydroxyethyl})\text{piperazine-}1,4\text{-dium}$) was obtained by the reaction of $HOEtPpz$ and $Py-2,6-H_2Dc$ [97] (Figure 16).

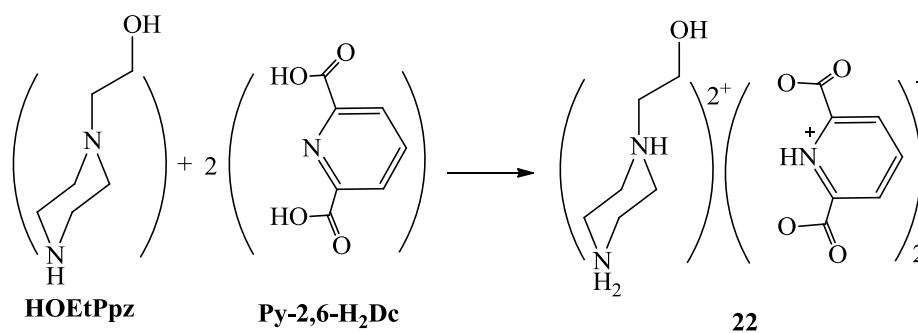


Figure 16. Synthesis of $(HOEtH_2Ppz)^{2+}(Py-2,6-HDc)_2^-$ (**22**).

¹H NMR spectrum of proton transfer salt (**22**) displayed signals at 3.35, 3.60 and 3.95 ppm for $H_2HOEtPpz^{2+}$ and at 8.35 and 8.57 ppm for $Py-2,6-HDc^-$ fragments.

Complexes of proton transfer salt **22** $(HOEtH_2Ppz)[M(Py-2,6-Dc)_2] \cdot 6H_2O$ ($M = Cu(II)$ (**23**), $Co(II)$ (**24**), $Ni(II)$ (**25**) and $Zn(II)$ (**26**)) consist of a $HOEtH_2Ppz^{2+}$ cation as a complementary ion, two $Py-2,6-Dc^{2-}$ anions as tridentate ligands and six uncoordinated water molecules (Figure 17) [97, 98].

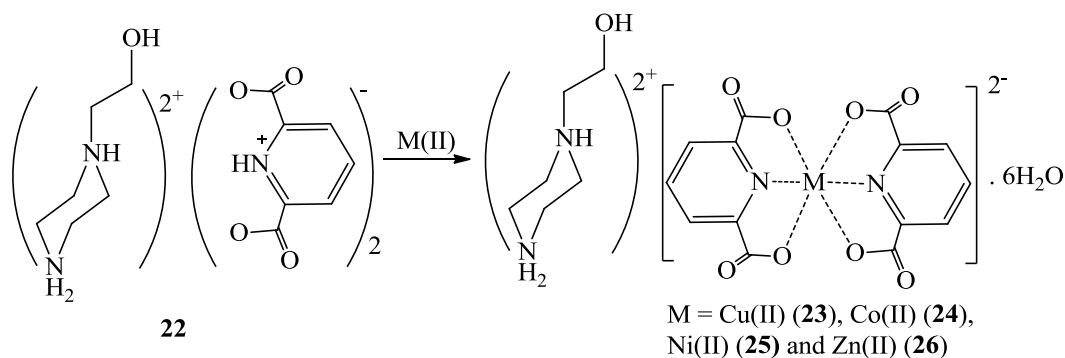


Figure 17. Synthesis of complexes **23-26**.

In crystal structure of Cu(II) (**23**) complex (Figure A7), O1–Cu–O4 and O7–Cu–O6 trans angles are low value as $156.3(3)^\circ$ and $155.6(3)^\circ$, respectively. Despite, the N1–Cu–N2 trans angle is $174.0(3)^\circ$, closer to 180° . The dihedral angle between the planes of the two Py-2,6-Dc²⁻ rings is 87.1° , indicating that the two Py-2,6-Dc²⁻ ligands are perpendicular to each other [97]. Cu–N and Cu–O bond lengths of are in agreement with similar Cu(II) compounds [99,100] The deviating from linearity bond angles around M(II) ions containing trans-donor atoms are $75.75(6)^\circ$ - $152.61(5)^\circ$ for Co(II) (**24**), $77.73(5)^\circ$ - $156.39(5)^\circ$ for Ni(II) (**25**) and $74.75(5)^\circ$ - $152.63(4)^\circ$ for Zn(II) (**26**). These values indicate that the ideal octahedral geometry is distorted due to the binding of Py-2,6-Dc²⁻ ions to M(II) ions as tridentate ligands (Figure A7). M–N and M–O bonds are within normal ranges for complexes **24-26** [98].

2.3.3.2. Mixed ligand complexes (27-36) of Py-2,6-H₂Dc

The mixed ligand complexes (**27-36**) of Py-2,6-H₂Dc with various metals as p-, d- and f-blocks were synthesized. The analyses, space groups and crystal systems of mixed-ligand complexes (**27-36**) are given in Table 4.

Table 4. The analyses, space groups and crystal systems of mixed-ligand complexes **27-36**.

Ref. No	Analyses	Complexes	Space Group	Crystal system
101	X-ray	$[(\text{H}_2\text{Ppz})[\text{Co}(\text{Py}-2,6\text{-Dc})_2] \cdot 4\text{H}_2\text{O}] \text{ (27)}$	$P2_1/n$	Monoclinic
103	X-ray, IR, NMR, UV-Vis, TGA and elemental analysis	$(\text{HPpzEa})[\text{Bi}_2(\text{Py}-2,6\text{-Dc})_3(\text{HPy}-2,6\text{-Dc})(\text{H}_2\text{O})_2] \cdot 5\text{H}_2\text{O} \text{ (28)}$	$P2_1/c$	Monoclinic
104	ICP, IR, TGA, X-ray, PXRD and elemental analysis	$(\text{H}_2\text{Ppz})_n[\text{Ce}_2(\text{Py}-2,6\text{-Dc})_4(\text{H}_2\text{O})_2]_n \text{ (29)}$	$P1$	Triclinic
104	ICP, IR, TGA, X-ray, PXRD and elemental analysis	$(\text{H}_2\text{Ppz})_n[\text{Pr}_2(\text{Py}-2,6\text{-Dc})_4(\text{H}_2\text{O})_2]_n \text{ (30)}$	$P1$	Triclinic
104	ICP, IR, TGA, X-ray, PXRD and elemental analysis	$(\text{H}_2\text{Ppz})_n[\text{Eu}_2(\text{Py}-2,6\text{-Dc})_4(\text{H}_2\text{O})_2]_n \text{ (31)}$	$P1$	Triclinic
105	ICP, IR, TGA, X-ray,	$(\text{H}_2\text{Ppz})_n[\text{Sm}_2(\text{Py}-2,6\text{-Dc})_4(\text{H}_2\text{O})_2]_n \text{ (32)}$	$P1$	Triclinic

	PXRD and elemental analysis			
109	IR, TGA, X-ray, and elemental analysis	$(\text{H}_2\text{Ppz})_3[\text{Tb}_2(\text{Py-2,6-Dc})_6] \cdot 15\text{H}_2\text{O}$ (33)	<i>P3</i>	
110	IR, TGA, X-ray, and elemental analysis	$(\text{H}_2\text{Ppz})[\text{Ce}_2(\text{Py-2,6-Dc})_4(\text{H}_2\text{O})_4] \cdot \text{H}_2\text{O}$ (34)	<i>P1</i>	Triclinic
111	ICPOES, IR, TGA, X-ray, PXRD and elemental analysis	$(\text{H}_2\text{Ppz})_n[\text{La}_2(\text{Py-2,6-Dc})_4(\text{H}_2\text{O})_2]_n$ (35)	<i>P1</i>	Triclinic
111	ICPOES, IR, TGA, X-ray, PXRD and elemental analysis	$(\text{H}_2\text{Ppz})_n[\text{Nd}_2(\text{Py-2,6-Dc})_4(\text{H}_2\text{O})_2]_n$ (36)	<i>P1</i>	Triclinic

2.3.3.2.1. Mixed-ligand complex $[(\text{H}_2\text{Ppz})[\text{Co}(\text{Py-2,6-Dc})_2] \cdot 4\text{H}_2\text{O}$ (**27**)

After mixing the aqueous solution of $\text{Co}(\text{NO}_3)_2 \cdot 6\text{H}_2\text{O}$ (2 mmol) and Py-2,6- H₂Dc (4 mmol) at room temperature for 45 minutes, an aqueous solution of piperazine (Ppz) (4 mmol) was added to this solution and the mixture was stirred for 4 h at 100 °C. The crystals of $[(\text{H}_2\text{Ppz})[\text{Co}(\text{Py-2,6-Dc})_2] \cdot 4\text{H}_2\text{O}$ (**27**) were obtained by evaporation of the solution at room conditions [101]. In the Co(II) complex, the piperazindium cation was found to be in the chair conformation. The Co(II) ion, which has a distorted octahedral geometry, is coordinated to the two nitrogens and four oxygens of the two Py-2,6-Dc²⁻ rings (Figure 18).

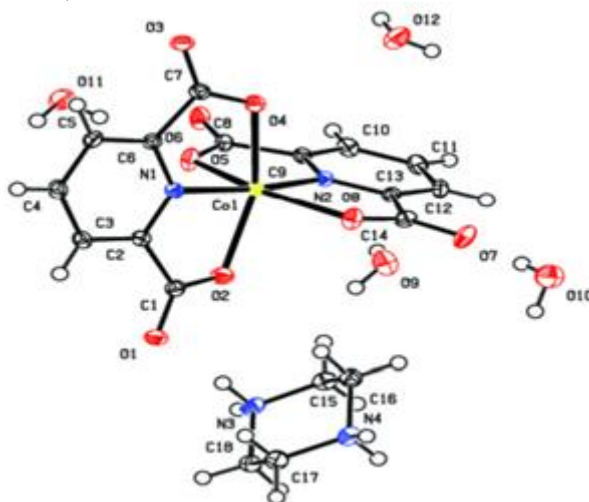


Figure 18. Molecular structure of $[(\text{H}_2\text{Ppz})[\text{Co}(\text{Py-2,6-Dc})_2] \cdot 4\text{H}_2\text{O}$ (**27**).

2.3.3.2.2. Mixed-ligand complex $(\text{HPpzEa})[\text{Bi}_2(\text{Py-2,6-Dc})_3(\text{HPy-2,6-Dc})(\text{H}_2\text{O})_2] \cdot 5\text{H}_2\text{O}$ (**28**)

Due to the large size of the Bi^{3+} ions, most Bi(III) compounds have a coordination number greater than six [102]. In dimeric complex $(\text{HPpzEa})[\text{Bi}_2(\text{Py-2,6-Dc})_3(\text{HPy-2,6-Dc})(\text{H}_2\text{O})_2] \cdot 5\text{H}_2\text{O}$ (**28**) (PpzEa = 2-piperazin-1-ylethanamine) Bi^{3+} has eight coordinated [103] (Figure 19).

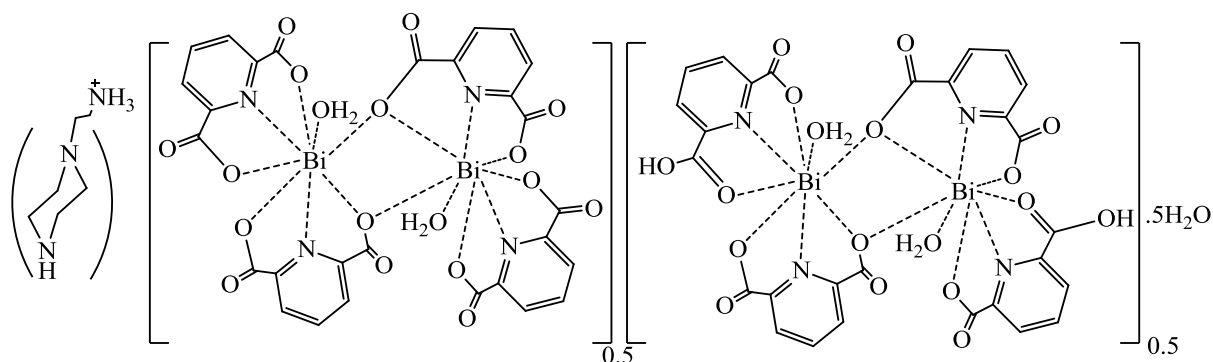


Figure 19. Structure of Bi(III) compound (**28**).

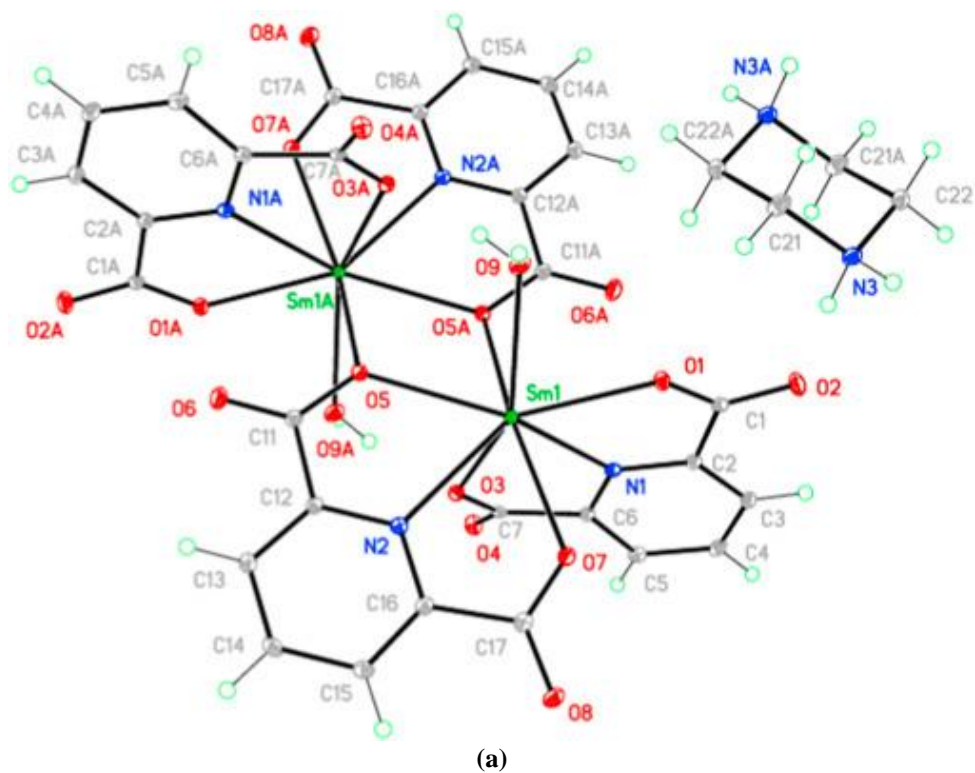
The asymmetric unit of **28** which obtained by hydrothermal method has two different bismuth ions, both Bi^{3+} cations bind to five oxygens and two nitrogens of three different Py-2,6-Dc²⁻ anions and one oxygen of an aqua ligand.

2.3.3.2.3. Mixed-ligand complexes Ce(III) (**29**), Pr(III) (**30**) and Eu(III) (**31**)

Hydrothermally obtained three metal-organic frameworks containing lanthanide metals Ce(III) (**29**), Pr(III) (**30**) and Eu(III) (**31**), formulated as $(\text{H}_2\text{Ppz})_n[\text{Ln}_2(\text{Py-2,6-Dc})_4(\text{H}_2\text{O})_2]_n$ are isomorphous [104]. The structures of complexes occur $[\text{Ln}_2(\text{Py-2,6-Dc})_4(\text{H}_2\text{O})_2]^{2-}$ anionic chains with $\{\text{H}_2\text{Ppz}\}^{2+}$ moiety occupying the interchain areas. The chains occur binuclear $[\text{Ln}_2(\text{Py-2,6-Dc})_4(\text{H}_2\text{O})_2]^{2-}$ structural constituents connected by *O,O'*-bridges of carboxylate fragments. In binuclear complexes, each of the lanthanide ions binds to five oxygens of the carboxylate groups of four Py-2,6-Dc²⁻ rings, two nitrogens, and two oxygens of the water ligands, forming a nine-coordinate structure.

2.3.3.2.4. Mixed-ligand complex $(\text{H}_2\text{Ppz})_n[\text{Sm}_2(\text{Py-2,6-Dc})_4(\text{H}_2\text{O})_2]_n$ (**32**)

The asymmetric unit of the hydrothermally synthesized MOF complex $(\text{H}_2\text{Ppz})_n[\text{Sm}_2(\text{Py-2,6-Dc})_4(\text{H}_2\text{O})_2]_n$ (**32**) contains the Sm(III) ion bonded to N and O atoms of the two Py-2,6-Dc²⁻ and the a H₂O ligand. It also contains half of the protonated piperazinium cation [105] (Figure 20a). The ladder structure in which pyridine-2,6-dicarboxylate is coordinated to the Sm(III) ion has been reported for the first time. The complementary piperazine cation is attached to the Sm(III) ladder by strong H-bonds. Also, there is an H-bond between one of the oxygens (O3) of the carboxylate groups and the coordinated water molecule (Figure 20b).



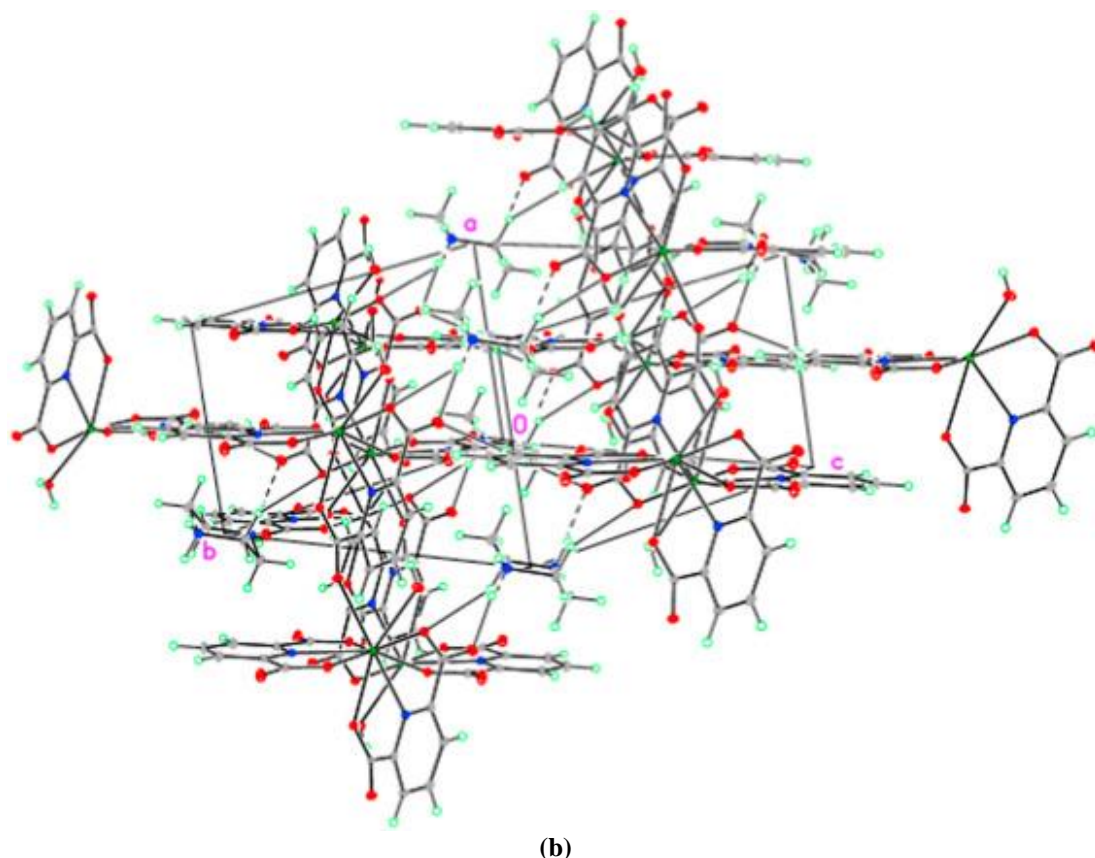


Figure 20. (a) Asymmetric unit of **32** (b) 3-D network of **32**.

The IR spectrum of the compound exhibits the bands at 3426 cm^{-1} for $\nu(\text{N-H})$ vibrations of complementary ion $\text{H}_2\text{Ppz}^{2+}$ and at 3247 cm^{-1} for $\nu(\text{O-H})$ vibrations of coordinate H_2O [106]. Free ligand and the Sm(III) complex showed $\nu(\text{C=O})$ stretching vibrations at 1688 cm^{-1} and 1622 cm^{-1} , respectively. This shift indicates that the oxygen atom of the carbonyl group is coordinated to the Sm(III) ion. The bands observed at 764 cm^{-1} for the $\nu(\text{Sm-O})$ vibration and at 433 cm^{-1} for the $\nu(\text{Sm-N})$ vibration indicate that the O- and N-atoms of the Py-2,6-Dc $^{2-}$ ligand are coordinated to the Sm(III) ion [107, 108].

2.3.3.2.5. Mixed-ligand complex $(\text{H}_2\text{Ppz})_3[\text{Tb}_2(\text{Py-2,6-Dc})_6] \cdot 15\text{H}_2\text{O}$ (**33**)

Hydrothermally synthesized Tb(III) complex [109], $(\text{H}_2\text{Ppz})_3[\text{Tb}_2(\text{Py-2,6-Dc})_6] \cdot 15\text{H}_2\text{O}$ (**33**), has an interesting structure because it contains 1-D water chains consisting of $(\text{H}_2\text{O})_{20}$ clusters. The complex is expanded into a 3-D supramolecular network structure *via* H-bonds by π - π stacking interactions. Besides the Tb(III) ion, the asymmetric unit of the complex consists of a Py-2,6-Dc $^{2-}$ ion as ligand, one half of the $\text{H}_2\text{Ppz}^{2+}$ cation as a counter ion, and five lattice water molecules (Figure 21a). The Tb(III) center is coordinated with three N and six O atoms from the three Py-2,6-Dc $^{2-}$ ligands and has a slightly distorted tricapped trigonal prismatic geometry (Figure 21b).

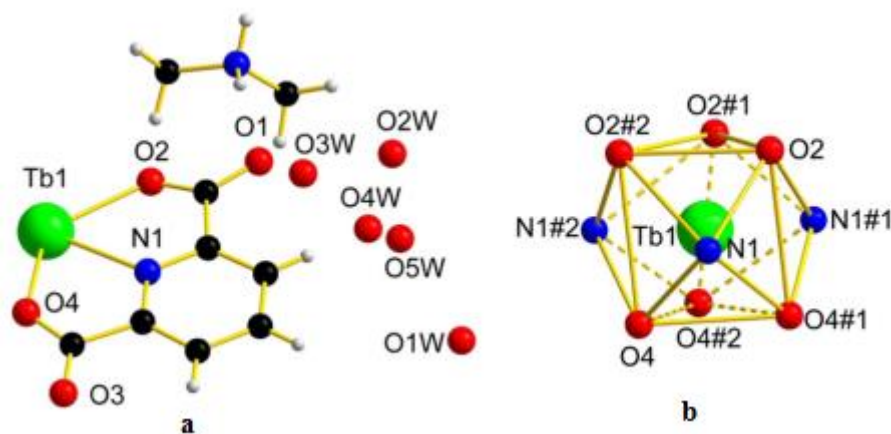


Figure 21. (a) Binding pattern of Tb1 in complex **33** (b) Distorted tricapped trigonal prism image of Tb1 in complex **33**.

2.3.3.2.6. Mixed-ligand complex $(\text{H}_2\text{Ppz})[\text{Ce}_2(\text{Py-2,6-Dc})_4(\text{H}_2\text{O})_4]\cdot\text{H}_2\text{O}$ (**34**)

The binuclear unit of $(\text{H}_2\text{Ppz})[\text{Ce}_2(\text{Py-2,6-Dc})_4(\text{H}_2\text{O})_4]\cdot\text{H}_2\text{O}$ (**34**) consists of Ce(III) cations bridged with two dpic anions [110] (Figure 22). In complex, Ce^{3+} ion is nine coordinated. The H-bonds in the molecular structure of the complex connect the binuclear units, piperazine and water molecules in a 3-D architecture.

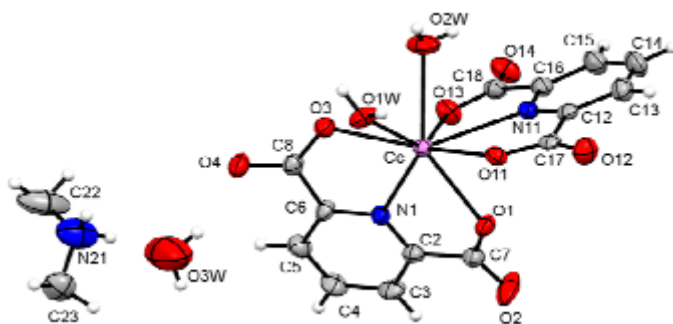


Figure 22. The asymmetric unit of $(\text{H}_2\text{Ppz})[\text{Ce}_2(\text{Py-2,6-Dc})_4(\text{H}_2\text{O})_4]\cdot(\text{H}_2\text{O})$ (**34**).

2.3.3.2.7. Mixed-ligand complexes $(\text{H}_2\text{Ppz})_n[\text{La}_2(\text{Py-2,6-Dc})_4(\text{H}_2\text{O})_2]_n$ (**35**) and $(\text{H}_2\text{Ppz})_n[\text{Nd}_2(\text{Py-2,6-Dc})_4(\text{H}_2\text{O})_2]_n$ (**36**)

Two Ln-MOFs obtained by the hydrothermal method, $(\text{H}_2\text{Ppz})_n[\text{La}_2(\text{Py-2,6-Dc})_4(\text{H}_2\text{O})_2]_n$ (**35**) and $(\text{H}_2\text{Ppz})_n[\text{Nd}_2(\text{Py-2,6-Dc})_4(\text{H}_2\text{O})_2]_n$ (**36**) contains the Py-2,6-Dc^{2-} anion and water molecules as ligands and exists as a complementary ion [111]. The asymmetric unit of complexes contain one Ln(III) ion, two Py-2,6-Dc^{2-} fragments, an aqua ligand and half of the uncoordinated piperazine ring. Geometry of complexes is distorted mono-capped square antiprism with four oxygen atoms on one face (O(1), O(2), O(5) and O(7)) and four nitrogen atoms on the opposite face (N(2), O(3), O(5) and O(9)) (Figure 23).

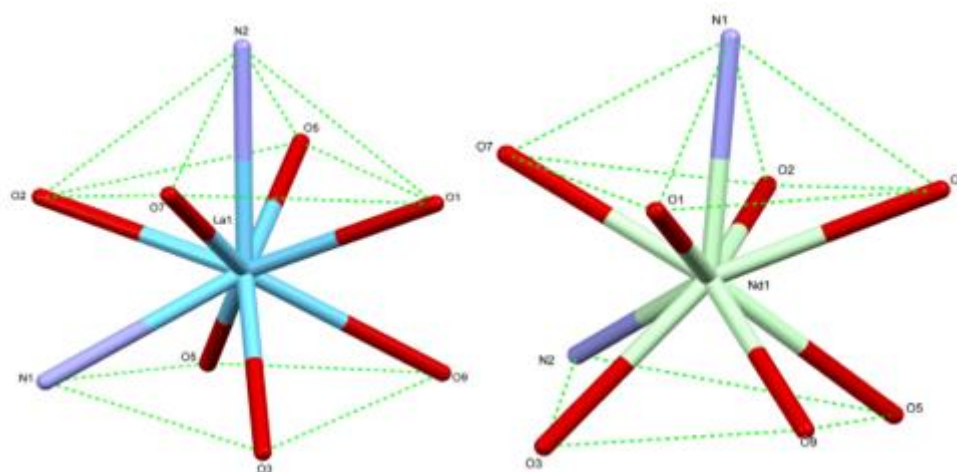


Figure 23. (a) Mono-capped square antiprism coordination geometry of La(III) (**35**) and (b) Nd(III) (**36**) ions.

3. CONCLUSIONS

In this short review, proton transfer salts and their complexes and mixed-ligand complexes obtained from pyridine-dicarboxylic acids and piperazines between 2009 and 2021 were investigated. Between these years, proton transfer salts and metal complexes obtained from the reaction of pyridine-2,4-, 3,4- and 3,5-dicarboxylic acids with piperazines were not encountered. In the examination, it was seen that Py-2,6-H₂Dc was used the most, followed by Py-2,5-H₂Dc. It was observed that piperazine was used mostly, as a base in the reactions, but its derivatives were used very little. Here in, metal ions of proton transfer salts and mixed ligand metal complexes include s-, p-, and mostly d- and f-block metals. It has been determined that H-bonding has an important contribution to the stabilization of the 3-D networks formed in the molecular structures of the compounds studied.

ACKNOWLEDGEMENT

I would like to thank Dr Halil İlkimen for his help in the literature survey.

REFERENCES

- [1] Gomtsyan, A., (2012), Heterocycles in drugs and drug discovery, *Chemistry of Heterocyclic Compounds*, 48(1), 7–10.
- [2] Chandrika, N. T., Shrestha, S. K., Ngo, H. X., Tsodikov, O. V., Howard, K. C., Garneau-Tsodikova, S., (2017), Alkylated Piperazines and Piperazine-Azole Hybrids as Antifungal Agents, *Journal of Medicinal Chemistry*, 61(1), 158–173.

- [3] Pytka, K., Rapacz, A., Zygmunt, M., Olczyk, A., Waszkielewicz, A., Sapa, J., Filipek, B., (2015), Antidepressant-like activity of a new piperazine derivative of xanthone in the forced swim test in mice: The involvement of serotonergic system, *Pharmacology Reports*, 67(1), 160–165.
- [4] Parai, M. K, Panda, G., Srivastava, K., Puri, S. K, (2008), Design, synthesis and antimalarial activity of benzene and isoquinoline sulfonamide derivatives, *Bioorganic and Medicinal Chemistry Letters*, 18(2), 776–781.
- [5] Brown, A. M, Patch, T.L., Kaumann, A. J., (1991), The antimigraine drugs ergotamine and dihydroergotamine are potent 5-HT_{1C} receptor agonists in piglet choroid plexus, *British Journal of Pharmacology*, 104, 45–48.
- [6] Le Bihan, G., Rondu, F., Pele-Tounian A, Wang, X., Lidy S, Touboul, E., Lamouri, A., Dive, G., Huet, J., Pfeiffer, B., Renard, P., Guardiola-Lemaitre, B., Manechez, D., Penicaud, L., Ktorza, A., Godfroid, J. J., (1999), Design and Synthesis of Imidazoline Derivatives Active on Glucose Homeostasis in a Rat Model of Type II Diabetes. 2, *Journal of Medicinal Chemistry*, 42(9), 1587–1603.
- [7] Ranise, A., Spallarossa, A., Bruno, O., Schenone, S., Fossa, P., Menozzi, G., Bondavalli, F., Mosti, L., Capuano, A., Mazzeo, F., Falcone, G., Filippelli, W., (2003), Synthesis of N-substituted-N-acylthioureas of 4-substituted piperazines endowed with local anaesthetic, antihyperlipidemic, antiproliferative activities and antiarrhythmic, analgesic, antiaggregating actions, *Farmaco*, 58(9), 765–780.
- [8] McNair, T. J., Wibin, F. A, Hoppe, E. T, Schmidt, J. L., dePeyster, F. A., (1963), Antitumor action of several new piperazine derivatives compared to certain standard anticancer agents, *Journal of Surgical Research*, 3(3), 130–136.
- [9] Kumar, C. S. A, Swamy, S. N, Thimmegowda, N. R, Prasad, S. B. B, Yip, G. W, Rangappa, K. S., (2007), Synthesis and evaluation of 1-benzhydryl-sulfonyl-piperazine derivatives as inhibitors of MDA-MB-231 human breast cancer cell proliferation, *Medicinal Chemistry Research*, 16(4), 179–187.
- [10] Ahmadi, A., Khalili, M., Nafarie, A., Yazdani, A. Nahri-Niknafs, B., (2012), Synthesis and anti-inflammatory effects of new piperazine and ethanolamine derivatives of H₁-antihistaminic drugs, *Mini-Reviews in Medicinal Chemistry*, 12(12), 1282–1292.
- [11] Guo, J., Tao, H., Alasadi, A., Huang, Q., Jin, S., (2019), Niclosamide piperazine prevents high-fat diet-induced obesity and diabetic symptoms in mice. *Eating and Weight Disorders - Studies on Anorexia, Bulimia and Obesity*, Eating and Weight Disorders, 24, 91–96.
- [12] Waszkielewicz, A. M., Kubacka, M., Panczyk, K., Mogilski, S., Siwek, A., Glich-Lutwin, M., Grybos, A., Filipek, B., (2016), Synthesis and activity of newly designed aroxyalkyl or aroxyethoxyethyl derivatives of piperazine on the cardiovascular and the central nervous systems, *Bioorganic Medicinal Chemistry Letters*, 26, 5315–5321.

- [13] Sharif, M. A., Aghabozorg, H., Shokrollahi, A., Kickelbick, G., Moghimi, A., Shamsipur, M., (2006), Novel Proton Transfer Compounds Containing 2,6-Pyridinedicarboxylic Acid and Melamine and Their PbII Complex: Synthesis, Characterization, Crystal Structure and Solution Studies, *Polish Journal of Chemistry*, 80 847- 863.
- [14] Moghimi, A., Sharif, M. A., Shokrollahi, A., Shamsipur, M., Aghabozorg, H., (2005), A Novel Proton Transfer Compound Containing 2, 6-Pyridinedicarboxylic Acid and Creatinine and its Zinc(II) Complex ? Synthesis, Characterization, Crystal Structure, and Solution Studies, *Zeitschrift für anorganische und allgemeine Chemie*, 631(5), 902–908.
- [15] Aghabozorg, H., Ramezanipour, F., Nakhjavan, B., Soleimannejad, J., Attar Gharamaleki, J., Sharif, M. A., (2007), Different complexation behavior of a proton transfer compound obtained from 1,10-phenanthroline and pyridine-2,6-dicarboxylic acid with Sn(IV), Sb(III) and Tl(I), *Crystal Research and Technology*, 42(11), 1137–1144.
- [16] Zhang, M., Chen, C., Wang, Q., Fu, W., Huang, K., Zhou, W., (2017), Metal-Organic Framework with Functionalized Piperazine Exhibiting Enhanced CH₄ Storage, *Journal of Materials Chemistry A*, 5, 349–354.
- [17] Lehn, J. -M., (1988), *Supramolecular Chemistry—Scope and Perspectives Molecules, Supermolecules, and Molecular Devices (Nobel Lecture)*, *Angewandte Chemie International Edition*, 27(1), 89–112.
- [18] Csöregi, I., Weber, E., Hens, T., (1998), The Role of Chloro Substituents in Solid Inclusion Formation. Crystal Structures Formed by a Bulky Hydroxy Host with Ethyl Acetate (2:1) and Cyclohexylamine (1:2) as Guest, *Supramolecular Chemistry*, 10(1), 133–142.
- [19] Groeneman, R. H., MacGillivray, L. R., Atwood, J. L., (1999), One-Dimensional Coordination Polymers Based upon Bridging Terephthalate Ions, *Inorganic Chemistry*, 38(2), 208–209.
- [20] Khalil, M. M., Attia, A. E., (1999), Potentiometric Studies on the Binary and Ternary Complexes of Copper(II) Containing Dipicolinic Acid and Amino Acids, *Journal of Chemical and Engineering Data*, 44(2), 180–184.
- [21] Tochikubo, K., Hachisuka, Y., Murachi, T., (1968), Properties of Glucose Dehydrogenase from Vegetative Cells of *Bacillus subtilis* and Effect of Dipicolinic Acid and its Chemical Analogues on the Enzyme, *Japanese Journal of Microbiology*, 12(4), 435–440.
- [22] Martin, B. L., (1997), Selective Activation of Calcineurin by Dipicolinic Acid, *Archives Biochemistry and Biophysics*, 345(2), 332–338.
- [23] Bannister, W. H., Bannister, J. V., Searle, A. J. F., Thornalley, P. J., (1983), The reaction of superoxide radicals with metal picolinate complexes, *Inorganica Chimica Acta*, 78, 139–142.
- [24] Aghabozorg, H., Manteghi, F., Sheshmani, S., (2008), A brief review on structural concepts of novel supramolecular proton transfer compounds and their metal complexes, *Journal of Iranian Chemical Society*, 5(2), 184–227.

- [25] Moghimi, A., Moosavi, S. M., Kordestani, D., Maddah, B., Shamsipur, M., Aghabozorg, H., Kickelbick, G., (2007), Pyridine-2,6-bis(monothiocarboxylic) acid and 2-aminopyridine as building blocks of a novel proton transfer compound: Solution and X-ray crystal structural studies, *Journal of Molecular Structure*, 828(1-3), 38–45.
- [26] Tunca, E., Bülbül, M., İlkimen, H., Canlıdınç, R. S., Yenikaya, C., (2020), Investigation of the effects of the proton transfer salts of 2-aminopyridine derivatives with 5-sulfosalicylic acid and their Cu(II) complexes on cancer-related carbonic anhydrases: CA IX and CA XII, *Chemical Papers*, 74, 2365–2374.
- [27] İlkimen, H., Yenikaya, C., Sarı, M., Bülbül, M., Tunca, E., Dal, H. (2013), Synthesis and characterization of a proton transfer salt between 2,6-pyridinedicarboxylic acid and 2-aminobenzothiazole, and its complexes and their inhibition studies on carbonic anhydrase isoenzymes, *Journal of Enzyme Inhibition and Medicinal Chemistry*, 29(3), 353–361.
- [28] İlkimen, H., Yenikaya, C., Sarı, M., Bülbül, M., Tunca, E., Süzen, Y. (2013), Synthesis and characterization of a proton transfer salt between dipicolinic acid and 2-amino-6-methylbenzothiazole and its complexes, and their inhibition studies on carbonic anhydrase isoenzymes, *Polyhedron*, 61, 56–64.
- [29] Yang, G., Park, S.-J., (2019), Conventional and Microwave Hydrothermal Synthesis and Application of Functional Materials: A Review, *Materials*, 12(7), 1177–1194.
- [30] Li, G., Li, L., Feng, S., Wang, M., Zhang, L., Yao, X., (1999), An Effective Synthetic Route for a Novel Electrolyte: Nanocrystalline Solid Solutions of $(\text{CeO}_2)_{1-x}(\text{BiO}_{1.5})_x$, *Advanced Materials*, 11(2), 146–149.
- [31] Cheetham, A. K., Férey, G., Loiseau, T., (1999), Open-Framework Inorganic Materials, *Angewandte Chemie International Edition*, 38(22), 3268–3292
- [32] Feng, S., Greenblatt, M., (1992), Galvanic cell type humidity sensor with NASICON-based material operative at high temperature, *Chemical Materials*, 4(6), 1257–1262.
- [33] Feng, S., Xu, R., (2001), New Materials in Hydrothermal Synthesis, *Accounts of Chemical Research*, 34(3), 239–247.
- [34] Che, G.-B., Liu, S.-Y., Zhang, Q., Liu, C.-B., Zhang, X.-J., (2015), Syntheses, structures and photoluminescence of lanthanide-organic frameworks assembled from multifunctional N,O-donor ligand, *Journal of Solid State Chemistry*, 225, 378–382.
- [35] Sun, F., Yin, Z., Sun, C. -G., Kurmoo, M., Zeng, M. -H., (2014), Design, structure and luminescent properties of a novel two-dimensional Cd(II) coordination polymer constructed from in situ generated 1-methyl-2-(3H-[1-3]triazol-4-yl)-1H-benzimidazole, *Inorganic Chemistry Communications*, 43, 78–80.

- [36] You, L. -X., Li, Z. -G., Ding, F., Wang, S. -J., Ren, B. -Y., Sun, Y. -G., (2014), Synthesis, structure and luminescence properties of lanthanide coordination polymers using in situ decarboxylation of a H₃cppdc ligand, *Inorganic Chemistry Communications*, 46, 340–343.
- [37] Semerci, F., Yeşilel, O. Z., Ölmez, H., Büyükgüngör, O., (2014), Supramolecular assemblies of copper(II)–pyridine-2,3-dicarboxylate complexes with N-donor ligands and clustered water molecules, *Inorganica Chimica Acta*, 409, 407–417.
- [38] Han, Z., Li, J., Gao, J., (2006), Synthesis, crystal structure and magnetic properties of 2D bi-layered coordination polymer, *Journal of Coordination Chemistry*, 59(14), 1641–1647.
- [39] Wibowo, A. C., Smith, M. D., zur Loye, H. -C., (2011), A new Kagomé lattice coordination polymer based on bismuth and pyridine-2,5-dicarboxylate: structure and photoluminescent properties, *Chemical Communications*, 47(26), 7371–7373.
- [40] Hamdy, L. B., Raithby, P. R., Thomas, L. H., Wilson, C. C., (2014), Self-assembly synthesis of precursors to potential open framework alkali earth metal–organic complexes, *New Journal of Chemistry*, 38(5), 2135–2143.
- [41] Shi, Q., Zhang, S., Wang, Q., Ma, H., Yang, G., Sun, W. -H., (2007), Synthesis and crystal structure of metal-organic frameworks [Ln₂(pydc-3,5)₃(H₂O)₉]_n3nH₂O (Ln=Sm, Eu, Gd, Dy; pydc-3,5=pyridine-3,5-dicarboxylate) along with the photoluminescent property of its europium one, *Journal of Molecular Structure*, 837(1-3), 185–189.
- [42] Song, Y., Wang, X., Zhang, S., Wang, J., Gao, S., Chen, S., (2016), Lanthanide-Coordination Polymers with Pyridinedicarboxylic Acids: Syntheses, Structures, and Luminescent Properties, *Zeitschrift für anorganische und allgemeine Chemie*, 642(11-12), 681–691.
- [43] Nandi, G., Thakuria, R., Titi, H. M., Patra, R., Goldberg, I., (2014), Synthesis, structure, topology and magnetic properties of new coordination polymers based on 5(-Br/-COOH)-substituted nicotinic acid, *CrystEngComm*, 16, 5244–5256.
- [44] Chauhan, S., Patel, P., Pandya, V., (2014), Studies of Some Novel Chromium Pyridine Dicarboxylate Complexes, *Oriental Journal of Chemistry*, 30(4), 1763–1769.
- [45] Barszcz, B., Hodorowicz, M., Jablonska-Wawrzycka, A., Masternak, J., Nitek, W. Stadnicka, K., (2010), Comparative study on Cd(II) and Ca(II) model complexes with pyridine-2,3-dicarboxylic acid: Synthesis, crystal structure and spectroscopic investigation, *Polyhedron*, 29, 1191–1200.
- [46] Li, L.-J., Li, Y., (2004), Hydrothermal synthesis and crystal structure of a novel 2-D coordination polymer [Mn₂(pdc)₂(H₂O)₃]_n2nH₂O (pdc=pyridine-2,3-dicarboxylate), *Journal of Molecular Structure*, 694(1-3), 199–203.
- [47] Kowalik, M., Masternak, J., Łakomska, I., Kazimierczuk, K., Zawilak-Pawlik, A., Szczepanowski, P., Barszcz, B., (2020), Structural Insights into New Bi(III) Coordination Polymers with Pyridine-2,3-Dicarboxylic Acid: Photoluminescence Properties and Anti-*Helicobacter pylori* Activity, *International Journal of Molecular Sciences*, 21(22), 8696–8721.

- [48] Aghabozorg, H., Manteghi, F., Ghadermazi, M., (2008), Piperazinediium bis(2-carboxypyridine-3-carboxylate), *Acta Crystallographica*, E64(1), o230–o230.
- [49] Aghabozorg, H., Daneshvar, S., Motyeian, E., Manteghi, F., Khadivi, R., Ghadermazi, M., Shamsipur, M., (2009), Synthesis and crystal structure of Mn(II) and Hg(II) compounds and solution studies of Mn(II), Zn(II), Cd(II) and Hg(II) compounds based on piperazinediium pyridine-2,3-dicarboxylate, *Journal of Iranian Chemical Society*, 6(3), 620–637.
- [50] Aghabozorg, H., Daneshvar, S., Motyeian, E., Ghadermazi, M., Gharamaleki, A. J., (2007), catena-Poly[piperazindium [zincate(II)-bis(μ -pyridine-2,3-dicarboxylato)- κ^3 N,O²:O³; κ^3 O³:N,O²] tetrahydrate], *Acta Crystallographica*, E63, m2468-m2469.
- [51] Aghabozorg, H., Motyeian, E., Khadivi, R., Ghadermazi, M., Manteghi, F., (2008), catena-Poly[[triacuacadmium(II)- μ -pyridine-2,3-dicarboxylato- κ^3 N,O²:O³], *Acta Crystallographica*, E64, m320-m321.
- [52] Manteghi, F., Ghadermazi, M., Kakaei, N., (2011), Piperazine-1,4-diium pyridine-2,3-dicarboxylate methanol monosolvate, *Acta Crystallographica*, E67(5), o1122–o1122.
- [53] Zhang, X., Huang, D., Chen, C., Liu, Q., Liao, D., Li, L., (2005), Synthesis, structural characterization and magnetic property of metal 2,5-pyridine dicarboxylate complex, *Inorganic Chemistry Communications*, 8(1), 22–26.
- [54] Xie, C., Zhang, B., Wang, X., Wang, R., Shen, G., Shen, D., (2006), The synthesis and structure of a novel alternating 1-D cobalt coordination polymer [Co(2,5-PDC)₂(H₂O)₂Co(H₂O)₄]-4H₂O, *Journal of Chemical Crystallography*, 37(1), 25–29.
- [55] Plater, M. J., St. J. Foreman, M. R., Howie, R. A., Lachowski, E. E., (1998), Hydrothermal Synthesis and Characterisation of M(pdc)-3H₂O (pdc=2,5-pyridinedicarboxylate); M=Co, Ni, CoxNiy (x=0.4–0.6, y=0.6–0.4), *Journal of Chemical Research, Part S* (12), 754–755.
- [56] Lee, J., Shim, H., Park, Y., Park, S., Shin, J., Yang, W., Lee, S., (2002), 2,5-Pyridinedicarboxylic acid derivatives as non-Nucleosidic Reverse transcriptase inhibitors of Hepatitis B Virus, *Bioorganic and Medicinal Chemistry Letters*, 12(19), 2715–2717.
- [57] Tucker, H., Thomas, D. F., (1992), Novel inhibitors of prolyl 4-hydroxylase. 2. 5-Amide substituted pyridine-2-carboxylic acids, *Journal of Medicinal Chemistry*, 35(5), 804–807.
- [58] Sengupta, P., Ghosh, S., Mak, T. C., (2001), A new route for the synthesis of bis(pyridine dicarboxylato)bis(triphenylphosphine) complexes of ruthenium(II) and X-ray structural characterisation of the biologically active trans-[Ru(PPh₃)₂(L₁H)₂] (L₁H₂=pyridine 2,3-dicarboxylic acid), *Polyhedron*, 20(9-10), 975–980.
- [59] Patrick, B. O., Stevens, C. L., Storr, A., Thompson, R. C., (2005), Coordination polymers incorporating copper(II) and manganese(II) centers bridged by pyridinedicarboxylate ligands: Structure and magnetism, *Polyhedron*, 24(16-17), 2242–2249.

- [60] Süss-Fink, G., Cuervo, L. G., Therrien, B., Stoeckli-Evans, H., Shul'pin, G. B., (2004), Mono and oligonuclear vanadium complexes as catalysts for alkane oxidation: synthesis, molecular structure, and catalytic potential, *Inorganica Chimica Acta*, 357(2), 475–484.
- [61] Sun, L.-P., Niu, S.-Y., Jin, J., Yang, G.-D., Ye, L., (2006), Synthesis, Structure and Surface Photovoltage of a Series of Ni(II) Coordination Polymers, *European Journal of Inorganic Chemistry*, 2006(24), 5130–5137.
- [62] Kita, E., Marai, H., Zając, K., (2007), Synthesis and kinetic studies in aqueous solution on chromium(III) complexes with isocinchomeric acid—potential new biochromium sources, *Transition Metal Chemistry*, 33(2), 211–217.
- [63] Jin, J., Li, D., Li, L., Han, X., Cong, S., Chi, Y., Niu, S., (2011), Synthesis, crystal structure and surface photo-electric property of a series of Co(II) coordination polymers and supramolecules, *Inorganica Chimica Acta*, 379(1), 44–55
- [64] Jin, J., Ding, Y., Gong, Y.-Y., Cong, S.-M., Chi, Y.-X., Zhang, G.-N., Niu, S.-Y., (2013), Synthesis, structure and surface photo-electric property of Ni(II) complexes, *Inorganica Chimica Acta*, 399, 227–235.
- [65] Manna, S. C., Jana, A. D., Drew, M. G. B., Mostafa, G., Ray Chaudhuri, N., (2008), Polymorphism in $[\text{Co}(\text{SCN})_4(\text{ppz-H})_2]$ (ppz, piperazine), *Polyhedron*, 27(4), 1280–1286.
- [66] Ay, B., Yildiz, E., Kani, İ., (2016), Novel heteroleptic lanthanide organic frameworks containing pyridine-2,5-dicarboxylic acid and in situ generated piperazine-2,5-dicarboxylic acid from piperazine: Hydrothermal synthesis and luminescent properties, *Journal of Solid State Chemistry*, 233 (2016) 44–51.
- [67] Zhang, L., Guo, J., Meng, Q., Pang, H., Chen, Z., Sun, D., (2012), Two novel isostructural Ln (III) 3D frameworks supported by 3,6-dibromobenzene-1,2,4,5-tetracarboxylic acid and in situ generated oxalate: Syntheses, characterization and photoluminescent property, *Inorganic Chemistry Communications*, 26, 51–55.
- [68] Hu, J. -Y., Wen, J., Yang, X. -G., Chen, M., Liu, C.-S., (2013), A 3-D lanthanide–organic framework based on in situ formed benzene-1,2,3,4-tetracarboxylate ligand, *Inorganic Chemistry Communications*, 33, 25–28.
- [69] Singha, D. K., Majee, P., Mondal, S. K., Mahata, P., (2017), Selective Luminescence-Based Detection of Cd^{2+} and Zn^{2+} Ions in Water Using a Proton-Transferred Coordination Polymer–Amine Conjugate Pair, *Chemistry Select*, 2(11), 3388–3395.
- [70] Singha, D. K., Mahata, P., (2017), Coordination polymer-derived nano-sized zinc ferrite with excellent performance in nitro-explosive detection, *Dalton Transactions*, 46(34), 11344–11354.

- [71] Debamalya, G., Debal, K. S., Lebedev, O. I., Seikh, M. M., Mahata, P., (2019), A remarkable annealing time effect on the magnetic properties of single-source coordination polymer precursor-derived CoFe_2O_4 nanoparticles, *New Journal of Chemistry*, 43(48), 19044–19052.
- [72] Debamalya, G., Ananya, P., Susanta, G., Arup, G., Seikh, M. M., Mahata P., (2019), Metal Ion Sensing and Electrochemical Behaviour of MOF Derived ZnCo_2O_4 , *European Journal of Inorganic Chemistry*, 3076–3083.
- [73] Moghimi, A., Sharif, M. A., Shokrollahi, A., Shamsipur, M., Aghabozorg, H., (2005), A Novel Proton Transfer Compound Containing 2, 6-Pyridinedicarboxylic Acid and Creatinine and its Zinc(II) Complex-Synthesis, Characterization, Crystal Structure, and Solution Studies, *Zeitschrift für anorganische und allgemeine Chemie*, 631(5), 902–908.
- [74] Aghabozorg, H., Akbari Saei, A., Ramezanipour, F., (2005), 2,6-Diaminopyridinium pyridinium-2,6-dicarboxylate: a redetermination, *Acta Crystallographica*, E61(10), o3242–o3244.
- [75] Aghabozorg, H., Manteghi, F., Ghadermazi, M., (2007), Ammonium 6-carboxypyridine-2-carboxylate, *Acta Crystallographica*, E63(11), o4454–o4454.
- [76] Sheshmani, S., Aghabozorg, H., Ghadermazi, M (2007), Piperazinedium pyridine-2,5-dicarboxylate dehydrate, *Acta Crystallographica*, E63(6), o2869–o2869.
- [77] Aghabozorg, H., Ghadermazi, M., Sheshmani, S., (2006), A novel proton-transfer compound: piperazinium oxalate monohydrate, *Acta Crystallographica*, E62(8), o3287–o3289.
- [78] Gonzalez-Baró, A. C., Castellano, E. E., Piro, O. E., Parajón-Costa, B. S., (2005), Synthesis, crystal structure and spectroscopic characterization of a novel bis (oxo-bridged) dinuclear vanadium(V)–dipicolinic acid complex, *Polyhedron*, 24(1), 49–55.
- [79] Setlow B, Setlow P., (1993), Dipicolinic acid greatly enhances the production of spore photoproduct in bacterial spores upon ultraviolet irradiation, *Applied and Environmental, Microbiology*, 59, 640–43.
- [80] Olar, R., Badea, M., Marinescu, D., Chifiriuc, C.-M., Bleotu, C., Grecu, M. N., Finaru, A., (2010), Prospects for new antimicrobials based on N,N-dimethylbiguanide complexes as effective agents on both planktonic and adhered microbial strains, *European Journal of Medicinal Chemistry*, 45(7), 2868–2875.
- [81] Gao, H.-L., Yi, L., Zhao, B., Zhao, X.-Q., Cheng, P., Liao, D.-Z., Yan, S.-P., (2006), Synthesis and Characterization of Metal–Organic Frameworks Based on 4-Hydroxypyridine-2,6-dicarboxylic Acid and Pyridine-2,6-dicarboxylic Acid Ligands, *Inorganic Chemistry*, 45(15), 5980–5988.
- [82] Zhao, B., Yi, L., Dai, Y., Chen, X.-Y., Cheng, P., Liao, D.-Z., Jiang, Z.-H., (2005), Systematic Investigation of the Hydrothermal Syntheses of Pr(III)–PDA (PDA=Pyridine-2,6-dicarboxylate Anion) Metal–Organic Frameworks, *Inorganic Chemistry*, 44(4), 911–920.

- [83] Aghabozorg, H., Ghadermazi, M., Manteghi, F., Nakhjavan, B., (2006), A Proton Transfer Compound of Piperazine with Pyridine-2,6-dicarboxylic Acid and Its Palladium(II) and Thallium(III) Complexes – Synthesis, Characterization and Crystal Structure, *Zeitschrift für anorganische und allgemeine Chemie*, 632(12-13), 2058–2064.
- [84] Aghabozorg, H., Manteghi, F., Ghadermazi, M., Mirzaei, M., Salimi, A. R., Shokrollahi, A., Eshtiagh-Hosseini, H., (2009), A novel supramolecular compound of cadmium(II): Synthesis, characterization, crystal structure, ab initio HF, DFT calculations and solution study, *Journal of Molecular Structure*, 919(1-3), 381–388.
- [85] Aghabozorg, H., Ghadermazi, M., Zabihi, F., Nakhjavan, B., Soleimannejad, J., Sadr-khanlou, E., Moghimi, A., (2008), Novel Complexes of Zinc(II) with Different Proton Transfer Ion Pairs Obtained from Dipicolinic Acid: Synthesis, Characterization and X-ray Crystal Structure, *Journal of Chemical Crystallography*, 38(9), 645–654.
- [86] Aghabozorg, H., Ghasemikhah, P., Ghadermazi, M., Attar Gharamaleki, J., Sheshmani, S., (2006), Piperazinium bis(pyridine-2,6-dicarboxylato)mercurate(II) hexahydrate, *Acta Crystallographica*, E62(9), m2269–m2271.
- [87] Aghabozorg, H., Manteghi, F., Ghadermazi, M., Mirzaei, M., Salimi, A. R., Eshtiagh-Hosseini, H., (2010), Synthesis, X-Ray characterization and molecular structure of a novel supramolecular compound of antimony(III); Theoretical investigation on molecular and electronic properties based on the ab initio HF and various DFT methods, *Journal of Iranian Chemical Society*, 7(2), 500–509.
- [88] Aghabozorg, H., Nemati, A., Derikvand, Z., Ghadermazi, M., (2008), Poly[piperazinediium [[aqua]bismuthate(III)]-di- μ -pyridine-2,6-dicarboxylato-bismuthate(III)-di- μ -pyridine-2,6-dicarboxylato] monohydrate], *Acta Crystallographica*, e64(2), m374–m374.
- [89] Aghabozorg, H., Motieyan, E., Salimi, A. R., Mirzaei, M., Manteghi, F., Shokrollahi, A., Eshtiagh-Hosseini, H., (2010), Piperazinediium, Zr(IV) and Ce(IV) pyridine-2,6-dicarboxylates: Syntheses, characterizations, crystal structures, ab initio HF, DFT calculations and solution studies, *Polyhedron*, 29(5), 1453–1464.
- [90] Aghabozorg, H., Moghimi, A., Manteghi, F., Ranjbar, M., (2005), A Nine-Coordinated Zr(IV) Complex and a Self-Assembling System Obtained from a Proton Transfer Compound Containing 2,6-Pyridinedicarboxylate and 2,6-Pyridinediammonium; Synthesis and X-ray Crystal Structure, *Zeitschrift für anorganische und allgemeine Chemie*, 631(5), 909–913.
- [91] Ghadermazi, M., Sheshmani, S., Shokrollahi, A., Arokhloo, J. K., (2014), Metal–organic polymers of Sr(II) and Ce(IV): structural studies, supramolecular synthons, and potentiometric measurements, *Journal of Coordination Chemistry*, 67(21), 3492–3509.
- [92] Chandramohan, A., Bharathikannan, R., Kandhaswamy, M. A., Chandrasekaran, J., Kandavelu, V., (2008), Synthesis, crystal growth, spectral, thermal and optical properties of acenaphthene picrate, *Crystal Research and Technology*, 43(1), 93–98.

- [93] K. Nakamoto, *Infrared and Raman Spectra of Inorganic and Coordination Compounds, Part B*, 5th Edn, Wiley, New York (1997)
- [94] Jayaraman, K., Choudhury, A., Rao, C. N. R., (2002), Sulfates of organic diamines: hydrogen-bonded structures and properties, *Solid State Sciences*, 4(3), 413–422.
- [95] Singh, M., Lofland, S. E., Ramanujachary, K. V., Ramanan, A., (2010), Crystallization of Anderson–Evans Type Chromium Molybdate Solids Incorporated with a Metal Pyrazine Complex or Coordination Polymer, *Crystal Growth and Design*, 10(12), 5105–5112.
- [96] Pavani, K., Singh, M., Ramanan, A., (2011), Oxalate Bridged Copper Pyrazole Complex Templated Anderson-Evans Cluster Based Solids, *Australian Journal of Chemistry*, 64(1), 68–76.
- [97] Büyükkıdan, N., Yenikaya, C., İlkimen, H., Karahan, C., Darcan, C., Şahin, E., (2012), Synthesis, characterization, and antimicrobial activity of a novel proton salt and its Cu(II) complex, *Russian Journal of Coordination Chemistry*, 39(1), 96–103.
- [98] Büyükkıdan, N., Yenikaya, C., İlkimen, H., Karahan, C., Darcan, C., Korkmaz, T., Süzen, Y., (2015), Synthesis, characterization and biological activities of metal(II) dipicolinate complexes derived from pyridine-2,6-dicarboxylic acid and 2-(piperazin-1-yl)ethanol, *Journal of Molecular Structure*, 1101, 139–146.
- [99] Kirillova, M. V., Guedes da Silva, M. F. C., Kirillov, A. M., Fraústo da Silva, J. J. R., Pombeiro, A. J. L., (2007), 3D hydrogen bonded heteronuclear CoII, NiII, CuII and ZnII aqua complexes derived from dipicolinic acid, *Inorganica Chimica Acta*, 360(2), 506–512.
- [100] Yeşilel, O. Z., İlker, İ., Refat, M. S., Ishida, H., (2010), Syntheses and characterization of two copper pyridine-dicarboxylate compounds containing water clusters, *Polyhedron*, 29(11), 2345–2351.
- [101] Raissi Shabari, A., Ghoddoosi, N., Pourayoubi, M., Moradi, S., (2011), Piperazine-1,4-dium bis(pyridine-2,6-dicarboxylato-κ3O2,N,O6)cobaltate(II) tetrahydrate, *Acta Crystallographica*, E67(7), m985–m986.
- [102] Thirumurugan, A., Cheetham, A. K., (2010), Anionic Metal-Organic Frameworks of Bismuth Benzenedicarboxylates: Synthesis, Structure and Ligand-Sensitized Photoluminescence, *European Journal of Inorganic Chemistry*, 3823–3828.
- [103] Hakimi, M., Motieian, E., Bertolotti, F., Marabello, D., , Nunes Rodrigues, V. H., (2015), Three new bismuth(III) pyridine-2,6-dicarboxylate compounds: Synthesis, characterization and crystal structures, *Journal of Molecular Structure*, 1099, 523–533.
- [104] Ay, B., Karaca, S., Yildiz, E., Lopez, V., Nanao, M. H., Zubieta, J., (2016), In situ hydrothermal syntheses, structures and photoluminescent properties of four novel metal-organic frameworks constructed by lanthanide (Ln=Ce(III), Pr(III), Eu(III)) and Cu(I) metals with

- flexible dicarboxylate acids and piperazine-based ligands, *Journal of Solid State Chemistry*, 233, 415–421.
- [105] Ay, B., Yildiz, E., Felts, A. C., Abboud, K. A., (2016), Hydrothermal synthesis, structure, heterogeneous catalytic activity and photoluminescent properties of a novel homoleptic Sm(III)-organic framework, *Journal of Solid State Chemistry*, 244, 61–68.
- [106] Gunasekaran, S., Anita, B., Spectral investigation and normal coordinate analysis of piperazine, *Indian Journal of Pure and Applied Physics*, 46 (2008) 833–838.
- [107] Ni, Y., Tao, J., Jin, J., Lu, C., Xu, Z., Xu, F., Kang, Z., (2014), An investigation of the effect of ligands on thermal stability of luminescent samarium complexes, *Journal of Alloys and Compounds*, 612, 349–354.
- [108] Ay, B., Doğan, N., Yildiz, E., Kani, İ., (2015), A novel three dimensional samarium(III) coordination polymer with an unprecedented coordination mode of the 2,5-pyridinedicarboxylic acid ligand: Hydrothermal synthesis, crystal structure and luminescence property, *Polyhedron*, 88, 176–181.
- [109] Li, M., Feng, R., Huang, Q. Z., Feng, Y. Q., Shi, H. Z., (2014), Synthesis, crystal structure and luminescent property of a novel lanthanide coordination polymer containing (H₂O)₂₀ clusters, *Inorganic Chemistry Communications*, 50, 8–12.
- [110] Derakhshandeh, P. G., Soleimannejad, J., Janczak, J., (2017), Preparation of CeO₂ nanoparticles from a new cerium(III) supramolecular compound, *Inorganica Chimica Acta*, 467, 132–135.
- [111] Ay, B., Yildiz, E., Kani, İ., (2018), Semiconducting lanthanide polymers of pyridine-2,6-dicarboxylate: Hydrothermal synthesis, structural characterization, electrical conductivity and luminescence properties, *Polyhedron*, 142, 1–8.

APPENDICES

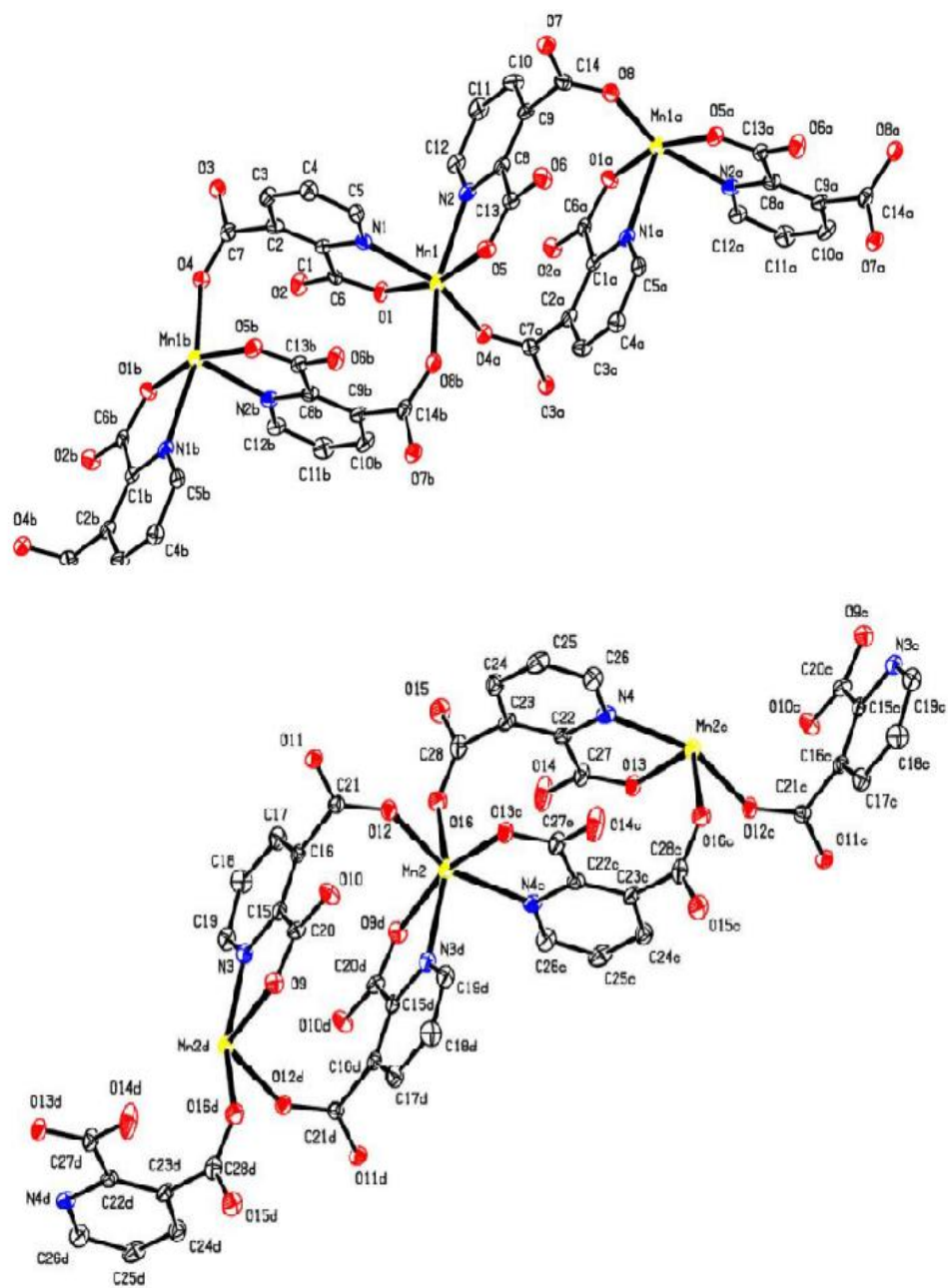


Figure A1. Polymeric chains of Mn²⁺ complex (2)

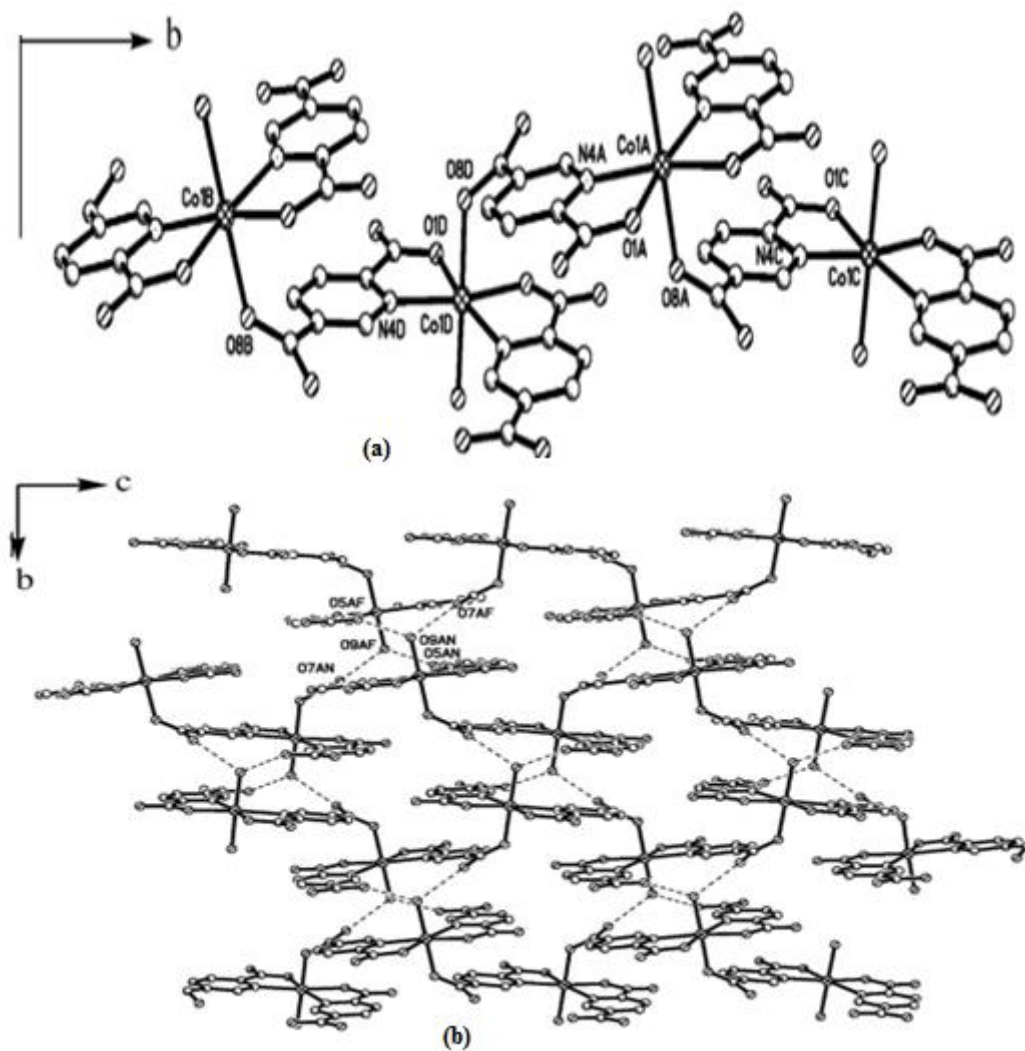


Figure A2. (a) The 1-D infinite chain of **5** along b-axis. (b) The 2-D H-bonded layer of **5** on bc plane

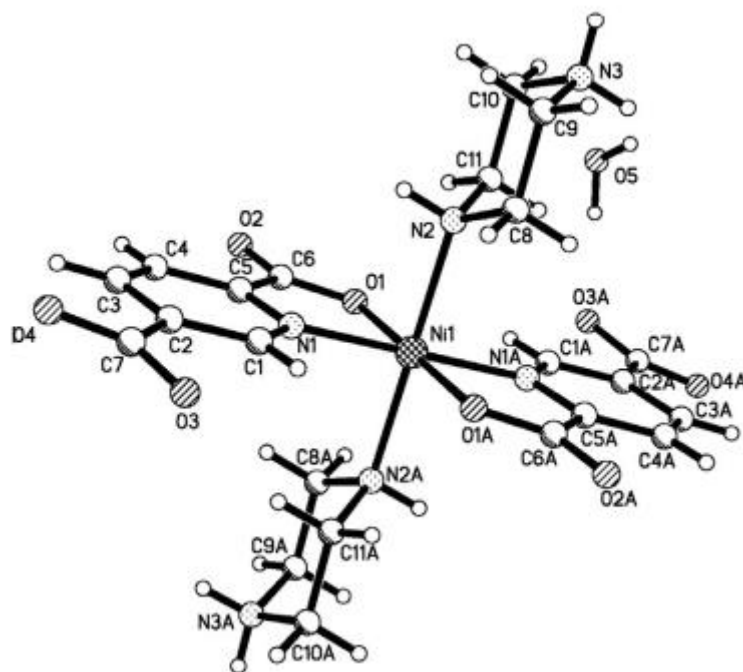


Figure A3. Molecular structure of $[\text{Ni}(\text{Py-2,5-Dc})_2(\text{HPpz})_2] \cdot \text{H}_2\text{O}$ (6)

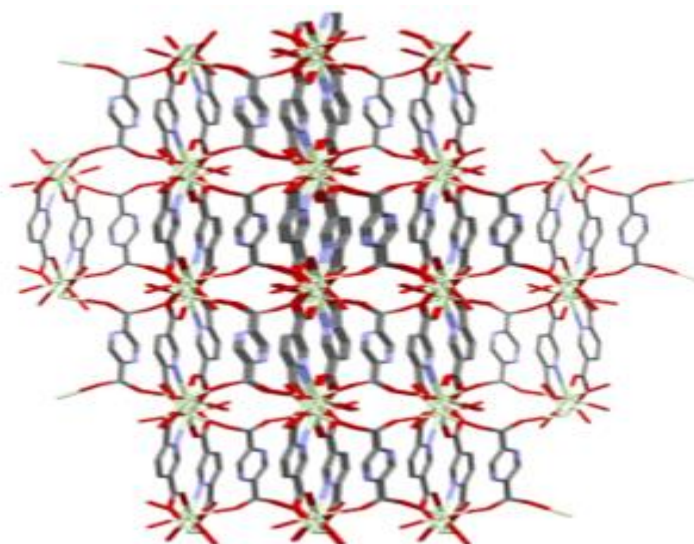


Figure A4. 3-D structure of compound 8

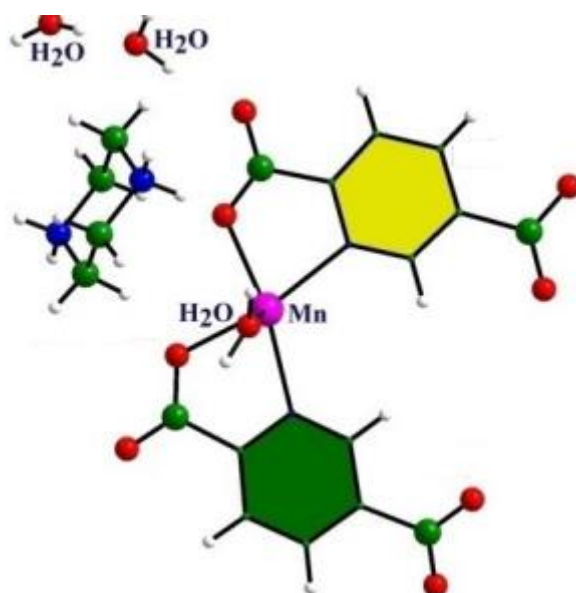
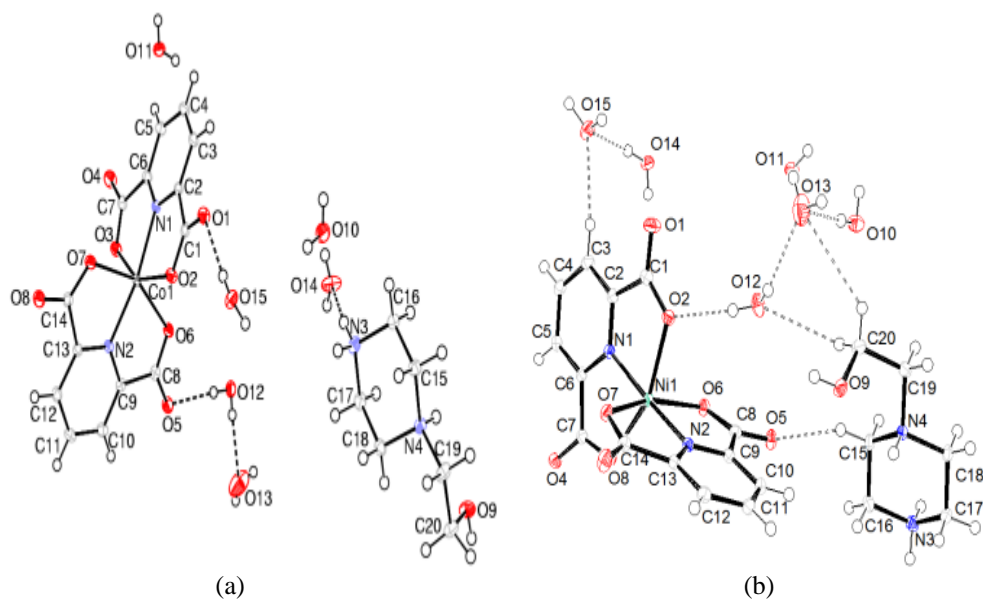


Figure A5. The asymmetric unit of $\{(H_2Ppz)[Mn(Py-2,5-Dc)_2(H_2O)] \cdot 2H_2O\} (9)$



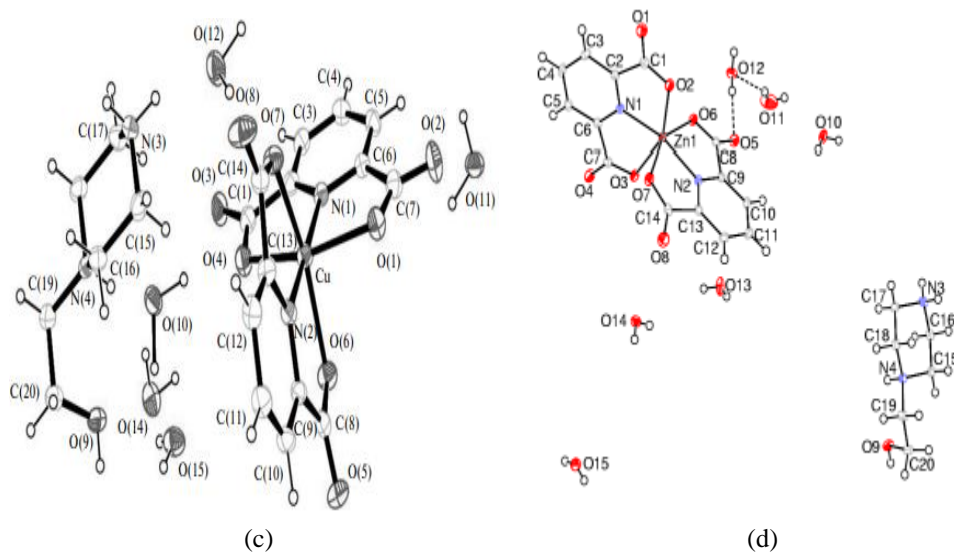


Figure A6. Molecular structure of complexes (a) for **23**, (b) for **24**, (c) for **25** and (d) for **26**